Cosmology with weak lensing voids and peaks

CHRISTOPHER THOMAS DAVIES

How to cite:

DAVIES, CHRISTOPHER THOMAS (2021) Cosmology with weak lensing voids and peaks. Doctoral thesis, Durham University.

Cosmology with weak lensing voids and peaks

Christopher T. Davies

Abstract: The goal of modern cosmology is to measure cosmological parameters as accurately and precisely as possible, with future stage-IV surveys aiming to achieve this at the sub-percent level. To maximise the utility of such surveys, we must develop methods that can more fully capture the wealth of cosmological information contained within the data. In this thesis, I develop new weak gravitational lensing statistics as a means to achieve this. To this end, I study in detail the properties of weak lensing voids and peaks. First, I establish weak lensing voids as a new statistic that corresponds to extended underdense regions of convergence maps, and show that they offer several advantages over galaxy voids, including larger lensing profile amplitudes. I then study a range of void finders to test the impact of the void definition on the resulting weak lensing void properties, and identify the tunnel algorithm as the most promising void finder. This is followed by wCDM parameter forecasts from an LSST-like survey for weak lensing voids, which shows that they perform better than the standard shear two-point correlation function. I then show that weak lensing voids also have higher sensitivity to modified gravity theories than galaxy voids. Next, I study the clustering of weak lensing peaks and present simple scaling relations for their two-point correlation function. I then make similar parameter forecasts for the peak two-point correlation function, and show that when combined with the peak abundance, peaks can give tighter constraints than the shear two-point correlation function. Finally, both the void and peak statistics presented in this thesis offer complementary parameter degeneracy directions to the shear two-point correlation function. This makes these statistics invaluable for cosmological parameter measurements from ongoing and future weak lensing surveys.

Cosmology with weak lensing voids and peaks

Christopher T. Davies

A thesis presented for the degree of
Doctor of Philosophy

Institute for Computational Cosmology
Department of Physics
Durham University
United Kingdom

October 2021

Contents

Declaration

The work in this thesis is based on research carried out in the Institute for Computational Cosmology, Department of Physics, Durham University, United Kingdom. No part of this thesis has been submitted elsewhere for any other degree or qualification and it is all my own work unless referenced to the contrary in the text.

The content presented in Chapters 2, 3, 4, 5, and 6 have been published in:

Davies, C.T., Cautun, M., Li, B. (2018) Weak lensing by voids in weak lensing maps. MNRAS, 480, L101. (Chapter 2)

Davies, C.T., Paillas, E., Cautun, M., Li, B. (2021) Optimal void finders in weak lensing maps. MNRAS, 500(2), 2417. (Chapter 3)

Davies, C.T., Cautun, M., Giblin, B., Li, B., Harnois-Déraps, J. Cai, Y. (2020) Constraining cosmology with weak lensing voids. arXiv e-prints, arXiv:2010.11954. (Chapter 4)

Davies, C.T., Cautun, M., Li, B. (2019) Cosmological test of gravity using weak lensing voids. MNRAS, 490(4), 4907. (Chapter 5)

Davies, C.T., Cautun, M., Li, B. (2019) The self-similarity of weak lensing peaks. MNRAS, 488(4), 5833. (Chapter 6)

The author of the thesis was primarily responsible for all aspects of this publication.

Acknowledgements

Anna: Thank you for your endless love and support. I realise as I look back how much easier you have made everything.

Baojiu and Marius: Thank you for being an excellent supervisory team. In particular I thank Baojiu for being so attentive to both my work and my broader development as an academic, and I thank Marius for always telling me when "something looks fishy".

Coffee Collect team and attendees: Thank you for the endless entertainment, this was always the best reason to take a break. In particular, thank you Andrew Griffin for showing me the way of the coffee collect.

Office mates: Josh and Cristian, thank you for doing the whole stint with me. Piotr, Ellen and Joaquin, thanks for being a part of the journey. You were all great, and I will miss working alongside all of you.

Aidan, Alex B, Alex S, Alex E, Alice, Amy, Andrew R, Aris, Anau, Ash, Behzad, Beni, Calvin, Cameron, Carol, Duncan, Ed, Giorgio, Jack B, Jack R, Jacob, Jake, James, Louise, Makun, Oliver, Ra'ad, Raj, Ruari, Sasha, Sergio, Stefan, Steve, Stuart, Tilly, Tom C, Tom R, Ugne, Vicky, Victor, Will and Willem: Thanks for being great department mates! (Sorry to those I inevitably missed).

My family: Thank you for having me home for as much holiday as I can squeeze in.

Brick $quad, Bownty Hunter$, Prebend St Victim Support and Morally Ambiguous Noobs: Thank you for so many excuses to go and do something fun. But less thanks for making me type out our ridiculous group chat names.

Chapter 1

Introduction

Under the current paradigm of modern cosmology, we measure the properties of the Universe by identifying its constituent components, determining their nature and calculating their contribution to the Universe's total content and its expansion history.

Over recent years, by adopting this methodology, and through the concordance of many observations, the standard cosmological model, ΛCDM (Λ-cold-dark-matter) has emerged. These observations include the measurements of type Ia supernova light curves (Riess et al., 1998; Perlmutter et al., 1999), which reveal an accelerated expansion at low redshift, that could be driven by a cosmological constant, Λ, coined dark energy. The measurements of temperature fluctuation in the cosmic microwave background (CMB) give strong evidence for the presence of cold dark matter (Planck Collaboration et al., 2018), the dominant matter component in this model, which is a form of non-relativistic matter that only interacts with gravity. Together, dark energy and dark matter, the so called dark sector, make up roughly 95% of the Universe's total contents today (Planck Collaboration et al., 2018). The remaining 5% of the Universe consists of baryonic matter, which interacts with all four fundamental forces, and is the only component of this model (alongside photons) that we can directly observe. Obviously, inferring the nature of the Universe from only 5% of its contents is a remarkably difficult task and poses many challenges. To achieve this goal, we must consider alternative models and extract information from a plethora of observations of the Universe's properties.

Many models beyond ΛCDM exist, and one such example that will be of interest in this thesis is modified gravity, which is a class of models in which the large-scale behaviour of gravity is different from General Relativity (GR). These models can be employed as tests of GR on cosmological scales, and may also offer an alternative explanation to the cosmic acceleration.

In order to ensure that our inferences about the underlying cosmological model of the Universe are as accurate as possible, it is important to measure various different observational properties of the universe, each of which serve as independent probes of the universe. With more probes, we are able to infer more about the underlying cosmological model. This approach allows us to test for the presence of new physics, such as modified gravity, or for unknown systematics, which may affect different probes in different ways.

The presence of any of the above unknown features will lead to disagreements in parameter measurements between probes. One such example in modern cosmology is given by the Hubble tension, which is a disagreement between the measurements of the Hubble constant from probes at high and low redshift (Verde et al., 2019).

The main goal of this thesis is therefore to present a new method that can be exploited to further our understanding of the universe and give improved cosmological parameter measurements. First I will present the relevant background information and use it to exemplify how we are able to model the different components that make up the universe. I will also present the relevant theory for inferring the distribution of dark matter in the universe through weak gravitational lensing (WL), a powerful probe that allows us to confront the challenge of probing dark matter through observations of baryonic matter alone. Then I will discuss how to interpret WL as a cosmological probe, along with the standard techniques used in WL analysis.

1.1 Friedmann–Lemaître–Robertson–Walker cosmology

In this section I will present the Friedmann–Lemaître–Robertson–Walker (FLRW) cosmology, and the corresponding equations. First we start with the cosmological principle, an assumption that on large scales (roughly above 100 Mpc) the universe is homogeneous and isotropic. This assumption allows us to define the following line element,

$$ds^2 = a^2 d\boldsymbol{x}^2 - c^2 dt^2 \,, \tag{1.1.1}$$

where $a = a(t)$ is the scale factor of the universe, $\boldsymbol{x} = (x_1, x_2, x_3)$ is a vector corresponding to the three spatial dimensions, and t corresponds to time.

Next we require Einstein's field equations,

$$G_{\mu\nu} + \Lambda g_{\mu\nu} = \frac{8\pi G}{c^4} T_{\mu\nu} \,, \tag{1.1.2}$$

with

$$G_{\mu\nu} = R_{\mu\nu} - \frac{1}{2} R_{\mu\nu} g_{\mu\nu} \,. \tag{1.1.3}$$

Here, $G_{\mu\nu}$ is the Einstein tensor, Λ is the cosmological constant, $g_{\mu\nu}$ is the metric tensor, G is Newton's gravitational constant, c is the speed of light, $T_{\mu\nu}$ is the stress-energy tensor, $R_{\mu\nu}$ is the Ricci curvature tensor and R is the scalar curvature. The Greek indices run through (0,1,2,3). This equation shows how the geometry of space-time (left hand side) is related to the distribution of matter (right hand side). Through the combination of Eqs. (1.1.1) and (1.1.2) it is possible to derive the following two FLRW equations, assuming a perfect fluid,

$$\left(\frac{\dot{a}}{a}\right)^2 = \frac{8\pi G\rho}{3} - \frac{kc^2}{a^2} + \frac{\Lambda c^2}{3} \,, \tag{1.1.4}$$

$$\frac{\ddot{a}}{a} = \frac{-4\pi G}{3}\left(\rho + \frac{3p}{c^2}\right) + \frac{\Lambda c^2}{3} \,. \tag{1.1.5}$$

Here, the dot (double dot) represents the time derivative (second time derivative), k is the spatial curvature, ρ is the matter density and p is the pressure.

From Eq. (1.1.4) we can define the critical density $\rho_c(t)$, which is the density required for a spatially flat universe, which gives

$$\rho_c(t) = \frac{3H(t)^2}{8\pi G} \,, \tag{1.1.6}$$

where $H(t) = \dot{a}/a$ is the Hubble constant. From here we can rewrite Eq. (1.1.4) in the following way (Ω is the density *parameter*),

$$\left(\frac{H}{H_0}\right)^2 = \frac{\Omega_r}{a^4} + \frac{\Omega_m}{a^3} + \frac{\Omega_k}{a^2} + \Omega_\Lambda \,, \tag{1.1.7}$$

where $\Omega_r = \rho_r/\rho_c$ and ρ_r is the present day radiation density, $\Omega_m = \rho_m/\rho_c$ and ρ_m is the present day total matter density (including both baryons and dark matter), $\Omega_k = -3kc^2/8\pi G\rho_c$ and $\Omega_\Lambda = \Lambda c^2/8\pi G\rho_c$. Note that here, ρ_c is the present day value of the critical density. Eq. (1.1.7) shows how the expansion history of the universe depends on its contents, and that this can be split up into its constituent components, including the matter density, radiation density, spatial curvature and a cosmological constant. Certainly there are other cosmological parameters not presented in the above equation that are also of interest, such as those dictating the clustering of matter, the dark energy equation of state parameter and modified gravity parameters. Nonetheless, this highlights how the different components of the universe come together to produce what we observe, which is one dominated by the dark sector, and that in order to fully understand the nature of the universe we must develop cosmological probes and statistical methods that allow us to accurately determine the values of each cosmological parameter.

1.2 Gravitational lensing

Gravitational lensing is the physical phenomenon in which light is deflected by gravitational potentials along the line of sight, which results in the distortion and magnification of distant galaxy images. Because the lensing is sensitive to the gravitational potentials, this allows us to probe both the baryonic and dark matter content of the universe. This phenomenon can be split into two regimes, strong and weak gravitational lensing. For strong gravitational lensing, observed galaxy images are visibly distorted and multiple images of the same source galaxy can be produced. In the case of weak gravitational lensing (WL), where image distortions are very small, the underlying lensing signal can be recovered by statistically correlating distortions in many source galaxy images over extended patches of the sky (Bacon et al., 2000; Kaiser et al., 2000; Van Waerbeke et al., 2000; Wittman et al., 2000). In particular, WL is sensitive to moderate variations in the mass distribution, such as the large-scale structure (LSS) of the universe, and allows us to map the cosmic mass content over a large range of scales, from kiloparsecs to hundreds of Megaparsecs (see Bartelmann & Schneider, 2001; Kilbinger, 2015, for a review).

For WL surveys, the precision with which cosmological parameters can be measured increases both with the survey area (which reduces the cosmic variance), and with the galaxy source number density (which reduces the noise in the measured WL signal). Maximising both of these features significantly increases costs, and so, in the absence of more powerful telescopes, the current generation of surveys tend to prioritise only one of these aspects. The current generation of WL surveys include DES (DES Collaboration et al., 2021), HSC (Hikage et al., 2019) and KiDS (Asgari et al., 2020). These surveys have a range of sky coverages, at 4143, 137 and 777 deg^2, and a range of source galaxy number densities, at 5.9, 17 and 6.2 arcmin^{-2}, respectively. It is clear that each survey in the current generation occupies a distinct position in the trade off between survey area and source number density, which makes the surveys complementary to each other. For the future generations of surveys, such as LSST and Euclid, the goal is to maximise both the survey area and the galaxy source number density, both of which will cover roughly half the sky ($\sim 20000\ \mathrm{deg}^2$) with a galaxy source number density at $\sim 25\ \mathrm{arcmin}^{-2}$. The increased amount of data from these surveys will prove invaluable in making WL measurements an exceptional observational probe of the Universe. In addition, both the current and upcoming generations of WL surveys can greatly benefit from the development of new statistics that can extract information beyond the standard shear two-point correlation function, which is a powerful and cost saving alternative to increasing the survey area or source density.

In this section I present the relevant theory and explanations for interpreting WL measurements.

1.2.1 Weak gravitational lensing theory

The lens equation for a gravitationally lensed image is

$$\boldsymbol{\alpha} = \boldsymbol{\theta} - \boldsymbol{\beta} \, , \tag{1.2.1}$$

where $\boldsymbol{\alpha}$ is the deflection angle between $\boldsymbol{\beta}$, the true position of the source on the sky, and $\boldsymbol{\theta}$, the observed position of the lensed image. The corresponding Jacobian matrix of the (linear) lens mapping is the deformation matrix $\mathbf{A}$,

$$A_{ij} = \frac{\partial \beta_i}{\partial \theta_j} = \delta_{ij} - \frac{\partial \alpha_i}{\partial \theta_j} \, . \tag{1.2.2}$$

Under the Born approximation and neglecting lens-lens coupling and other second-order effects, the deflection angle can be expressed as the gradient of a 2D lensing potential ψ,

$$\boldsymbol{\alpha} = \boldsymbol{\nabla} \psi \, , \tag{1.2.3}$$

where ψ is given by

$$\psi(\boldsymbol{\theta}, \chi) = \frac{2}{c^2} \int_0^{\chi} \frac{\chi - \chi'}{\chi \chi'} \Phi(\chi' \boldsymbol{\theta}, \boldsymbol{\theta}) d\chi' \, . \tag{1.2.4}$$

Here, χ is the comoving distance from the observer to the source and χ' is the comoving distance from the observer to the continuously-distributed lenses, which is also the integration variable, and Φ is the 3D lensing potential of the lens. Φ is related to the non-relativistic matter density contrast, $\delta = \rho/\bar{\rho} - 1$, through the Poisson equation

$$\nabla^2 \Phi = 4\pi G a^2 \bar{\rho} \delta \, , \tag{1.2.5}$$

where ρ is the matter density of the universe (with a bar denoting the mean).

Eq. (1.2.4) shows that the lensing potential is a line-of-sight integral of the matter distribution from the source to the observer. The contribution that matter at distance χ' along the line of sight makes to the total lensing potential is weighted by $(\chi - \chi')/\chi\chi'$ and so depends on its distances from the source and observer.

Eq.(1.2.3) allows Eq. (1.2.2) to be expressed in terms of ψ

$$A_{ij} = \delta_{ij} - \partial_i \partial_j \psi \, , \tag{1.2.6}$$

where partial derivatives are taken with respect to $\boldsymbol{\theta}$. The matrix $\boldsymbol{A}$ can be parameterised through the more physically instructive terms convergence, κ, and shear, $\gamma = \gamma_1 + i\gamma_2$, as

$$\boldsymbol{A} = \begin{pmatrix} 1-\kappa-\gamma_1 & -\gamma_2 \\ -\gamma_2 & 1-\kappa+\gamma_1 \end{pmatrix} . \tag{1.2.7}$$

This parameterisation allows the convergence and shear to be related to the lensing potential via

$$\kappa \equiv \frac{1}{2}\nabla^2_{\boldsymbol{\theta}}\psi\,, \tag{1.2.8}$$

and

$$\gamma_1 \equiv \frac{1}{2}\left(\nabla_{\boldsymbol{\theta}_1}\nabla_{\boldsymbol{\theta}_1} - \nabla_{\boldsymbol{\theta}_2}\nabla_{\boldsymbol{\theta}_2}\right)\psi, \qquad \gamma_2 \equiv \nabla_{\boldsymbol{\theta}_1}\nabla_{\boldsymbol{\theta}_2}\psi, \tag{1.2.9}$$

where $\nabla_{\boldsymbol{\theta}} \equiv (\chi')^{-1}\nabla$. It is important to note that WL convergence maps are not directly observable, but can be obtained from the reduced shear, $g = \gamma/(1-\kappa)$, where in the weak lensing regime it can be assumed that $g = \gamma$ because $\kappa \ll 1$.

Eq. (1.2.8) can be interpreted as a 2D Poisson equation, and so by substituting Eq. (1.2.5) and Eq. (1.2.4) into Eq. (1.2.8), the convergence can be expressed in terms of the matter overdensity

$$\kappa(\boldsymbol{\theta}, \chi) = \frac{3H_0^2\Omega_{\rm m}}{2c^2}\int_0^{\chi}\frac{\chi-\chi'}{\chi}\chi'\frac{\delta(\chi'\boldsymbol{\theta}, \chi')}{a(\chi')}d\chi'\,. \tag{1.2.10}$$

This shows that the observed WL convergence can be interpreted as the projected density perturbation along the line of sight, weighted by the lensing efficiency factor $(\chi-\chi')\chi'/\chi$. Here, the lensing efficiency is greatest at $\chi' = \chi/2$, when the lens is halfway between the source and the observer.

The above derivation assumes a fixed source plane. However, in real WL observations, the source galaxies do not occupy a single plane at a fixed distance from the observer. The observed catalogue of source galaxies has a probability distribution $n(\chi)$ that spans over a range of χ values, and Eq. (1.2.10) must be weighted by this source galaxy distribution in order to obtain $\kappa(\boldsymbol{\theta})$ (see, e.g., Kilbinger, 2015, for details)

$$\kappa(\boldsymbol{\theta}) = \int_0^{\chi} n(\chi')\kappa(\boldsymbol{\theta}, \chi')d\chi'\,. \tag{1.2.11}$$

In this thesis, we will measure the κ profile, $\kappa(r)$, in and around objects defined within the WL map. However, as $\kappa(r)$ is not directly observable, it is also useful to relate it to the radial tangential shear profile, $\gamma_t(r)$, through

$$\gamma_{\rm t}(r) = \bar{\kappa}(<r) - \kappa(r)\ , \tag{1.2.12}$$

where

$$\bar{\kappa}(< r) = \frac{1}{\pi r^2} \int_0^r 2\pi r' \kappa(r') dr' \tag{1.2.13}$$

is the mean enclosed convergence within radius r. Notice that here and throughout this thesis we use r rather than θ to represent the 2D projected distance from the centre of a circle placed on the map, which is a definition that will be useful later on in this thesis.

WL observations rely on accurately measuring the shapes of galaxies, and cross correlating the shapes of neighbouring galaxies. However, any correlation in shape due to lensing is dominated by the random shapes and orientations of galaxies, which is the leading source of noise in WL observations, referred to as galaxy shape noise (GSN). Because the lensing signal is weak by definition, when identifying WL peaks (local maxima in the convergence field $\kappa(\boldsymbol{\theta})$) it is convenient to express the convergence relative to the standard deviation of the corresponding GSN component of the field. This is given by

$$\nu = \frac{\kappa}{\sigma_{\rm GSN}}, \tag{1.2.14}$$

where $\sigma_{\rm GSN}$ is the standard deviation of the contributions to the signal from galaxy shape noise. $\sigma_{\rm GSN}$ can be calculated by generating mock GSN maps and applying any transformations also applied to the convergence maps, such as smoothing. Mock GSN maps are generated by assigning to pixels random convergence values from a Gaussian distribution with standard deviation

$$\sigma^2_{\rm pix} = \frac{\sigma^2_{\rm int}}{2\theta^2_{\rm pix} n_{\rm gal}}\,, \tag{1.2.15}$$

where $\theta_{\rm pix}$ is the width of each pixel, $\sigma_{\rm int}$ is the intrinsic ellipticity dispersion of the source galaxies, and $n_{\rm gal}$ is the measured source galaxy number density.

In the later Chapters it will also be useful to compare constraints from new statistics to those from the standard shear two-point correlation function. This will show how much additional information can be extracted from the techniques presented in this thesis compared to the current paradigm. The shear two-point correlation function is given by

$$\xi_{\pm}(\boldsymbol{\theta}) = \langle \gamma_t \gamma_t \rangle \pm \langle \gamma_\times \gamma_\times \rangle = \frac{1}{2\pi} \int_0^\infty dl l P_\kappa(l) J_{0,4}(l\boldsymbol{\theta})\,, \tag{1.2.16}$$

where $\gamma_t = -\mathbb{R}(\gamma e^{-2i\phi})$ (equivalent to Eq. (1.2.12), but presented for completeness), $\gamma_\times = -\mathbb{I}(\gamma e^{-2i\phi})$, ϕ is the polar angle of the separation vector $\boldsymbol{\theta}$, J_0 and J_4 are the Bessel functions for ξ_+ and ξ_- respectively, and l is the Fourier mode.

1.2.2 Interpreting weak lensing measurements

From section 1.2.1 it is clear that WL measurements correspond very closely to the projected total matter density along the line of sight. The lensing signal can be expressed in terms of both the shear and the convergence, and Fig. 1.1 shows how to physically interpret these quantities. The three rows show how each component contributes to the lensing transformation, that is the transformation that maps the unlensed image (exemplified by the green circle in this case) onto the lensed image (the black circle outlines). The top row shows this for the convergence, and the middle and bottom rows show this for the real and imaginary components of the shear. In the case of the convergence, positive (negative) values correspond to a magnification (demagnification) of the image size. For the shear, the real component stretches the image along an orthogonal set of axis, with positive (negative) values stretching the image along the x-axis (y-axis). The imaginary component of the shear behaves in the same way, except the axis upon which elongation occurs are rotated by 45 degrees relative to the former axes.

Finally, I will discuss the impact of GSN on our ability to measure WL convergence maps. Fig 1.2 shows simulated convergence maps in three cases. The left sub-panel shows the true convergence field as measured from an N-body simulation. Here, there is clear structure in the WL map, which can be easily interpreted as the projected total matter density. The middle sub-panel shows the same convergence field, but with the inclusion of GSN (that matches the noise level expected for an LSST-like survey). It is immediately apparent that the presence of GSN (which is unavoidable in WL observations) wipes out all structure in the map, which becomes indistinguishable from a noise field, and imposes significant limitations on our ability to measure the true underlying convergence field. However, this problem can be overcome through smoothing the WL map. This is shown by the right sub-panel, which is the same as the middle panel, except now the WL map is smoothed with a Gaussian filter, with a length scale of 1 arc-minute. Here, we can see that the true convergence field is mostly recovered, however some limitations remain. Whilst the GSN has been highly suppressed, it does induce some spurious features in the final WL map, and by smoothing the map to recover the physical signal, we are unable to access information about the convergence field on scales below the smoothing length. Throughout this thesis it will therefore be important to make considerations on how the WL statistics measured here are impacted by GSN.

---

[1] Image source: https://commons.wikimedia.org/wiki/File:Shear-components.svg

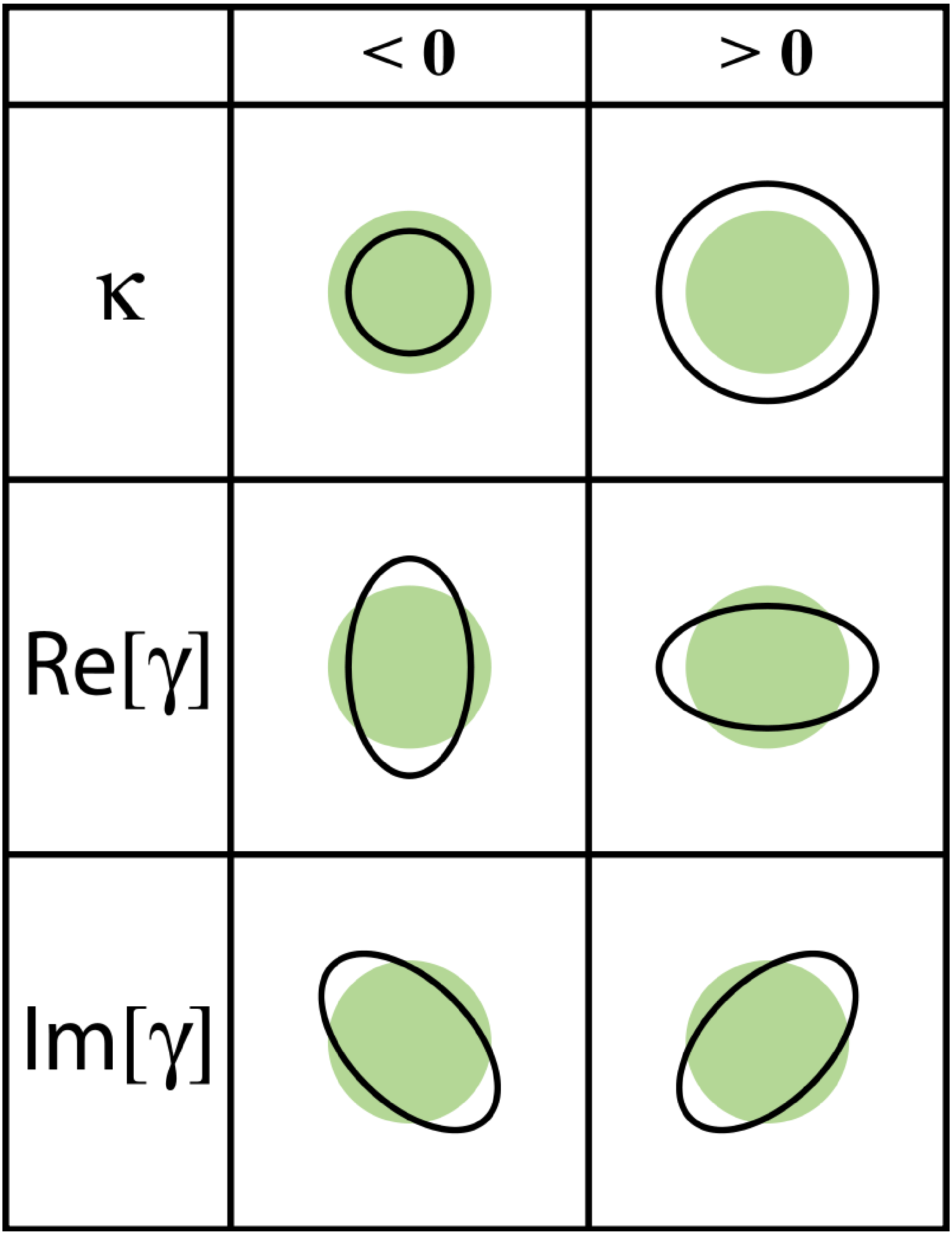

Figure 1.1: An illustration of how the lensing convergence and shear transform an unlensed image.[1]

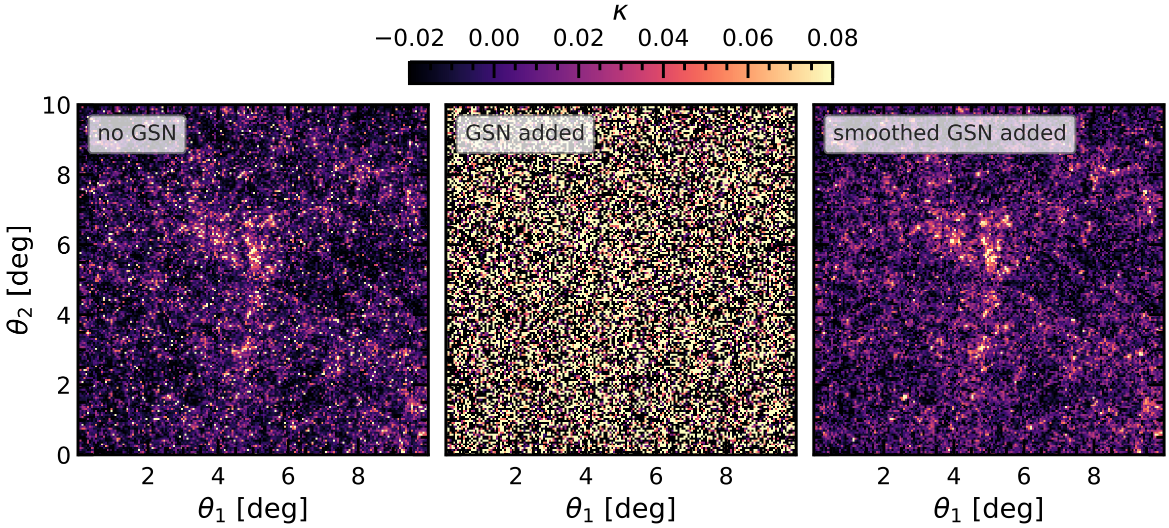

Figure 1.2: Simulated weak lensing convergence maps for three cases. Left: A convergence map without the inclusion of galaxy shape noise and no smoothing. Middle: The same as the left panel, but with galaxy shape noise added. Right: The same as the middle panel, but smoothed over a 1 arcminute scale. The convergence maps cover a 10×10 deg^2 patch of the sky. θ_1 and θ_2 denote two orthogonal directions on the sky.

1.3 This Thesis

Throughout this thesis I will present both a new probe of cosmology, WL voids, and some additional methods that can further push the utility of WL peaks. In Chapter 2 I establish how WL voids are identified as underdense 2D regions in WL convergence maps, I then show that WL voids have lensing profiles with larger amplitudes than voids identified in the galaxy distribution, indicating a higher signal-to-noise ratio for WL voids. Next, in Chapter 3 I study in detail various possible definitions of WL voids through the modification of 7 different void finders typically applied to the galaxy distribution. I test the impact of GSN on the different WL void definitions and measure the signal-to-noise ratio of their lensing profiles in each case, concluding that the tunnel algorithm offers the best compromise between high signal-to-noise and minimal impact from GSN. In Chapter 4 this is followed by a forecast of wCDM parameter constraints from WL voids for an LSST-like survey, which shows that WL voids are able to measure cosmological parameters with higher accuracy than the standard method, the shear-shear two-point correlation function. Then, in Chapter 5, I show how WL voids are also a promising probe of modified gravity and that they can distinguish between ΛCDM and modified gravity cosmologies with a signal-to-noise ratio that is over twice as large as that from galaxy voids. In 6 I present some numerically calibrated scaling relations for the clustering of WL peaks which provides a basis for further investigation into the WL void abundance scaling relation from Chapter 2. In the final science Chapter 7, by adopting the same framework from Chapter 4, I present the WL peak two point correlation function as a cosmological probe, and show that this also shows significant promise as a method to further improve the constraining power of WL peaks, and that they are complementary to WL voids. Finally, in Chapter 8 I summarise the results from this thesis and discuss possible future works.

Chapter 2

Weak lensing by voids in weak lensing maps

2.1 Introduction

The large-scale structures of the Universe, collectively called the cosmic web, describe the matter distribution in our Universe in the forms of structures such as voids, sheets, filaments and knots. These structures result from the anisotropic gravitational collapse of matter on cosmic scales. These components are intertwined in a complex web where the knots form at the intersections of filaments, filaments form at the intersections of sheets, and voids occupy the underdense space between all three (Bond et al., 1996).

Voids, which represent large regions mostly devoid of matter and galaxies, have attracted a lot of interest as powerful probes of cosmological parameters (Lavaux & Wandelt, 2012; Hamaus et al., 2016), dark energy (Li, 2011; Bos et al., 2012; Pisani et al., 2015) and dark matter (Massara et al., 2015). Voids are especially useful for testing cosmological models that make environmentally dependent predictions, such as the fifth force of modified gravity theories which, while screened in high density regions, attains maximum values in voids (Clampitt et al., 2013; Cai et al., 2015; Barreira et al., 2015; Falck et al., 2018; Baker et al., 2018). The largest constraining power of voids comes from measuring their total matter content (e.g. Cautun et al., 2018), which can be achieved via gravitational lensing (Melchior et al., 2014; Gruen et al., 2015; Clampitt et al., 2016; Sánchez et al., 2017; Cai et al., 2017), redshift space distortions (Hamaus et al., 2015; Cai et al., 2016) as well as the integrated Sachs-Wolfe effect in the cosmic microwave background (Granett et al., 2008; Nadathur, 2016). In particular, weak lensing (WL) measurements using upcoming large area and deep imaging surveys such as EUCLID and LSST will result in tight constraints on the mass profile of voids (Krause et al., 2013; Cautun et al., 2018).

Theoretically, voids correspond to low density regions in the large-scale matter field (Sheth & van de Weygaert, 2004; van de Weygaert & Platen, 2011; Aragon-Calvo & Szalay, 2013). However, because the full mass distribution is not easily observable, observational studies typically identify voids using the galaxy distribution (e.g. Nadathur, 2016). Due to the sparsity of galaxy tracers and their bias, which depends on environment (Neyrinck et al., 2014), the relation between matter and galaxy voids is a complex one, with galaxy voids being typically less underdense than would have otherwise been identified using the full matter density field. This could potentially weaken the lensing signals (which are produced by the total matter) from galaxy voids, and, due to difficulties in simulating galaxies in cosmological volumes, it is also more challenging to test cosmology using galaxy void properties such as abundances and sizes (see, e.g., Cautun et al., 2018).

In this Chapter, we propose a new paradigm for void studies: the identification of voids from weak lensing convergence maps, which we refer to as VOLEs (VOids from LEnsing). The convergence field represents the projected line-of-sight density field weighted by the lensing kernel, and thus the identified underdensities correspond to voids in the projected density field (for example Chang et al. 2018 have shown that the deepest minima of the convergence field have good correspondence to galaxy voids). This approach represents a simple way of finding voids that relates directly to our theoretical understanding of voids as underdensities in the total matter field. As void lensing is a key observable, it is only natural to identify voids and extract their lensing signal from the very same observations, such as a convergence map. VOLEs not only help avoid some of the disadvantages of galaxy voids, but also allow for a more complete exploitation of lensing maps by naturally combining VOLEs with other statistics, such as WL peaks and Minkowski functionals.

There are many void finders in the literature (e.g. see the void comparison project of Colberg et al., 2008) and here we choose to illustrate our methodology using the tunnel finding method (Cautun et al., 2018), but, in principle, many of the previous void finding approaches can be applied to the lensing convergence maps by using the convergence field itself, rather than using peaks as tracers. Our choice of tunnels is based on the Cautun et al. (2018) and Paillas et al. (2019) studies which find that WL by tunnels identified in the galaxy distribution is the most promising method for testing a wide range of modified gravity theories.

2.2 Method

2.2.1 N-body and ray-tracing simulations:

The WL maps used in this analysis are made using an analytical on-the-fly ray tracing algorithm, RAY-RAMSES (Li, 2011; Barreira et al., 2016), which is inbuilt in the publicly available N-body and hydrodynamical adaptive mesh refinement simulation code RAMSES (Teyssier, 2002). The N-body evolution part is done using the default RAMSES code. To construct the first map, five independent realisations of simulations evolving 1024^3 particles in a 512 h^{-1}Mpc box are tiled together to form a light cone up to a source redshift $z_s = 1$ (see Fig.1 of Barreira et al. 2016 for an illustration). The second map is constructed from the same box repeated 5 times. The cosmological parameters adopted are $\Omega_m = 0.32$, $\Omega_\Lambda = 0.68$ and $H_0 = 67$ km s^{-1} Mpc^{-1}. The two WL convergence maps cover a field of view of 10×10 deg^2 with a resolution of 2048^2 pixels. In order to use information from separate maps in conjunction with each other, we respectively subtract the mean convergence value of each map, to give us zero-mean convergence maps.

2.2.2 Galaxy shape noise:

The convergence field is determined observationally by averaging over a large number of source galaxies, which, due to their intrinsic ellipticity, leads to measurement uncertainties. This effect is known as galaxy shape noise (GSN) and can be a main uncertainty source on small angular scales. To allow our method to be interpreted in the context of observations, we generate WL maps with added GSN and compare the VOLEs identified with and without GSN. For each pixel of the WL maps, we add GSN by drawing from a Gaussian with standard deviation given by Eq (1.2.15). Here we use $\sigma_{\mathrm{int}} = 0.4$ and $n_{\mathrm{gal}} = 40$ arcmin^{-2} corresponding to LSST (LSST Science Collaboration et al., 2009).

2.2.3 Peak extraction:

In a first step, we identify peaks in the convergence map. In order to suppress GSN, we smooth the convergence map using a Gaussian window with a smoothing scale, θ_s, of 2.5 arcmin (unless otherwise stated). We define a peak as a pixel whose convergence value is greater than that of its 8 neighbours. We also trim the peaks in each map within one smoothing length of the edge of the map to exclude the boundary effects of smoothing a finite map. Each peak is characterised by the lensing convergence at its position, which we express as a signal-noise-ratio (SNR), $\nu \equiv \kappa/\sigma$, where σ is the standard deviation of the smoothed convergence maps, which is 0.011 and 0.012 for the maps without and with GSN, respectively.

The resulting number density of WL peaks averaged across both of our convergence maps as a function of SNR, ν, is shown in Fig. 2.1. It shows that the number of peaks is largest for small SNR, increasing from 2 deg^{-2} at SNR$\simeq$ 3 to 20 deg^{-2} at SNR$\simeq$ 0. Fig. 2.1 shows that our choice of θ_s (2.5 arcmin) leads to only small differences in the peak number densities. We have checked that both the number density and the two point correlation functions of peaks agree with previous studies (e.g. Shan et al., 2014; Shirasaki, 2017). For each map, we generate peak catalogues by selecting all the peaks with SNR, ν, above a given threshold value. Throughout this Chapter, we mainly identify voids from three peak catalogues corresponding to $\nu > 1$, $\nu > 2$ and $\nu > 3$, but in some places we also use catalogues with $\nu > 1.5$ and $\nu > 2.5$.

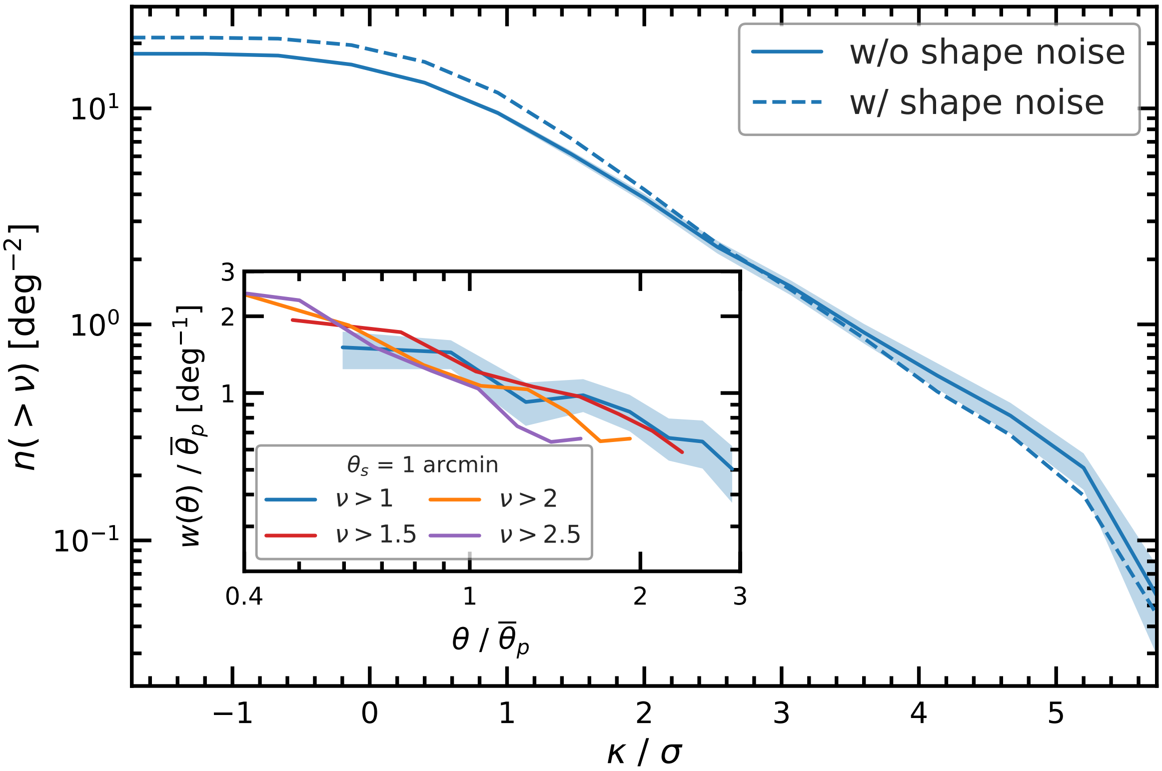

Figure 2.1: (Colour Online) Cumulative number per unit area of convergence peaks as a function of peak SNR, $\nu = \kappa/\sigma$, for the maps with and without GSN. The inlay plot shows the two-point peak correlation functions, $w(\theta)$, for peak catalogues with ν thresholds indicated in the legend, identified using $\theta_s = 1$ arcmin, with the peak pair separation θ (horizontal axis) and $w(\theta)$ (vertical axis) both scaled by $\bar{\theta}_p$, the mean peak separation in the respective peak catalogue. Though noisy due to the small map size, the rescaled curves show self-similarity for a range of ν thresholds. The shaded regions show 1σ uncertainties.

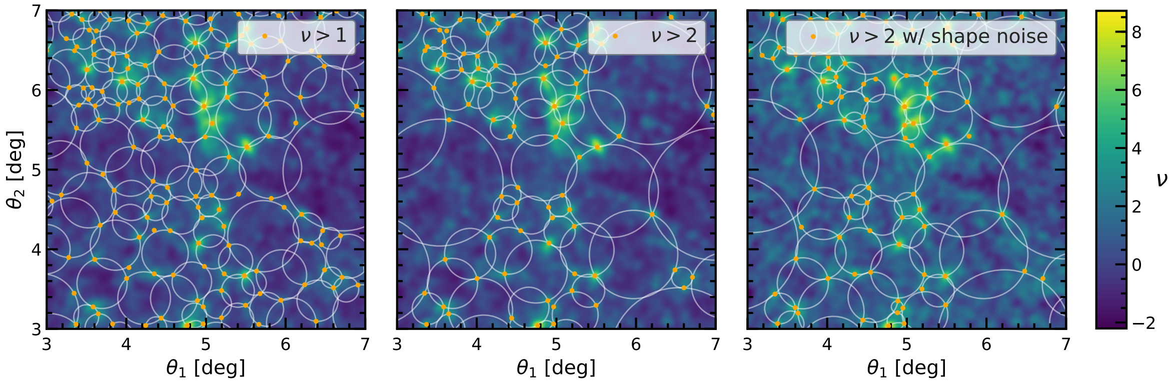

Figure 2.2: (Colour Online) Visualisation of 2D voids found in a small region of the smoothed lensing convergence maps (with and without galaxy shape noise). The panels show the voids for two convergence peak selection criteria, from left to right: $\nu > 1$, $\nu > 2$, and the third panel shows $\nu > 2$ with galaxy shape noise added to the map. The background colours show the convergence map, expressed in terms of ν. The dots show the peaks that satisfy each selection criterion, and the circles show the voids identified in each peak catalogue. θ_1 and θ_2 denote angular coordinates of the map in two orthogonal directions.

2.2.4 Void identification:

We identify voids using the tunnel finding algorithm of Cautun et al. (2018), which is so-named because it has been developed to find regions in the projected distribution of galaxies that do not contain any galaxies. The method can easily be extended and applied to the WL peak field by identifying the largest circles that are devoid of peaks. Thus, the tunnels correspond to circles in the 2D convergence map that contain no WL peaks.

The tunnels are obtained by first constructing a Delaunay tessellation with its vertices chosen to be the WL peaks. By definition, the circumcircle of every Delaunay triangle does not enclose any WL peak. The WL peaks, which define the triangle, reside directly on its circumcircle. Thus, each circumcircle represents a candidate tunnel with radius, R_{v}, and centre given by that of the corresponding circumcircle. We further discard any tunnels whose centres are found inside a larger tunnel. A visualisation of the tunnels found from the WL peak catalogues in one of our maps is shown in Fig. 2.2.

2.2.5 Calculating void profiles:

We calculate the convergence profiles of voids by using annuli of thickness $R_{\mathrm{v}}/N_{\mathrm{bin}}$, where R_{v} is the void radius and $N_{\mathrm{bin}} = 20$, and then stack all the voids in terms of the scaled radial distance, r/R_{v}. To get better statistics, we average over both lensing maps.

The tangential shear profile $\gamma_t(r)$ is calculated from the convergence profile using Eq (1.2.12).

All of our uncertainties, including those of the convergence and shear profiles, are estimated using bootstrap sampling. For each of the two maps we generate 100 bootstrap resamples, which we then combine and quote the uncertainties obtained by taking the 16th and 84th percentiles of these resamples.

2.3 Results

Fig. 2.2 shows that, as the ν threshold increases, the WL peaks are more spread out, and less numerous, resulting in larger voids. This is as expected because high-SNR peaks generally correspond to more massive structures or more structures aligned along the line of sight, which are rarer (e.g., Liu & Haiman, 2016). The third panel shows how adding GSN can slightly alter the void catalogue. The dependence of void size on ν is quantitatively confirmed in the cumulative void radius distribution given in Fig. 2.3, which shows that the $\nu > 1$ void

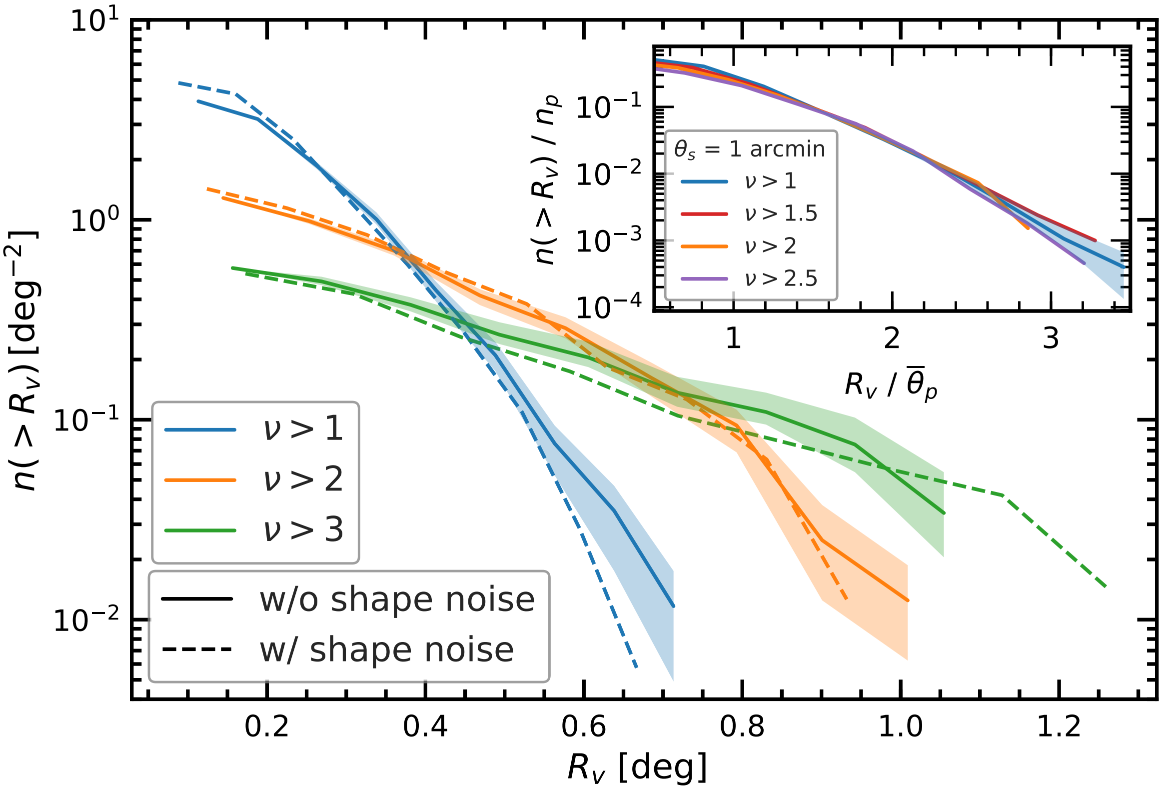

Figure 2.3: (Colour Online) Cumulative number density of voids as a function of the void radius, R_v. The curves correspond to void catalogues defined using WL peaks above different ν thresholds. The inlay plot shows a universal relation in the void abundance for catalogues with $\theta_s = 1$ arcmin, where R_v, is scaled by the mean peak separation, $\bar{\theta}_p$, and $n(> R_v)$, is divided by the mean peak number density, n_p, of the corresponding peak catalogue. The shaded regions show 1σ uncertainties.

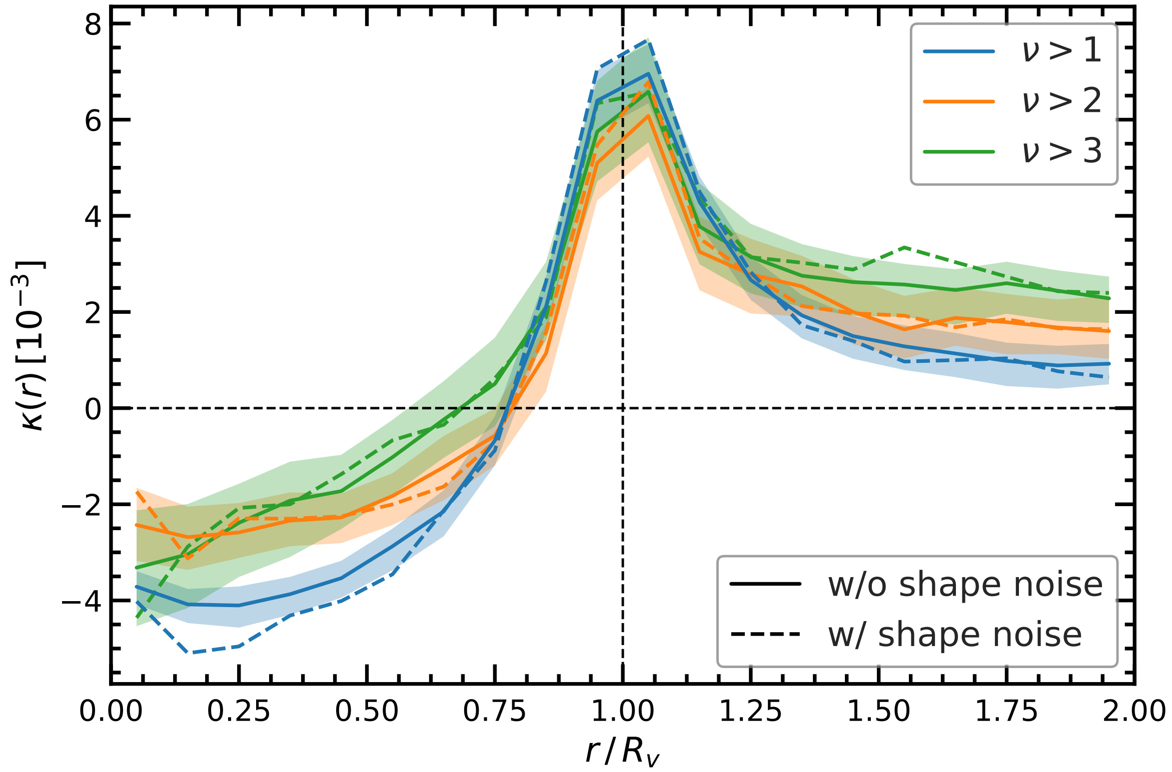

Figure 2.4: (Colour Online) The stacked convergence profiles of WL voids. Each curve corresponds to an average over all of the objects in each of the void catalogues. The dashed lines show the added GSN case. The shaded regions show the 1σ bootstrap uncertainties of the no GSN catalogues, which are similar to the GSN added case.

catalogue has more small voids and fewer large voids, with none above $R_\mathrm{v} \sim 0.7$ deg, while the $\nu > 3$ catalogue has fewer small voids and more large voids with radii up to $R_\mathrm{v} \sim 1.1$ deg. Again we can see that GSN has a small impact on the VOLEs size distribution, where the addition of spurious peaks tend to slightly reduce the size of the VOLEs. The inlay plot in Fig. 2.3 shows self-similarity in the void abundance across the void catalogues with peak thresholds $\nu \geq 1$, which is achieved by dividing the void radius by the mean peak separation and the void number density by the mean peak number density. We find this self-similarity for a range of smoothing scales, but we show only results for a small smoothing scale, $\theta_s = 1$ arcmin, which gives the largest number of VOLEs and thus provides the most stringent test of self-similarity. We also found that adding GSN has very little impact on the self-similarity of the void abundance, which allows us to choose the previously stated smaller smoothing scale. This self-similar scaled void abundance is likely related to the self-similarity in the peak two-point correlation functions from the peak catalogues with different SNR thresholds (see the inlay panel of Fig. 2.1), and we will present a detailed analysis on this, based on larger and more realistic lensing maps, in a forthcoming work.

2.3.1 Void convergence profiles:

Fig. 2.4 shows the convergence profiles as a function of scaled radial distance, r/R_v, averaged over all voids in both lensing maps. The profiles are plotted up to twice the void radius to show how, at large distances, they return to background levels (which we have set to be 0). Each curve corresponds to one of the three void catalogues. For $r \lesssim 0.75 R_\mathrm{v}$, we find negative convergence values, which indicates that the voids are underdense in those regions. Interestingly, the $\nu > 3$ void catalogue has the least underdense voids. This is to be expected, since the $\nu > 3$ voids are the largest and can enclose inside them slightly overdense regions, i.e. with $\kappa > 0$. As the peak SNR threshold used to identify voids decreases, the voids become smaller, they enclose fewer overdense regions and thus have lower overall κ values. The maximum convergence is achieved at $r = R_\mathrm{v}$ and all three void catalogues have roughly similar maximum values. At even larger radii, the convergence profiles decrease towards the mean background value of $\kappa = 0$. Of the three catalogues, $\nu > 3$ voids take the longest to reach the background value, which is a manifestation of the fact that the large peak values that define the boundary of $\nu > 3$ voids are typically found in large-scale overdense regions. Voids identified using high SNR peaks, i.e. $\nu \gtrsim 2$, have the same profiles in WL maps with and without GSN, but differences appear when using low SNR peaks, i.e. $\nu \lesssim 1$, where GSN

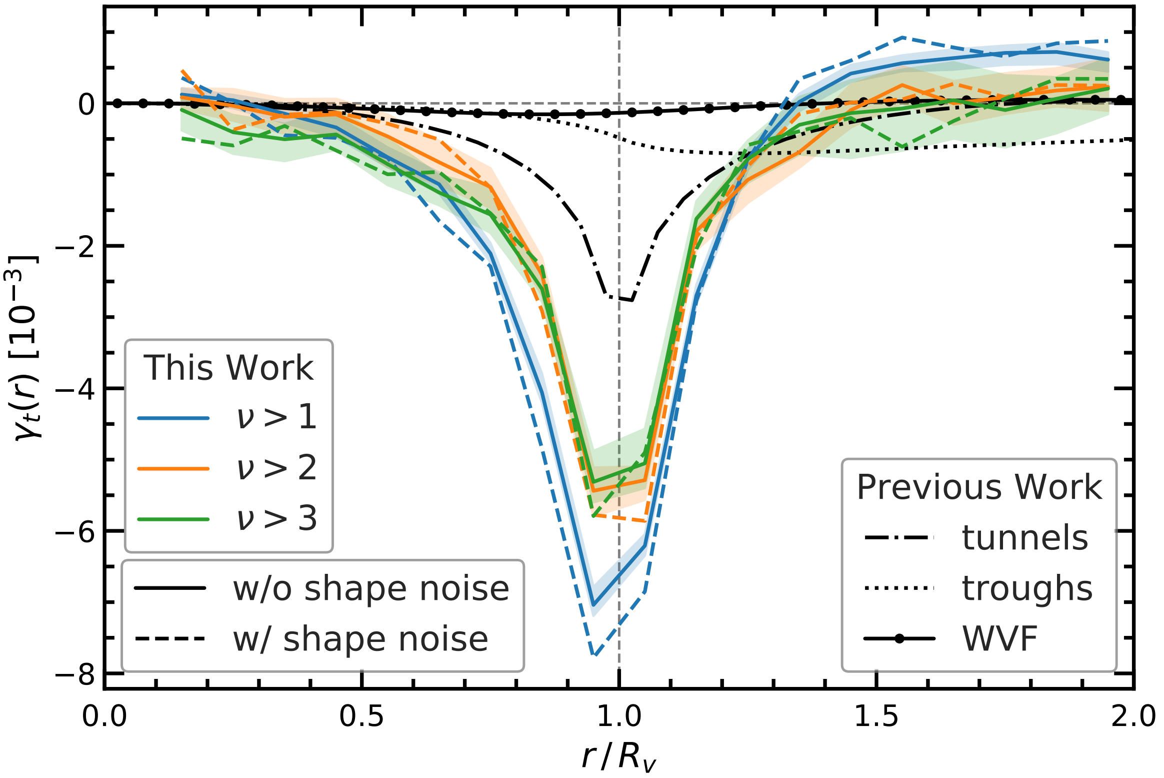

Figure 2.5: (Colour Online) The stacked tangential shear profiles of WL voids. The coloured lines show the average profile for the void catalogues identified in this Chapter, without GSN (solid) and with GSN (dashed). The shaded regions, show the 1σ bootstrap uncertainties. The black patterned lines correspond to the shear profile of underdensities identified in the *galaxy distribution*: tunnels (dot-dashed), troughs (dotted) and Watershed Void Finder (WVF; circle-solid) voids (Cautun et al., 2018).

can lead to spurious peaks, and thus spurious voids.

A final feature of the convergence profiles is that the width of the convergence maximum somewhat decreases as we increase the ν threshold of the WL peaks used for finding voids. This is due to the profiles being plotted against the rescaled distance, $r/R_{\rm v}$, rather than the physical distance, r. The $\nu > 2$ and 3 voids actually have wider convergence maxima when expressed as a function of r, but this larger width is overcompensated by their even larger radii which results in a narrower maxima when expressed in rescaled distances.

2.3.2 Tangential shear profiles:

Fig. 2.5 shows the tangential shear profiles of the VOLEs, calculated using Eq. (1.2.12). These profiles are qualitatively similar with the tangential shear of galaxy voids (e.g., Cautun et al., 2018) and show a maximum signal at $r = R_{\rm v}$. The maximum signal has a negative value, indicating that voids lead to diverging lensing, similar to a concave lens. Like the convergence profiles, larger ν thresholds reduce the width associated to the maximum tangential shear signal, while the height and position of the maximum signal are almost independent of the ν threshold from $\nu > 2$. The shear signals are very similar for the case with GSN, with the greatest deviation at the lower ν threshold, $\nu > 1$ due to spurious peaks from GSN, which create spurious voids.

The error bars for the tangential shear profiles are smaller than those for the convergence profiles (see Fig. 2.4). The uncertainty in the convergence profile is dominated by modes many times larger than the void size, which determines on average a systematic shift up or down between the convergence profiles of voids some distance apart. We checked that the voids in different regions of the lensing map have the same convergence profile up to some constant shift in κ values. In contrast, the tangential shear profiles are only sensitive to the shape of the convergence profiles, and are not affected by a constant shift of the latter. Thus, given one WL peak catalogue, different VOLEs have very similar lensing profiles, however the profiles show a weak dependence on the ν threshold used to define the peak catalogue. It remains to be seen whether there is a strong cosmological model dependence of the VOLEs γ_t profiles, which we will study in Chapter 4.

Fig. 2.5 also compares the VOLEs tangential shear profiles to results from other void definitions used in previous works. We compare the VOLEs with three types of voids identified in the galaxy distribution: 3D watershed voids (WVF, Platen et al. 2007), fixed-aperture cylinders along lines-of-sight with low projected galaxy number densities (troughs; Gruen et al., 2016) and tunnels (the same as the method used in this Chapter but applied to galaxy fields). These three void catalogues are obtained from a $z = 0.5$ halo occupation distribution galaxy catalogue that matches the clustering of SDSS-CMASS which has a galaxy number density, $\bar{n}_g \approx 3 \times 10^{-4} h^3 \mathrm{Mpc}^{-3}$ (see Cautun et al., 2018, for more details). This represents a typical galaxy catalogue at redshift, $z = 0.5$. We take the WL signals of the galaxy voids from Cautun et al. (2018), and we rescale them to match our source galaxies' redshift, $z_s = 1$.

We find that the maximum γ_t signal of VOLEs is roughly twice as large as tunnels identified from a galaxy field, and about 10 and 40 times larger than the signals of troughs and WVF voids, respectively. The stronger lensing signal in VOLEs is not surprising since the WL peaks are taken straight from the convergence field itself, which is directly related to the projected total matter distribution. The projected galaxy number density used to identify the Cautun et al. tunnels and troughs is $\sim$500 gal deg^{-2} and is much larger than that used for the VOLEs catalogues (see Fig. 2.1). We find that using higher number density peak catalogues, which could be obtained with a smaller smoothing scale and smaller GSN, results in VOLEs with an even higher tangential shear signal and thus increases further the differences between VOLEs and galaxy tunnels.

2.4 Conclusions and future work

Cosmic voids are becoming an increasingly important cosmological probe. While theoretical studies usually focus on voids identified from the dark matter field, in observations galaxies are usually used as tracers to find voids. Here, we have proposed an alternative: to identify voids in the WL convergence field (dubbed VOLEs), which, since it represents the line-of-sight projected matter distribution, is conceptually closer to identifying voids as underdensities in the matter distribution. This opens a new window for exploring the cosmic mass distribution and, in particular, for designing novel environment-sensitive cosmological tests.

As an example, we identified VOLEs by applying the tunnel algorithm of Cautun et al. (2018) to the WL lensing peak distribution, and investigated several properties, including their abundance, convergence and tangential shear profiles. Using peaks with lower SNR leads to finding smaller voids, which are on average more underdense. The void convergence profiles, which are indicative of the projected matter density inside and around the voids, are negative for $r \leq 0.75R_{\mathrm{v}}$, which corresponds to line-of-sight underdensities, and show a sharp overdense peak at the void edge, $r = R_v$. In terms of tangential shear profiles, the VOLEs show a maximum signal at $r = R_{\mathrm{v}}$, with the maximum signal height somewhat independent of the peak catalogue used to identify the voids. However, the width of the tangential shear signal decreases when using peaks corresponding to a higher SNR threshold. We found that the amplitude of the maximum signal in the tangential shear profiles for the VOLEs is roughly twice as large as that of voids generated using the same void finder (tunnels) but by using galaxies as tracers. The amplitude is more than an order of magnitude larger compared to those corresponding to galaxy voids identified using other algorithms (troughs and WVF voids). This shows the benefit of using a more reliable tracer of the projected total matter field.

The method introduced here represents a new avenue to identify 2D voids rather than a new void-finding algorithm, in the sense that many, if not all, existing void finders (troughs, spherical void finders, WVF, ZOBOV, etc.) can be applied to the WL convergence maps. Indeed, in principle one can use the WL convergence field itself (i.e. not just the peaks from it) as a tracer field for void identification. The study of void identification and void lensing from the same WL observation is also convenient in practice, because there is no need for foreground galaxies, whose redshifts are hard to measure accurately and can be affected by the peculiar velocities of the galaxies. Instead, the particular lensing map that is used to study void lensing is expected to offer sufficient information for locating those very voids. With the upcoming WL surveys (HSC, EUCLID, LSST, etc.) which offer lensing maps with increasing sky coverage, we hope that this approach will take us a step forward in extracting information from such maps in a maximal way.

Unlike galaxy voids, for VOLEs it is also possible to use void abundance to discriminate different models as there is no ambiguity in modelling the galaxy populations for these models. The universal scaled void abundance shown in Fig. 2.3 implies that it is possible to find generic simulation-calibrated fitting formulae for these void properties (e.g., Hamaus et al., 2014) which can be used as theoretical templates in cosmological tests. For the latter purpose, it is also critical to test the VOLEs void finding method in real weak lensing data sets to understand how observational systematics and galaxy formation physics can affect the void properties. These possibilities will be investigated in follow-up studies.

Chapter 3

Optimal void finders in weak lensing maps

3.1 Introduction

WL represents a powerful cosmological probe because it is an unbiased tracer of the cosmic LSS, whose properties and evolution are governed by the underlying cosmological model, including the matter content in the Universe and the law of gravity. Thus, WL can be used to constrain cosmological parameters within the standard ΛCDM paradigm, as well as models beyond ΛCDM (Albrecht et al., 2006; LSST Dark Energy Science Collaboration, 2012; Amendola et al., 2013; Weinberg et al., 2013). In order to achieve this, one must construct statistics which efficiently capture the cosmological information embedded within WL maps. This can be achieved through two-point statistics such as the power spectrum or the two-point correlation function. One such example is the shear-shear correlation function which has been used to provide constraints on cosmological parameters within ΛCDM (e.g. Schneider et al., 2002; Semboloni et al., 2006; Hoekstra et al., 2006; Fu et al., 2008; Heymans et al., 2012; Kilbinger et al., 2013; Hildebrandt et al., 2017). The convergence power spectrum and shear-shear correlation have also been used to test modified gravity theories beyond ΛCDM (e.g. Schmidt, 2008; Tsujikawa & Tatekawa, 2008; Huterer, 2010).

The power spectrum encapsulates all the information required to describe a Gaussian random field, which is an accurate representation of the matter distribution in the Universe at early times. However, the growth of LSS is governed by gravity which induces non-Gaussian features due to nonlinear evolution at late times, when the power spectrum becomes an incomplete description of the underlying matter field. Therefore, for non-Gaussian observables such as WL maps, it is important to develop complementary statistics beyond the power spectrum in order to maximise the cosmological information that can be extracted.

A popular and simple alternative WL statistic that is complementary to the WL power spectrum is the abundance of WL peaks (Jain & Van Waerbeke, 2000; Pen et al., 2003; Dietrich & Hartlap, 2010), which are usually defined as the local maxima in the convergence field. The strongest WL peaks are typically produced by the most massive structures in the universe, such as galaxy clusters (Yang et al., 2011; Liu et al., 2015; Liu & Haiman, 2016), and so the abundance of these WL peaks is directly sensitive to the non-Gaussian features of the cosmic web. Furthermore, low amplitude WL peaks have been shown to contain useful cosmological information (Dietrich & Hartlap, 2010; Kratochvil et al., 2010; Yang et al., 2011), making the study of weak lensing peaks crucial for cosmological constraints. This complementary information contained in the abundance of WL peaks has been exploited to improve cosmological constraints on ΛCDM parameters (Shan et al., 2012; Van Waerbeke et al., 2013; Shan et al., 2014; Liu et al., 2015), modified gravity (Cardone et al., 2013; Liu et al., 2016b; Higuchi & Shirasaki, 2016; Shirasaki et al., 2017; Peel et al., 2018), dark energy (Giocoli et al., 2018), and the sum of neutrino masses (Li et al., 2019). Additional WL peak statistics, such as the two point correlation function, will be shown to be sensitive to the ΛCDM parameters in Chapters 6 and 7.

There are multiple other WL statistics beyond the power spectrum that have been utilised to constrain cosmology, and we briefly mention a few here. The first is Minkowski functionals, which can provide additional constraints on the dark energy equation of state parameter (Kratochvil et al., 2012; Petri et al., 2013; Ling et al., 2015; Marques et al., 2019). The WL bispectrum, which is sensitive to non-Gaussianity by definition, has been shown to be a useful statistic for future surveys (Cooray & Hu, 2001; Rizzato et al., 2019; Munshi et al., 2020), and can be used to improve parameter constraints, such as neutrino masses (Coulton et al., 2019a). And finally, WL minima, local minima in the convergence field, are less sensitive to baryonic effects, and offer certain advantages over WL peaks (Coulton et al., 2019b). Every such novel statistic offers its own unique advantages, which makes the study of novel statistics crucial.

The goal of this Chapter is to explore the properties of another such statistic, WL voids, first introduced in Chapter 2. Typically voids are identified in the full 3D distribution of the LSS, as regions with low densities of matter or tracers. The void abundance, their radial profiles and shapes contain higher order clustering information (and hence non-Gaussian information; White 1979; Fry 1986; Biswas et al. 2010; Bos et al. 2012; Lavaux & Wandelt 2012). Most studies have focused on galaxy voids, which corresponds to underdensities in the galaxy distribution (e.g. Paz et al., 2013; Sutter et al., 2014; Cautun et al., 2016; Nadathur, 2016). The statistics of galaxy voids contain complementary information to the galaxy power spectrum and baryonic acoustic oscillations (e.g. Pisani et al., 2015; Hamaus et al., 2016; Nadathur et al., 2019). One useful void statistic is their WL profiles, which have been argued to represent a powerful cosmological probe (Cai et al., 2015; Barreira et al., 2015; Falck et al., 2018).

Compared with galaxy voids, WL voids have been shown in the previous Chapter to correspond to deeper line-of-sight projected underdensities and thus they have a larger tangential shear signal. This potentially makes WL voids better cosmological probes than galaxy voids. This will be exemplified in Chapter 5 in the context of a class of modified gravity models, which can be considerably better constrained with 2D WL voids than with galaxy voids.

The total SNR of void lensing profiles depends on the number of voids and the amplitude of the lensing profile. Depending on how voids are identified, either fewer or more 2D voids can be obtained relative to 3D voids. However, most importantly, the 2D void lensing profiles have amplitudes roughly an order of magnitude larger than those of 3D voids (Cautun et al., 2018; Davies et al., 2018). This is the most important factor that contributes to higher SNR for 2D WL voids compared to 3D voids in the cosmic web.

Chapter 2 focused on a particular class of WL voids, called VOLEs (VOids from LEnsing), where the voids are identified as circles devoid of weak lening peaks. However, as for 3D voids, the definition and therefore the finding algorithm of 2D voids are not unique. There are multiple methods of finding underdensities, and thus multiple approaches to define voids (e.g. Colberg et al., 2008; Cautun et al., 2018). This ambiguity can lead to systematic differences in void observables among the various void finders. However this ambiguity can also be exploited, by picking the void-finding algorithm that best suits the intended purpose. In our case, we want to maximise the amplitude of the WL void lensing profiles (or similarly the SNR of the WL void lensing profiles), whilst also limiting the impact of observational noises on the resulting void statistics. To this end, we will present WL void statistics for a range of void-finding algorithms, and discuss the limitations and advantages of each void finder.

Here, we compare seven different void definitions. These can be split into two classes. First and seemingly the most natural approach, consists of the methods which identify voids directly from the WL convergence field. In the following, we denote the convergence with κ. The simplest objects that can be considered as WL voids are the WL minima (i.e., local minima in the κ field) where the deepest minima have been shown to correspond to large supervoids along the line of sight (Chang et al., 2018). More advanced void definitions include the watershed void finder (WVF; Platen et al. 2007), which identifies voids as the watershed basins of the convergence field, the spherical void finder (SVF; e.g., Padilla et al. 2005) applied to the convergence field (which we denote as SVF κ), which finds the largest circles whose mean κ is below a given threshold, and troughs (denoted with Troughs κ; Gruen et al. 2015), which consists of fixed sized circles whose mean convergence is below a given threshold.

By construction, the number and properties of voids identified in the convergence field are sensitive to the lowest κ values. These regions are the ones affected the most by galaxy shape noise (GSN). For this reason we consider a second class of void finders, which consists of methods that identify voids using a distribution of tracers, which we take to be the peaks of the convergence field (as we shall discuss, the peaks are less affected by GSN). We study three methods in this class: the 'tunnel' algorithm (Cautun et al., 2018) employed in Chapter 2, which identifies voids as the largest circles devoid of tracers, the SVF but now applied to the peak distribution (hereafter referred to as 'SVF peak'), and troughs identified in the peak distribution (denoted with 'Troughs peak'), which consists of fixed sized circles that enclose fewer than a given number of peaks. A detailed description of each WL void finder is presented in Section 3.3.

The content of the Chapter is as follows: The numerical simulations and galaxy shape noise prescription used in this study are presented in Section 3.2 along with the basic WL map statistics which will help the interpretation of results from different WL void finders. The void finders studied here are presented in Section 3.3, and the statistics describing the WL voids associated to each WL void finder are presented and discussed in Section 3.4. We then compare useful properties of the WL void finders in Section 3.5, with the discussion and conclusions in Section 3.6. We also present the correlation matrices of the tangential shear profiles for different void finders in Appendix .1. In Appendix .2 we test how WL voids behave in WL maps with only GSN i.e. WL maps with no physical signal, and discuss how WL voids are sensitive to the physical information in WL maps.

3.2 Weak lensing maps

In this section, we briefly outline the numerical simulations and the weak lensing maps used in this study, our prescription for including galaxy shape noise in our analysis, and a discussion on the relevant WL statistics that will inform the interpretation of our results from different void finders.

3.2.1 Numerical simulations

To study WL voids we use WL maps generated from N-body simulations taken from Takahashi et al. (2017) (herein T17) which provide publicly-available all-sky WL convergence maps. The WL maps are generated with the ray tracing algorithm from Hamana et al. (2015) (see also Shirasaki et al., 2015). These WL convergence maps have a HEALPix resolution of $N_{\rm side} = 16384$, and a source redshift of $z_{\rm s} = 1$. The N-body simulations have a particle number of 2048^3, and the particle mass varies with the box size ranging from 8.2×10^8 to $2.3 \times 10^{12} M_\odot$ (see Table 1 of T17 for more details). To avoid repeating structures along the line-of-sight, T17 constructed the light cone by stacking cubic simulation boxes of increasing size, with comoving sizes $L, 2L, 3L, \cdots, 14L$, where $L = 450h^{-1}$Mpc. These boxes are then duplicated 8 times and nested around the observer, where nests of larger boxes contain nests of smaller boxes at their centres. The matter distribution of these nested boxes is projected onto the nearest spherical shell centered on the observer, where the shells have radii of $N \times 150\ h^{-1}$Mpc with $N = 1, \cdots, 14$ (see T17 for illustration). The cosmological parameters used for these WL maps correspond to a flat universe with $\Omega_{\rm m} = 0.279$, $\Omega_\Lambda = 0.721$, $\sigma_8 = 0.820$ and $h = 0.7$, where $h = H_0/100$ km s^{-1} Mpc^{-1}.

We split the all sky WL convergence maps into 192 10×10 deg^2 maps and then extend the map boundaries by a further 5 deg on all sides giving us 192 20×20 deg^2 maps with a resolution of 4096^2 pixels. This approach results in maps where the central 10×10 deg^2 region of each map does not overlap with the central 10×10 deg^2 region of any of the remaining 191 maps. The use of the 192 smaller maps allows us to stick to the flat sky approximation. Void detection is carried out on the full 20×20 deg^2 and voids with centres outside of the central 10×10 deg^2 are discarded. Additionally, voids that are within twice their radius from the map boundary are discarded when calculating the void lensing profiles. This approach guarantees that void identification is not biased away from large voids due to boundary effects. For more details on our projection method, see Appendix .7

3.2.2 Galaxy shape noise

The observed correlation in galaxy shapes induced by gravitational lensing is entirely dominated by the random shapes and orientations of galaxies, which are referred to as galaxy shape noise (GSN). As shown by Van Waerbeke (2000), GSN can be modelled by adding random values drawn from a Gaussian distribution to each pixel of our simulated WL maps. The standard deviation of this distribution is given by Eq. (1.2.15) We use $\sigma_{\rm int} = 0.4$ and $n_{\rm gal} = 40$ arcmin^{-2}, which match LSST specifications (LSST Science Collaboration et al., 2009).

The inclusion of GSN results in noise-dominated WL maps. Nevertheless, the noise effect can be suppressed by smoothing with a (usually) Gaussian filter with smoothing length $\theta_{\rm s}$. Using a small value for $\theta_{\rm s}$ allows a given WL statistic to probe the smallest scales and maximise the information gained, however this also leaves significant contamination from GSN. Using larger $\theta_{\rm s}$ values reduces the GSN contamination, but suppresses the small scale information within the WL maps. This means that a trade off must be struck between sufficiently suppressing GSN and retaining WL information on small scales. Additionally, the analysis carried out here relies on WL maps generated from dark matter only simulations, and do not include baryon physics. To suppress the differences between dark matter only and full hydrodynamic simulations, Weiss et al. (2019) found that very large smoothing scales must be used. Furthermore, Liu et al. (2015) found that constraints on cosmological parameters from WL peaks are improved when multiple smoothing scales are used. These imply that there is no single best choice of smoothing scale that fits all purposes when analysing WL statistics. So in order to explore this fully, all statistics in this Chapter will be shown for multiple smoothing scales, $\theta_{\mathrm{s}} = 1$ (blue), 2.5 (orange), and 5 (green) arcmin, both in the presence (dashed) and absence (solid) of GSN.

By presenting all statistics for multiple smoothing scales, with and without GSN, we will be able to identify the void finders that are the least affected by GSN. However at this point the impact of GSN on cosmological parameter constraints from WL voids is not known. It is possible that the inclusion of GSN may improve cosmological parameter constraints from WL voids by increasing the signal-to-noise (SNR) ratio relative to the case where GSN is not included, as has been found with WL peaks (Yang et al., 2011). However, GSN could also bias or degrade the cosmological parameter constraints from WL voids. We leave such an investigation to further work and focus on identifying void finders that are the least affected by GSN in this Chapter.

For the analysis of WL peaks it is useful to define the amplitude of a given peak relative to the r.m.s. fluctuation of the added GSN component of the WL field. As such ν is defined as

$$\nu \equiv \frac{\kappa}{\sigma_{\mathrm{GSN}}(\theta_{\mathrm{s}})}\,, \tag{3.2.1}$$

where $\sigma_{\mathrm{GSN}}(\theta_{\mathrm{s}})$ is the standard deviation of the smoothed GSN map (without contributions from the physical WL convergence map i.e. noise only) and varies depending on the smoothing scale with which the WL peak is identified, with $\sigma_{\mathrm{GSN}} = 0.0126, 0.0051$ and 0.0025 for $\theta_{\mathrm{s}} = 1, 2.5$ and 5 arcmin respectively.

3.2.3 Convergence PDF and WL peak abundance

In order to aid the interpretation of the various WL void statistics, we first present some simple statistics that describe the information given to the WL void finders. In the cases of void finders applied directly to the convergence field this is the WL convergence probability distribution function (PDF) shown in the left panel of Fig. 3.1, and for the void finders that

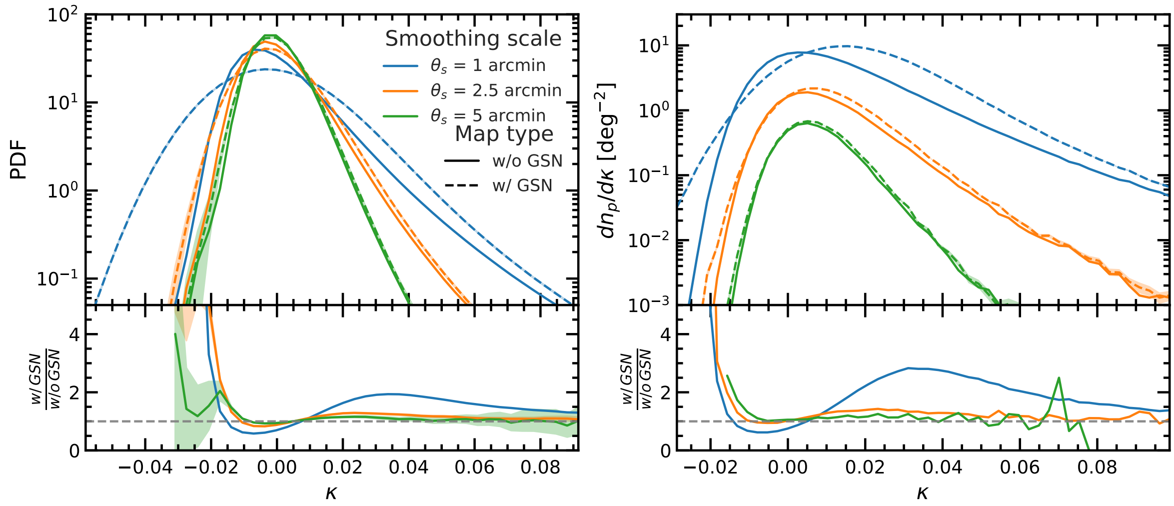

Figure 3.1: Left panels: the probability distribution function (PDF) of the WL convergence field, κ. Right panels: The differential abundance of WL peaks as a function of peak height ν. The results shown here are obtained using a $\sim$19,000 deg^2 area with the shaded regions denoting the one sigma error bars (most of the time the errors are smaller than the line thickness). The dashed and solid lines correspond to the WL convergence maps with and without GSN respectively. The colours correspond to different smoothing scales of the κ field: 1.0 (blue), 2.5 (orange) and 5.0 (green) arcmin. The relative differences between the cases with and without GSN are shown in the lower sub-panels.

use weak lensing peaks as tracers this is the WL peak abundance shown in the right panel Fig. 3.1. Note that we define a WL peak as a pixel with a convergence value larger than that of its eight neighbours.

The left panel of Fig. 3.1 shows the WL convergence PDF for the three smoothing scales (1, 2.5 and 5 arcmin), for cases with and without the inclusion of GSN (dashed and solid). The convergence PDF is well described by a log normal distribution convolved with a Gaussian when GSN is included (Clerkin et al., 2017). The different colours show that as the smoothing scale increases, the width of the distribution decreases, suppressing the non-Gaussian structures within the WL map, and the agreement between the cases with and without GSN improves. The relative differences in the convergence PDF between the no-GSN and the GSN-added cases are larger for $\kappa < 0$ than for $\kappa > 0$, as can be seen more clearly in the lower panel. Therefore in order to find agreement in WL void statistics with and without the inclusion of GSN we will likely require larger smoothing scales than what is required to get the same agreement for WL peak statistics. Finally, for a smoothing scale of 1 arcmin (blue curves), the inclusion of GSN introduces a significant number of negative convergence values that are much lower than the lowest convergence values found in the WL maps without GSN. This indicates that 1 arcmin smoothing might be too small for WL void finders applied directly to the convergence field in order to agree before and after GSN is added. However, agreement between the two cases is largely improved once the smoothing scale is increased to 2.5 or 5 arcmin.

The differential WL peak abundances identified from WL maps with and without GSN smoothed over the three smoothing scales (1, 2.5 and 5 arcmin) are displayed in the right panel of Fig. 3.1. By adding GSN, the peak of the distribution is shifted to the right, and more peaks are created. The addition of these spurious peaks from GSN will lead to the identification of spurious voids for void finders that find voids in the WL peak distribution. The differences between WL peak catalogues for maps with and without GSN is suppressed as the smoothing scale increases, but this also decreases the overall abundance of the WL peaks. It can also be seen that, as κ increases, the differences between the maps with and without GSN decreases. This is because the largest WL peaks are less affected by GSN, since the physical peak signal dominates over the noise.

The right panel of Fig. 3.1 also shows that there are many WL peaks with negative convergence values, which are local maxima in underdense regions of the WL convergence maps. This is as expected, since most regions have $\kappa < 0$ (see left panel in Fig. 3.1) and thus many local maxima will have heights $\kappa < 0$. As we will discuss in Section 3.3, the void finders based on the peak distribution identify the voids as the regions that are largely devoid of peaks. Including all the WL peaks in our analysis can raise two problems. Firstly, it reduces the contrast in peak number density between overdense and underdense regions, and thus makes it difficult to robustly identify the underdense regions. Secondly, the location and height of $\kappa \lesssim 0$ peaks is much more affected by GSN than for the high κ peaks. This defeats the main reason for identifying voids using the WL peaks, which is to mitigate the effect of GSN on the WL void population. Therefore, to deal with these two issues, we proceed by imposing a peak height cut on the WL peak catalogues, and remove all peaks below a given threshold. This adds a free parameter to the analysis and thus, for the void finders that use WL peaks as tracers, we will present results for peak catalogues with peak heights of $\nu > 2$ and $\nu > 4$.

3.3 Void finders

In this section, we describe the implementation of each WL void finder used in this Chapter. These void finders were originally developed to identify voids in a 3D galaxy or matter distribution, which means that some must be modified slightly to identify 2D WL voids. In each case we try to minimise the extent of the modification so that the interpretation of results can remain as similar as possible to the interpretation of 3D voids. Furthermore, where possible, we apply each void finder to both the WL peak distribution and the WL convergence field to see which approach provides the most information (in terms of the signal-to-noise ratio, SNR) and which is least affected by GSN. Finally, all void identification is carried out on the full 20×20 deg^2 maps, while the voids whose centres reside outside of the central 10×10 deg^2 are discarded. This ensures that the void identification process is not contaminated by edge effects, and that we do not bias our results away from large voids, since larger voids are more likely to intersect the map boundary.

3.3.1 Minima

Weak lensing minima are the simplest objects which can be interpreted as WL voids, which correspond to the most underdense lines of sight within the WL convergence maps. Here we define WL minima as local minima in the convergence field, which is a pixel whose κ value is lower than those of its eight neighbours. We identify WL minima in the smoothed convergence field and discard all minima with a positive κ value, because a positive κ value indicates that the minimum and its neighbours reside within a local overdensity. This allows us to remain consistent with the general definition of a WL void, which is an underdense patch of the WL convergence map.

3.3.2 Troughs

Troughs (Gruen et al., 2015) are underdense circles of a fixed size. Typically troughs are identified by randomly placing circles of that fixed size in a projected galaxy field and discarding the circles that contain the most galaxies, leaving only those that contain the least galaxies. Here we adapt the trough algorithm and apply it to both the WL peak field and the WL convergence field.

For troughs applied directly to the convergence field (Troughs κ), we first place 5000 circles[1] randomly such that their centres fall into the central 10×10 deg^2 of the WL convergence map. For each of these circles, the mean enclosed convergence is calculated. The trough catalogue consists of the 20% of the circles with the lowest mean enclosed convergence. The

---

[1] We have also run the trough algorithm with 10 times as many randomly placed circles, and find that this does not change the SNR values of the trough tangential shear profiles. Therefore in this Chapter we stick to 5000.

above procedure is carried out for circles with radii of 10, 20 and 30 arcmin, which correspond to the typical values used in previous studies (e.g., Barreira et al., 2017; Gruen et al., 2018).

For troughs identified in the WL peak distribution (Troughs peak), the same steps are repeated except that, rather than calculating the mean enclosed convergence, we count the number of enclosed peaks, and keep the 20% of circles which contain the fewest peaks. Again, these steps are repeated for circles of radii of 10, 20 and 30 arcmin.

The number of randomly placed circles and the upper fraction of circles to be discarded are both free parameters. However, to keep the analysis in this Chapter simple we do not vary these parameters, and their values above have been chosen to match the typical abundances of WL voids produced by the other algorithms for a fair comparison.

3.3.3 Watershed void finder (WVF)

The watershed void finder (Platen et al., 2007, WVF) defines voids as the watershed basins, which are analogous to water basins formed from rain running down a landscape. To identify the watershed basins, each pixel of the convergence map is connected to its neighbour with the lowest density, and this process is repeated for successive neighbours until a local minima is reached. All pixels connected to the same minima then belong to the same watershed basin. This results in ridges of local overdensities along the basin boundaries.

To mitigate the impact of GSN, we compare the average amplitude of each basin boundary with the amplitude of their corresponding minima. If the absolute difference in amplitude between the two is less than h_{boundary}, we merge that basin with its neighbour, which creates a single larger basin. In this analysis we choose $h_{\mathrm{boundary}} = \sigma_{\mathrm{GSN}}/2$, which allows watershed basins that have been artificially split by spurious structures introduced by GSN to be remerged. Adding the basin merge criteria means that h_{boundary} is an additional free parameter in the WVF algorithm. We have tested the impact of varying h_{boundary} and find that it has little impact on our results. We choose $h_{\mathrm{boundary}} = \sigma_{\mathrm{GSN}}/2$ as a compromise between mitigating the impacts of GSN on watershed basins and over merging, which would on average flatten out void lensing profiles.

This algorithm generates irregular basins which span the entire area of the WL convergence map. In order to calculate the stacked lensing profiles of the voids, we must define their void centres and radii using the information of the corresponding basins. We take the void centres as the area-weighted barycentre of all the pixels in each basin and define an effective void radius of $R_{\rm v} = (A/\pi)^{1/2}$ (which is the radius of a circle with the same area A as the irregular basin) when calculating the WVF lensing profiles.

When the watershed algorithm is applied to the galaxy distribution to find 3D voids in the LSS, the galaxies are first used as tracers to construct an estimate of the underlying density field using a Delaunay tessellation field estimation (DTFE) (Schaap & van de Weygaert, 2000; Cautun & van de Weygaert, 2011). This in principle means that WL peaks could also be used to identify WL voids with the watershed algorithm, by using the WL peaks to construct a WL peak density field. However, we find that the usual DTFE approach is insufficient, since it results in WL voids identified from the WL peak distribution that bear little correlation to underdensities in the original convergence map. While it may be possible to improve this procedure by using information about the WL peak heights in the DTFE reconstruction, this is beyond the scope of this Chapter, and we thus instead choose to only study voids identified by applying the watershed algorithm to the WL convergence field.

3.3.4 Spherical void finder (SVF)

The spherical void finder (SVF) (e.g., Padilla et al., 2005) identifies underdense spherical regions in the galaxy distribution, by growing spheres around regions that are empty of galaxies. When applied to find WL voids, the SVF identifies circular regions in the WL convergence or peak fields that are below a specified ‘density’ threshold. In practice, in order to allow SVF voids to ‘grow’ as large as possible, circles are shrunk from some arbitrarily large size around candidate void centres until the threshold is met.

For the SVF applied directly to the WL convergence map (SVF κ), local minima are considered as prospective void centres. Starting from a large radius, circles are then shrunk around these void centres until the mean enclosed convergence reaches a predefined threshold, $\kappa_{\rm thresh}$. Here, larger values of $\kappa_{\rm thresh}$ result in larger voids, and note that we require $\kappa_{\rm thresh}$ to be negative so that the SVF finder identifies regions that enclose underdense sections of the convergence map. We have tested a range of values for $\kappa_{\rm thresh}$, and as a compromise between identifying the most underdense regions and allowing voids to grow as large as possible, we set $\kappa_{\rm thresh} = -0.01$ in this analysis. Once all prospective voids are shrunk until their mean convergence is $\kappa_{\rm thresh}$, we proceed to remove the objects that overlap significantly. That is, if the distance between any two prospective voids is less than half the sum of their radii, we discard the smaller of the two. Finally, we remove all voids with radii less than twice the smoothing scale that is applied to the convergence map ($\theta_{\rm s}$) to reduce the number of spurious voids.

For the SVF applied to the WL peak distribution (SVF peak), a Delaunay triangulation of the peak field is performed, and the circumcentres associated to each triangle are considered as potential void centres. Starting from a large radius, circles around those centres are shrunk, until the mean enclosed WL peak number density reaches a predefined fraction of the mean WL peak number density. We find that the resulting void catalogues are somewhat insensitive to the exact choice of this threshold value, and therefore pick 40% as a good compromise between allowing SVF voids to grow as large as possible and ensuring these voids correspond to underdense regions of the WL convergence maps. Next, we randomly shift void centre positions within the void radius, in order to verify if it is possible for the void to 'grow' a bit more (i.e., to reach the density threshold at a slightly larger radius). Finally, if the centres of two voids are separated by less than half of the sum of their radii, we remove the smaller of the two.

3.3.5 Tunnels

The tunnel algorithm (Cautun et al., 2018) identifies the largest circles in a 2D tracer catalogue that are empty of tracers. Initially, a Delaunay tessellation with WL peaks as the vertices is constructed. This produces a tessellation of Delaunay triangles, with a WL peak at the corner of each triangle, and no WL peaks within the triangles. Each Delaunay triangle is then used to construct its corresponding circumcircle, which is the circle that resides directly on top of the Delaunay triangle, with the three vertices of the triangle falling on the circumcircle's circumference. This unique tessellation, by definition, produces circles which do not enclose any WL peaks. To avoid highly overlapping objects, we discard any tunnels whose centres reside within a larger tunnel.

3.3.6 Visualisation

Fig. 3.2 shows a visualisation of each of the void finders studied in this Chapter. The eight panels in the top section (1A – 1H) show results for WL maps without GSN and the eight panels in the bottom section (2A – 2H) are results for WL maps with GSN. Each panel corresponds to a different void finder, apart from the first panels of each section (panel 1A and 2A) which show only the WL convergence field for reference. Only the central 6×6 deg^2 of one of the maps are shown, to avoid over crowding whilst still displaying a fair sample of each void catalogue. The results shown here are for a smoothing scale of $\theta_\mathrm{s} = 2.5$ arcmin and

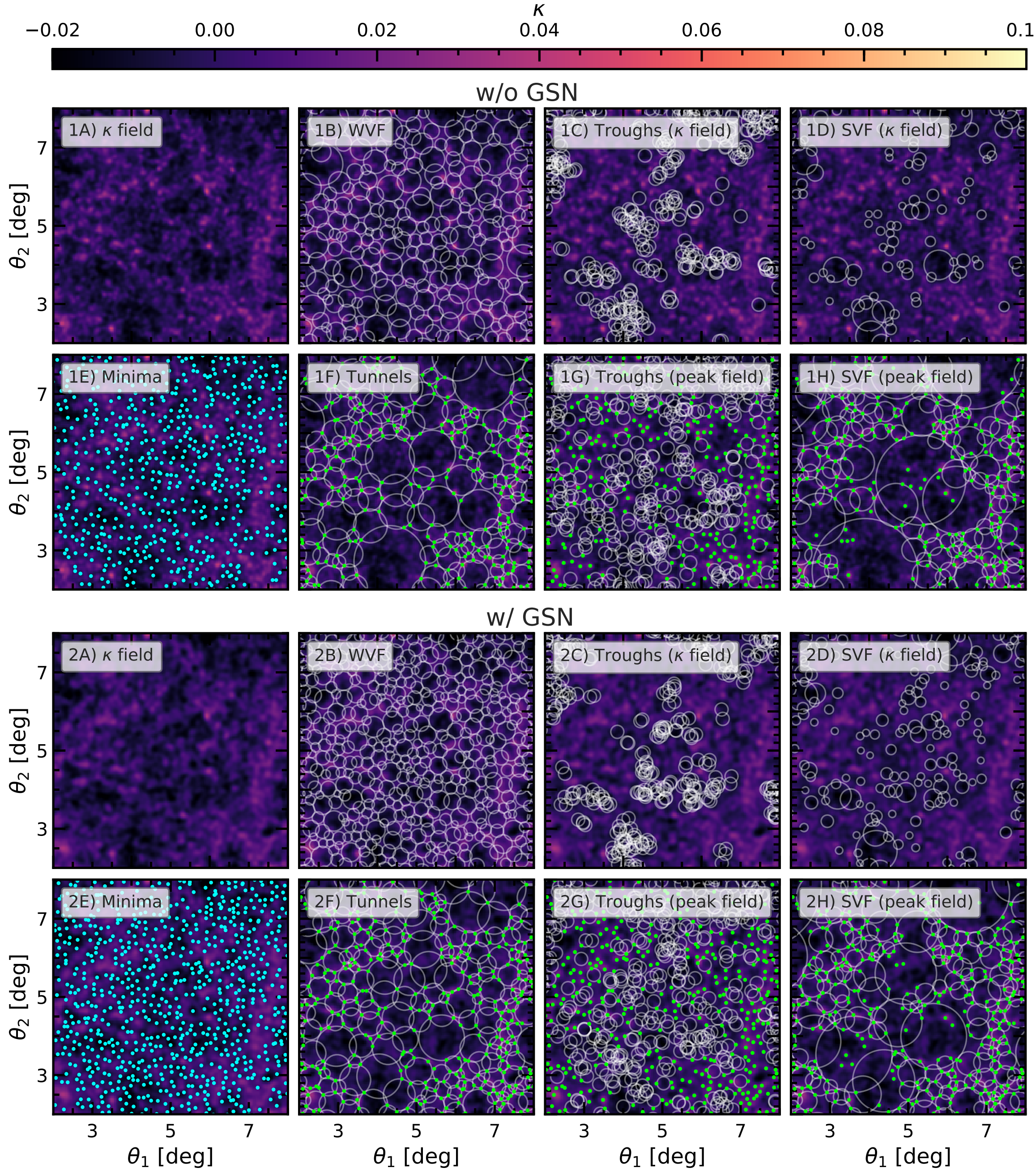

Figure 3.2: A visualisation of the weak lensing void finders discussed in this Chapter. The convergence field is shown by the background colour map in each panel, with the convergence values illustrated by the colour-bar at the top of the figure. Here the brightest (orange) colours correspond to high κ values and the darkest (purple) colours show low κ regions. The results presented here are for a Gaussian smoothing scale, $\theta_s = 2.5$ arcmin. The top eight panels are for WL maps with no GSN (1A to 1H), and the bottom eight panels are for WL maps with GSN (2A to 2H). Panels 1A and 2A show only the convergence fields as a reference point. The panels 1B to 1E and 2B to 2E show voids identified in the convergence field and correspond to: WVF, troughs and SVF applied to the κ field, and minima. The remaining panels (1F to 1H and 2F to 2H) show voids identified using WL peaks with height, $\nu > 2$, and correspond to: tunnels, troughs and SVF applied to the peak distribution. Only the central 6×6 deg^2 of the convergence maps are shown to avoid overcrowding.

for peak catalogues with WL peak heights of $\nu > 2$ (where applicable). The top row of each section (panels 1A - 1D and 2A - 2D) corresponds to voids identified in the WL convergence maps and the bottom rows (panels 1E - 1H and 2E - 2H) corresponds to voids identified in the WL peak distribution. The WL peaks are shown by the green points, while the WL minima are shown by the cyan points.

Panels 1B and 2B of Fig. 3.2 shows the WVF voids identified in the WL convergence map. These voids tend to avoid the more overdense patches of the convergence map, since these more overdense regions reside at the watershed basin boundaries. The WVF voids occupy most of the area of the WL convergence map, which is due to every pixel within the map being assigned to a watershed basin. In some cases, the largest voids enclose smaller voids, as can be seen towards the top left of Panel 1B. The overlap is an artefact of illustrating the WVF as circles when actually these voids have highly non-circular and non-overlapping shapes (e.g. see Platen et al., 2007; Cautun et al., 2016). By adding GSN, the size of the WVF voids is reduced and their abundance is increased.

Troughs identified directly on the convergence map are shown in Panels 1C and 2C, where it can be seen that these troughs trace only the most underdense regions of the convergence maps, which is by construction. The consequence of this algorithm is that many troughs significantly (or nearly entirely) overlap with other troughs, with very few troughs existing in isolation from other troughs. This will lead to highly correlated information in the statistics describing these troughs, as will be seen in their correlation matrices in Appendix .1. Panel 2C shows how adding GSN can change the spatial distribution of the troughs, although the degree of overlap between neighbouring troughs remains similar to the no-GSN case in panel 1C.

Panels 1D and 2D show the SVF voids identified in the convergence field. As can be seen there, the abundance of these voids is significantly lower compared to void catalogues from other algorithms, and more small voids are generated. However, these voids trace the underdensities of the convergence map reasonably well, as can be seen by their dark interiors. There are more voids in panel 2D, indicating that GSN increases the abundance of these voids.

The WL minima are displayed in Panels 1E and 2E. We remind the reader that we only study underdense minima, i.e., $\nu < 0$, and so only these minima are shown in the figure. These panels illustrate that the WL minima are slightly different from the typical WL void definition used in this Chapter, since they have no size or radius, which has the advantage of simplicity. In later sections we'll discuss the abundance of WL minima as a function of their amplitude, rather than as a function of their size, and the abundance of WL minima has been shown to provide complementary cosmological information to the WL peak abundance (Coulton et al., 2019b). We also discuss, for the first time, the potential for the radial lensing profiles of WL minima to be used in a cosmological analysis. There are more WL minima in panel 2E compared to 1E, indicating that there are more spurious minima created by GSN than physical minima removed by GSN.

A visualisation of the tunnel algorithm is shown in Panels 1F and 2F. The WL peaks used to identify the tunnels are shown by the green points, highlighting that the tunnels do not enclose any WL peaks, and that the peaks only reside on the void boundaries. Like the WVF, the tunnels occupy most of the area of the convergence map, however the tunnel algorithm identifies a wider range of void sizes, producing more large voids than those identified in the convergence maps. Smaller tunnels tend to cluster more than the larger ones, with the former appearing more in the overdense parts of the convergence map. Also similar to the WVF voids, panel 2F contains more tunnels which are on average smaller than the tunnels in panel 1F. This is because the spurious WL peaks created by GSN break up the larger tunnels in panel 1F into the multiple smaller tunnels seen in panel 2F.

Panels 1G and 2G show the troughs identified in the WL peak distribution. The troughs identified in this way still have a significant degree of overlap, however the overlap in this case is much weaker than for the troughs identified in the convergence maps. There are underdense patches in which no troughs have been placed, whilst many overlapping troughs can be seen in other regions. This highlights the inefficiency of the trough algorithm when applied to a WL peak distribution. This may be solved by increasing the number of troughs that are placed, however this will also increase the number of significantly overlapping troughs. As with the troughs applied to the convergence map, the troughs identified in the WL peak distribution trace different regions of the WL maps when GSN is added, and the degree of overlap between neighbouring troughs appears similar in both panels 1G and 2G.

Finally, Panels 1H and 2H show the SVF voids identified in the WL peak distribution. This algorithm produces the largest voids of all void finders and, similar to the WVF and tunnel algorithms, populates most of the area of the convergence map with voids. Also similar to the tunnels, the largest voids are in underdense regions and the smaller voids cluster in the overdense patches. It is interesting to note that in some cases, the tunnels and SVF identify the same voids in the WL peak distribution, as can be seen towards the top left of panels 1F and 1H. Panel 2H shows that the SVF voids identified in the WL peak distribution respond to GSN in the same way as tunnels and WVF, where these voids become smaller and more abundant in the presence of GSN.

3.4 Void statistics

In this section we discuss the statistics of each of the seven void populations analysed here and study how the physical signal is affected by GSN in each case. We also investigate the impact of varying the smoothing scale to quantify how this mitigates the impact of GSN. For each void type we present the abundance, convergence profiles and tangential shear profiles. Then, in Section 3.5, we will compare the different void populations and investigate which type of void is least affected by GSN while giving rise to the strongest tangential shear signature.

3.4.1 Minima

Fig. 3.3 shows the statistics of the WL minima depicted in Panels 1E and 2E of Fig. 3.2 with and without GSN (dashed and solid lines respectively) for three smoothing scales, 1, 2.5 and 5 arcmin (blue, orange and green respectively).

The top panel shows the differential WL minima abundance as a function of amplitude κ. The distribution peaks at $\kappa \sim -0.01$, with the peak shifting closer to 0 as the smoothing scale increases. The distributions are also positively skewed, highlighting the non-Gaussian properties of WL minima. When GSN is included, the abundance of minima is significantly contaminated, especially for small smoothing scales. For $\theta_\mathrm{s} = 1$ arcmin, GSN introduces a large amount of spurious negative minima, while minima with such low negative amplitudes do not exist in the no GSN case. This is shown by the steep cutoff at $\kappa = -0.03$ for the no GSN case, while the minima abundance is still steadily decreasing below $\kappa = -0.03$ in the GSN-added case. A non negligible amount of spurious positive minima are also added by GSN, however this affect is less extreme than for negative minima. The creation of spurious minima due to GSN is suppressed as the smoothing scale increases, however even with $\theta_\mathrm{s} = 5$ arcmin, there is still a noticeable amount of spurious negative minima. For each smoothing scale it can be seen that the WL minima are significantly more impacted by GSN than WL peaks by comparing with the right panel of Fig. 3.1.

Lensing profiles are calculated from minima with amplitudes $\kappa < 0$, as indicated by the shaded grey region in the top panel. The middle panel shows the mean stacked radial convergence profiles around the WL minima out to 12 arcmin. For $\theta_\mathrm{s} = 1$ arcmin, by comparing the blue

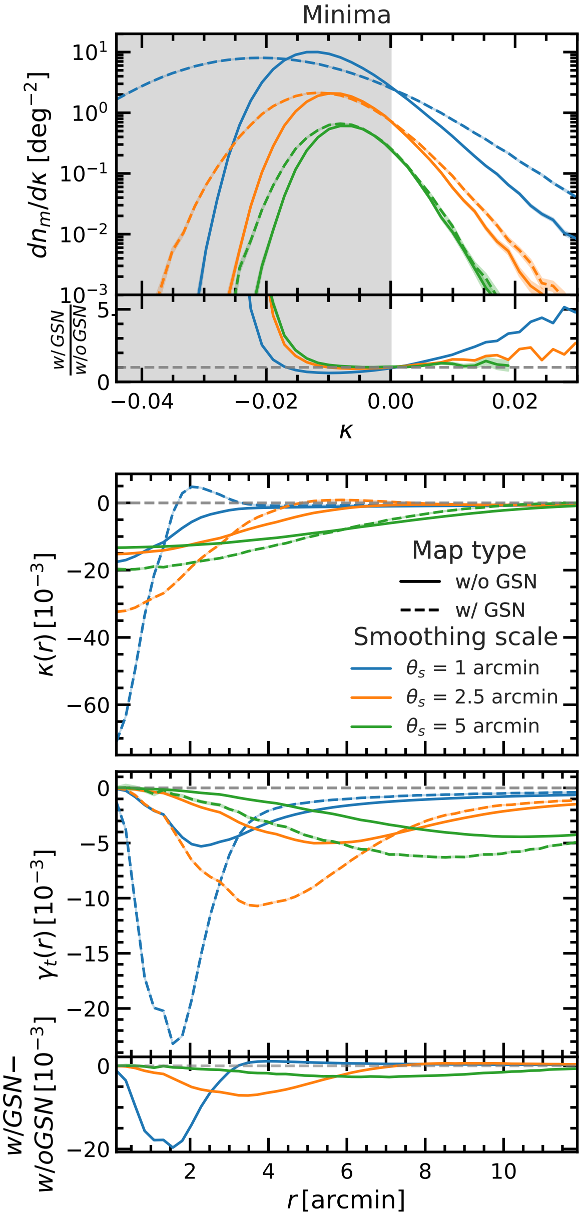

Figure 3.3: The statistics describing the properties of WL minima depicted in panel E of Fig. 3.2. Solid lines show the properties of WL minima identified in WL maps with no GSN, while dashed lines show the properties of WL minima identified in WL maps with GSN. Different colours correspond to different smoothing scales applied to the convergence maps before identifying the minima, with blue, orange and green for $\theta_\mathrm{s} = 1$, 2.5 and 5 arcmin respectively. One sigma standard error bars corresponding to the uncertainties associated to our analysis (which makes use of a 19200 deg^2 sky area) are given by the shaded coloured regions around each curve, however in most cases these error bars are a similar thickness to the curves. The top panel shows the WL minima abundance as a function of their WL convergence amplitude κ, and the shaded grey region indicates the minima that are used to calculate the lensing profiles. The middle panel shows the radial WL convergence profiles of the WL minima out to 12 arcmin, and the bottom panel shows the corresponding WL tangential shear profiles. The lower sub-panel in the top (bottom) panel shows the relative (absolute) difference between the minimum abundances (tangential shear profiles) measured in WL maps with and without GSN.

solid and dashed lines, it can be seen that the addition of GSN artificially boosts the depth of the convergence profile at $r \sim 0$ by over a factor of 3. This is caused by the creation of a significant number of spurious minima with unphysically deep negative κ values, as shown by the minima abundance in the top panel. For the GSN case, the minima convergence profile briefly becomes positive between ~ 1.5 and 3 arcmin, which is possibly due to the creation of spurious (negative) minima in local overdensities from GSN. In contrast, for the no GSN case, the convergence profile gradually approaches the mean background value of $\kappa = 0$. For larger smoothing scales, similar behaviour is still present, with the κ amplitude at $r = 0$ still artificially boosted by GSN, however this boost decreases with increasing smoothing scale.

The bottom panel shows the tangential shear profiles around the WL minima, $\gamma_{\mathrm{t}}(r)$, calculated from $\kappa(r)$ using Eq. (1.2.12). As the smoothing scale increases, the peak of the tangential shear profile moves to outer radii, whereas the inclusion of GSN shifts the peak to inner radii relative to the no GSN case. The difference in amplitude between the no GSN and GSN cases for the tangential shear profiles is smaller than for the convergence profiles, but significant contamination due to GSN still remains. For the no GSN maps, the height of the peak of the tangential shear profiles is somewhat insensitive to the smoothing scale, whilst increasing θ_{s} quickly suppresses the peak in the tangential shear profiles for the GSN-added maps.

These statistics in Fig. 3.3 show that the WL minima are significantly affected by GSN and are more susceptible to GSN than WL peaks.

3.4.2 Troughs in the convergence map

Fig. 3.4 shows the statistics of troughs identified directly in the convergence field. The top row shows the probability distribution function (PDF) of the mean enclosed convergence within all randomly placed circles, and the three columns (from left to right) are for trough radius R_{v} equal to 10, 20 and 30 arcmin respectively. The shaded grey regions show the circles with a mean enclosed convergence in the bottom 20% of all circles, which are the troughs that are used to calculate the trough lensing profiles. For a fixed trough radius, the κ value above which circles are discarded depends on the smoothing scale and whether or not the WL maps include GSN. For simplicity the shaded grey regions shown here are for $\theta_{\mathrm{s}} = 2.5$ arcmin in WL maps without GSN.

Increasing the smoothing scale θ_{s} decreases the width of the PDFs, and improves the agreement between the no GSN and GSN maps. As with the minima abundances, the largest

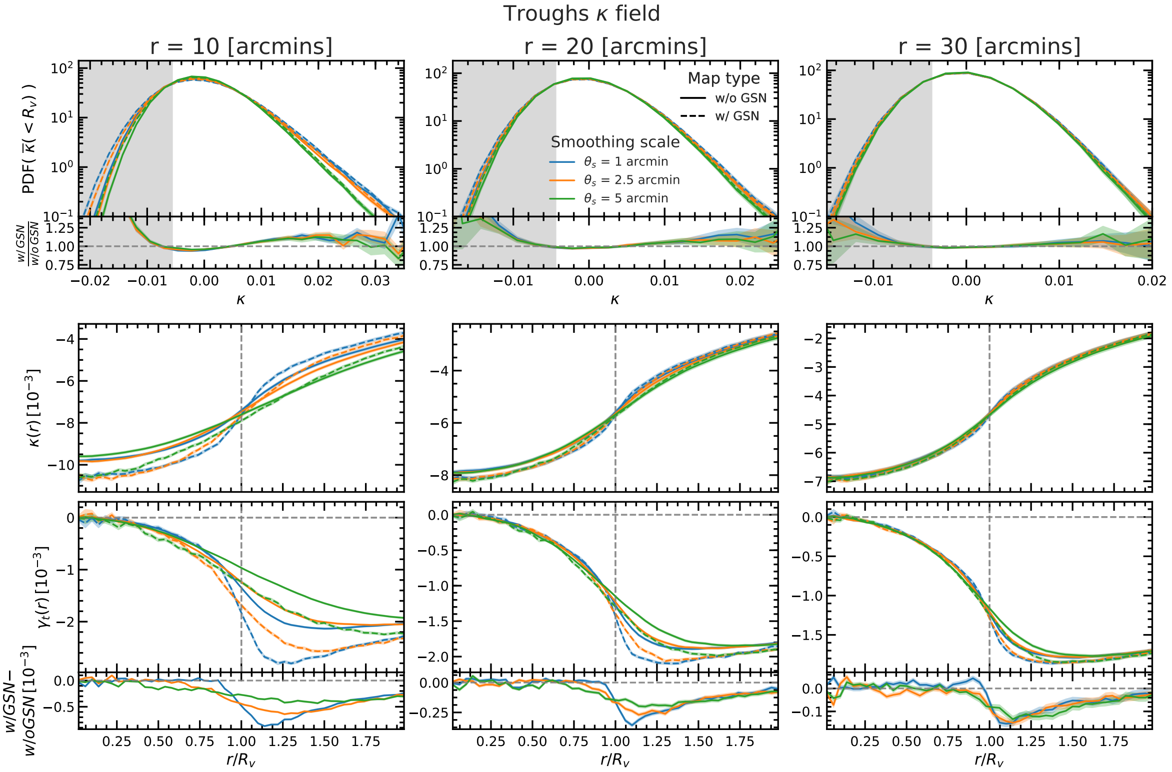

Figure 3.4: The statistics describing troughs identified directly in the convergence field. For the meaning of line colours and line types see the legend and, for more details, the caption of Figure 3.3. The top row shows the PDF of the mean enclosed convergence within all randomly placed circles. The shaded grey region indicates the circles we define as troughs, that is the ones with a mean enclosed convergence in the bottom 20% of all circles (here we show the threshold for maps without GSN and for $\theta_\mathrm{s} = 2.5$ arcmin; the exact threshold depends slightly on smoothing scale and if GSN is included). The middle row shows the mean convergence profiles and the bottom row shows the mean tangential shear profiles. The three columns correspond to troughs of different sizes: 10 (left), 20 (centre) and 30 (right) arcmin. The lower sub-panels in the top (bottom) row shows the relative (absolute) difference between the trough κ PDFs (tangential shear profiles) measured in WL maps with and without GSN.

differences between the no GSN and GSN maps are found at the negative-κ regions of the PDF. As the trough radius increases, the agreement between the no GSN and GSN maps improves, and so does the agreement between different smoothing scales. These PDFs are all positively skewed indicating that the troughs identify more underdense regions than overdense regions.

The middle row shows the mean stacked convergence profiles of the troughs for different radii. The troughs have very underdense centres, and κ gradually increases with r. This increase gets sharper near $r = R_{\rm v}$ and then slows down further outside the trough radius. The depth of the convergence profiles is larger for the GSN maps, and the smoothing scale has a relatively small impact. As the trough radius increases, the overall depth of the convergence profiles decreases, however the shapes of the convergence profiles remain the same. The impact of GSN on the convergence profile decreases with $R_{\rm v}$, with the case $R_{\rm v} = 30$ arcmin showing little difference between the GSN and no GSN cases.

The bottom row shows the tangential shear profiles of troughs, which are characterised by a maximum amplitude that is roughly an order of magnitude smaller than that of the WL minima. The inclusion of GSN has little impact on the trough tangential shear profiles for $r \lesssim R_{\rm v}$ (especially for the 20 and 30 arcmin troughs). At larger distances, GSN leads to an increase in tangential shear which persists even up to $r = 2R_{\rm v}$. The difference between the maximum tangential shear amplitude for the no GSN and GSN maps is very small relative to the same feature in the WL minima. The difference between the no GSN and GSN maps is somewhat insensitive to the smoothing scale, and depends more strongly on the trough radius. As the trough radius increases, the amplitude of the tangential shear profiles decreases slightly and so does the difference between the no GSN and GSN maps.

The statistics describing the troughs identified directly in the convergence maps are significantly less contaminated by the inclusion of GSN than the WL minima. However, the overall amplitude of the tangential shear profile of troughs is also significantly lower, which, as we shall see in Section 3.5, implies that we need a larger survey to measure trough profiles with the same SNR as the minima profiles.

3.4.3 Troughs in the peak distribution

We next study the troughs identified in the distribution of WL peaks. Before identifying troughs, we first remove all peaks below a predetermined ν threshold from the peak catalogue. This reduces the impact of GSN by discarding peaks with low height. This approach adds

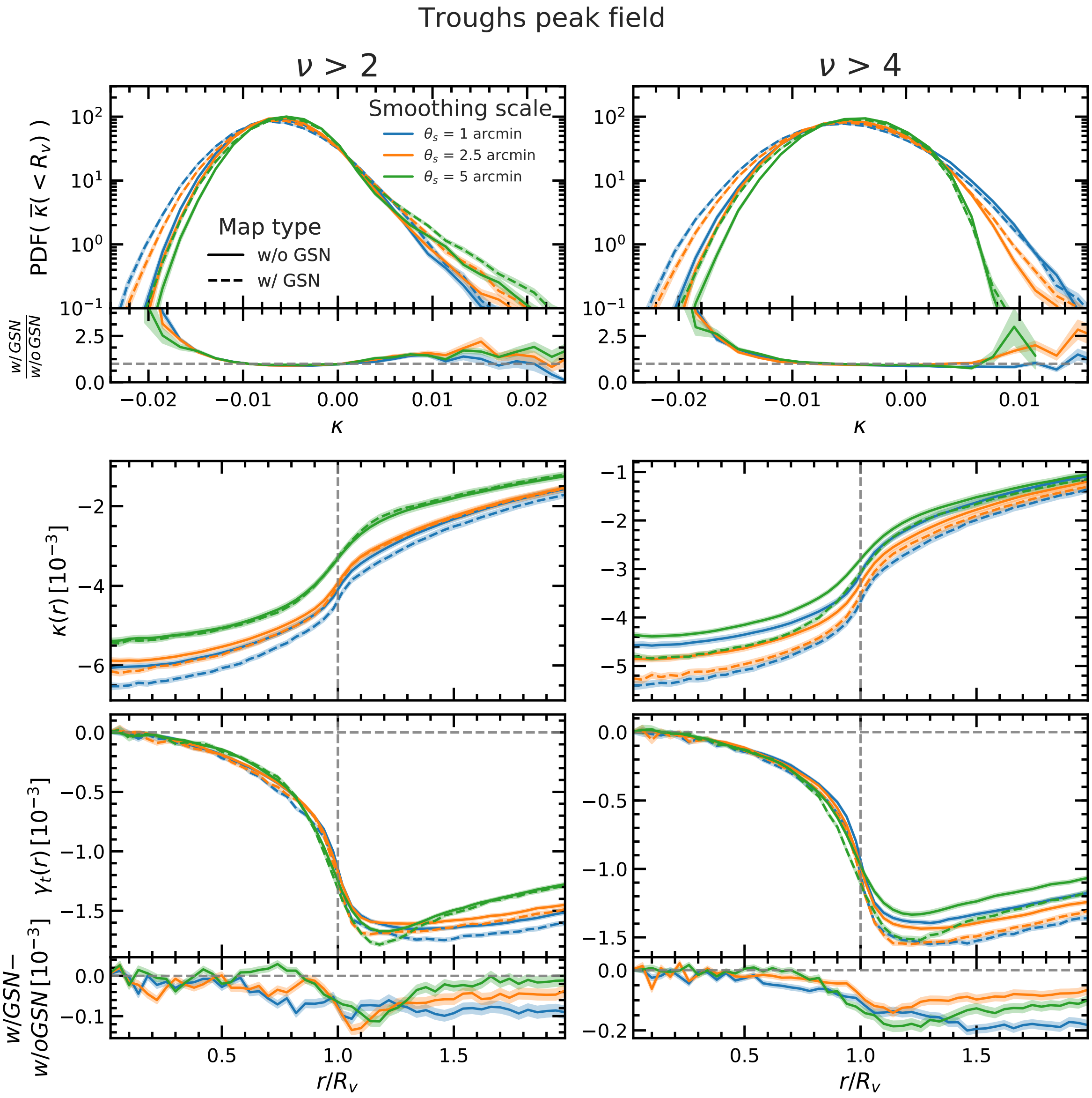

Figure 3.5: The statistics for troughs identified in the distribution of WL peaks. For the meanings of line colours and line types see the legend and, for more details, the caption of Figure 3.3. The top row shows the PDF of the mean enclosed convergence within the troughs, the middle row shows the mean convergence profiles of the troughs and the bottom row shows the mean tangential shear profiles of the troughs. All results shown here are for a fixed trough size of $r = 30$ arcmin. We identify troughs using only the high WL peaks and we show results for two peak height selections: $\nu > 2$ (left column) and $\nu > 4$ (right column). The lower sub-panel in the top (bottom) panel shows the relative (absolute) difference between the trough κ PDFs (tangential shear profiles) measured in WL maps with and without GSN.

another free parameter to the void identification process compared to troughs identified in the convergence field, the ν threshold for peak heights. In Fig. 3.5, we present results for two ν thresholds, $\nu > 2$ and $\nu > 4$, to test the impact of this threshold on the resulting trough statistics. To improve clarity, in Fig. 3.5 all results are presented for a fixed trough size of $R_{\mathrm{v}} = 30$ arcmin, which is chosen because it is the trough radius at which results for the troughs agree best between the no GSN and GSN maps.

The top row of Fig. 3.5 shows the PDFs of the mean enclosed convergence for troughs identified from WL peak catalogues with heights $\nu > 2$ and $\nu > 4$. Note that this is the trough PDF, which is calculated after the randomly placed circles with $\overline{\kappa}(< R_{\mathrm{v}})$ in the top 80% are discarded, unlike in Fig. 3.4. Away from the peak of the PDF, the results from the no GSN and GSN maps disagree for all smoothing scales for both peak thresholds. However, the agreement between the no GSN and GSN maps is good near the positive-κ end of the PDF for all smoothing scales in the $\nu > 4$ catalogue. For the $\nu > 2$ catalogue, the PDFs are positively skewed, indicating that the trough algorithm is preferentially selecting underdense regions, however for the $\nu > 4$ catalogues the PDFs are more symmetric. This is due to the sparsity of tracers at this threshold, where the low number density of WL peaks implies that the $\nu > 4$ catalogue does not give an accurate representation of the underlying convergence field since, for example, many overdense regions of the convergence map do not have peaks with $\nu > 4$. Despite this, the maximum of the PDF is still below zero indicating that we predominantly select underdense regions.

The middle row shows the radial convergence profiles of the troughs identified in the WL peak distribution. These profiles have a similar shape to those of the troughs identified in the WL convergence maps. For the $\nu > 2$ catalogue, agreement between the no GSN and GSN maps improves as the smoothing scale increases, and the two convergence profiles are within the one sigma standard error for $\theta_{\mathrm{s}} = 5$ arcmin. Here, the overall depth of the convergence profiles also decreases with increasing smoothing scale. However, for the $\nu > 4$ catalogues, increasing the smoothing scale only slightly improves the agreement between the no GSN and GSN maps, and there is no trend between smoothing scale and convergence profile depth, since $\theta_{\mathrm{s}} = 2.5$ arcmin produces the deepest convergence profile. This is due to the sparsity of WL peaks for $\nu > 4$, which results in the troughs more randomly tracing the underlying convergence field when compared to a lower ν threshold. This is evident from the fact that the convergence profiles are not as deep in the $\nu > 4$ catalogue when compared to the $\nu > 2$ catalogue.

The bottom row shows the radial tangential shear profiles of the troughs identified in the WL peak distribution. For all smoothing scales and both the no GSN and the GSN maps, the tangential shear profiles agree with each other reasonably well below $r = R_{\mathrm{v}}$, for both ν thresholds. This is due to the consistent shape of the convergence profiles (with only constant shifts with respect to each other) in all cases, which is the main feature that the tangential shear profile is sensitive to. The tangential shear profiles peak at $r \sim 1.2R_{\mathrm{v}}$, which is where results from the different smoothing scales separate. The difference between the no GSN maps and the GSN maps is largest at the peak of the tangential shear, and slowly reduces out to larger radii. These tangential shear profiles are also noisier than for other void finders – this is due to the larger scatter in the locations of the troughs identified in the peak distribution, as can be seen in Panel G of Fig. 3.2, which results in a larger scatter of convergence profiles.

Compared to troughs found directly in the κ map, troughs identified using peaks have tangential shear profiles that have slightly lower amplitudes, however the agreement between the no GSN and GSN cases is better, which is a consequence of the fact that the WL peaks are less affected by GSN than the convergence field in the low κ regions of the WL map.

3.4.4 WVF voids

Fig. 3.6 shows the properties of the WVF voids. The top panel shows the differential void abundance as a function of void radius R_{v}. For the smallest smoothing scale, the largest void that is identified is 0.2 deg, and as the smoothing scale increases the sizes of the voids also increases, which also reduces the total number of voids. The size distributions of the voids are significantly different between the no GSN and GSN maps, where including GSN increases the total number of voids and reduces their size. This is due to GSN adding spurious features to the convergence field such as artificial ridges and minima, which results in the production of spurious voids. Since the WVF voids fill the entire area of the convergence map, having more voids implies that the average void size decreases. Even for $\theta_{\mathrm{s}} = 5$ arcmin, there is still a disagreement in the size distribution between the no GSN and GSN maps, and this disagreement is much larger than the one-sigma standard error bars (shown by the shaded regions around the curves).

The convergence profiles of WVF voids are shown in the middle panel. They have a smooth shape, with negative convergence values at $r = 0$, gradually increasing outwards and crossing $\kappa = 0$ at $r \sim 0.7R_{\mathrm{v}}$. The convergence profiles continue to smoothly increase until $r = R_{\mathrm{v}}$, at which point they start to decrease and return to the mean background value of $\kappa = 0$ far

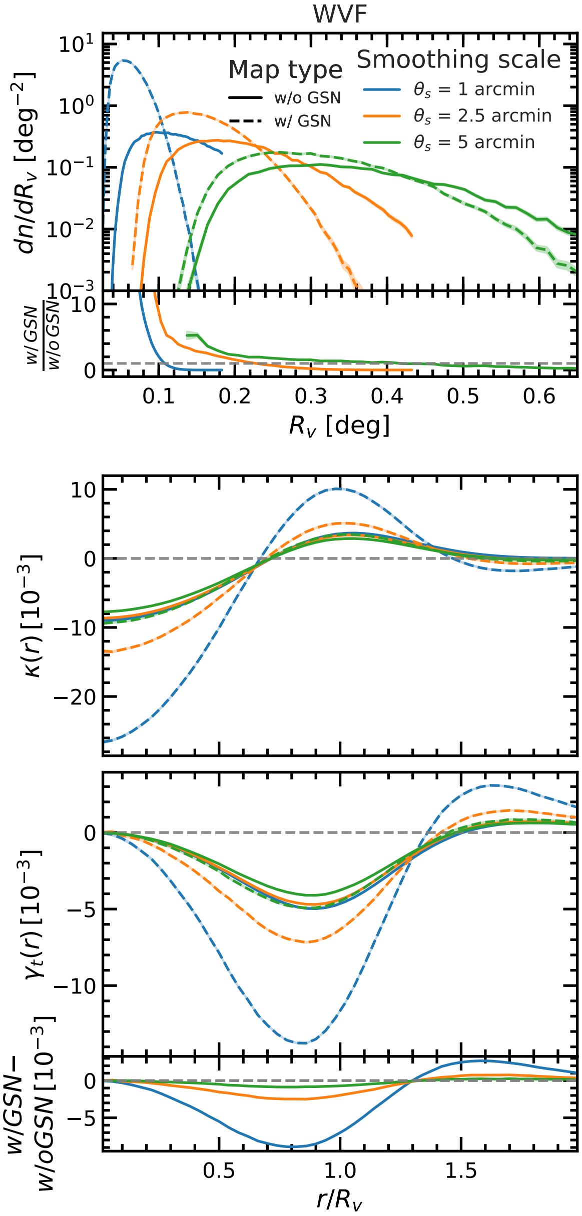

Figure 3.6: The abundance (top row), and the convergence (middle row) and tangential shear (bottom row) profiles of WVF voids. For the meanings of line colours and line types see the legend and, for more details, the caption of Figure 3.3. The lower sub-panel in the top (bottom) panel shows the relative (absolute) difference between the WVF void abundances (tangential shear profiles) measured in WL maps with and without GSN.

outside of the void radius. At $r \sim 1.5R_\mathrm{v}$ some of the void profiles briefly become underdense, which is because the boundary of each void is also the boundary of one of its neighbours voids, which has an underdense interior. This feature is exaggerated for the smaller voids since averages are taken over smaller areas.

In the absence of GSN, the convergence profiles are very similar for different θ_s values. However, after adding GSN, the convergence profiles are heavily dependent of the chosen smoothing scale. For $\theta_\mathrm{s} = 1$ arcmin, the addition of GSN significantly reduces the κ value at $r \sim 0$, which is very similar to the behaviour seen in the WL minima convergence profiles. The similarity between the two is due to the fact that each watershed basin is connected to a local minima, which on average resides close to the centre of the void, and GSN produces a large number of spurious local minima, which can often be deeper than true minima (Fig. 3.3, top panel). This same feature will be seen in SVF voids found from the κ field below. Furthermore, the amplitude of convergence profile in the positive regions is also boosted by GSN, which makes the peak at $r = R_\mathrm{v}$ significantly higher. The above behaviour occurs because the boundary of WVF voids consists of ridges in the κ field and positive GSN values can move and enhance the height of these ridges (the algorithm chooses the highest local ridge and thus preferentially selects the regions with positive GSN values). This is more apparent for smaller smoothing scales, where GSN has not been sufficiently suppressed. The differences between the no GSN and GSN convergence profiles are quickly suppressed with increasing θ_s.

The bottom panel shows the tangential shear profiles for the watershed voids, which peak at $r \sim 0.85R_\mathrm{v}$ and converge to $\gamma_\mathrm{t} \simeq 0$ at large distances. Again, the γ_t profiles are significantly boosted by GSN, and quickly converge back to the no GSN counterparts as the smoothing scale increases. However, visible difference still remains even with $\theta_\mathrm{s} = 5$ arcmin.

3.4.5 SVF in the convergence map

Fig. 3.7 shows the statistics for SVF voids identified directly in the convergence field (SVF κ). The shape of the void abundance function is different from the other void finders, declining faster with void radius than for other void types. Additionally, there is no turning point at the small-radius part of the distribution. For example, the WVF finds few very small voids, where the abundance of small voids briefly increases as the void radius increases, before the peak of the distribution. This is not the case for the abundance of SVF κ voids, which does not reach a peak even at the smallest radii plotted. This is due to the SVF identifying voids

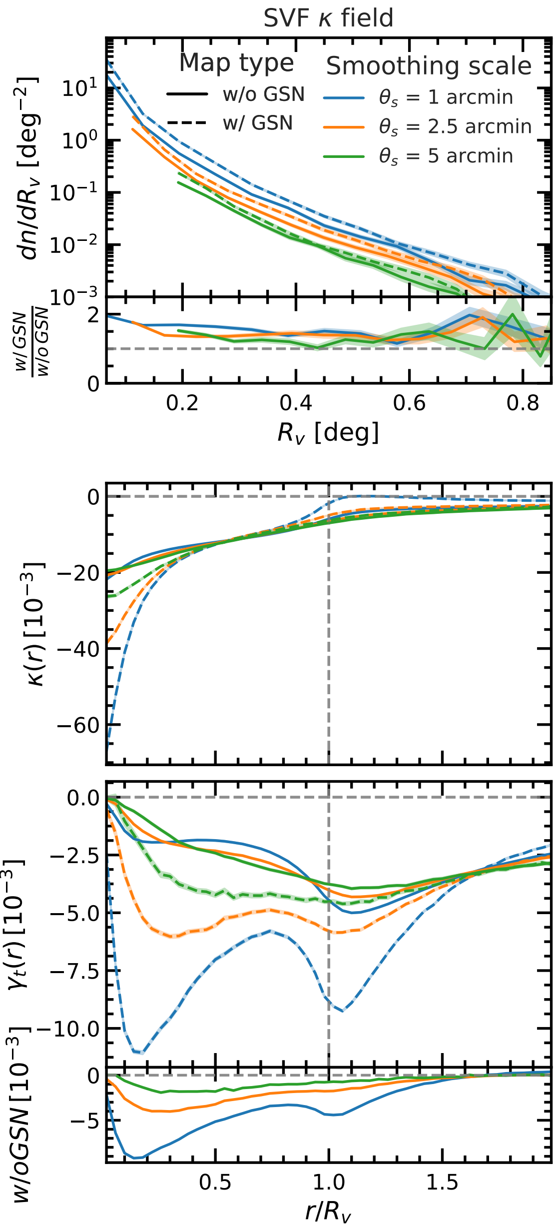

Figure 3.7: The statistics describing the SVF applied directly to the convergence maps: the abundance (top row), and the convergence (middle row) and tangential shear (bottom row) profiles of SVF κ voids. For the meanings of line colours and line types see the legend and, for more details, the caption of Figure 3.3. The lower sub-panel in the top (bottom) panel shows the relative (absolute) difference between the SVF-κ void abundances (tangential shear profiles) measured in WL maps with and without GSN.

with sizes down to the pixel resolution. As mentioned above, in this Chapter we remove very small voids by imposing a minimum void size, $R_\mathrm{v} \geq 2\theta_\mathrm{s}$.

The abundance of voids is systematically larger for the GSN maps than the no GSN maps, for all smoothing scales. In the case of the WVF, GSN increases the abundance of small voids but decreases the abundance of large voids, due to spurious structures introduced by GSN splitting the larger voids into smaller objects. For the SVF, the abundance of large voids is much lower to start with, and the voids populate the convergence maps much more sparsely, as shown in Panel D of Fig. 3.2. This means that the spurious structures introduced by GSN contribute less to the degradation of true voids and largely only produce spurious voids, which is due to the addition of spurious minima from GSN (Fig. 3.3, top panel) which are the seeds for the SVF κ voids; this can be visibly seen by comparing panels 1D and 2D in Fig. 3.2. Also, note that the abundance of SVF κ voids decreases for all void radii when θ_s increases, which is because the abundance of WL minima decreases with increasing θ_s, as shown by the top panel of Fig. 3.3.

The middle panel shows the mean radial convergence profiles of the SVF κ voids. These voids are very deep at $r \sim 0$, similar to the WL minima, and the convergence increases continuously out to $r = 2R_\mathrm{v}$. Like in the WFV case, the convergence profiles in the no-GSN maps are somewhat insensitive to the chosen smoothing scale, whereas the depth of the profiles for the GSN maps is quickly suppressed with increasing θ_s. The depth of the convergence profiles at $r \sim 0$ is artificially boosted when GSN is included (e.g. by a factor of 3 for $\theta_\mathrm{s} = 1$ arcmin), which is again due to the creation of spurious minima with very low κ values. However by $r = 0.5R_\mathrm{v}$ the no GSN and GSN maps agree reasonably well, apart from the voids in the GSN added map for $\theta_\mathrm{s} = 1$ arcmin, whose convergence profile returns to $\kappa = 0$ faster than the other voids.

The bottom panel shows the tangential shear profiles for the SVF κ voids. For all other void finders, the inclusion of GSN boosts the amplitude of the tangential shear profile, and in some cases also changes slightly the radius where the signal reaches maximum. For the SVF κ voids, the γ_t signal, which is maximal at $r \sim 1.1R_\mathrm{v}$, is also boosted in the GSN maps relative to the no GSN maps. But here we find a secondary peak of γ_t at $r/R_\mathrm{v} \sim 0.15$, which is particularly strong for small smoothing scales and when GSN is included. This is due to the flattening of the κ profile at $0.3 \lesssim r/R_\mathrm{v} \lesssim 0.8$ following a steep increase at $r/R_\mathrm{v} \lesssim 0.3$. Such a large inner gradient of the κ profile is due to these voids being centred on local WL minima, and this is more true in the GSN maps for which many of the SVF void centres correspond to spurious WL minima that are typically considerably deeper than the physical minima, as can be seen from the abundance of WL minima shown in the top panel of Fig. 3.3 (and also the middle panel of Fig. 3.3). These spurious minima, on average, have much lower κ values than their neighbours that manifests as a strong κ gradient, which explains why the secondary peak is more pronounced for the case of GSN maps.

The agreement between the tangential shear profiles in the no-GSN maps and the GSN maps improves slightly as the smoothing scale increases. However, a significant difference remains even for $\theta_{\rm s} = 5$ arcmin, as in the case of WVF voids, highlighting the fact that the impact of GSN is hard to be completely eliminated for voids identified from the WL convergence map.

3.4.6 SVF in the peak distribution

Fig. 3.8 shows the statistics for SVF voids identified in the WL peak distribution (SVF peak). The top panel shows the differential void abundance. The SVF peak algorithm identifies the largest voids of all the void finders studied in this Chapter, with some voids as large as two degrees in radius. Here larger smoothing scales reduces the total number of voids but creates larger voids, and including GSN adds spurious small voids and reduces the abundance of large voids. This is due to the generation of spurious WL peaks from the addition of GSN, where a higher number density of tracers split large voids into multiple smaller ones. Fewer voids are detected overall in the $\nu > 4$ catalogue compared to the $\nu > 2$ catalogue, however these voids are larger than their counterparts in the $\nu > 2$ catalogue. This is again due to the reduced number density of WL peaks that are used as tracers in the void identification. Apart from this the abundances of the voids in the two catalogues appear qualitatively similar.

The middle row shows the convergence profile for the SVF peak voids, which are underdense close to the void centre and overdense near the void boundary. Outside of the void radius the convergence gradually approaches the background value of $\kappa = 0$. The depths of the void centres and amplitudes at the void radius are boosted in the GSN maps, however the difference between the void convergence profiles in the no-GSN and GSN added maps is quickly suppressed as the smoothing scale increases, and at $\theta_{\rm s} = 5$ arcmin the difference is small. The depth close to the void centres and the peak at the void boundary also decrease when the smoothing scale increases. These voids are less underdense than most of the other void types.

The bottom row presents the tangential shear profiles for the SVF peak voids. These profiles have a sharp peak at $r = R_{\rm v}$ and the amplitude of these peaks is large despite the shallow

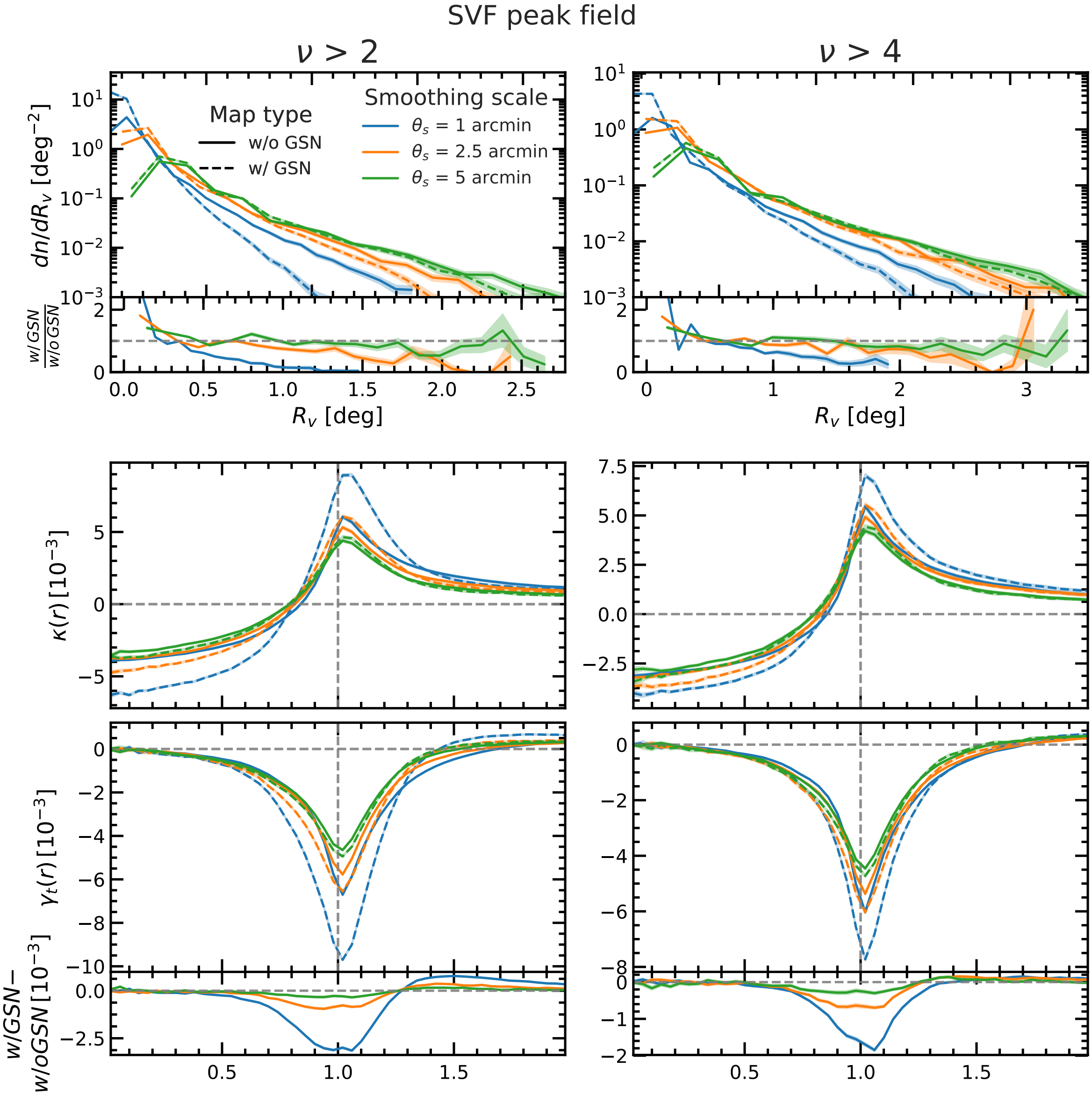

Figure 3.8: The statistics describing the SVF applied to the WL peak distribution: the abundance (top row), and the convergence (middle row) and tangential shear (bottom row) profiles of SVF peak voids. For the meanings of line colours and line types see the legend and, for more details, the caption of Figure 3.3. Each column corresponds to voids identified in a different WL peak catalogue, $\nu > 2$ on the left and $\nu > 4$ on the right. The lower sub-panel in the top (bottom) panel shows the relative (absolute) difference between the SVF-peak void abundances (tangential shear profiles) measured in WL maps with and without GSN.

convergence profiles near the void centres. This is due to the rapid increase in $\kappa(r)$ seen in the range $r/R_{\mathrm{v}} \in [0.7, 1.0]$, with the $\gamma_{\mathrm{t}}(r)$ amplitude being largest when $\kappa(r)$ changes rapidly. This highlights that identifying the deepest underdensities is not the most important criterion when the tangential shear profile is the observable of main interest. Similar to the other void finders, the peak of the tangential shear profiles is boosted in the GSN maps, however, as with the convergence profiles this difference is quickly suppressed as θ_{s} increases, with most of the difference removed with $\theta_{\mathrm{s}} = 5$ arcmin. The amplitude of the tangential shear profiles is slightly smaller for the peak catalogue with a larger ν threshold, indicating that it does not depend strongly on the ν threshold used for WL peak selection. The main difference comes from the fact that having a higher ν threshold results in fewer voids that, as we shall see in Section 3.5, means a lower SNR when measuring the shear profiles of these voids for a given sky area.

3.4.7 Tunnels

Fig. 3.9 shows the statistics of voids identified in the WL peak distribution using the tunnel algorithm, where the left and right columns correspond to tunnels identified in WL peak catalogues with heights $\nu > 2$ and $\nu > 4$ respectively. The top row shows the differential void abundance of the tunnels. The tunnel algorithm also identifies some of the largest voids studied in this Chapter, although the largest SVF peak voids are larger than the largest tunnels. Consistent with other void finders, the tunnel algorithm identifies more voids in total in the maps that include GSN, and fewer large voids. The abundance of the tunnels decreases, and the size of the tunnels, increases with increasing θ_{s}. The differences in the void abundances between the no-GSN and GSN maps decreases with increasing θ_{s} and the difference becomes small at $\theta_{\mathrm{s}} = 5$ arcmin.

The middle row shows the tunnel convergence profiles, which have a very similar shape to that of the SVF peak voids. This is to be expected as in some cases both of these algorithms identify the same voids. Beyond their similarities, the tunnel algorithm identifies voids with slightly deeper convergence profiles near the centre and more overdense ridges at the boundary. This is because the tunnels by definition do not enclose any WL peaks but instead only have peaks residing at their boundaries, whereas the SVF peak algorithm allows WL peaks to reside within voids, which can lead to higher κ values inside SVF peak voids than inside tunnels. Similar to other void types, adding GSN leads to lower κ values at the tunnel centres and a higher overdensity at the tunnel boundaries. This difference is again

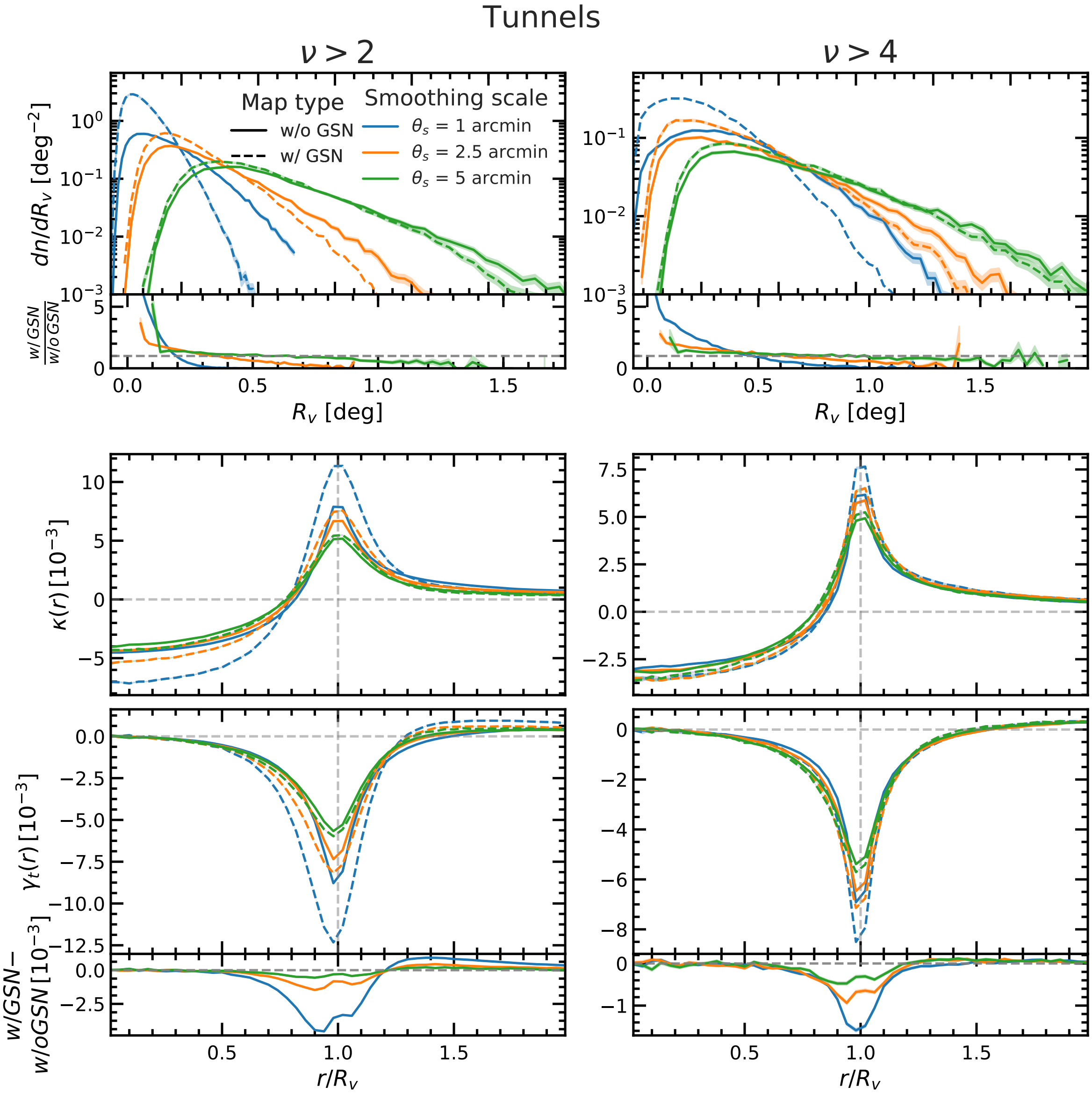

Figure 3.9: The statistics describing the Tunnels identified in the WL peak distribution: the abundance (top row), and the convergence (middle row) and tangential shear (bottom row) profiles of tunnels. For the meanings of line colours and line types see the legend and, for more details, the caption of Figure 3.3. The left and right columns correspond to tunnels identified in WL peak catalogues with heights $\nu > 2$ and $\nu > 4$ respectively. The lower sub-panel in the top (bottom) panel shows the relative (absolute) difference between the tunnel abundances (tangential shear profiles) measured in WL maps with and without GSN.

strongly suppressed for $\theta_{\rm s} = 5$ arcmin. The tunnels behave similarly to the SVF peak voids when the ν threshold of the WL peak catalogue is increased, slightly reducing the depth of κ profiles at the void centre and the peak at the void boundary, whilst the peak becomes sharper.

The bottom row shows the tangential shear profiles which are qualitatively similar to the results of SVF peak voids, except that the tunnels have a higher peak at $r = R_{\rm v}$. The difference between the no-GSN and GSN-added maps respond to the chosen smoothing scale in the same way as the convergence profile, with little difference remaining when $\theta_{\rm s}$ increases to 5 arcmin. Changes in the tangential shear in response to increasing the ν threshold are also the same as in the convergence profiles. Here we note that for the $\nu > 4$ WL peak catalogue, the convergence and tangential shear profiles for all smoothing scales, and for maps with and without GSN, are all very similar and follow each other closely, overlapping in some places. The main difference between the different curves can be seen at the peak of the profiles where most of the information in terms of SNR is contained (Cautun et al., 2018).

3.5 Comparison of different void definitions

In this section we quantify the relative merit of each void finder. There are many criteria that one could use to quantify the suitability of a specific void finder for a given purpose (e.g. see Cautun et al., 2018; Paillas et al., 2019). Here we are interested in a rather general comparison of the various methods that identify WL voids. We choose to do so by answering two questions: i) Which void populations are least affected by GSN? and ii) Which void types have the highest tangential shear signal, as quantified in terms of SNR? These questions are motivated by the goal of using WL voids to constrain cosmological parameters and alternative cosmological models. To a first approximation, we expect that the constraints derived from voids will be maximal when their signal, such as $\gamma_{\rm t}$ profiles, can be measured with low uncertainties (i.e., high SNR) and when the effects of GSN are minimised (e.g. see Cautun et al., 2018; Paillas et al., 2019). This might not always be the case as we discuss later on, but nonetheless is a good starting point for a general comparison.

3.5.1 Impact of GSN

GSN is the leading contribution to noise that contaminates the observed WL signal, and for this reason it is important to understand how the void finders respond to GSN, before the statistics developed here can be used to constrain cosmological parameters. As we saw in Section 3.4, GSN can lead to the identification of spurious voids and to the breaking of physical voids into more objects. This could potentially degrade the cosmological information contained in the statistics of voids, and thus lower the cosmological constraints that can be inferred using WL voids.

To assess the effect of GSN, we proceed by comparing voids in maps with and without GSN. Such a test requires us to choose a WL void statistic to measure the impact of GSN. Up to now, we have studied the abundances and γ_{t} profiles with and without GSN, and here we choose to focus on the tangential shear profile, which will be shown to provide tighter cosmological constraints, such as when testing modified gravity models in Chapter 5. We measure the change in the amplitude of the γ_{t} signal when GSN is added, as a means to quantify the impact of GSN on the lensing profile. Typically, for the void γ_{t} profiles most of the cosmological constraining power comes from the bins where the amplitude of the signal is maximal (e.g., Cai et al., 2015; Barreira et al., 2015; Cautun et al., 2018; Davies et al., 2019a) and, as such, we measure the impact of GSN at this location.

The left panel of Fig. 3.10 shows the relative difference, $|\gamma_{\mathrm{t}}^{\mathrm{GSN}}-\gamma_{\mathrm{t}}^{\mathrm{no-GSN}}|/|\gamma_{\mathrm{t}}^{\mathrm{no-GSN}}|$, between γ_{t} in the GSN-added and no-GSN convergence maps, at the radius at which the amplitude of γ_{t} in the no-GSN is maximal (i.e., where γ_{t} has the most negative value), for all void finders studied in this Chapter. Here, lower values correspond to a small relative impact on the γ_{t} amplitude from GSN while large values indicate that GSN is significantly boosting the γ_{t} amplitude (for all void populations studied here, GSN always increases the amplitude of the γ_{t} signal; see Appendix .2 for a discussion of the reason behind that).

We find that GSN has the largest impact on the γ_{t} profiles of WL minima. This is due to the fact that GSN creates more spurious minima than spurious structures in the other void finders, which is one drawback of the simplicity of the WL minima definition. The boost from GSN is somewhat decreased for the minima when larger smoothing scales are applied. However, in many cases the boost to the minima γ_{t} profiles from GSN with $\theta_{\mathrm{s}} = 5$ arcmin (about 55%) is larger than the γ_{t} boost from GSN for other void finders with $\theta_{\mathrm{s}} = 1$ arcmin. The γ_{t} signal for SVF κ is also boosted by GSN by a similar (relative) amount as the WL minima, which is due to the minima being used as prospective void centres at the start of the SVF κ void identification process. For SVF κ the relative difference between the no-GSN and GSN γ_{t} amplitudes is more quickly suppressed by increasing θ_{s} than for the WL minima, reaching $\sim 20\%$ for $\theta_{\mathrm{s}} = 5$ arcmin. The WVF voids also appear to respond to GSN in a

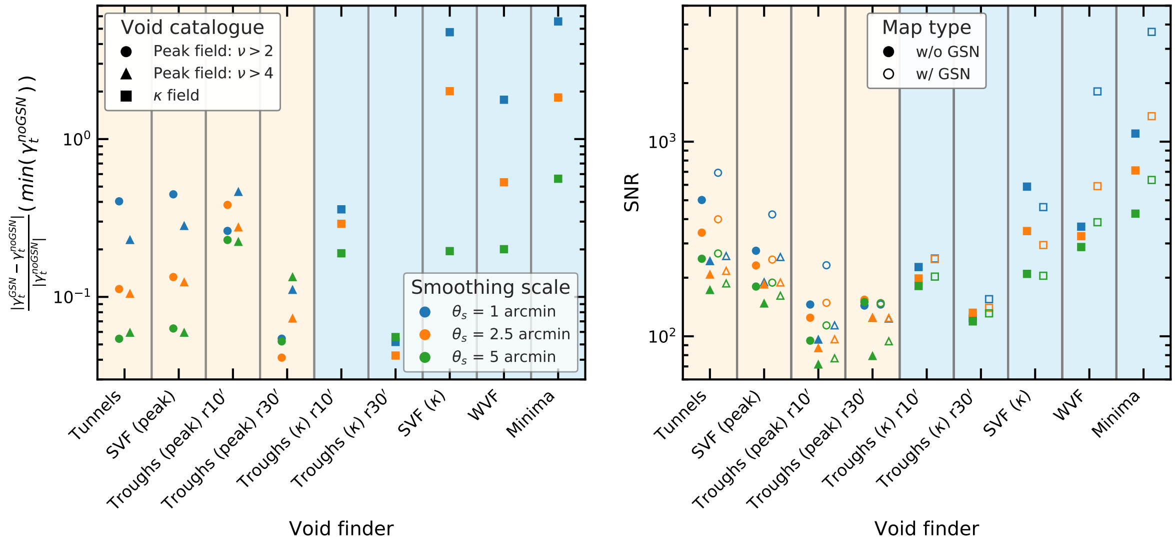

Figure 3.10: Comparisons of the seven void populations studied here in terms of the impact of GSN and in terms of the SNR associated to the tangential shear measurement for a LSST like survey. *Left panel:* the relative difference between $\gamma_{\rm t}$ in the GSN-added and no-GSN convergence maps, at the radius at which the amplitude of $\gamma_{\rm t}$ in the no-GSN maps is highest ($\gamma_{\rm t}$ is lowest). *Right panel:* An LSST forecast of the total SNR with which the $\gamma_{\rm t}(r)$ profile will be measured for each void type. All results in both panels are for all void finders studied in this Chapter (x-axis). A yellow background indicates results for void finders applied to the WL peak distribution and a blue background indicates results for void finders applied directly to the WL convergence maps. Circles correspond to results from voids identified in WL peak catalogues with $\nu > 2$, triangles are for $\nu > 4$, and squares are from voids identified directly in convergence maps. Blue, orange and green markers indicate different smoothing scales, with $\theta_{\rm s} = 1, 2.5$ and 5 arcmin, respectively. In the right panel solid markers indicate results from no GSN maps, and empty markers show results for WL maps with GSN added. Here we plot troughs with a radius of $R_{\rm v} = 10$ and 30 arcmin (labelled as $r10'$ and $r30'$, respectively), to show the impact of changing the trough radius.

similar way to the WL minima and SVF κ, however the amplitude of the boost due to GSN is slightly lower. Finally, for all of the void finders applied directly to the convergence maps, troughs κ appears to be the least impacted by GSN, and they also see the smallest impact on the agreement between the no-GSN and GSN maps from increasing θ_s, as can also be seen in Fig. 3.4.

The void populations that are the least impacted by GSN are those identified in the distribution of WL peaks. This is due to high amplitude WL peaks (Fig. 3.1, right panel) being more resilient to GSN than underdense regions, i.e., $\kappa < 0$, which are the ones determining most of the properties of voids identified directly in the convergence field.

We find that both the tunnels and SVF peak voids respond to GSN in very similar ways and that the impact of GSN is reduced for voids identified in peak catalogues with larger ν thresholds. Finally, the trough peak void finder is the most resilient to GSN of all the methods that employ WL peaks, however in contrast to the tunnels and SVF peak, the impact of GSN increases when the ν threshold increases, which is because troughs peak is more sensitive to tracer sparsity than tunnels and SVF peak.

Both of the trough algorithms are the least impacted by GSN for $R_\mathrm{v} = 30$ arcmin, however for a trough radius of 10 arcmin, the impacts of GSN on the tangential shear profiles for both trough peak and trough κ voids becomes worse than tunnels and SVF peak.

3.5.2 The SNR of tangential shear profiles

Next we investigate the signal-to-noise ratio (SNR) with which we can measure the tangential shear signal of WL voids. Our goal is to assess which void type has the largest SNR since potentially those voids are the most promising to use for cosmological constraints. For examples, Cautun et al. (2018) and Paillas et al. (2019) have studied the signature of modified gravity models in the void population identified using multiple void finders. For 2D voids, they have found that all methods show roughly equal fractional differences in the void shear profiles when comparing modified gravity with the standard model, and thus the optimal void type to constrain such alternative cosmological models is the one in which the γ_t profile can be measured with the highest SNR.

We define the SNR with which we can measure the tangential shear profile of voids as:

$$\mathrm{SNR}^2 \equiv \sum_{i,j} \gamma_\mathrm{t}(i)\ \alpha\ \mathrm{Cov}^{-1}(i,j)\ \gamma_\mathrm{t}(j)\ , \qquad (3.5.1)$$

where the sum is over all bins of $r/R_\mathrm{v} \in [0, 2]$, i and j denote the bins to be summed over, and Cov^{-1} is the inverse of the covariance matrix for the tangential shear measurements. Here γ_t is the mean tangential shear measured from all voids from all 192 maps used in this study and α is the Anderson-Hartlap factor (Anderson, 2003; Hartlap et al., 2007) which we use to compensate for the bias introduced by inverting a noisy covariance matrix. The α factor is given by

$$\alpha = \frac{N - N_\mathrm{bin} - 2}{N - 1} \, , \tag{3.5.2}$$

where $N = 192$ is the number of realisations used to calculate the covariance matrix, and $N_\mathrm{bin} = 50$ is the number of radial bins. We calculate the covariance matrix using the central $10 \times 10 \ \mathrm{deg}^2$ region of the 192 maps described in Section 3.2. We then rescale the SNR values by $\sqrt{A_\mathrm{LSST}/A} = 13.4$ in order to present a forecast for an LSST like survey that has a sky coverage, $A_\mathrm{LSST} = 18,000 \ \mathrm{deg}^2$.

The right panel of Fig. 3.10 shows the SNR (see Eq. (3.5.1)) for the tangential shear profiles from each void finder we have studied. The coloured symbols indicate the results for the three smoothing scales we have studied and we present the SNR values for convergence maps with (open symbols) and without (filled symbols) GSN. This allows us to characterise how the SNR changes when identifying voids in noisy maps.

For all void types, we find that increasing the θ_s smoothing length decreases the SNR ratio; the only exceptions are the troughs peak ($R_\mathrm{v} = 30$ arcmin) and troughs κ voids ($R_\mathrm{v} = 10$ and 30 arcmin), for which the SNR is roughly the same for all three smoothing scales that we used. For the voids found in the peak distribution, increasing the peak threshold leads to lower SNR. Thus, the SNR is maximised for small smoothing scales and for peak catalogues with small ν thresholds.

The right panel of Fig. 3.10 reveals a rather interesting result, which is surprising at first. All void types (except SVF κ) identified in the maps with GSN show a larger SNR than the voids found in the map without GSN. This might be counter-intuitive since, as we discussed, GSN fragments large voids into two or more components and adds spurious objects to the sample, which potentially reduces the sensitivity of voids to cosmology. The answer is given by the fact that the SNR we calculate describes how well we can measure the γ_t signal of a void and not the amount of cosmological information it contains.

The SNR of WL voids in maps with GSN is higher than for the maps without GSN due to two factors: i) adding GSN increases the amplitude of the mean γ_t profile, and ii) it leads to identifying more voids, as shown in Figs. 3.3-3.9. The change in void shear profiles and abundance is an artificial one and it is due to using the same noisy map to identify voids and calculate their profiles. For example, adding a negative GSN value to a pixel makes it more likely to be associated to the interior of a void, and, as a result, the interior of voids is deeper for maps with GSN since it is more likely to contain regions with negative GSN contributions than positive ones. The opposite holds true for the void boundaries. A pixel with a positive GSN value is more likely to be identified as part of a void's edge, and thus the void boundaries in maps with GSN contain a higher fraction of pixels with positive GSN values, which artificially boosts the mean κ value at the void boundary. These two effects lead to an artificially stronger tangential shear profile for voids in GSN maps (for a more detailed discussion and examples see Appendix .2).

We find that the WL minima tangential shear profiles have the largest SNR both in the no-GSN maps and the GSN-added maps, which indicates that they are promising cosmological probes. The WVF has the second highest SNR in the GSN-added maps, but is beaten by SVF κ in the no-GSN maps. Both of the trough algorithms give the lowest SNR values despite being the least affected by GSN in the left panel of Fig. 3.10. SVF peak gives reasonable SNR values, but fares slightly less well in almost all cases than tunnels, which gives SNR values comparable to the void finders applied directly to the WL convergence maps.

3.5.3 Which void definition is best?

Ideally, the optimal void finder would be the one least affected by GSN while having the largest SNR for its tangential shear profile. Fig. 3.10 shows that these two requirements are not compatible: the void finders least affected by GSN (either troughs peak or troughs κ) have the lowest SNR for γ_t, while the voids with the highest SNR (WL minima) are strongly impacted by GSN. The same behaviour is seen when varying the void parameters studied here. Increasing the κ smoothing length, θ_s, used to identify voids, while lowering the impact of GSN, also decreases the SNR for tangential shear. For voids identified in the peak distribution, increasing the ν threshold used for selecting the peak catalogue mitigates the effect of GSN, but again reduces the γ_t SNR. Therefore, there is no clear choice for the best void finder or the best selection of void finding parameters, such as θ_s or WL peak ν threshold.

In general, we find that the void finders that use WL peaks as tracers are less impacted by GSN, while the void finders applied directly to the WL convergence maps give higher SNR values. The void finder that generally offers a good compromise between minimal impact from GSN and a high SNR value is the tunnel algorithm. It has a $\gamma_{\rm t}$ SNR similar to that of the SVF and WVF κ field voids finders while being the second least affected by GSN, after troughs.

We would also like to point out that GSN does not necessarily decrease the amount of cosmological information contained by a probe, and that in some special circumstances it can help make this information more easily accessible. For example, this has been pointed out by Yang et al. (2011), who have shown that the abundance of WL peaks in maps that include GSN provides better cosmological constraints than for maps without GSN. Yang et al. have attributed this effect to stochastic resonance, which is a well-studied phenomenon (Gammaitoni et al., 1998) where a signal in a physical system may be boosted when a source of noise is added, under certain conditions. The conditions required for stochastic resonance to take place within a system are: i) a form of a threshold, ii) a weak coherent input, and iii) a source of noise that adds to the coherent input. From the above it is clear that all three of these conditions apply to WL peaks as discussed in Yang et al., and hence they also apply to WL voids. The first requirement for stochastic resonance is a form of threshold, which in the context of WL voids is the criteria that all void finders identify underdense regions through one means or another. The second requirement is a weak coherent input, which in this context is the WL convergence map. The WL map can be considered weakly coherent because GSN dominates the signal (before smoothing), but contains coherent information due to physical correlations in the map induced by gravitational collapse. Finally, for stochastic resonance we require a source of noise that is added to the WL convergence map, which exactly matches our prescription for modelling GSN.

In the case of WL voids, stochastic resonance occurs because the void finders are designed to identify underdense regions, or underdense regions enclosed by overdense regions etc.. The inclusion of GSN exaggerates some underdense regions and some overdense regions. However, since GSN is random and uncorrelated (neglecting higher order effects such as intrinsic alignment), it could also make some underdense and overdense regions flatter (i.e., smoothed out). Because all void finders fulfil a set of criteria when identifying voids, they will preferentially select the regions that have been exaggerated by GSN and neglect the regions that have been flattened by GSN. Furthermore, distinct deep voids in the physical maps (without GSN) are less likely to be removed by GSN, because the physical signal will dominate the GSN. However less distinct voids that might be missed in the physical maps have a chance to be randomly boosted by GSN, which will result in their detection in the GSN-added maps. These are competing factors with the consequence that GSN can affect true voids and generate spurious fake voids, though true voids are rarely destroyed by GSN but instead are most commonly split up into smaller voids (e.g., as discussed with the tunnel algorithm). It is currently unclear whether or not the boost in SNR from GSN seen in Fig. 3.10 will translate to improved parameter constraints relative to the case without GSN (which is unobservable), however we leave this to a future study. For this reason, we have focused on identifying the void finder that is the least impacted by GSN, whilst still producing high SNR values.

3.6 Discussion and conclusions

In this Chapter we have presented a comparison of different void finders used to identify WL voids within WL convergence or peak fields. The void finders discussed in this Chapter are modified versions of popular void finders that are typically applied to the galaxy distribution. We have shown how each void finder can be modified such that it can be applied to WL maps and have discussed the impact of varying each free parameter associated with the void finders (see Section 3.3). The WL void finders have been split broadly into two classes: i) those that can identify voids directly in the WL convergence maps, and ii) those that require WL peaks as tracers in order to define the voids. We have found that both void classes offer useful information.

We investigate the WL void abundances, convergence profiles and tangential shear profiles for all void finders (where applicable) in Section 3.4. The average void convergence profile consists of an underdense region (i.e. $\kappa < 0$) for $r \lesssim R_{\rm v}$ (with $R_{\rm v}$ the void radius), an overdensity at $r \sim R_{\rm v}$ (not present for troughs), followed by a slow convergence to the background expectation of $\kappa = 0$ at large radial distances. This translates into a negative tangential shear profile for voids, with the amplitude of $\gamma_{\rm t}$ being maximal at $r \simeq R_{\rm v}$. We found that WL minima and SVF κ produce the deepest (most underdense) convergence profiles at $r = 0$, and the $\gamma_{\rm t}$ profiles with the largest amplitudes are produced by tunnels (without GSN) and WL minima (with GSN).

To differentiate the various void finders, we have studied, for each void type, the impact of GSN and the SNR with which their tangential shear profiles can be measured in an LSST like survey. In general, voids identified directly in the convergence field have the highest $\gamma_{\rm t}$ SNR but are also most severely affected by GSN. The void finders based on the peak distribution have moderate SNR and are less affected by GSN. Troughs with large sizes are least impacted by GSN but are also the ones with the lowest γ_t SNR. Increasing the smoothing length or the peak threshold used to identify voids, while it lowers the impact of GSN, also decreases the SNR with which the void tangential shear profile can be measured. The tunnel algorithm provides a good compromise between mitigating the impact from GSN and producing objects with a large γ_t SNR.

In the later Chapters we will use WL voids to provide cosmological parameter constraints and investigate how WL void statistics can be used in a manner that is complementary to constraints from other probes such as WL peaks and the convergence power spectrum. This will be especially interesting in the context of the $\Omega_m - \sigma_8$ degeneracy. Both galaxy voids and WL peaks have been shown to be able to help break this parameter degeneracy (Nadathur et al., 2019; Dietrich & Hartlap, 2010; Davies et al., 2019b), and WL voids may offer another promising avenue to do so.

For parameter constraints, tunnels may prove useful, since we have found it to be the best WL void finder working in the WL peak distribution, in terms of both large SNR value and small impact from GSN, followed closely by SVF peaks. The high SNR values from the WL minima and WVF tangential shear profiles make these WL void definitions viable candidates for parameter constraints as well. It is possible that void finders applied directly to the convergence field may be complementary to those that use WL peaks, since they are sensitive to different aspects of the WL convergence maps when identifying voids.

Additionally, some of the void finders have high SNR values for all smoothing scales studied here. This makes combining different smoothing scales a possible and potentially useful approach when applied to cosmological parameter constraints, since it has been shown that constraints from WL peaks are improved when multiple smoothing scales are used (Liu et al., 2015). Finally, in this Chapter we discuss the merit of a given WL void in terms of their tangential shear profiles, however other WL void statistics such as the void abundance and void correlation functions may also provide useful cosmological information.

When considering the impact of baryons on the WL void statistics, sufficiently large smoothing scales must be used in order to get agreement between hydro simulations and dark matter only simulations, as is the case with other WL statistics (Weiss et al., 2019). Paillas et al. (2017) have shown that voids in the LSS are less impacted by baryons, and Coulton et al. (2019b) have shown that WL minima are more robust to baryons than WL peaks. Therefore, given that Chang et al. (2018) have also shown that the deepest WL minima correspond to large supervoids, confirming that the underdense regions of the WL convergence maps are due to underdensities along the line of sight, it is reasonable to expect that the WL voids identified directly in the convergence maps may be more resilient to baryonic physics. However, the void finders which use WL peaks as tracers will be more affected since WL peaks are more sensitive to baryons (Osato et al., 2015; Weiss et al., 2019; Coulton et al., 2019b), and changes to the WL peak distribution could impact the resulting void catalogues. More detailed studies, potentially with the aid of cosmological hydrodynamic simulations, are needed to better understand these issues.

Chapter 4

Constraining cosmology with weak lensing voids

4.1 Introduction

Some of the most recent WL observations that supplement the parameter measurements from the CMB include the DES (Troxel et al., 2018) [1], HSC (Hikage et al., 2019) [2] and KiDS (Asgari et al., 2020) [3] WL surveys. However, all of these surveys measure lower values of σ_8 compared to Planck, with a statistically significant disagreement arising in the comparison between the Planck and KiDS constraints. More recent measurements from DES however, are consistent with the CMB (DES Collaboration et al., 2021). This is one example of the parameter tensions that have arisen in recent years, where different observations point to slightly different values of certain cosmological parameters, implying the presence of either unaccounted for systematics or new physics which are unaccounted for. Another example is the H_0 tension, where multiple observations find that measurements from the early Universe are broadly inconsistent with those of the late universe (Verde et al., 2019), particularly the distance scale measurement of H_0 based on Cepheids by the SH0ES collaboration (Riess et al., 2019).

In order to address these parameter tensions, it is important to measure cosmological parameters as precisely as possible, by maximising the information that can be extracted from a given survey. The standard approach for weak lensing surveys is to measure ΛCDM parameters with two-point statistics such as the shear-shear correlation function or the convergence power spectrum (Schneider et al., 2002; Semboloni et al., 2006; Hoekstra et al., 2006; Fu et al., 2008; Heymans et al., 2012; Kilbinger et al., 2013; Hildebrandt et al., 2017; Troxel et al., 2018; Hikage et al., 2019; Aihara et al., 2019; Asgari et al., 2020). However, two-point statistics do not capture non-Gaussian information, and weak lensing data are highly non-Gaussian due to the non-linear evolution of the Universe. To address this loss, many complementary statistics have been developed, which encapsulate information beyond two-point statistics. A common and popular example is the abundance of WL peaks, which has been shown to be complementary to the two-point function and helps break the Ω_m-σ_8 parameter degeneracy (Jain & Van Waerbeke, 2000; Pen et al., 2003; Dietrich & Hartlap, 2010). Peaks are also shown to outperform the standard methods for constraining the sum of neutrino mass (Li et al., 2019) and w_0 Martinet et al. (2020). By including complementary statistics, the measurement errors on cosmological parameters can be reduced, which will help inform the

---

[1] `https://www.darkenergysurvey.org/`

[2] `https://hsc.mtk.nao.ac.jp/ssp/`

[3] `http://kids.strw.leidenuniv.nl/`

statistical significance of any parameter tensions between multiple observations.

The goal of this Chapter is to present parameter constraint forecasts for one such complementary probe, WL voids. Voids are typically identified within the full 3D distribution of matter as regions of low matter density or low tracer density, for which void statistics such as their abundance, radial profiles and shapes contain useful non-Gaussian information (see, e.g., White, 1979; Fry, 1986; Lee & Park, 2009; Biswas et al., 2010; Bos et al., 2012; Lavaux & Wandelt, 2012; Jennings et al., 2013; Hamaus et al., 2014). Most studies use galaxy voids, which are identified as underdense regions in the galaxy distribution (e.g., Pan et al., 2012; Paz et al., 2013; Sutter et al., 2014; Cautun et al., 2016; Nadathur, 2016; Mao et al., 2017; Pollina et al., 2019; Hamaus et al., 2020; Aubert et al., 2020), where galaxy void statistics are complementary to the galaxy power spectrum and baryonic acoustic oscillations (e.g., Pisani et al., 2015; Hamaus et al., 2016; Nadathur et al., 2019). Recently, void WL profiles have also been shown to be a powerful cosmological probe (see, e.g., Melchior et al., 2014; Clampitt & Jain, 2015; Cai et al., 2015; Barreira et al., 2015; Gruen et al., 2016; Barreira et al., 2017; Falck et al., 2018; Baker et al., 2018; Fang et al., 2019).

While less explored compared with 3D voids, voids can also be identified in projection, such as in the projected galaxy distribution (e.g. Gruen et al., 2015; Barreira et al., 2017; Sánchez et al., 2017; Cautun et al., 2018) or in a weak lensing map (e.g. Davies et al., 2018; Coulton et al., 2019b). Here, we follow the latter approach and define WL voids generally as 2D regions within WL convergence maps that contain low convergence or few to no tracers. In a previous Chapter, we have shown that the lensing profiles of WL voids identified directly in WL convergence maps can be measured with a larger signal-to-noise ratio (SNR) than those of galaxy voids. This is because WL voids correspond to deeper underdensities projected along the line of sight than galaxy voids, and hence they have larger tangential shear profiles. The higher signal-to-noise ratio from WL voids also means that they are better at distinguishing between cosmological models in terms of the signal-to-noise ratio, such as modified gravity models, than galaxy voids as we will see in Chapter 5. Additionally, compared to other WL statistics, WL voids are less affected by baryonic physics (Coulton et al., 2019b).

In this Chapter we use the *cosmo*-SLICS simulation suite (Harnois-Déraps et al., 2019) to identify a particular class of WL voids, the *tunnels*, for a range of cosmological parameters. We use this data to train a Gaussian process regression emulator, which, combined with Markov chain Monte Carlo, allows us to generate likelihood contours and provide forecast parameter constraints for an LSST-like survey.

The tunnel algorithm we use here is one possible choice of WL void finder. In fact, similar to voids identified in the galaxy distribution (e.g. Colberg et al., 2008; Cautun et al., 2018; Baker et al., 2019), there are several void finding methods that have been successfully applied to WL maps. For example, in Chapter 3 we have carried out a detailed analysis on the impact that varying the WL void definition might have on the resulting WL void statistics. It showed that the 'tunnel' void finding algorithm offers a great trade off between maximising the observable tangential shear profile SNR and minimising the impact of observational noise on the void statistics. Therefore, we limit our analysis to only tunnels, and we defer a more detailed study comparing the parameter constraining powers of different void finders to a future work. For galaxy voids, studies have shown that combining different void definitions can lead to improved cosmological constraints (e.g. Paillas et al., 2019).

The layout of the Chapter is as follows. In Section 4.2 we describe our mock observational data, emulation and likelihood analysis pipeline and void finding algorithm. In Section 4.3 we present the WL void statistics used in our analysis and in Section 4.4 we present our parameter constraint forecasts. Finally we conclude in Section 4.5. For completeness, we also have three appendices where we study respectively the accuracy of our emulator, the impact of varying the smoothing scale of WL maps, and present the covariance matrix used in our analysis.

4.2 Methodology

In this section we describe the methodology followed in this Chapter, including the simulations, mock lensing data, emulation, likelihood analysis and the weak lensing void (tunnels) finding algorithm.

The goal of this Chapter is to present the maximum constraining power that can be achieved with WL voids, in order to motivate further development such as theoretical models and dealing with observational systematics, all of which will be studied in a future work. We note that (Harnois-Déraps et al., 2020) present a methodology for using the emulated WL peak abundance to constrain cosmological parameters from the DES year 1 data whilst accounting for observational systematics, and that this approach can be generalised to any non-Gaussian statistic, which would be appropriate for future WL void studies.

4.2.1 Mock Data

In this Chapter we use mock WL convergence maps generated from the *cosmo*-SLICS and SLICS simulation suites (Harnois-Déraps & van Waerbeke, 2015; Harnois-Déraps et al., 2018, 2019), which we briefly outline in this subsection.

The *cosmo*-SLICS suite is a set of N-body dark-matter-only simulations run for 26 cosmology nodes in the $[\Omega_m, S_8, h, w_0]$ parameter space. Here Ω_m is the matter density parameter today, $S_8 = \sigma_8(\Omega_m/0.3)^{0.5}$, $h = H_0/100\text{kms}^{-1}\ \text{Mpc}^{-1}$ is the reduced Hubble constant, and w_0 is the dark energy equation of state parameter, which is assumed to be a constant. The σ_8 parameter is the present-day root-mean-squared matter density perturbation smoothed on $8h^{-1}$ Mpc scales.

The four dimensional parameter space is sampled using a Latin hypercube, which is a sampling algorithm designed to give a high interpolation accuracy for a low node count. The exact cosmological parameter space that is modelled by each simulation node is shown in Fig. 4.1. At each node, a carefully-designed pair of simulations are run, for which sampling variance is highly suppressed. This is achieved by selecting a pair of initial conditions out of a large number of random realisations, such that the mean matter power spectrum closely matches the ensemble average. The random phases of this pair of initial conditions are used for all cosmology nodes. The simulation volume is a cube with length $L = 505\ h^{-1}\text{Mpc}$, with $N = 1536^3$ dark matter particles.

For each node, 50 pseudo-independent light-cones are constructed by resampling projected mass sheets, which are then ray-traced under Born approximation to construct lensing maps and catalogues (see Harnois-Déraps et al., 2019, for full details about the light-cone and catalogue construction).

We use the *cosmo*-SLICS source catalogue down-sampled to match LSST specifications with a source redshift distribution of $z_s = [0.6, 1.4]$, which gives a conservative source galaxy number density of 20 arcmin^{-2}. From this we generate 50 WL convergence maps for each of the 26 cosmology nodes, with a sky coverage of 10×10 deg^2 each and pixel grid of dimensions 3600^2 (Giblin et al., 2018). These maps are smoothed with a Gaussian filter with smoothing scale $\theta_s = 1$ arcmin.

For estimates of the covariance matrices, we use the SLICS suite to produce 615 WL convergence maps at the fiducial cosmology, which match the properties of the *cosmo*-SLICS maps. However, unlike the *cosmo*-SLICS maps, the SLICS maps are fully independent which allows

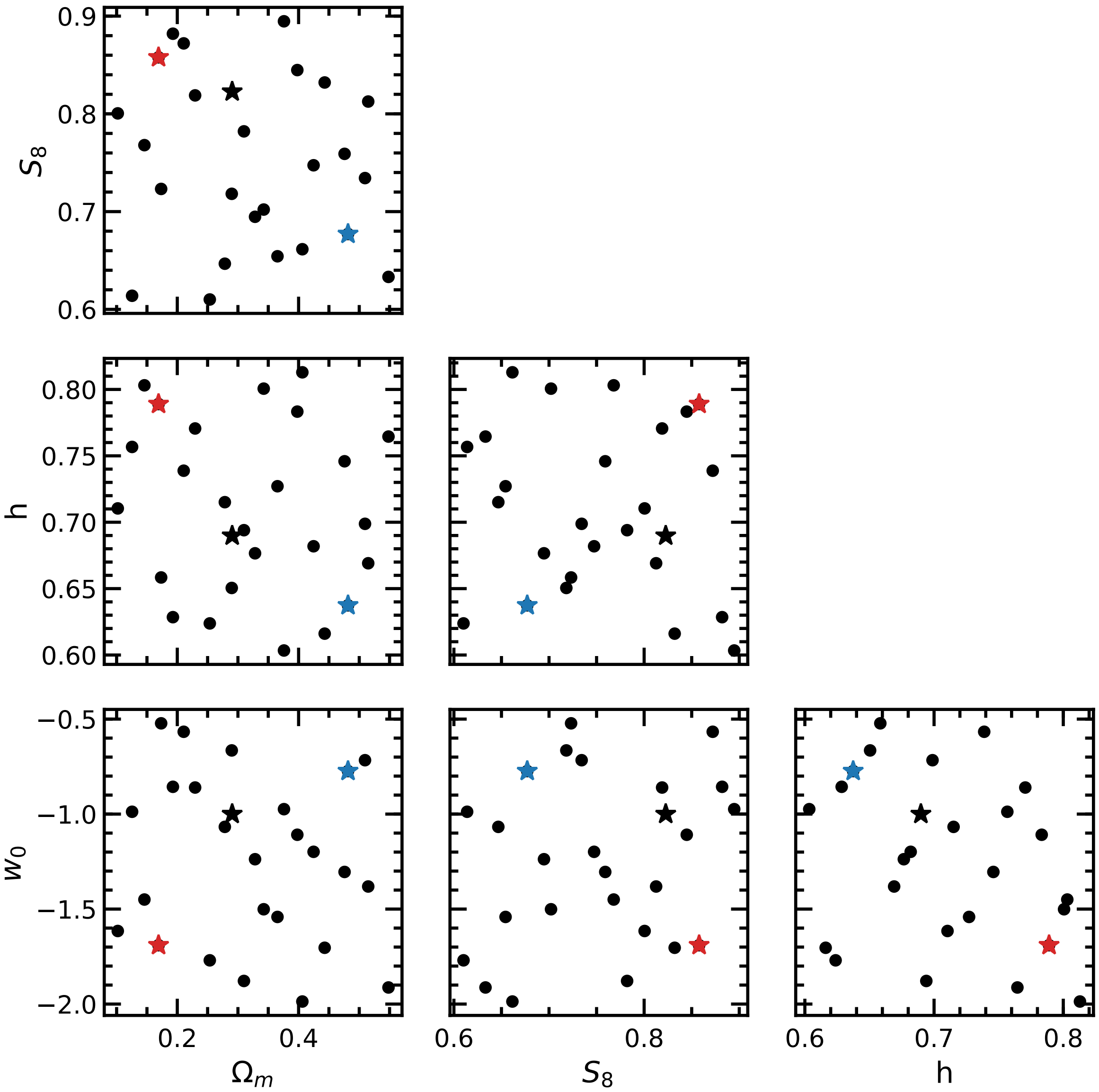

Figure 4.1: The four dimensional parameter space ($[\Omega_m, S_8, h, w_0]$) sampled by the *cosmo*-SLICS simulation suite. The fiducial cosmology is indicated by a star with parameter values [0.29, 0.82, 0.69, −1.00]. We have highlighted two additional nodes with blue ([0.48, 0.68, 0.64, −0.77]) and red ([0.17, 0.86, 0.79, −1.69]) stars, which are selected as nodes in separate regions of the parameter space, used to exemplify the behavior of WL voids as a function of cosmological parameters.

us to completely capture the sample variance of the probes studied in this Chapter. Additionally, the larger number of SLICS realisations relative to *cosmo*-SLICS allows for larger data vectors in the likelihood analysis when measuring and combining probes.

4.2.2 Emulation and likelihood analysis

In this subsection, we outline the procedure used to test the sensitivity of WL void statistics to the cosmological parameters Ω_m, S_8, h and w_0.

The first step is to measure the WL void statistics from the 50 convergence maps for each of the 26 cosmo-SLICS cosmologies shown in Fig. 4.1. Then, in order to make predictions of the WL void statistics at arbitrary points in the 4D parameter space shown in Fig. 4.1, we use a Gaussian process (GP) regression emulator from scikit-learn (Pedregosa et al., 2011) to interpolate the void statistics between nodes. GP regression is a non-parametric Bayesian machine learning algorithm used to make probabilistic predictions that are consistent with the training data (see, e.g., Habib et al., 2007; Schneider et al., 2008, for some of its early applications in cosmology). The emulator requires the training data to sample the parameter space sufficiently, and generally the accuracy of the emulator is limited by the availability of training data. The accuracy of the GP emulator trained on *cosmo*-SLICS was tested extensively and found to yield few per cent accuracy in its predictions of weak lensing two-point correlation functions (Harnois-Déraps et al., 2019), density split statistics (Burger et al., 2020) persistent homology statistics Heydenreich et al. (2020) and aperture mass statistics (Martinet et al., 2020). In this Chapter the average void statistics and their standard errors at each node are used as the training data for the emulator. We present results showing the accuracy of the emulator in Appendix .3.

Finally, once the emulator has been trained we use Monte Carlo Markov Chain (MCMC) to estimate the posteriors of the parameters for the entire parameter space and produce likelihood contours. We use the emcee python package (Foreman-Mackey et al., 2013) to conduct the MCMC analysis in this Chapter sampling the 4D parameter space as follows.

We employ a Bayesian formalism, in which the likelihood, $P(\boldsymbol{p}|\boldsymbol{d})$, of the set of cosmological parameters $\boldsymbol{p} = [\Omega_m, S_8, h, w_0]$ given a data set $\boldsymbol{d}$, is given, according to Bayes' theorem, by

$$P(\boldsymbol{p}|\boldsymbol{d}) = \frac{P(\boldsymbol{p})P(\boldsymbol{d}|\boldsymbol{p})}{P(\boldsymbol{d})}, \tag{4.2.1}$$

where $P(\boldsymbol{p})$ is the prior, $P(\boldsymbol{d}|\boldsymbol{p})$ is the likelihood of the data conditional on the parameters, and $P(\boldsymbol{d})$ is the normalisation. In our analysis we use flat priors with upper and lower limits respectively for $\Omega_{\rm m}$: [0.10, 0.55], S_8: [0.61, 0.89], h: [0.60, 0.81], w_0: [-1.99, -0.52]. These priors match the parameter space sampled by the nodes in Fig. 4.1.

The log likelihood can be expressed as

$$\log(P(\boldsymbol{d}|\boldsymbol{p})) = -\frac{1}{2}\left[\boldsymbol{d} - \mu(\boldsymbol{p})\right] C^{-1} \left[\boldsymbol{d} - \mu(\boldsymbol{p})\right] \ , \tag{4.2.2}$$

where $\mu(\boldsymbol{p})$ is the prediction generated by the emulator for a set of parameters $\boldsymbol{p}$, and C^{-1} is the inverse covariance matrix. In practice we use the emulator's prediction of a statistic at the fiducial cosmology as the data $\boldsymbol{d}$. This choice is for presentation purposes since it ensures that the confidence intervals are always centred on the true values of the cosmological parameters and thus allows for easier comparisons between multiple probes.

The likelihood returns a 4D probability distribution that indicates how well different regions of the parameter space describe the input data $\boldsymbol{d}$. Note that in Eq. (4.2.2) we have assumed that the covariance matrix does not vary with a change in the cosmological parameters.

We calculate the covariance matrices from the 615 WL map realisations from the SLICS suite which match the fiducial cosmology, and divide it by a factor of 180 in order to rescale the covariance matrix from a 100 deg^2 area to the LSST survey area, which we take as $18,000$ deg^2. The joint covariance matrix for all probes studied in this Chapter is presented appendix .5. We also multiply the inverse covariance matrix by a factor α, which accounts for the bias that is present when inverting a noisy covariance matrix (Anderson, 2003; Hartlap et al., 2007), given by:

$$\alpha = \frac{N - N_{\rm bin} - 2}{N - 1} \ , \tag{4.2.3}$$

where $N = 615$ is the number of weak lensing maps that have been used to calculate the covariance matrix and $N_{\rm bin}$ is the number of bins for which the statistic is computed. We note however that Sellentin & Heavens (2016) present an alternative approach to robustly account for the uncertainty in the estimated covariance, via a student-t likelihood distribution.

4.2.3 The tunnel algorithm

To identify WL voids, we use the tunnel algorithm initially proposed in Cautun et al. (2018), which identifies the largest circles in a 2D tracer catalogue that are empty of tracers. We choose to use this void finding algorithm since, compared with several other common 2D void finders, it gives void lensing profiles with high SNR, whilst also being least affected by the observational noises associated with weak lensing measurements, such as galaxy shape noise

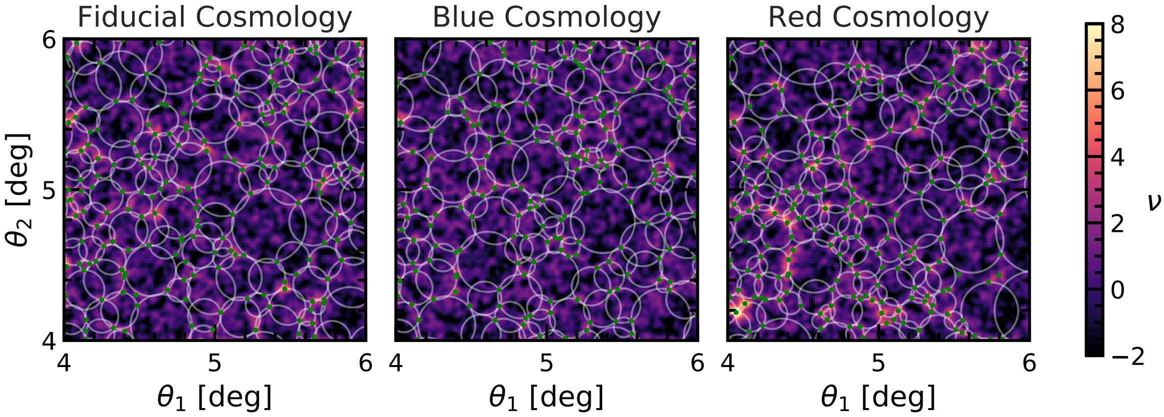

Figure 4.2: (Colour Online) A visualisation of WL peaks (green points) used to identify the tunnels (white circles) in the WL convergence maps (colour map) for the $\nu > 2$ catalogues. The left panel shows tunnels for the fiducial cosmology, while the middle and right panels show tunnels for the blue and red cosmologies highlighted in Fig. 4.1 respectively. The colour bar on the right indicates the convergence field in units of $\nu = \kappa/\sigma_{\mathrm{GSN}}$.

(Chapter 3). The tunnel algorithm requires an input tracer catalogue to identify voids. For the identification of WL voids, we use WL peaks as tracers of the underlying convergence field (this avoids the necessity to have a synthetic 2D galaxy map for this analysis). Here we define WL peaks as local maxima in the WL convergence map as in Eq. (1.2.14).

To identify tunnels, we first construct a Delaunay triangulation of the tracers (WL peaks). This produces a unique tessellation of the map with triangles, where each vertex is a tracer and the tessellated triangles enclose no tracers. From each triangle, a corresponding circumcircle can be defined, which is a circle that is directly on top of its Delaunay triangle with all vertices of the latter residing on the circumcircle's circumference. This tessellation is unique, and by definition gives circles that do not enclose any tracers. To avoid identifying the same regions as voids multiple times, we discard any circumcircles whose centers reside inside a larger circumcircle. The resulting list represents our tunnel catalogue, where each tunnel is characterized in terms of the centre and radius of its corresponding circumcircle.

The WL peak catalogues that may be used to identify tunnels contain peaks with a range of amplitudes (or heights) ν. WL peaks of different amplitudes trace different components of the WL map, where the peaks with low or negative amplitudes trace underdense regions of the map, and those with high amplitudes trace overdense regions. Furthermore, peaks with low amplitudes are more susceptible to either being created or contaminated by GSN. It is therefore convenient to generate multiple sub-catalogues of a given WL peak catalogue, by retaining only the peaks with amplitudes larger than a given ν value. Varying the ν thresholds allows us to study how the tunnels respond to tracer catalogues with different

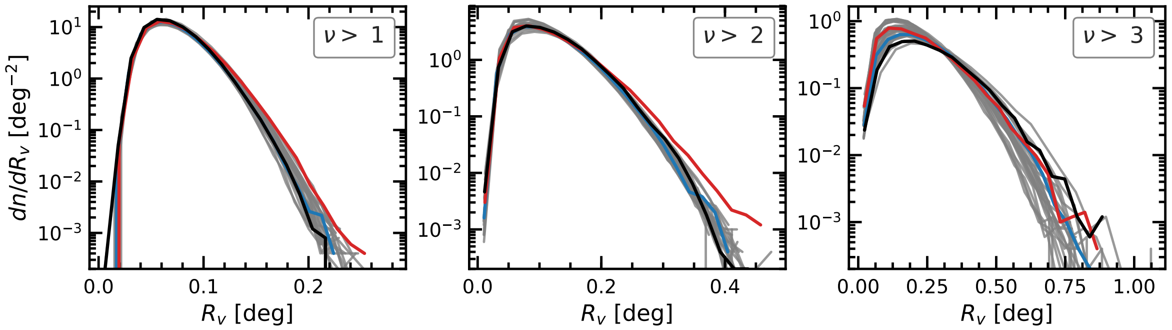

Figure 4.3: (Colour Online) The differential void abundance as a function of void radius R_V. The three panels correspond to voids identified in different WL peak catalogues, with peak heights $\nu > 1, 2$ and 3 (from left to right). The void abundances for all cosmologies in Fig. 4.1 are plotted in grey. Results for the fiducial (black), red (red) and blue (blue) cosmologies are over-plotted in colour.

properties. In this Chapter we use WL peak catalogues with amplitudes of $\nu > 1, 2$ and 3 to identify tunnels, and will also use these ν values to denote the corresponding tunnel catalogues.

In Fig. 4.2 we show a visualisation of tunnels identified from catalogues of WL peaks with amplitudes $\nu > 2$. The figure shows WL maps, WL peaks and tunnels for the fiducial cosmology (left), and two sample cosmologies, blue (middle) and red (right) to exemplify the impact of changing cosmological parameters. Here it can be seen in the bottom left part of the panels that the red cosmology, which has the highest S_8 value of the three highlighted cosmologies, contains more overdense (orange) regions than the other two cosmologies. The changes in overdensity in the red-cosmology leads to more small tunnels in the bottom left of the panel, and more large tunnels at the top of the panel relative to the other two cosmologies. This highlights how changing the cosmological parameters changes the structure observed in WL maps and the corresponding WL void properties.

4.3 Weak lensing void statistics

In this section we present the weak lensing void statistics used in this analysis, showing their abundance in Section 4.3.1, and the tangential shear profiles in Section 4.3.2.

4.3.1 Void abundance

Fig. 4.3 shows the differential void abundance per unit area as a function of void radius. The three panels correspond to voids identified in three WL peak catalogues, with peak

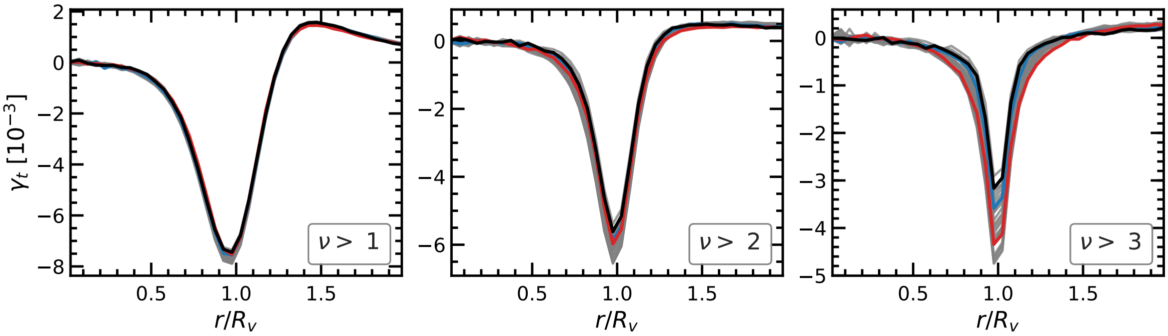

Figure 4.4: (Colour Online) The tangential shear profiles as a function of re-scaled distance to void centre, r/R_V. The three panels correspond to voids identified in three WL peak catalogues with peak heights $\nu > 1, 2$ and 3 (from left to right). The tangential shear profiles for all cosmologies in Fig. 4.1 are plotted in grey. Results for the fiducial cosmology (black), red (red) and blue (blue) cosmologies are over-plotted in colour.

heights $\nu > 1, 2$ and 3. Void abundances for each of the nodes in Fig. 4.1 are plotted in grey, the fiducial cosmology in black and two sample cosmologies in colour (blue and red – corresponding to the two cosmologies in the middle and right panels of Fig. 4.2).

The figure shows that as the ν threshold increases, the total number of WL voids decreases (given by the area under the curves), and the average size of the voids increases. The spread in the void abundances over all cosmologies is largest for the $\nu > 3$ catalogue. However, the data is also noisier in this catalogue, because there are fewer peaks with $\nu > 3$ and subsequently fewer tunnels.

The red cosmology produces more large voids for the $\nu > 1$ and 2 catalogues than the fiducial and blue cosmologies. However, the same behaviour is not seen for the $\nu > 3$ catalogue, which may indicate that the sensitivity of the void abundance to specific cosmological parameters changes as fewer tracers are used to identify WL voids. The red cosmology has the largest S_8 and smallest Ω_m compared to the fiducial and blue cosmologies. Increasing S_8 or Ω_m increases the clustering of matter which leads to a wider range of WL void sizes, as we have seen in Fig. 4.2: this is because the enhanced clustering creates more peaks with $\nu > 1$ or 2 in dense regions, reducing the void sizes there, and at the same time reduces the amplitudes of some low peaks in underdense regions, increasing void sizes there. On the other hand, for the $\nu > 3$ catalogue, the peaks are sparser in all three cosmologies (hence voids are larger), and the fact that the red cosmology has more peaks at $\nu > 3$ again restricts the sizes of its voids, this time affecting the largest ones.

For $\nu > 1$ the fiducial cosmology produces the fewest large voids compared to the red and blue cosmologies, however for $\nu > 3$ it produces the most large voids. The change in rela-

Table 4.1: Forecast of percentage uncertainties obtained from various WL void statistics for an LSST-like survey. The first block of 4 rows show 68% CL while the bottom 4 rows show 95% CL. In each block, the results shown in the first three lines are quoted from the tightest contours in each figure in Section 4.4 (see first column for more details). In the last line of each block, 'γ-2PCF' stands for the parameter constraints using the cosmic shear two-point correlation functions for the same maps as used for the cosmic void statistics.

Statistic	Ω_m	S_8	h	w_0
68% confidence limits				
dn/dR_v (combined)	1.7%	0.4%	2.1%	3.0%
γ_t (combined)	2.3%	0.5%	2.3%	4.4%
dn/dR_v and γ_t (combined)	1.5%	0.3%	1.5%	2.7%
γ-2PCF	1.5%	0.5%	1.0%	3.9%
95% confidence limits				
dn/dR_v (combined)	3.4%	0.8%	4.0%	5.9%
γ_t (combined)	4.6%	0.9%	4.5%	8.6%
dn/dR_v and γ_t (combined)	2.9%	0.7%	2.9%	5.3%
γ-2PCF	3.1%	1.1%	2.1%	8.0%

tive behaviour between the fiducial, red and blue cosmologies as the ν threshold increases, indicates that void abundances measured from different WL peak catalogues contain complementary information to each other. We will see this point more clearly later when looking at the constraints from void abundances.

For the $\nu > 1$ catalogue, it is difficult to distinguish between the blue and fiducial cosmology, despite the two cosmologies occupying distinctly separate regions of the parameter space. This is because the cosmological parameters are degenerate, where different combinations of parameters can produce the same void abundances. The degeneracy between parameters also changes between different catalogues.

4.3.2 Lensing tangential shear profiles

Fig. 4.4 shows the tangential shear profiles for WL voids, where the panels (from left to right) show WL voids identified in the $\nu > 1, 2$ and 3 catalogues. Tangential shear profiles for all cosmologies are plotted in grey, with the fiducial and two highlighted cosmologies plotted in colour as in Fig. 4.3. The tangential shear profiles are calculated by first measuring the convergence profiles in annuli centered on the void center (pixels are interpolated for small annuli), where the number of annuli used is the lensing profile bin number. The annuli are then stacked as a function of relative angular size (r/R_V), weighted by their corresponding void area. Using Eq. 1.2.12, this is then converted to the tangential shear profiles.

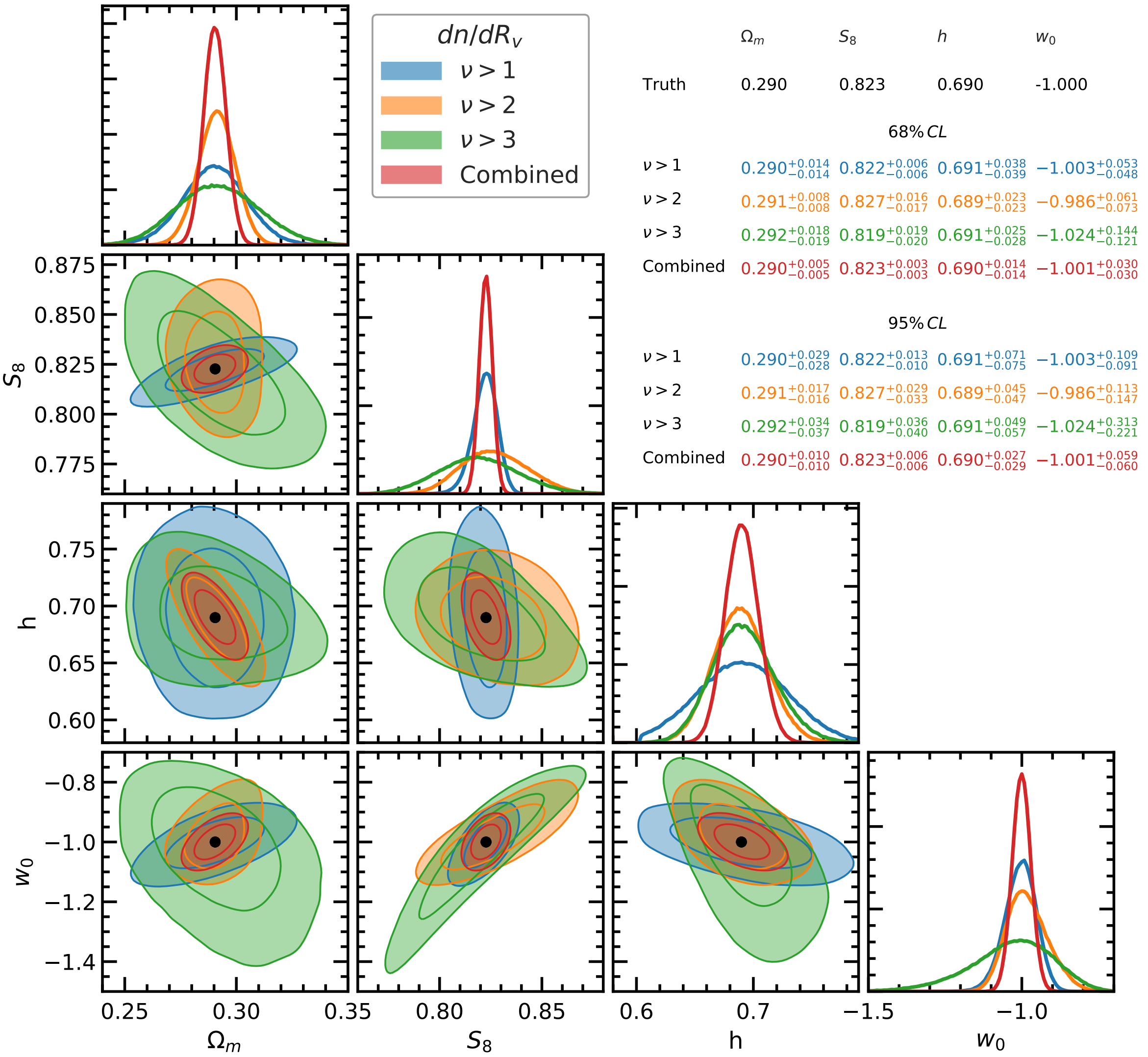

	Ω_m	S_8	h	w_0
Truth	0.290	0.823	0.690	-1.000
		68% CL		
$\nu > 1$	$0.290^{+0.014}_{-0.014}$	$0.822^{+0.006}_{-0.006}$	$0.691^{+0.038}_{-0.039}$	$-1.003^{+0.053}_{-0.048}$
$\nu > 2$	$0.291^{+0.008}_{-0.008}$	$0.827^{+0.016}_{-0.017}$	$0.689^{+0.023}_{-0.023}$	$-0.986^{+0.061}_{-0.073}$
$\nu > 3$	$0.292^{+0.018}_{-0.019}$	$0.819^{+0.019}_{-0.020}$	$0.691^{+0.025}_{-0.028}$	$-1.024^{+0.144}_{-0.121}$
Combined	$0.290^{+0.005}_{-0.005}$	$0.823^{+0.003}_{-0.003}$	$0.690^{+0.014}_{-0.014}$	$-1.001^{+0.030}_{-0.030}$
		95% CL		
$\nu > 1$	$0.290^{+0.029}_{-0.028}$	$0.822^{+0.013}_{-0.010}$	$0.691^{+0.071}_{-0.075}$	$-1.003^{+0.109}_{-0.091}$
$\nu > 2$	$0.291^{+0.017}_{-0.016}$	$0.827^{+0.029}_{-0.033}$	$0.689^{+0.045}_{-0.047}$	$-0.986^{+0.113}_{-0.147}$
$\nu > 3$	$0.292^{+0.034}_{-0.037}$	$0.819^{+0.036}_{-0.040}$	$0.691^{+0.049}_{-0.057}$	$-1.024^{+0.313}_{-0.221}$
Combined	$0.290^{+0.010}_{-0.010}$	$0.823^{+0.006}_{-0.006}$	$0.690^{+0.027}_{-0.029}$	$-1.001^{+0.059}_{-0.060}$

Figure 4.5: (Colour Online) Constraint forecasts on cosmological parameters measured from void abundances. Contours are shown for WL voids identified in WL peak catalogues with $\nu > 1$ (blue), $\nu > 2$ (orange), $\nu > 3$ (green) and the combination of all three catalogues (red). The true cosmological parameter values used to generate the data are indicated by the black point. The diagonal panels show the 1D marginalised probability distribution, and remaining panels show the marginalised 2D probability contours enclosing the 68% and 95% confidence intervals. The table in the top right shows true parameter values (top) and the inferred parameter values for the different peak catalogues with 68% (upper section) and 95% (lower section) confidence limits.

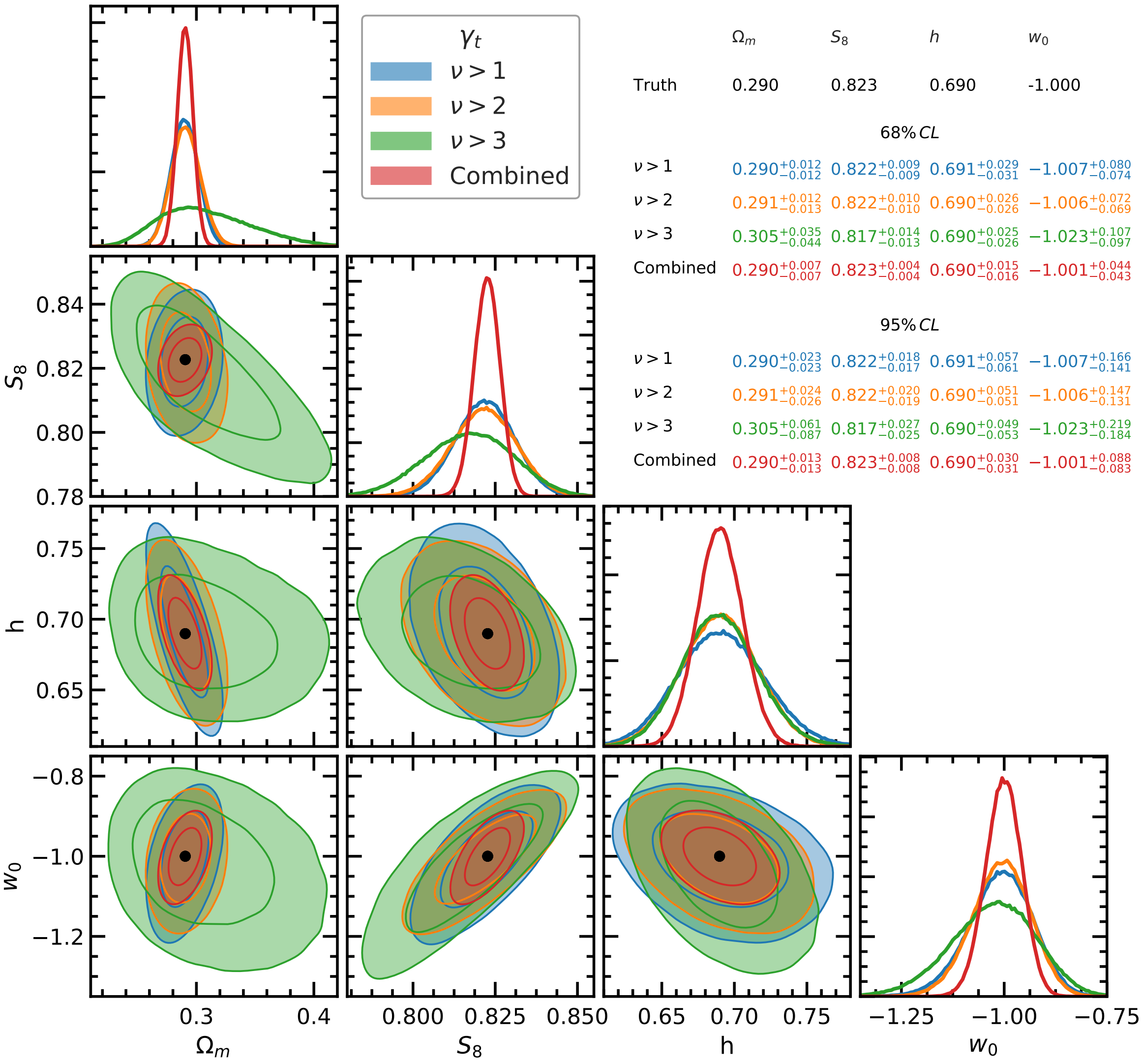

	Ω_m	S_8	h	w_0
Truth	0.290	0.823	0.690	-1.000
		68% CL		
$\nu > 1$	$0.290^{+0.012}_{-0.012}$	$0.822^{+0.009}_{-0.009}$	$0.691^{+0.029}_{-0.031}$	$-1.007^{+0.080}_{-0.074}$
$\nu > 2$	$0.291^{+0.012}_{-0.013}$	$0.822^{+0.010}_{-0.010}$	$0.690^{+0.026}_{-0.026}$	$-1.006^{+0.072}_{-0.069}$
$\nu > 3$	$0.305^{+0.035}_{-0.044}$	$0.817^{+0.014}_{-0.013}$	$0.690^{+0.025}_{-0.026}$	$-1.023^{+0.107}_{-0.097}$
Combined	$0.290^{+0.007}_{-0.007}$	$0.823^{+0.004}_{-0.004}$	$0.690^{+0.015}_{-0.016}$	$-1.001^{+0.044}_{-0.043}$
		95% CL		
$\nu > 1$	$0.290^{+0.023}_{-0.023}$	$0.822^{+0.018}_{-0.017}$	$0.691^{+0.057}_{-0.061}$	$-1.007^{+0.166}_{-0.141}$
$\nu > 2$	$0.291^{+0.024}_{-0.026}$	$0.822^{+0.020}_{-0.019}$	$0.690^{+0.051}_{-0.051}$	$-1.006^{+0.147}_{-0.131}$
$\nu > 3$	$0.305^{+0.061}_{-0.087}$	$0.817^{+0.027}_{-0.025}$	$0.690^{+0.049}_{-0.053}$	$-1.023^{+0.219}_{-0.184}$
Combined	$0.290^{+0.013}_{-0.013}$	$0.823^{+0.008}_{-0.008}$	$0.690^{+0.030}_{-0.031}$	$-1.001^{+0.088}_{-0.083}$

Figure 4.6: (Colour Online) The same as Fig. 4.5 but for the tangential shear profiles. See the caption in Fig.4.5 for more details

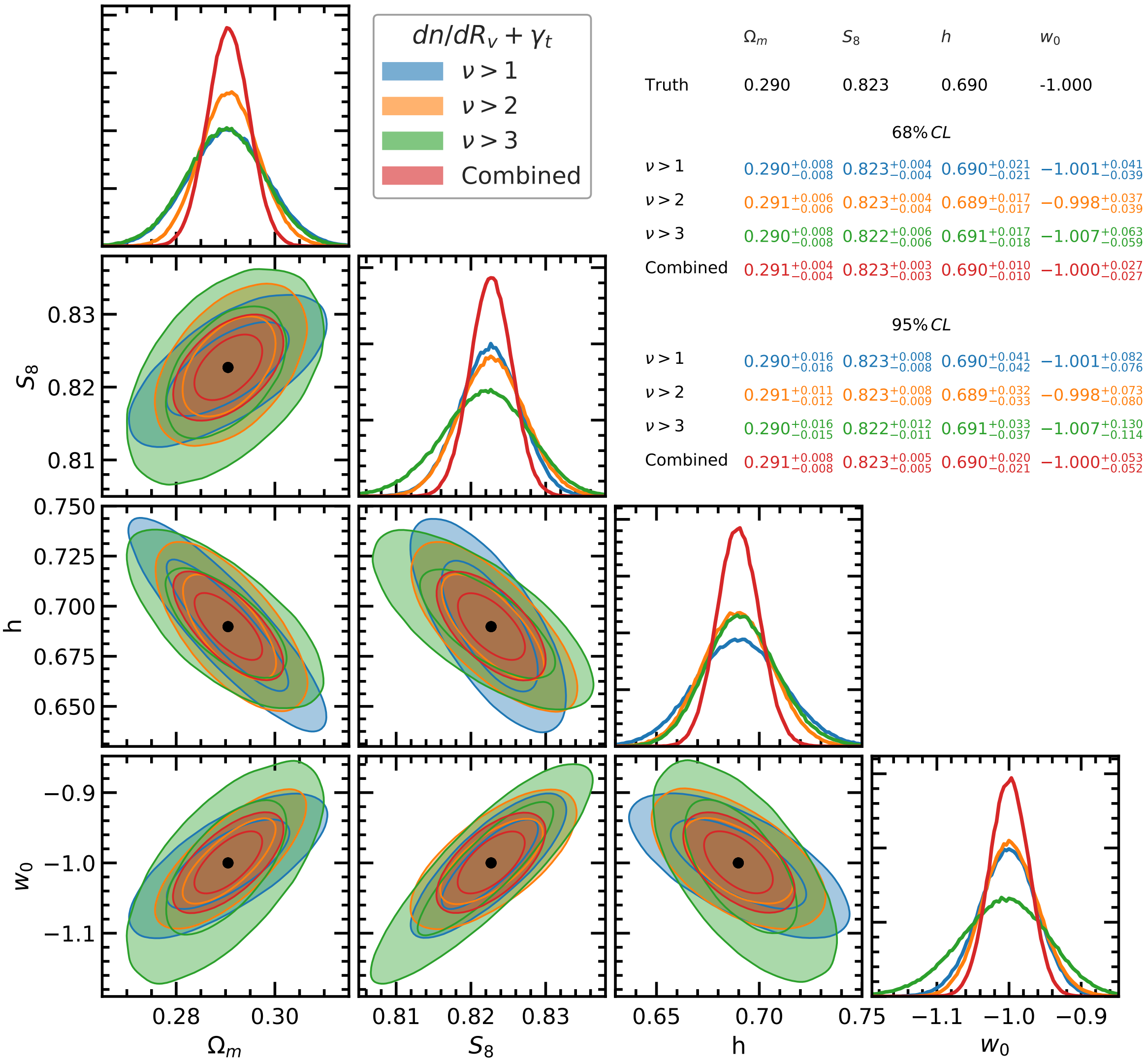

	Ω_m	S_8	h	w_0
Truth	0.290	0.823	0.690	-1.000
		68% CL		
$\nu > 1$	$0.290^{+0.008}_{-0.008}$	$0.823^{+0.004}_{-0.004}$	$0.690^{+0.021}_{-0.021}$	$-1.001^{+0.041}_{-0.039}$
$\nu > 2$	$0.291^{+0.006}_{-0.006}$	$0.823^{+0.004}_{-0.004}$	$0.689^{+0.017}_{-0.017}$	$-0.998^{+0.037}_{-0.039}$
$\nu > 3$	$0.290^{+0.008}_{-0.008}$	$0.822^{+0.006}_{-0.006}$	$0.691^{+0.017}_{-0.018}$	$-1.007^{+0.063}_{-0.059}$
Combined	$0.291^{+0.004}_{-0.004}$	$0.823^{+0.003}_{-0.003}$	$0.690^{+0.010}_{-0.010}$	$-1.000^{+0.027}_{-0.027}$
		95% CL		
$\nu > 1$	$0.290^{+0.016}_{-0.016}$	$0.823^{+0.008}_{-0.008}$	$0.690^{+0.041}_{-0.042}$	$-1.001^{+0.082}_{-0.076}$
$\nu > 2$	$0.291^{+0.011}_{-0.012}$	$0.823^{+0.008}_{-0.009}$	$0.689^{+0.032}_{-0.033}$	$-0.998^{+0.073}_{-0.080}$
$\nu > 3$	$0.290^{+0.016}_{-0.015}$	$0.822^{+0.012}_{-0.011}$	$0.691^{+0.033}_{-0.037}$	$-1.007^{+0.130}_{-0.114}$
Combined	$0.291^{+0.008}_{-0.008}$	$0.823^{+0.005}_{-0.005}$	$0.690^{+0.020}_{-0.021}$	$-1.000^{+0.053}_{-0.052}$

Figure 4.7: (Colour Online) The same as Fig. 4.5 but for the combination of the tangential shear profiles and the void abundance. Results are shown for the three WL Peak catalogues with $\nu > 1$ (blue), $\nu > 2$ (orange), $\nu > 3$ (green). See the caption in Fig. 4.5 for more details.

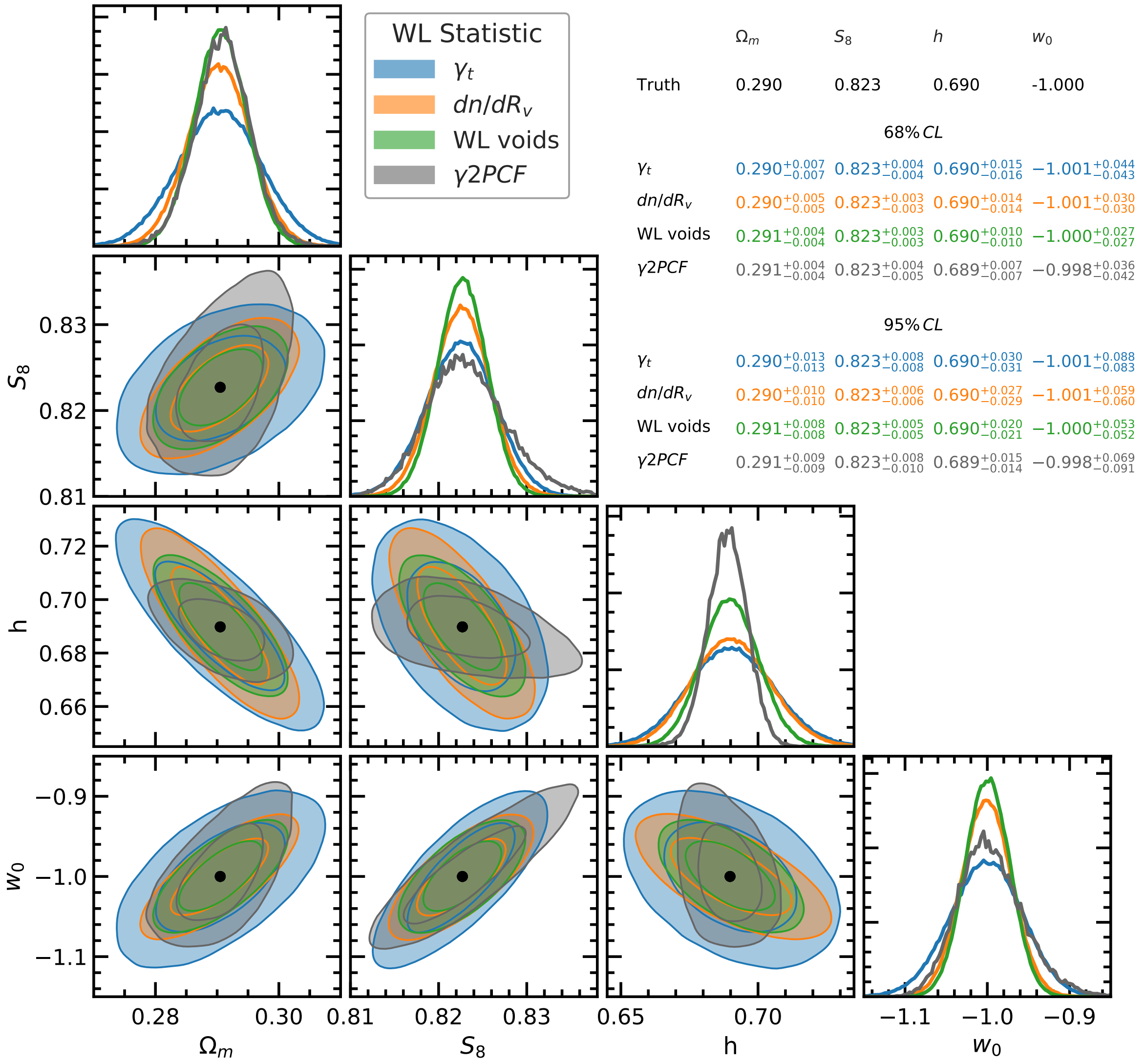

	Ω_m	S_8	h	w_0
Truth	0.290	0.823	0.690	-1.000
		68% *CL*		
γ_t	$0.290^{+0.007}_{-0.007}$	$0.823^{+0.004}_{-0.004}$	$0.690^{+0.015}_{-0.016}$	$-1.001^{+0.044}_{-0.043}$
dn/dR_v	$0.290^{+0.005}_{-0.005}$	$0.823^{+0.003}_{-0.003}$	$0.690^{+0.014}_{-0.014}$	$-1.001^{+0.030}_{-0.030}$
WL voids	$0.291^{+0.004}_{-0.004}$	$0.823^{+0.003}_{-0.003}$	$0.690^{+0.010}_{-0.010}$	$-1.000^{+0.027}_{-0.027}$
$\gamma 2PCF$	$0.291^{+0.004}_{-0.004}$	$0.823^{+0.004}_{-0.005}$	$0.689^{+0.007}_{-0.007}$	$-0.998^{+0.036}_{-0.042}$
		95% *CL*		
γ_t	$0.290^{+0.013}_{-0.013}$	$0.823^{+0.008}_{-0.008}$	$0.690^{+0.030}_{-0.031}$	$-1.001^{+0.088}_{-0.083}$
dn/dR_v	$0.290^{+0.010}_{-0.010}$	$0.823^{+0.006}_{-0.006}$	$0.690^{+0.027}_{-0.029}$	$-1.001^{+0.059}_{-0.060}$
WL voids	$0.291^{+0.008}_{-0.008}$	$0.823^{+0.005}_{-0.005}$	$0.690^{+0.020}_{-0.021}$	$-1.000^{+0.053}_{-0.052}$
$\gamma 2PCF$	$0.291^{+0.009}_{-0.009}$	$0.823^{+0.008}_{-0.010}$	$0.689^{+0.015}_{-0.014}$	$-0.998^{+0.069}_{-0.091}$

Figure 4.8: (Colour Online) The same as Fig. 4.5 but for the tangential shear profiles (blue) and void abundance (orange). Results are shown for the combination of all three WL peak catalogues. See the caption in Fig. 4.5 for more details. Note that, for comparison, we have added the contours from the shear-shear two-point correlation function (without tomography) extracted from the same maps in grey colour, and the corresponding constraints on the parameters are also listed in the table in grey.

The tangential shear profiles plotted here are negative, which indicates that the WL voids behave like concave lenses and their interiors correspond to underdense regions. The figure shows that as the ν threshold increases, the depth of the tangential shear profiles at $r/R_V = 1$ decreases, but meanwhile the spread in the amplitude of the tangential shear profiles, as well as the spread in the width of the peak around $r/R_V = 1$, amongst all cosmologies, increases. Note that the peaks of the tangential shear profiles appear to be narrower as the ν threshold increases, but this is an artificial consequence of the fact that these plots are made against r/R_V with the void radius R_V larger for larger ν thresholds.

For the $\nu > 1$ catalogue, the fiducial, red and blue cosmologies all lie on top of each other. For $\nu > 2$, the red cosmology (with the largest S_8 value) has a deeper tangential shear profile compared to the other two cosmologies. For $\nu > 3$ the difference in amplitude increases further between the three reference cosmologies, with the fiducial cosmology having the lowest (absolute) amplitude, however the general trend between the three reference cosmologies is the same for all ν thresholds. Part of this can again be attributed to the high S_8 value in the red cosmology, which enhances the clustering of matter, resulting in low-density regions becoming more underdense. However, the three highlighted cosmologies have very distinct values for the other three parameters, in particular Ω_m, which means that an intuitive and yet complete explanation of their relative behaviours is difficult to gauge by eye.

The observation that, although the spread in shapes amongst all cosmologies increases with the ν threshold, the general order in which they appear does not change, indicates that there may not be much complementary information between tangential shear profiles measured from different ν thresholds. Also, while the differences between the different cosmologies are larger for the $\nu > 3$ catalogue, the fact that there are relatively fewer voids in this catalogue means that its constraining power is not necessarily stronger than the other two catalogues, as we will see shortly.

4.4 Parameter constraints forecast

In this section we present parameter constraint forecasts for an LSST-like survey from the void abundances and tangential shear profiles of WL voids, as well as their combinations.

4.4.1 Void abundance constrains

Fig. 4.5 shows the likelihood contours for measuring the four cosmological parameters with the WL void abundance. The diagonal panels of the figure show the 1D marginalised likelihood distribution and remaining panels show the 2D marginalised likelihood contours. For each inference case, the inner and outer contours indicate respectively the 68% and 95% confidence limits (CL). As mentioned above, we use the fiducial cosmology as our 'observed' data set, which is indicated by the black point. The figure shows results for three ν thresholds with $\nu > 1$ (blue), $\nu > 2$ (orange) and $\nu > 3$ (green). We also show results for the combination of all three catalogues (red). The table in the top right of the figure indicates the estimated cosmological parameters with their corresponding 68% (top) and 95% (bottom) CL, for each of the contours. The tightest contours are for the $\Omega_m - S_8$ plane, which is expected since these are the cosmological parameters to which WL analysis is the most sensitive.

For nearly every combination of parameters, the three contours for the $\nu > 1$, 2 and 3 void catalogues occupy different parts of the marginalised 2D parameter space, or have different degeneracy directions, where most of the overlapping occurs around the true values. As suggested by the behaviour of the three reference cosmologies discussed in Section 4.3.1, this indicates that void abundances measured from different catalogues contain complementary information to each other. We therefore also show parameter likelihood contours for the combination of the WL void abundances from the three catalogues in red.

We note that for the panels that include h, the $\nu > 1$ contours are slightly cut off by the lower prior boundary on h. The CLs on h for the $\nu > 1$ catalogue are therefore likely to be slight underestimates compared to the case where a larger prior range on h is used. We do not expand the priors to account for this since the emulator accuracy quickly diminishes outside of the parameter space for which we have training data (which matches our prior range). This does not impact the resulting contours and CLs when all catalogues are combined, since the 'Combined' contours are much smaller and do not approach the prior boundaries.

The 'Combined' contours are smaller than any of the individual contours, for all combinations of parameters. This shows that parameter measurements from the WL void abundances are significantly improved when multiple catalogues are used. The 68% and 95% CL percentage accuracy that the combined WL void abundance is able to measure the parameters which is shown in Table 4.1.

The WL void abundances for all catalogues are initially measured with 30 bins, which spans the entire range of the WL void sizes measured across all cosmologies. However, since some cosmologies produce more large voids than others. As the void size increases, the point at which the WL void abundance becomes discontinuous due to sample sparsity varies for each cosmology. Therefore, for each catalogue, all bins (for all cosmologies) above the point at which the first discontinuity in any cosmology occurs are discarded. This leads to the WL void abundance being measured with roughly 20 bins, that varies slightly between catalogues, where the largest voids are discarded to due sample sparsity.

Theoretically, the abundance of tunnels identified from a WL peak catalogue depends not only on the number of peaks, but also on their clustering pattern. We therefore expect that the information contained within the WL void abundance and peak correlation functions may have a substantial overlap. The latter probe has been studied in detail in previous Chapters, with certain scaling properties observed. While it is beyond the scope of the current Chapter, we will conduct a similar analysis by forecasting the parameter constraining power by WL peak two-point correlation functions in Chapter 7.

4.4.2 Tangential shear constraints

Fig. 4.6 shows likelihood contours for the four cosmological parameters from the tangential shear profiles. The colours of the contours correspond to the same void catalogues as in Fig. 4.5. Again, the contours are smallest in the Ω_m-S_8 plane. The figure shows that the contours from $\nu > 1$ and $\nu > 2$ are similar in size, and the $\nu > 3$ contours are significantly larger and in most cases entirely enclose the other contours. All of the contours in this figure, unlike in the case of the void abundances, occupy similar regions of the parameter space, or have similar degeneracy directions. This confirms our conclusion based on the observation of Fig. 4.4, namely the tangential shear profiles from different peak catalogues do not offer much complementarity.

As in Section 4.4.1, we combine the tangential shear profiles from all three catalogues to generate ‘Combined’ likelihood contours. Note that for individual catalogues the tangential shear profiles are calculated with 30 bins each. In the likelihood analysis the first two bins are removed. This is because at $r/R_v = 0$, $\gamma_t = 0$, and so the variance is also 0. This feature induces a singularity close to the origin when inverting the covariance matrix, and so bins near the origin must be removed.

By combining catalogues, we find an improvement in contour size relative to the $\nu > 1$ catalogue, which again suggests that there is complementary information between the different ν catalogues for the tangential shear profiles.

The strongest constraints from the tangential shear profiles are for the combined contour. We summarise the 68% and 95% CL for the γ_t combined case in Table 4.1.

4.4.3 Constraints by combining void abundance and tangential shear

In this section we present parameter constraint forecasts for the combination of the WL void abundance and tangential shear profiles.

Fig. 4.7 shows contours for the WL void abundance and tangential shear profiles combined, for the three catalogues $\nu > 1$ (blue), 2 (orange) and 3 (green) and for the combination of all three catalogues (red). The smallest contours for an individual catalogue are for the $\nu > 2$ catalogue, and the $\nu > 3$ threshold has the largest contour size, which almost entirely encloses the smaller contours in all cases. This is likely because the number of voids decreases as the ν threshold increases, meaning that by $\nu > 3$, the statistical uncertainties are large and the constraining power is weakened.

Nevertheless, it is interesting to note that in Fig. 4.6 the tangential shear contours for the $\nu > 3$ catalogue are large. The same is also true in Fig. 4.5 with the WL void abundance for the same catalogue. The resulting contour when the two statistics are combined however is significantly smaller, as shown by the green contour in Fig. 4.7. So even for this catalogue where individual constraints are poor, their combination is highly beneficial.

Fig. 4.8 shows contours for the tangential shear profiles (blue) and WL void abundance (orange) for all three catalogues combined. Note that these contours are also presented as the red contours in Fig. 4.5 and Fig. 4.6 respectively. The combination of these two probes, labelled WL voids, is shown by the green contour (repeated from Fig. 4.7). We also include the shear-shear two-point correlation function constraints as a comparison, which are obtained using the same methodology as that for WL voids. We follow Asgari et al. (2020) and sample the 2PCF using 9 logarithmically-spaced angular separation bins from 0.5 to 300 arcmin, and use both the ξ_+ and ξ_- correlation functions, which gives us 18 bins in total. We show the percentage errors (at 68% and 95% CL) for the combination of the shear two-point correlation functions (γ-2PCF) in Table 4.1.

For all combinations of parameters, the WL void abundance contours and the tangential shear contours occupy similar regions of the parameter space and have similar degeneracy directions, where the void abundance contours are slightly smaller than the tangential shear profile contours. Compared to the shear 2PCF, both the WL void abundance and tangential shear profiles are able to constrain S_8 with greater accuracy, and the abundance also provides tighter constraints on w_0.When all of the WL void statistics are combined, the WL void contours are smaller than the shear 2PCF contours for every combination of parameters, except the Ω_m-h plane, where the two contours have comparable sizes. However, in this plane the two contours also appear to have complementary degeneracy directions. Furthermore, there also appears to be stronger complementary degeneracy directions between the green and grey contours in the S_8-h plane and the h-w_0 plane. Finally, the combined WL void constraints are significantly tighter on w_0 compared to the shear 2PCF.

We show the percentage errors (at 68% and 95% CL) for the combination of the WL void abundance and tangential shear profiles over all three catalogues in Table 4.1. The table shows that, compared to the shear 2PCF, the combined WL void statistics are able to provide tighter constraints on S_8 and w_0 at the 68% CL, and tighter constraints on Ω_m, S_8 and w_0 at the 95% CL. Although the shear 2PCF provides tighter constraints on h, Fig. 4.8 shows that the WL void statistics have complementary degeneracy directions to the shear 2PCF in all panels that include h. This indicates that the WL void statistics will also be useful for constraining h when combined with the shear 2PCF.

4.5 Discussion and conclusions

In this Chapter we have tested the sensitivity of the WL void abundances and tangential shear profiles to four cosmological parameters: Ω_m, S_8, h and w_0. To this end, we have trained a Gaussian Process emulator with 26 cosmologies sampled in this 4D parameter space using a Latin hypercube, which can be used to predict these two void statistics for arbitrary cosmologies (within the range spanned by the training cosmologies). We have investigated the impact of changing the number of WL peaks used as tracers to identify voids, and ran Markov Chain Monte Carlo samplings from our mock weak lensing data to forecast the accuracies at which these four parameters can be constrained by a future, LSST-like, lensing survey, using different combinations of the above WL void statistics.

The results from Fig. 4.5 show that the WL void abundance combined over all catalogues gives the tightest parameter constraints, where the greatest sensitivity is to the S_8 parameter. This is because the abundances of WL voids identified from WL peak catalogues at different ν thresholds have different dependencies and degeneracy directions in the studied parameter space. We suspect that there is a close interlink between the void abundance and the peak two-point correlation function, but will defer a detailed study of the latter to a follow-up work. For now, we conclude that complementary information is contained in the abundances of voids from different WL peak catalogues, a fact that should be utilised in order to maximise the use and scientific return of future lensing data.

WL void tangential shear profiles, in contrast, provide slightly less tight constraints on the same cosmological parameters, and the results from different peak catalogues do not seem to be complementary to each other. In particular, for low-ν peak catalogues such as $\nu > 1$ (Fig. 4.6), there is little degeneracy between Ω_m and S_8; this is because S_8 is designed to break the degeneracy between Ω_m and σ_8 for standard WL analysis, e.g., shear two-point correlation function, and the low-ν peaks have little bias with respect to the underlying convergence field, so that their tangential shear profiles follow more closely the parameter dependency of the shear two-point correlation functions. WL void abundances, on the other hand, can have further degeneracies between Ω_m and S_8 (as seen in Fig. 4.5), indicating that they have different degeneracy directions between Ω_m and σ_8 compared with the shear two-point function, and therefore can lead to additional constraints to the latter.

Nevertheless, we highlight that the above conclusions only apply to the 4D parameter space that we have focused on in this Chapter. This may change if additional ΛCDM parameters such as the spectral index are included. Our results may also be sensitive to changes in curvature, massive neutrinos or other sources of additional physics. In Chapter 5 we will show that the tangential shear profiles are able to distinguish between modified gravity models with a larger signal-to-noise ratio than the void abundance. This suggests that there may be other cosmological parameters not studied here, such as those governing modified gravity laws, to which the tangential shear profile is more sensitive than the WL void abundance. We leave an exploration of this possibility to future works.

Finally, we have found that combining void abundance and tangential shear is another way to obtain tighter parameter constraints. Even for the $\nu > 3$ catalogues, for which these two void statistics give poor individual constraints, significant improvement has been found with their synergy.

Overall, we find that weak lensing voids can be a promising cosmological probe to constrain models. The cosmological parameter to which the WL void statistics are most sensitive is S_8, which can be measured at the sub percent level (68% CL). We also find that Ω_m can be measured to within $\simeq 2\%$, h to within $\simeq 2\%$ and w_0 within $\simeq 3\%$ (all 68% CL).

As a comparison, we find that parameter constraints from the combination of void abundances and tangential shear profiles are tighter than those from the shear two-point correlation function (which were obtained from the same WL maps, using the same methodology) at the 68% and 95% CLs for all parameters, except h. However, the void statistics also have complementary degeneracy directions to the shear 2PCF for all combinations of parameters that include h, which indicates that WL voids are also useful for constraining h when combined with the shear 2PCF, even if the constraints from WL voids alone are not tighter than those from the shear 2PCF.

Additionally, the WL void constraints presented here are for the combination of three peak catalogues. These constraints can be further improved through the inclusion of additional peak catalogues, which may be able to make WL voids a significantly more powerful probe than the shear 2PCF.

We also note that constraints from the shear two-point correlation function can be improved by using tomography (Martinet et al., 2020), and it is therefore also important to test how tomography can improve the constraints from WL void statistics in the future.

Throughout this study, we have adopted a Gaussian smoothing of $\theta_s = 1$ arcmin. It may also be interesting to study how the parameter constraints depend on the smoothing scale used to smooth the WL convergence maps. We know from Chapter 3 that using larger smoothing scales increases the size of the WL voids and reduces their total number. A larger number of WL map realisations will then be required in order to accurately measure WL void statistics for larger smoothing scales, so we leave such a study to future work. Nevertheless, we have performed a test by using a larger smoothing scale, $\theta_s = 2$ arcmin, and in Appendix .4 we give a brief summary of the resulting parameter constraints. We can see that the results are similar to what we have found for a 1 arcmin smoothing, cf. Fig. 4.8.

It will also be important to develop an understanding of how the void function is affected by systematics including intrinsic alignments, baryonic feedback, and masking (which can bias statistics measured from convergence maps, e.g. see Giblin et al. (2018)), which we leave to future study.

In Chapter 3 we studied the differences in WL void statistics between WL voids identified from different void finders. We found that the tunnel algorithm offered one of the best compromises between high signal-to-noise ratio and small impact from galaxy shape noise in the tangential shear profiles. However, it will also be interesting to assess the constraining power of WL voids identified using other void finders such as the watershed algorithm. The aim is to have a fully comprehensive study of the many different and unexplored ways to use future high-quality weak lensing data to maximise our ability to test cosmological models and constrain cosmological parameters.

Chapter 5

Cosmological test of gravity using weak lensing voids

5.1 Introduction

One of the fundamental questions of cosmology concerns the cause of the accelerated expansion of the Universe, first detected by Riess et al. (1998) and Perlmutter et al. (1999). Many possible explanations have been proposed (e.g. see the recent review by Caldwell & Kamionkowski, 2009), but a very intriguing one concerns modifying gravity on large cosmological scales by including an extra scalar field, which mediates an additional, or fifth, force. However, GR has been shown to conform accurately with gravity tests in the Solar System (Bertotti et al., 2003; Will, 2014), and, since any modifications to GR must pass the same tests, it requires that the fifth force must be suppressed in our Solar System. One way to achieve this suppression is through screening mechanisms, where the effects of the fifth force only become important in under-dense regimes (Brax, 2013). One of such phenomenological models which contains a screened fifth force is the normal branch of the Dvali-Gabadadze-Porrati braneworld models (nDGP) (Dvali et al., 2000). In the nDGP model, the fifth force is suppressed through Vainshtein screening (Vainshtein, 1972), which is least effective far from massive objects, and so we expect that the greatest detectable signatures of the fifth force would be most apparent within voids.

Given that WL maps correspond closely to the projected LSS, it is only natural to use them to identify structures such as high density peaks as well as low density regions. In this Chapter, we study the latter, i.e., *WL voids*, by employing the method from Chapter 2 of identifying voids in the WL convergence field. The objective is to study the potential of these WL voids to constrain modified gravity models. Our study was motivated by the results of Cautun et al. (2018) and Paillas et al. (2019) who found that voids identified in the galaxy distribution are emptier in modified gravity models compared to the standard cosmological model, ΛCDM, and that this signature can be measured in the tangential shear profile of voids. The first Chapter showed that the tangential shear of WL voids is about 3 times higher than that of galaxy voids and therefore WL voids represent a promising approach for testing MG models. We exemplify the constraining power of WL voids by studying the nDGP model above, and the results will have implications for upcoming surveys, such as LSST (LSST Science Collaboration et al., 2009) and Euclid (Refregier et al., 2010), which aim to provide high resolution WL maps over a large fraction of the sky. Studying WL voids represents a new approach of maximising the information that can be gained from such future data sets.

This Chapter is structured as follows: in Section 5.2 we discuss the relevant modified gravity and weak lensing theory, in Section 5.3 we present the data used in this study. We describe the prescription we follow to include galaxy shape noise (GSN) in our analysis in Section 5.3.2. The void finder used in this Chapter is described in Section 5.4, followed by results for the WL peak abundance, void abundance, void convergence profile and void shear profile in ΛCDM and MG in Section 5.5. We finally conclude in Section 5.6.

5.2 Theory

In this section, for completeness, we very briefly describe the main points of the nDGP model and the weak lensing theory.

5.2.1 Modified gravity theory

nDGP is a brane-world model in which the 4D spacetime (a brane) is embedded in a 5D spacetime called the bulk. Matter particles are confined to the brane, while gravitons can move through the extra dimensions of the bulk. A scalar field is introduced to represent the coordinate of the brane in the extra dimension, known as the brane-bending mode. The scalar field is a physical degree of freedom in the model which mediates a fifth force, and the strength of the fifth force is controlled by a crossover scale r_c, the scale at which the behaviour of gravitons changes through 4D or 5D. The nDGP action for gravity is

$$S = \int_{\text{bulk}} d^5x\sqrt{-g^{(5)}}\frac{R^{(5)}}{16\pi G^{(5)}} + \int_{\text{brane}} d^4x\sqrt{-g}\frac{R}{16\pi G}\,, \tag{5.2.1}$$

where g is the determinant of the metric tensor, R is the Ricci scalar, G is the gravitational constant, all on the brane, and a superscript $^{(5)}$ denotes the 5D bulk counterparts to the above 4D brane terms. The cross-over scale at which gravity transitions from 5D to 4D is related to G and $G^{(5)}$ as

$$r_c = \frac{1}{2}\frac{G^{(5)}}{G}\,, \tag{5.2.2}$$

and the modified Poisson equation receives an additional contribution from the scalar field ψ in the form

$$\nabla^2\Psi = \nabla^2\Psi_N + \frac{1}{2}\nabla^2\psi\,, \tag{5.2.3}$$

where Ψ_N is the standard Newtonian potential satisfying

$$\nabla^2\Psi_N = 4\pi G a^2\delta\rho\,, \tag{5.2.4}$$

a is the scale factor, ∇ is the spatial derivative and $\delta\rho = \rho - \overline{\rho}$, where ρ is the matter density and $\overline{\rho}$ is the background matter density.

The equation of motion of ψ is given by

$$\nabla^2\psi + \frac{r_c^2}{3\beta(a)a^2}\Big[(\nabla^2\psi)^2 - \nabla^i\nabla^j\psi\nabla_i\nabla_j\psi\Big] = \frac{8\pi G}{3\beta(a)}\delta\rho a^2\,, \tag{5.2.5}$$

where i, j run through 1,2 and 3, and β, which dictates the strength of the fifth force, is a function of time given as

$$\begin{aligned}\beta(a) &= 1 + 2Hr_c\left(1 + \frac{\dot{H}}{3H^2}\right)\\ &= 1 + \left[\frac{\Omega_{m0}a^{-3} + \Omega_{\Lambda 0}}{\Omega_{\rm rc}}\right]^{\frac{1}{2}} - \frac{1}{2}\frac{\Omega_{m0}a^{-3}}{\sqrt{\Omega_{m0}a^{-3} + \Omega_{\Lambda 0}}}\,,\end{aligned} \tag{5.2.6}$$

where H is the Hubble parameter, H_0 its present day value, $\dot{H}$ is its time derivative, Ω_{m0} is the present-day matter density parameter, $\Omega_{\Lambda 0}$ is the present-day vacuum energy density parameter and $\Omega_{\rm rc} = 1/4H_0^2r_c^2$. By linearising Eq. (5.2.5), the modified Poisson equation can be written as

$$\nabla^2\Psi = 4\pi G a^2\left(1 + \frac{1}{3\beta(a)}\right)\delta\rho\,. \tag{5.2.7}$$

Any modification to GR must pass the stringent Solar System tests of gravity, which means the fifth force must be well ‘screened’ in environments like the Solar System, though it can still attain its full strength in under-dense regions. In the nDGP model, the fifth force is suppressed in over-dense regions through the Vainshtein mechanism in which, for an object in isolation, the radius within which screening is efficient is given by the Vainshtein radius r_V,

$$r_V^3 = \frac{4GM}{9\beta^2H_0^2\Omega_{rc}}. \tag{5.2.8}$$

The fifth force becomes unscreened on scales $r \gtrsim r_V$.

5.2.2 Weak lensing theory

The convergence κ, for a single object along a line of sight, is linked to the lensing potential by

$$\kappa = \frac{1}{2}\nabla^2\Psi_{\rm 2D}\,, \tag{5.2.9}$$

where $\Psi_{\rm 2D}$ is the lensing potential

$$\Psi_{\rm 2D}(\boldsymbol{\theta}) = \frac{D_{ls}}{D_lD_s}\frac{1}{c^2}\int_0^{z_s}\Phi_{\rm len}(D_l\boldsymbol{\theta}, z)dz\,, \tag{5.2.10}$$

in which $\boldsymbol{\theta}$ is the sky coordinate of the lensed object, D_s, D_l and D_{ls} are respectively the angular diameter distances between the observer and source, observer and lens, and lens and source, z_s the source redshift, c the speed of light and $\Phi_{\rm len}$ is the gravitational potential that couples to photons (not matter) which determines photon geodesics.

The distinction between different types of potentials is important for modified gravity, since in some models the fifth force acts only on the massive matter particles (e.g., the default nDGP model), while in other models the fifth force directly modifies the photon geodesics (e.g. our nDGPlens model). In this Chapter we consider two MG models, nDGP and nDGPlens (Barreira et al., 2017), where the only difference between the two models is the form of $\Phi_{\rm len}$, which for nDGP is

$$\nabla^2\Phi_{\rm len}^{\rm nDGP} = \nabla^2\Phi_{\rm len}^{\rm GR} = 4\pi G a^2\delta\rho\,, \tag{5.2.11}$$

and which for the so-called *nDGPlens* model is given by

$$\nabla^2\Phi_{\rm len}^{\rm nDGPlens} = \nabla^2\Phi_{\rm len}^{\rm GR} + \frac{1}{2}\nabla^2\psi = 4\pi G a^2\delta\rho + \frac{1}{2}\nabla^2\psi. \tag{5.2.12}$$

These imply that in nDGPlens, the lensing of photons receives an extra contribution from the scalar field, when compared to ΛCDM and nDGP. nDGPlens is created by us to illustrate the behaviour of a MG model where photon geodesics are modified as well, and such models do exist in the literature, such as the cubic Galileon model studied in (Barreira et al., 2015)[1].

The previous equations apply to the lensing induced by a single lens, however for cosmic shear it is important to consider lensing contributions from all matter along the line of sight. So κ can be written more generally as

$$\kappa(\boldsymbol{\theta}) = \int_0^{z_s} W(z)\delta\rho(D_l(z)\boldsymbol{\theta}, z)dz\,, \tag{5.2.13}$$

for a lensing potential given by Eq. (5.2.11), i.e., one that is the same as the GR case. Where $W(z)$ is the lensing kernel that includes the redshift distribution of the multiple lenses, given by

$$W(z) = \frac{3H_0^2\Omega_{m0}}{2c}\frac{1+z}{H(z)}\chi(z)\int_z^{z_s}\frac{dn}{dz_s}dz_s\frac{\chi(z_s)-\chi(z)}{\chi(z_s)}\,, \tag{5.2.14}$$

χ denotes the comoving distance, and $\frac{dn}{dz_s}$ is the redshift distribution of sources. If, however,

---

[1] Note that in the nDGP model considered here the accelerated expansion is driven by an additional dark energy species, which we tune to ensure that the background expansion history is identical to that of ΛCDM, while in the Galileon model self-acceleration by the scalar field can be achieved and the expansion history is generally different from ΛCDM. The nDGPlens model is chosen to have the same expansion history as nDGP, and so it is different from cubic Galileon, and is only used as a toy model to single out the effect of modified photon geodesics.

the lensing potential is modified as in Eq. (5.2.12), κ (in the linear regime) becomes

$$\kappa(\boldsymbol{\theta}) = \int_0^{z_s} W(z)\left(1 + \frac{1}{3\beta(\alpha)}\right)\delta\rho(D_l(z)\boldsymbol{\theta}, z)dz\,, \tag{5.2.15}$$

which indicates that the convergence values will be rescaled by a constant (in space) across a WL map. Due to the Vainshtein screening, however, the MG effect on κ is more complicated and can only be accurately predicted through simulations.

5.3 Weak lensing maps

All the convergence maps used in this Chapter cover a 10×10 deg^2 sky area and have a resolution of 2048^2 pixels per map and a source redshift of $z_s = 1$. Throughout this Chapter, we will make use of WL maps generated from two sets of simulations. The first data set we use are three WL maps from Barreira et al. (2017) (hereafter B17) with ΛCDM, nDGP and nDGPlens cosmologies respectively, generated from the modified N-body code ECOSMOG (Li et al., 2012, 2013) and ray tracing performed with RAY-RAMSES (Barreira et al., 2016), a code that implements the on-the-fly ray tracing algorithm proposed by White & Hu (2000); Li et al. (2011). These maps are used to predict the differences of several lensing and void observables between the different gravity models. Secondly, in order to generate covariance matrices and error bars used in the SNR analysis in Section 5.5, we use the all-sky ΛCDM WL maps from Takahashi et al. (2017) (hereafter T17) which we split into 184 non-overlapping 10×10 deg^2 maps following the method presented in Chapter 6.

5.3.1 Numerical simulations

The lightcone geometry used to generate the WL maps from B17 consists of seven tiled dark-matter-only simulation boxes, of which the first five (the ones closest to the observer) have a box size of $L = 300\ h^{-1}$Mpc and the remaining two boxes, in order of increasing distance from the observer, have sizes $L = 350\ h^{-1}$Mpc and $L = 450\ h^{-1}$Mpc. Each of the seven N-body simulations were run using a particle number of $N_p = 512^3$. The cosmological parameters used for B17 were the fractional baryon density $\Omega_b = 0.049$, fractional dark matter density $\Omega_{\rm dm} = 0.267$, dimensionless Hubble rate $h = H_0/100$ km s^{-1} Mpc^{-1} $= 0.6711$, primordial scalar spectral index $n_s = 0.9624$ and root-mean-squared (rms) density fluctuation smoothed over 8 h^{-1}Mpc $\sigma_8 = 0.8344$. For a more detailed description of the simulation procedure used to generate the B17 maps we refer the reader to Barreira et al. (2017, 2016).

For the WL maps from T17, a series of dark matter-only simulation boxes with comoving sizes $L, 2L, 3L, ..., 14L$ where $L = 450\ h^{-1}$Mpc are produced. Each of these simulation boxes are duplicated eight times and then nested around the observer, such that the larger boxes enclose and overlap with the smaller boxes (see Figure 1 of Takahashi et al. (2017) for an illustration). Ray tracing was performed with the algorithm from Hamana et al. (2015), on the mass distribution from the nested simulation boxes projected onto spherical shells with a thickness of 150 h^{-1}Mpc. The simulation used a partical number of 2048^3 and cosmological parameters $\Omega_b = 0.046$, $\Omega_{\rm dm} = 0.233$, $\sigma_8 = 0.820$, $n_s = 0.97$ and $h = 0.7$. For a more detailed description see Takahashi et al. (2017).

5.3.2 Galaxy shape noise

Weak lensing maps obtained from observational data require measurements of redshifts and shapes for a large number of background galaxies. Intervening cosmic structure acts as a lens for the source galaxies and induces small correlations in galaxy shapes across the sky, from which the cosmic shear signal can be extracted. However the amplitude of this correlation is small, and is largely dominated by the random orientation of galaxies, which is referred to as galaxy shape noise (GSN).

Here, we are interested in characterising how well the difference between the ΛCDM and MG models, can be measured observationally so we add GSN to all of the convergence maps used in this study. We smooth the convergence maps with a compensated Gaussian filter U (Hamana et al., 2012), which satisfies $\int^{\theta_o} U(\theta)\theta d\theta = 0$, where

$$U = \frac{1}{\pi\theta_s^2} e^{-\theta^2/\theta_s^2} - \frac{1}{\pi\theta_o^2}(1 - e^{-\theta_o^2/\theta_G^2}) \tag{5.3.1}$$

for $\theta < \theta_o$, and $U = 0$ otherwise, with $\theta_s = 2.5$ arcmin, and $\theta_o = 15$ arcmin. This choice of filter allows us to account for the mass sheet degeneracy (Schneider, 1996), and removes the long wavelength modes. For the peak and void abundances discussed in Sections 5.5.1 and 5.5.2 we also show results for the ΛCDM case using Gaussian smoothing (with $\theta_s = 1.5$ arcmin). We make this comparison since both the compensated Gaussian filter (e.g. Hamana et al., 2012; Shirasaki et al., 2018) and the Gaussian filter (e.g. Liu et al., 2015) are common choices for weak lensing studies, and we include SNR values for both filters for all statistics measured throughout this Chapter. This comparison allows us to demonstrate the impact the choice of filter can have on measurements made in WL maps, beyond variations in the smoothing scale.

Our prescription for including GSN is based on Van Waerbeke (2000), where we add random values to each pixel taken from a Gaussian distribution with standard deviation, $\sigma_{\rm pix}$, given by

$$\sigma^2_{\rm pix} = \frac{\sigma^2_{\rm int}}{2\theta_{\rm pix} n_{\rm gal}} \ , \tag{5.3.2}$$

where $\sigma_{\rm int}$ is the dispersion of source galaxy intrinsic ellipticity, $\theta_{\rm pix}$ is the angular width the pixels in the WL maps, and $n_{\rm gal}$ is the number density of source galaxies. In order to make a forecast for LSST, we use $\sigma_{\rm int} = 0.4$ and $n_{\rm gal} = 40$ arcmin^{-2} (LSST Science Collaboration et al., 2009).

For consistent definitions between the different cosmological models, we define the amplitude ν of a κ pixel as

$$\nu = \frac{\kappa}{\sigma_{\rm GSN}}, \tag{5.3.3}$$

where $\sigma_{\rm GSN} = 0.007$ is the standard deviation of the GSN map (smoothed with the compensated filter) that is added to the data.

5.4 Void finding algorithm

In this Chapter we apply the tunnel algorithm of Cautun et al. (2018) to find voids. This is a 2D void finding algorithm which identifies voids based on an input tracer catalogue. This algorithm first constructs a Delaunay tessellation with the tracers as its vertices of the cells, and then voids are identified as the circumcircles of every Delaunay triangle, which is, by definition, empty of tracers. A void's centre corresponds to the centre of its respective Delaunay circumcircle and the void size, $R_{\rm v}$, is given by the radius of the respective circumcircle.

To apply the tunnel algorithm to WL maps, we use WL peaks as the input tracer catalogue. This produces 2D voids found in the WL convergence maps that, by definition, are devoid of WL peaks, with the closest peaks being found on the boundaries of the voids. To deal with the boundaries of the map, for the void abundance we remove any voids whose distance from the boundary is smaller than their radius, for the convergence and tangential shear (γ_t) profile plots we remove voids whose centres are within $2R_{\rm v}$ from the map boundary.

Furthermore, in order to increase the number of voids, which is necessary because of the small area of our WL maps, we consider all possible voids, including neighbouring ones which have a large degree of overlap (i.e., we do not exclude small voids which overlap with larger ones). The convariance matrix calculation, which is based on a much larger number of ΛCDM maps, ensures that the duplicate information is counted accordingly.

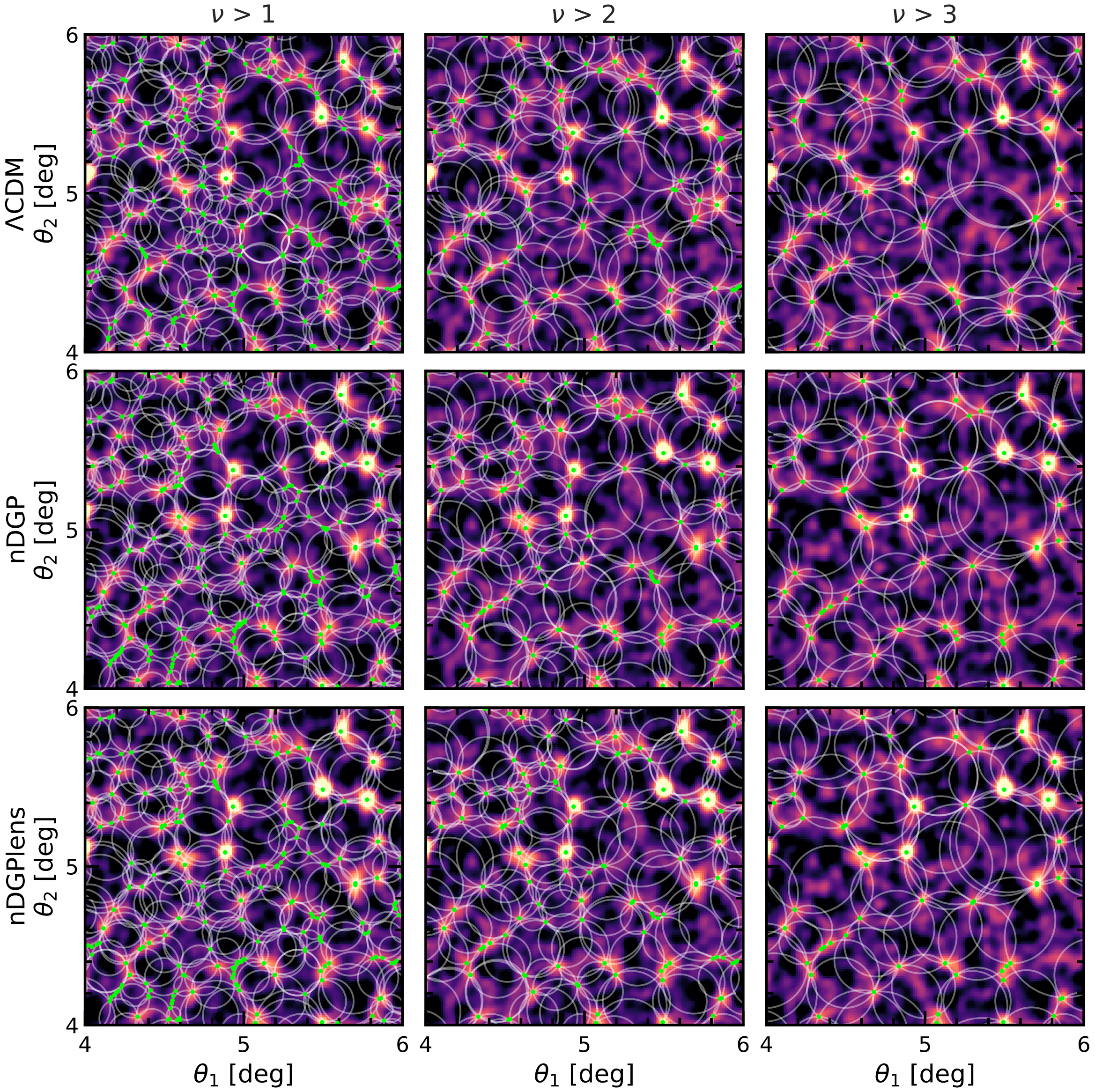

Figure 5.1: Illustration of the convergence field, and the peak and void catalogues in the ΛCDM (top row), nDGP (middle row) and nDGPlens (bottom row) models studied here. The κ values are shown by the background colours, with bright colours corresponding to high κ values and dark colours to low κ values. The axes θ_1 and θ_2 are two orthogonal angular coordinates, and only the central regions of the κ maps are shown to avoid overcrowding the visualisation. The WL peaks identified in these κ maps are indicated by the green points, with the three columns corresponding to peaks of different heights: $\nu > 1$ (left column), $\nu > 2$ (middle column) and $\nu > 3$ (right column). The white circles show the size and distribution of voids for each of the three peak catalogues.

To identify WL peaks, we first smooth the convergence maps with a compensated Gaussian filter with smoothing scale $\theta_s = 2.5$ arcmin. From the smoothed WL maps, we identify WL peaks as pixels whose convergence values are larger than those of their eight neighbours. The peak catalogue used for the tunnel algorithm is created using information about the position and height of the WL peaks in the WL maps. For a given WL map and its associated peak population, we obtain three peak catalogues by selecting the peaks according to their height. The catalogues are comprised of peaks higher than a given ν threshold, with $\nu > 1, 2$ and 3. For each WL map, we generate void catalogues from each of the three peak catalogues.

A visualisation of the tunnels identified in the WL maps studied here is shown in Fig. 5.1, where each row corresponds to one of the three models studied here. The columns correspond to peaks of different heights, and the associated void catalogues, with $\nu > 1, 2$ and 3 from left to right. It is evident from this figure that the $\nu > 1$ peak catalogues produce the most voids, while the $\nu > 3$ catalogues produce more large voids. This means that the different void catalogues should respond to the large scale modes of the κ maps differently, and so it is possible that the tightest constraints may be achieved through a combination of all three void catalogues, however due to the limited sample, this remains to be tested. The differences between ΛCDM and MG in Fig. 5.1, can be studied quantitatively using peak and void abundances as well as void WL profiles, which is the subject of the next section.

5.5 Results

In this section we discuss the properties of voids identified in WL maps, and present signal-to-noise-ratios (SNR) for the peak abundance, void abundance and tangential shear profiles as measures of the ability to distinguish between MG and GR.

We define the SNR for a given statistic S as

$$\mathrm{SNR}^2 \equiv \sum_{i,j} \delta S(i)\ \mathrm{cov}^{-1}(i,j)\ \delta S(j)\ , \tag{5.5.1}$$

where $\delta S = S_{\mathrm{MG}} - S_{\mathrm{GR}}$ is the difference in that statistic between MG and standard GR, cov^{-1} is the inverse of the covariance matrix for the statistic S and i and j indicate the bin numbers that are summed. We multiply the cov^{-1} term by the Anderson-Hartlap factor α (Anderson, 2003; Hartlap et al., 2007) in order to compensate for the bias present when inverting a noisy covariance matrix. The Anderson-Hartlap factor is given by

$$\alpha = \frac{N - N_{\mathrm{bin}} - 2}{N - 1}\ , \tag{5.5.2}$$

Table 5.1: Forecasted SNR with which an LSST-like survey could discriminate between the two MG models studied here and ΛCDM. We show SNR values for WL peak and void abundance, as well as for the void tangential shear profile. For voids, we consider three different catalogues that were identified using the distribution of WL peaks with heights, $\nu > 1, 2$ and 3.

ν range	Compensated Gaussian		Gaussian	
	nDGP	nDGPlens	nDGP	nDGPlens
peak abundance, $n(>\nu)$ – Fig. 5.2				
$1 \leq \nu \leq 5$	71	146	110	195
void abundance, $n(>R_{\rm v})$ – Fig. 5.3				
$\nu > 1$	44	58	29	32
$\nu > 2$	68	49	29	44
$\nu > 3$	50	42	49	53
void tangential shear, $\gamma_t(r)$ – Fig. 5.5				
$\nu > 1$	46	80	51	68
$\nu > 2$	50	68	41	59
$\nu > 3$	51	64	35	48

where $N = 184$ is the number of realisations (WL maps) used to estimate the covariance matrix, and $N_{\rm bin}$ is the number of bins. The covariance matrices used for SNR measurements, using the compensated Gaussian filter, are shown and discussed in Appendix .6. The covariance matrices used for the Gaussian filter are qualitatively similar to the compensated Gaussian case, and so we do not include them for brevity. The SNR values that we present in this Chapter are forecast for LSST so we rescale the SNR values calculated from the $A = 100$ deg^2 maps by $\sqrt{A_{\rm LSST}/A} = 13.4$, assuming LSST will achieve a sky coverage of $A_{\rm LSST} = 18000$ deg^{-2}.

5.5.1 WL peak abundance

Whilst the primary purpose of the WL peaks in this Chapter is to be used as tracers for void identification, it is also interesting to consider how their abundance is affected by the MG models.

In the top panel of Figure 5.2, we show the number density of WL peaks as a function of peak height, ν, for ΛCDM, nDGP and nDGPlens. The bottom panel shows the difference between the MG models and the fiducial ΛCDM one. The shaded regions in the figure (which are very small) indicate the uncertainties with which the ΛCDM peak abundance will be measured by LSST and are obtained from the peak abundance covariance matrix calculated using the T17 maps. In the top panel, we can see that the modified gravity models produce slightly fewer

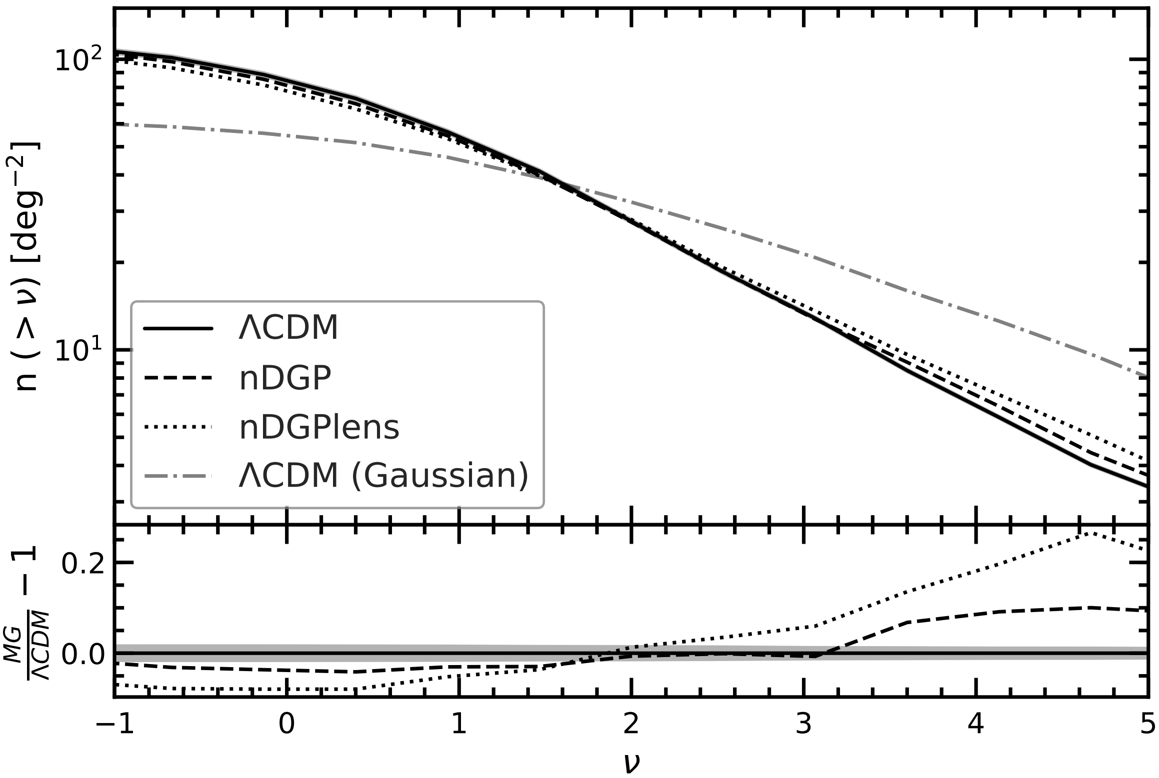

Figure 5.2: Top panel: the WL peak abundance for ΛCDM (solid), nDGP (dashed) and nDGPlens (dotted) plotted as a function of peak height, ν. The shaded regions indicate 1σ uncertainties for the ΛCDM result expected for an LSST-like survey. The WL peak abundance for ΛCDM smoothed with a Gaussian filter is shown by the grey dot-dashed line Bottom panel: the relative difference of the peak abundance between the MG models and ΛCDM. Only the error bars for the ΛCDM curve have been plotted for clarity.

small peaks with $\nu < 2$. For $\nu > 2$, nDGP and nDGPlens produce a higher number of large peaks than ΛCDM at fixed ν, which is a consequence of the enhanced structure formation present in these MG models. This difference is present even for peaks with $\nu > 3$, which typically correspond to massive haloes, whose growth in the nDGP model is significantly enhanced. In each instance, the nDGPlens models shows the largest deviation from ΛCDM. Whilst the matter distribution is the same in nDGP and nDGPlens, the extra contribution to the lensing potential from the scalar field in nDGPlens allows for further modifications to the final WL maps, which boosts the amplitude of the peaks and thus results in more peaks for a fixed ν value.

The WL peak abundance for the ΛCDM map smoothed with a Gaussian filter ($\theta_s = 1.5$) is shown by the grey dot-dashed line in the top panel of Figure 5.2. The exact value of θ_s impacts the overall amplitude of the peak abundance, but the shape of the curve remains largely unaffected by changes in θ_s, and so we choose a smoothing scale for the Gaussian filter that gives roughly the same number of peaks with $\nu > 2$ as the compensated Gaussian case. The grey dot-dashed line illustrates that the Gaussian filter produces a shallower curve than the compensated Gaussian filter. This is possibly because more large peaks are identified with the Gaussian filter since the peaks receive contributions to their height from the large scale modes, which in the case of over-densities, will boost their height. These large scale modes are removed with the compensated Gaussian, which produces fewer large peaks. The affect this has on the void abundance is discussed in section 5.5.2.

The differences in peak abundance between various MG models and the fiducial cosmology can be used as a cosmological test. For example, Liu et al. (2016b) have shown that the WL peak abundance in the Canada-France-Hawaii-Telescope Lensing Survey (Erben et al., 2013) can be used to make tight constraints on the parameters of $f(R)$ gravity. Motivated by this, the first row in Table 5.1 shows the SNR with which LSST data for the peak abundance can distinguish between the MG models studied in this Chapter and ΛCDM. We calculated the SNR using all peaks with $1 \leq \nu \leq 5$, since peaks $\nu < 1$ are most likely to be contaminated by GSN, and peaks with $\nu > 5$ will be subject to stronger influence by sample variance due to the small sizes of the available WL maps. The SNR values for the Gaussian smoothing case are larger since this filter identifies more large peaks, which correspond to large haloes that are more likely to receive a boost in their growth due to MG. The model differences are qualitatively similar between the Gaussian and compensated Gaussian cases. In the next subsection, we study the extent to which the void abundance can also be used as a cosmological test.

5.5.2 Void size function

Fig. 5.3 shows the distribution of void sizes for voids identified from the three WL peak catalogues that we study here, with $\nu > 1, 2$ and 3. The error bars are calculated from the void abundance covariance matrix obtained using the 184 T17 maps and are scaled up to the area of the LSST survey. As we have already seen from Fig. 5.1, the smallest voids are generated by the $\nu > 1$ WL peak catalogue, which also produces the most voids. As the ν threshold increases, the typical void size increases, however there are fewer voids overall. For $\nu > 1$ and 2, the total peak abundance is similar between ΛCDM and MG, which yields similar void abundances for all models in the $\nu > 1$ and 2 void catalogues. For $\nu > 3$, there are more peaks for MG than for ΛCDM, which manifests itself as creating more small voids and fewer large voids in MG than in ΛCDM. This is a consequence of the larger number of peaks in the MG models that end up splitting large voids into several smaller ones. We note that the (very few) largest voids in each catalogue are not plotted in Fig. 5.3, and are also left out of the SNR calculation, since the differences between the models appear to be dominated by sample variance. This allows us to give more conservative estimates of the SNR for the void abundance, which are less affected by noise.

The SNRs with which the void abundance measurements in an LSST-like survey can distinguish between ΛCDM and the considered MG models are shown in middle rows in Table 5.1. In all cases, the void abundances produce lower SNR values than the peak abundance. The $\nu > 1$ catalogue produces the largest SNR values for nDGPlens, and the $\nu > 2$ catalogue gives the highest SNR for nDGP. Although the model differences between ΛCDM and nDGPlens are larger, the SNR values are not consistently higher than for nDGP. This is due to the relation between various entries of the covariance matrix that arises from the fact that fewer large voids imply more smaller voids, and thus the void abundance signature of nDGPlens is more similar to the trends expected from ΛCDM sample variance than for the nDGP case.

The faded dot-dashed lines show the void abundance for the Gaussian smoothing case. For the $\nu > 1$ catalogue, there is a larger total number of voids, and fewer large voids, than in the compensated Gaussian case. This is unexpected since the abundance of peaks with $\nu > 1$ is lower for the Gaussian filter case than for the compensated Gaussian one, and typically having fewer peaks implies fewer voids too. However, we find that most of the extra peaks in the compensated Gaussian case are very highly clustered along the void boundaries for the $\nu > 1$ catalogue, and these peaks do not contribute additional voids to the catalogue despite contributing additional peaks. These highly clustered peaks on the void boundary for the

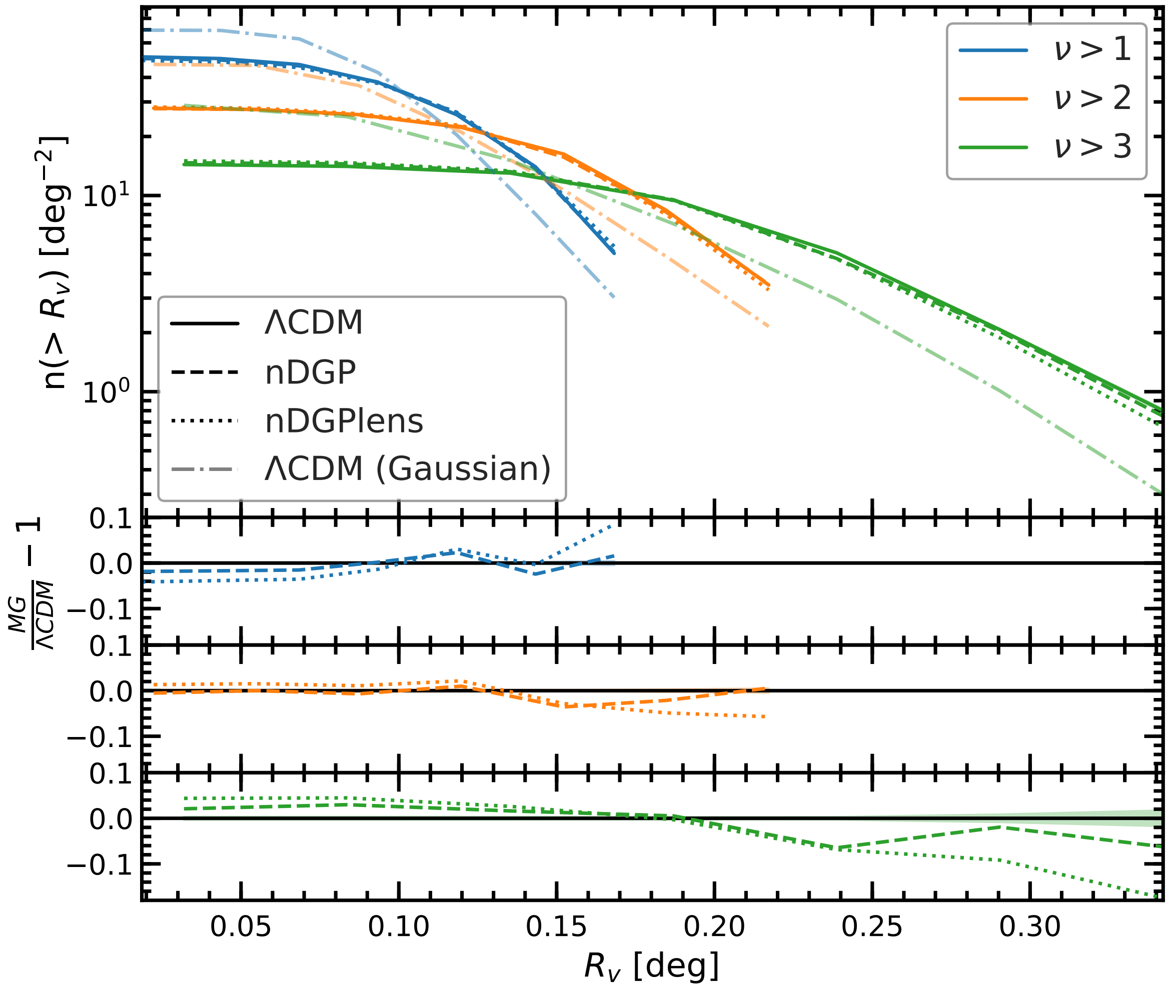

Figure 5.3: Top panel: the void abundance as a function of void radius. The coloured curves correspond to voids identified in the WL peak distribution with heights: $\nu > 1$ (blue), $\nu > 2$ (orange), $\nu > 3$ (green). The void abundance for ΛCDM is shown by the solid line, nDGP is shown by the dashed line and nDGPlens is shown by the dotted line. The shaded region around the ΛCDM curve indicates 1σ error bars expected for a LSST-like WL survey (the error bar is roughly the same size as the thickness of the curves). Bottom panel: the relative difference between the void abundances in MG models and the fiducial ΛCDM cosmology for the three void catalogues shown in the top panel.

$\nu > 1$ catalogue can be seen in the left column of Figure 5.1. The void abundance SNR values for the Gaussian smoothing case are on average lower than those for the compensated Gaussian one.

The voids are generated from the spatial distribution of the WL peaks, and hence depend on the clustering of these peaks. One way to measure this is through the N-point correlation functions of the peak catalogues. Therefore, an alternative way to exploit the void abundance is to study the N-point correlation functions of the WL peaks, or the cross correlations between the void centres and the WL peaks. However, we find that within the limited statistics of our small maps, the 2-point correlation functions of WL peaks do not show any significant differences between ΛCDM and the MG models.

5.5.3 Convergence profiles

In the MG models studied here, the fifth force enhances structure formation, which results in more underdense voids than in the fiducial GR case (e.g. Falck et al., 2018), with the excess matter that was evacuated from voids being deposited in the walls and filaments of the cosmic web that surround the voids (Cautun et al., 2016; Paillas et al., 2019). These differences in the clustering of matter manifest themselves in both the distribution of voids (as was seen in the previous section) and in the density profiles of voids. The κ values in a WL map correspond to the projected matter density weighted by the lensing kernel and thus the differences in the matter content of voids are likely to be manifested also in the void κ profiles. In this section, we study the mean convergence profiles of our three void catalogues and compare these profiles between different cosmological models.

We calculate the average κ profile of voids by stacking all the voids in a given catalogue. Since the void size can vary by a factor of several between the largest and the smallest voids, we stack the voids in terms of the rescaled radial distance from the void centre, $r/R_{\rm v}$, i.e., we express the distance in units of the void radius. Note that while the WL voids are identified in the smoothed WL maps, for calculating the κ profiles we use the unsmoothed convergence map. Using instead the smoothed κ map results in shallower void profiles because the smoothing “redistributes" the high κ values found at a void’s edge over the entire area of the void.

Figure 5.4 shows the κ profiles for each void catalogue in each of the cosmological models studied here. Similarly as before, the barely visible shaded regions correspond to error bars for an LSST-like survey and were obtained form the covariance matrix calculated from the

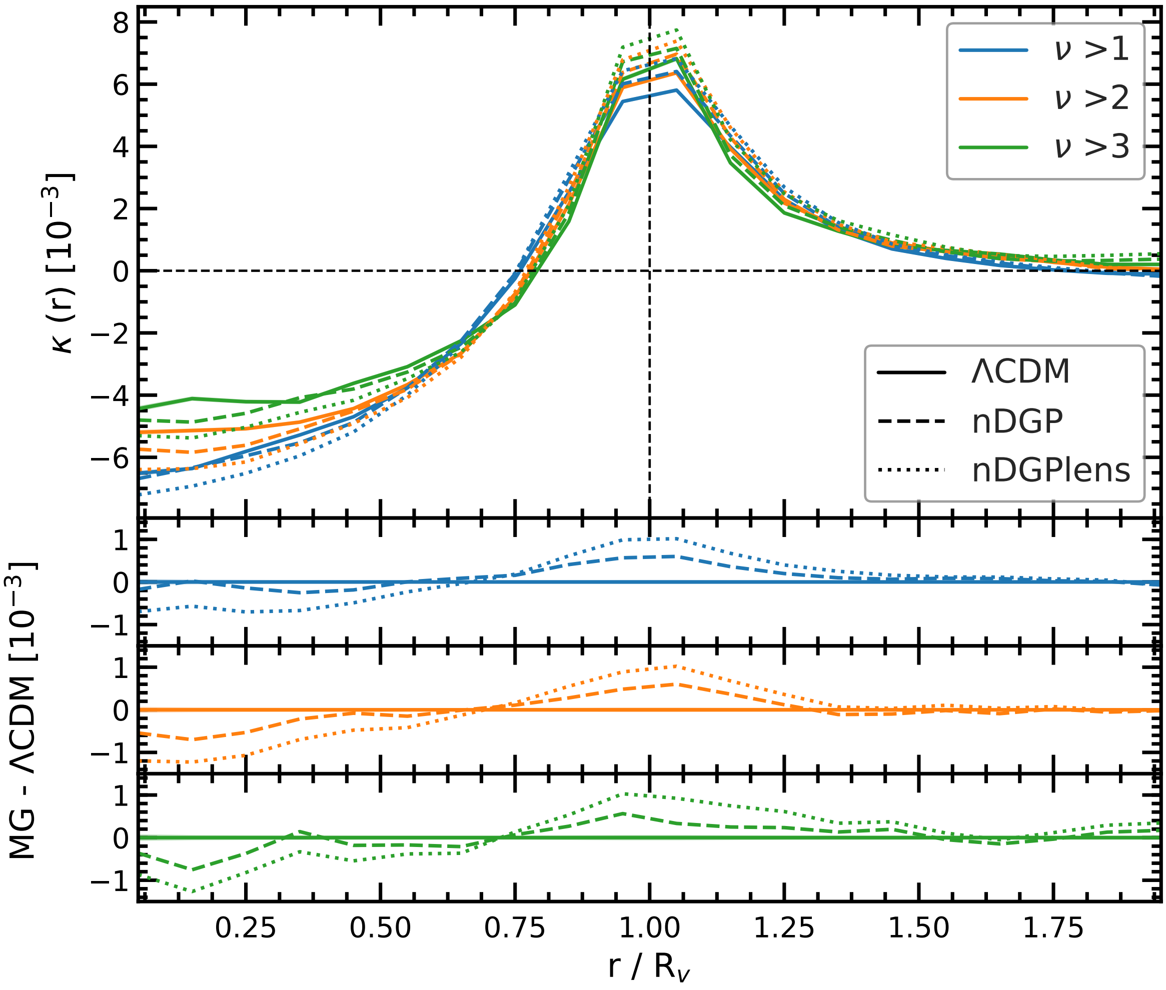

Figure 5.4: Top panel: The stacked radial convergence profiles of the voids shown in Fig. 5.1 (excluding those within $2R_\mathrm{v}$ from the map boundary). The three coloured curves correspond to voids identified from the three WL peak catalogues with $\nu > 1$ (blue), $\nu > 2$ (orange) and $\nu > 3$ (green) respectively. The ΛCDM model is shown by the solid line, nDGP by the dashed line and nDGPlens by the dotted line. The shaded regions around the ΛCDM results show the 1σ error bars for an LSST-like survey. Bottom panel: The relative difference of the κ profiles between the MG models and ΛCDM.

184 T17 maps. The overall shape of the profile shows that the voids identified in the WL maps correspond to projections of under-dense structures since for $r < 0.75R_{\rm v}$ all κ profiles have negative convergence values. The κ profile peaks at $r = R_{\rm v}$ for the void catalogues with the height of the maximum increasing as the ν threshold of the WL peak catalogues increases. The depth of the under-densities decreases as the ν threshold increases. This is because the void catalogues with a larger ν threshold contain larger voids, and since larger voids cover a larger number of pixels of the WL map (whose mean κ value is 0), their profiles in general tend to 0. It can also be seen that the regions outside of the void boundary remain over-dense at least up to a radial distance, $r = 2R_{\rm v}$ for the $\nu > 3$ catalogue, with the smaller ν catalogues returning to 0 at lower $r/R_{\rm v}$.

In general, we find that the void interiors ($r < 0.75R_{\rm v}$) in MG models have slightly lower κ values than the corresponding points in ΛCDM (this effect is most readily visible in the $\nu > 1$ and 2 catalogues, while for the other void catalogue the signal is slightly more noisy, in good agreement with previous studies (e.g., Falck et al., 2018; Paillas et al., 2019). Once the κ profiles of voids become over-dense at $r/R_{\rm v} = 0.75$ the MG profiles become more over-dense than the ΛCDM ones out to $r = 2R_{\rm v}$. The maximum difference in the κ profiles between each model can be found at the void radius $r = R_{\rm v}$.

5.5.4 Tangential shear profiles

Next we calculate the tangential shear profile $\gamma_t(r)$, for the different void catalogues. The tangential shear profile can be related to the convergence profile through Eq. 1.2.12. Whilst the convergence profiles of voids allow for a simple physical interpretation of their mass content, where positive and negative κ correspond to projected over-dense and under-dense regions, it is the shear which can be measured directly in observations. Therefore, to more easily compare with observations, we also study the void tangential shear profiles.

Fig. 5.5 shows the tangential shear profiles for the three void catalogues studied here. The typical shear value is negative indicating that voids act as concave lenses that bend light outwards from the void centres. It can be seen that the tangential shear peaks at $r = R_{\rm v}$ and the amplitude of this peak is largest for the $\nu > 3$ catalogue.

Voids in MG models have larger tangential shear profiles, and the difference is the largest for the nDGPLens model, in which the fifth force both enhances structure formation and also directly affects the photon geodesics. To quantify the potential of void γ_t profiles as a

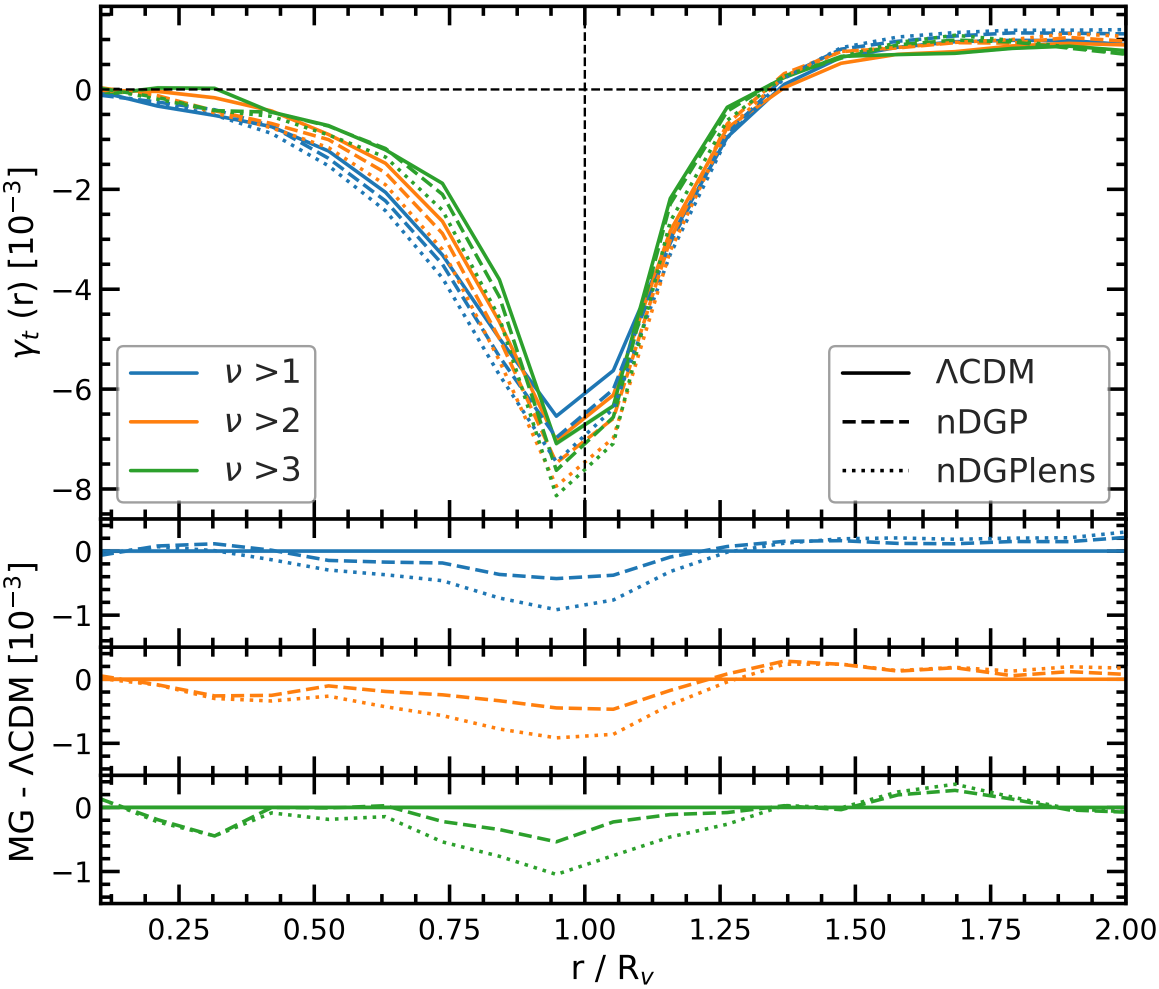

Figure 5.5: The same as Fig. 5.4 but for void tangential shear profile γ_t.

cosmological test, we summarise in the bottom three rows of Table 5.1 the SNRs with which an LSST-like survey can distinguish the MG models studied here from ΛCDM.

Table 5.1 shows that the SNR values of the γ_t profiles in the nDGP model are roughly the same for all three void catalogues, although the $\nu > 3$ catalogue has a slightly larger SNR. For the nDGPlens model the SNR vary more between the various void catalogues, being the largest for $\nu > 1$ case. Overall the SNR values are highest for the nDGPlens model. Again, we find that on average the compensated Gaussian filter can discriminate MG model better than the Gaussian filter.

It was found in Paillas et al. (2019) that, with the same void finder and the same nDGP variant (N1), galaxy voids give an SNR value of 20, whereas here we find that voids identified directly in weak lensing maps produce SNR values up to 51. This shows that voids identified in weak lensing maps are ideal objects for studying the tangential shear profile. This is further motivation for the use of voids identified in weak lensing maps as complementary statistics to the WL peak abundance, two-point correlation function and power spectrum.

5.6 Discussion and conclusions

We have investigated the potential of voids identified in WL maps to distinguish between ΛCDM and a popular class of MG models, nDGP and its variant nDGPlens. For this, we smooth the WL maps with a 2.5 arcmin compensated Gaussian filter, before we identify WL peaks and use them as tracers for the tunnel void finding algorithm. We have then done a forecast for LSST, in which GSN is properly included and found that the WL void statistics, such as abundances and tangential shear profiles, are different in MG models compared to ΛCDM and can distinguish between ΛCDM and MG up to an SNR of about 80. The SNR values from $\gamma_t(r)$ for voids identified in WL maps are over two times larger than those of galaxy voids, making a strong case for the use of voids identified in WL maps as a complementary probe of the LSS, and as a test of gravity.

Throughout the Chapter, for the void abundance and the tangential shear profiles, we have used a range of ν thresholds in order to generate multiple void catalogues. However, from Table 5.1, there is no clear systematic trend which would indicate the best choice of ν threshold. Given the large range of void sizes in Fig. 5.3, it is possible that each catalogue will respond to the small and large scale modes of the WL maps differently, and so there is potential for the multiple catalogues to provide complementary information to each other in the case of modified gravity. This has been verified for wCDM cosmologies in the previous Chapter.

We find that the peak abundance gives larger SNR values than either the WL void abundance or the tangential shear profiles. This indicates that it is likely that the peak abundance will be able to provide tighter constraints on MG. However, the extent to which voids identified in weak lensing maps provide complementary constraining power to the peak abundance remains to be studied, as the two statistics may respond differently to the changes in structure formation induced by MG, or have different degeneracy directions with other cosmological parameters. Additionally, it is possible that the results for the voids in this study are not fully converged due to the limited sample size: because the voids are physically larger than the peaks, it is possible that the voids require a larger sample area than the peaks before the measured SNR values are robust to changes in map area.

In order to reliably constrain MG with future surveys, further systematics must be taken into account. This includes the effect of baryons on simulated WL convergence maps, since we have used dark matter only simulations in this Chapter. The full extent to which baryons alter WL statistics from dark matter only simulations depends on the sub grid model used. Yang et al. (2013) found that there is a significant amplitude increase in the WL power spectrum, and that low amplitude WL peaks remain unaffected by baryons, whilst the number of large peaks is increased by the inclusion of baryons. Weiss et al. (2019) found that in order for WL statistics from dark matter only and hydro simulations to agree, very large smoothing scales must be used ($8-16$ arcmins), which is partly due to the inclusion of AGN feedback in the hydro simulations (with sub grid physics). Osato et al. (2015) found that baryon physics can induce significant biases when applied to parameter constraints, and Fong et al. (2019) state that these biases are still present even with baryon physics, unless massive neutrinos are also considered. So a complete understanding of the impact baryons may have on voids identified in WL maps will be important before cosmological constraints can be made. Furthermore, it is possible that baryons may have different impacts on the peak and void statistics, which is motivation for studying the use of weak lensing voids as a complementary probe to WL peaks.

It will also be interesting to consider other MG or dark energy theories such as those with different screening mechanisms. The models tested in this Chapter employ the Vainshtein screening mechanism which depends on derivatives of the scalar field, where other screening mechanism such as chameleon screening in $f(R)$ gravity may leave different imprints on the WL convergence maps, and hence on the statistics of WL voids. For galaxy voids, the tunnel algorithm is a better test of chameleon screening (Cautun et al., 2018) than Vainshtein screening (Paillas et al., 2019). So it will be important to consider multiple screening mechanisms, where this method can then be used to place constraints on the screening thresholds for MG theories.

To summarise, the work presented here shows that the study of 2D voids identified in WL maps can be a useful statistic to develop in order to maximise the information that can be gained from future surveys. Further development such as testing multiple screening mechanisms, the impact of baryon physics on the peak and void statistics in MG will be left for future work.

Chapter 6

The self similarity of weak lensing peaks

6.1 Introduction

The most commonly used WL statistics are the shear correlation function and convergence power spectrum. These two-point statistics alone, however, cannot account for the non-Gaussian features introduced by the nonlinear evolution of structures in the Universe, and other statistics can provide additional and complementary information. In this Chapter we study one such additional probe, WL peaks, which are the maxima of the WL convergence field. The WL peak abundance is a good example of a statistic that contains complementary information to two-point statistics (Jain & Van Waerbeke, 2000; Pen et al., 2003; Dietrich & Hartlap, 2010; Shirasaki et al., 2018), and can be used to constrain cosmological parameters within ΛCDM (Shan et al., 2012; Van Waerbeke et al., 2013; Shan et al., 2014; Liu et al., 2015), to test alternative cosmological models such as modified gravity (Cardone et al., 2013; Liu et al., 2016b; Higuchi & Shirasaki, 2016; Shirasaki et al., 2017; Peel et al., 2018), dark energy (Giocoli et al., 2018), and to measure the neutrino mass (Li et al., 2019). WL peaks can also be extracted from CMB lensing to provide cosmological constraints (Liu et al., 2016a). Various models have been developed to accurately describe high signal-to-noise-ratio (SNR) WL peaks (e.g., Hamana et al., 2004; Hennawi & Spergel, 2005; Maturi et al., 2005; Fan et al., 2010; Marian et al., 2012; Hamana et al., 2012; Liu & Haiman, 2016; Shan et al., 2018; Wei et al., 2018).

In contrast to high WL peaks, there have been relatively few studies on the abundance of low and intermediate peaks (see, e.g., Yang et al., 2011; Lin & Kilbinger, 2015; Shirasaki, 2017), which nevertheless contains rich cosmological information (Dietrich & Hartlap, 2010; Kratochvil et al., 2010; Yang et al., 2011), and even fewer on the spatial correlation of such peaks (e.g., Marian et al., 2013; Shan et al., 2014). Upcoming wide and deep field galaxy surveys such as EUCLID (Refregier et al., 2010) and LSST (LSST Science Collaboration et al., 2009) will produce large high-resolution WL maps, with significant improvements compared to the current generation of WL observations. Understanding how WL peak statistics behave will be important if we want to maximise the cosmological information that can be gained from the new surveys. In particular, the higher source number density of these surveys will lead to a reliable determination of peak abundance and clustering down to low SNR values, so it is important to have accurate models to describe the statistics of low- and intermediate-height peaks.

In this Chapter we study properties of WL peak statistics in ΛCDM, by modelling the peak abundance, peak two-point correlation functions (2PCFs) and the convergence rms fluctuation (convergence map standard deviation). Most importantly, we identify a universal self-similar behaviour in the peak 2PCF, which holds for a large range of peak heights and different cosmologies. The self-similarity is observed when expressing the 2PCF in terms of the angular separation divided by the mean peak separation, with the resulting rescaled 2PCFs lying on top of each other. We propose a general model that describes the abundance and clustering of WL peaks and that allows us to access cosmological information contained on non-linear scales.

The structure of the Chapter is outlined as follows: in Section 6.2 we describe the numerical simulations used to construct the WL maps, and introduce the statistics we use to study WL peaks. Next, in Section 6.3 we present the WL peak abundance, WL peak 2PCF, and identify a self similarity in the peak 2PCF for a given fiducial cosmology. Then, in Section 6.4 we give general fitting functions that describe the convergence rms fluctuation, peak abundance, 2PCF and its self similarity in ΛCDM for a large range of Ω_m and σ_8 values. We then show in Section 6.5 that our model can accurately reproduce the original peak 2PCF. Finally, in Section 6.6 we show that the self similarity of the 2PCF is robust to the inclusion of galaxy shape noise.

6.2 Simulations and analysis pipeline

In this section we describe the simulations and methodology used in this Chapter to study WL peak statistics.

As shown in previous Chapters, the WL convergence corresponds to the projected mass density contrast weighted by a geometric factor, and thus positive and negative κ values correspond to overdense and underdense lines of sight. For self consistency across different convergence maps we define the SNR, ν, as

$$\nu = \frac{\kappa - \mu}{\sigma}, \tag{6.2.1}$$

where μ is the mean value of the convergence field of a given map, and σ is its rms fluctuation. We have subtracted the map mean μ in the definition of SNR because our maps are relatively small and can have non-zero means due to sample variance that vary from map to map, which can affect the consistency of the SNR definition. Note that the subtraction of μ does not affect σ, and it is not needed in the case of κ reconstructed from the (directly observable) cosmic shear field. An example of a κ map generated from numerical simulations through ray tracing is shown in Fig. 6.1.

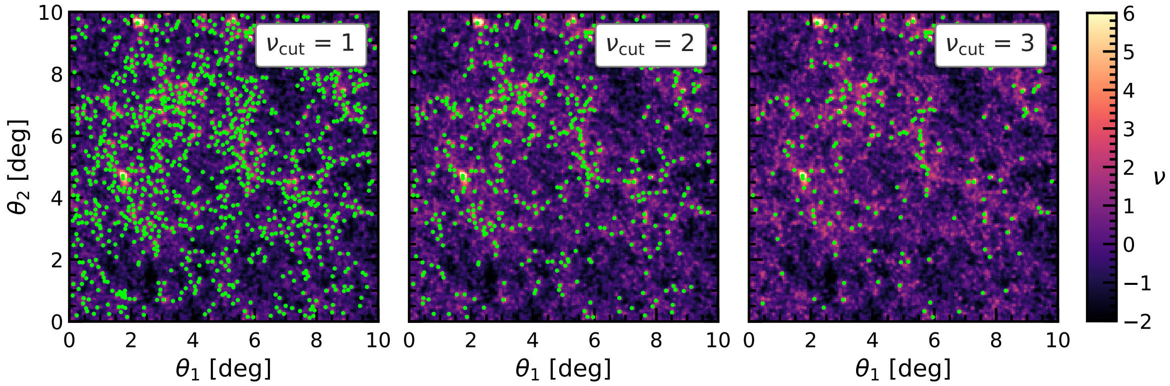

Figure 6.1: An illustration of a WL convergence map and the distribution of peaks of different heights (green points). The convergence field is expressed in terms of the SNR, ν, as indicated by the colour-bar on the right. Peaks with a height below $\nu_{\rm cut} = 1, 2$ and 3 are removed to produce the three peak catalogue shown in the three panels (all plotted on the same convergence map). The axes θ_1 and θ_2 give angular coordinates of the map in two orthogonal directions. The map is smoothed with $\theta_s = 2$ arcmin before the peaks are identified. We use 2 arcmin smoothing here for visualisation purposes, to clearly show the presence of WL peaks in a convergence map. As 1 arcmin smoothing (which is used in the main analysis of the Chapter) results in a large number of peaks that would reduce the clarity of the figure.

For most of the Chapter, the lensing quantities are measured in maps obtained from cosmological simulations without added noise, except for Section 6.6 where galaxy shape noise is included and all quantities are measured from the noise-added maps (for more details see Section 6.6).

6.2.1 Numerical simulations

In order to study weak lensing peak statistics, in this Chapter we use a large suite of WL convergence maps constructed from two sets of N-body simulations. The first are the publicly-available all-sky convergence maps of Takahashi et al. (2017) (hereafter T17). These maps have a source redshift of $z_s = 1$ and have been generated using the ray tracing algorithm described in Hamana et al. (2015) (see also Shirasaki et al., 2015), with a HEALpix resolution of $N_{\rm side} = 16384$. To avoid probing the same structures along the line-of-sight, T17 constructed the light cone by stacking a hierarchy of cubic simulation boxes, with comoving sizes $L, 2L, 3L, \cdots, 14L$, where $L = 450h^{-1}$Mpc. The simulations had a particle number of 2048^3, where the particle mass depends on the box size, and ranges from 8.2×10^8 to $2.3 \times 10^{12} M_\odot$ (see Table 1 of T17 for more details). Each of the simulation boxes was duplicated 8 times and nested around the observer, such that nests of larger boxes contain nests of smaller boxes at their centers. Ray tracing was then performed on the nested simulation boxes by taking the projected mass distribution in spherical shells of 150 h^{-1}Mpc in thickness centred on the observer (see T17 for illustration). The cosmological parameters adopted for the T17 simulations are $\Omega_m = 0.279$, $\sigma_8 = 0.820$ and $h = 0.7$, where $h = H_0/100$ km s^{-1} Mpc^{-1}. Throughout this Chapter we have split the T17 all-sky map into 184 separate 10×10 deg^2 maps with 2048^2 pixels per map, for which we can use the flat sky approximation to simplify our analysis. A detailed description of the method we use to split the all-sky map into smaller squares is given in Appendix .7.

The second set of WL maps we use are taken from Matilla et al. (2016) (hereafter Z16; see also Gupta et al. 2018) and consist of maps for 96 different cosmologies. It was built with the simulation pipeline described in Petri (2016). For each cosmology, the maps were obtained from an N-body simulation of a periodic box with length $L = 240$ h^{-1}Mpc and 512^3 simulation particles with a particle mass of $\sim 10^{10} h^{-1} M_{\odot}$ (the exact value depends on the actual cosmology). Ray tracing was then performed by using a source redshift of $z_s = 1$ and by stacking particles into lens planes with a thickness of 80 h^{-1}Mpc between the source and the observer. The lens planes were generated by taking a slice along a coordinate axis of the original simulation box and applying a random shift and rotation. This process was repeated to generate 512 3.5×3.5 deg^2 maps per cosmology with 1024×1024 pixels per map. Note that each of the 512 maps were obtained from the same periodic simulation by varying the orientation of the line-of-sight direction. For a more detailed description we refer the reader to Z16.

In total we have two sets of maps, one with 184 10×10 deg^2 maps for a fixed cosmology and the other with 512 3.5×3.5 deg^2 maps for 96 cosmologies with different values of Ω_m and σ_8. Larger maps are ideal for 2PCF studies as the 2PCF cannot be reliably calculated at large separations where pair measurements are affected by the finite size of the map. However, the differences in the two simulation data sets used here bring some benefits for our analysis. First, given the simulations use different ray tracing codes and box tiling methods, if we are able to identify certain features of the WL peak statistics in both simulations, this can be a check that the said features are not an unphysical consequence of the procedure used to generate the convergence maps. Second, the different simulation maps have different angular sizes and resolutions, which can help highlight any potential systemics in our analysis due to the box size or the pixel resolution.

6.2.2 Weak lensing peaks

WL peaks in this Chapter are defined as the maxima of the convergence field, which trace local over-densities in a range of environments. To extract the WL peaks, we first smooth the convergence map with a Gaussian filter. The convergence field has power on all scales, so the number and spatial distribution of WL peaks depends on the smoothing scale, with a larger smoothing washing out low contrast peaks and merging neighbouring peaks. We mainly study peaks identified with a Gaussian filter with smoothing length $\theta_s = 1$ arcmin, a range of smoothing scales have been studied in Liu et al. (2015), showing that this smoothing scale is ideal for WL peak studies. In some cases (which will be explicitly mentioned), we vary θ_s to understand how the results depend on smoothing scale. Next we identify WL peaks by finding all pixels in the maps whose values are larger than those of their 8 neighbours, and peaks within $3\theta_s$ of the map boundary are removed to avoid edge effects where the Gaussian filter is truncated. The height of a peak is given by the ν value of the smoothed convergence field at the peak position. For a given convergence map, we can generate multiple peak catalogues by imposing a $\nu_{\rm cut}$ threshold and keeping only peaks with $\nu \geq \nu_{\rm cut}$.

Fig. 6.1 illustrates the distribution of peaks (shown as green dots) for three different SNR thresholds, $\nu_{\rm cut} = 1, 2$ and 3. To highlight the distribution of peaks on both small and large scales, we show peaks identified with a Gaussian smoothing scale, $\theta_s = 2$ arcmin; using a smaller θ_s value would result in many more peaks and make the graph less legible.

Fig. 6.1 shows that peak catalogues with different $\nu_{\rm cut}$ values trace different features of the convergence field. The catalogue with $\nu_{\rm cut} = 1$ traces the over-dense regions of the convergence map, whilst avoiding the darker under-dense regions. In particular, many peaks seem to be arranged in a somewhat filamentary pattern. By increasing $\nu_{\rm cut}$ to 2, we find that the resulting catalogue has a significantly lower number of peaks and the peaks are now more clustered. Most of these peaks are found in highly over-dense regions, with some small filamentary patterns still remaining. Finally, there are few peaks with $\nu_{\rm cut} = 3$, but they show a high degree of spatial clustering and are located in the very over-dense regions of the map.

The description of Fig. 6.1 above highlights two important features in the behaviour of WL peaks: the number of WL peaks and their clustering, which are respectively quantified by two commonly used statistics, the peak abundance and the peak two point correlation function (2PCF). The former is well studied and has been considered for many cosmological applications (e.g., Liu et al., 2015; Liu & Haiman, 2016; Liu et al., 2016b; Shirasaki et al., 2017; Shirasaki, 2017; Shan et al., 2018; Li et al., 2019; Wei et al., 2018), whereas weak lensing 2PCFs are usually measured as shear-shear correlations (Fu et al., 2008; Heymans et al., 2012; Kilbinger et al., 2013), with very few studies directly focused on the peak 2PCFs (Marian et al., 2013; Shan et al., 2014).

The two point correlation function measures the probability of finding two points (or in our case, WL peaks) at a given separation (θ for angular separations on the sky). It can also be interpreted as a measure of the excessive clustering of a distribution of points relative to the clustering of randomly distributed points. To estimate the 2PCFs, we use the Landy-Szalay estimator (Landy & Szalay, 1993), which is a robust way of measuring 2PCFs, especially for small maps and low tracer number densities. Using this estimator requires a catalogue of randomly distributed points, whose role is to account for boundary effects and serves as a proxy for the volume (area in 2D) of the sample. The Landy-Szalay estimator is evaluated as

$$\xi_{\mathrm{LS}}(\theta) = 1 + \left(\frac{N_R}{N_D}\right)^2 \frac{DD}{RR} - \left(\frac{N_R}{N_D}\right) \frac{DR}{RR}\,, \tag{6.2.2}$$

where N_D and N_R are the numbers of data and random points and DD, DR and RR are the number of data-data, data-random and random-random pairs in bins $\theta \pm \delta\theta$. We calculate the 2PCFs by taking the average over many small maps (see description in section 6.2.1). Since the maps are small, taking the average of the ξ values measured for each map leads to biased results and we discuss this subtlety in detail in appendix .8. To obtain unbiased results, we calculate the average of the DD, DR and RR pair counts over all maps, and then we insert the average pair counts into Eq. (6.2.2).

6.3 Weak lensing statistics

As mentioned above, we are mainly interested in the one- and two-point statistics of WL peaks. In order to gain some first insight into the properties of these quantities, we use the large, 100 deg^2, maps from the T17 simulations for the results shown in this section. In the next section we shall use the small maps from the Z16 simulations to quantify the dependence of peak statistics on cosmology.

6.3.1 Peak abundance

We start by studying the mean abundance of WL peaks, which is expressed in terms of the cumulative peak abundance, $n(>\nu)$. This represents the number density in deg^{-2} of all

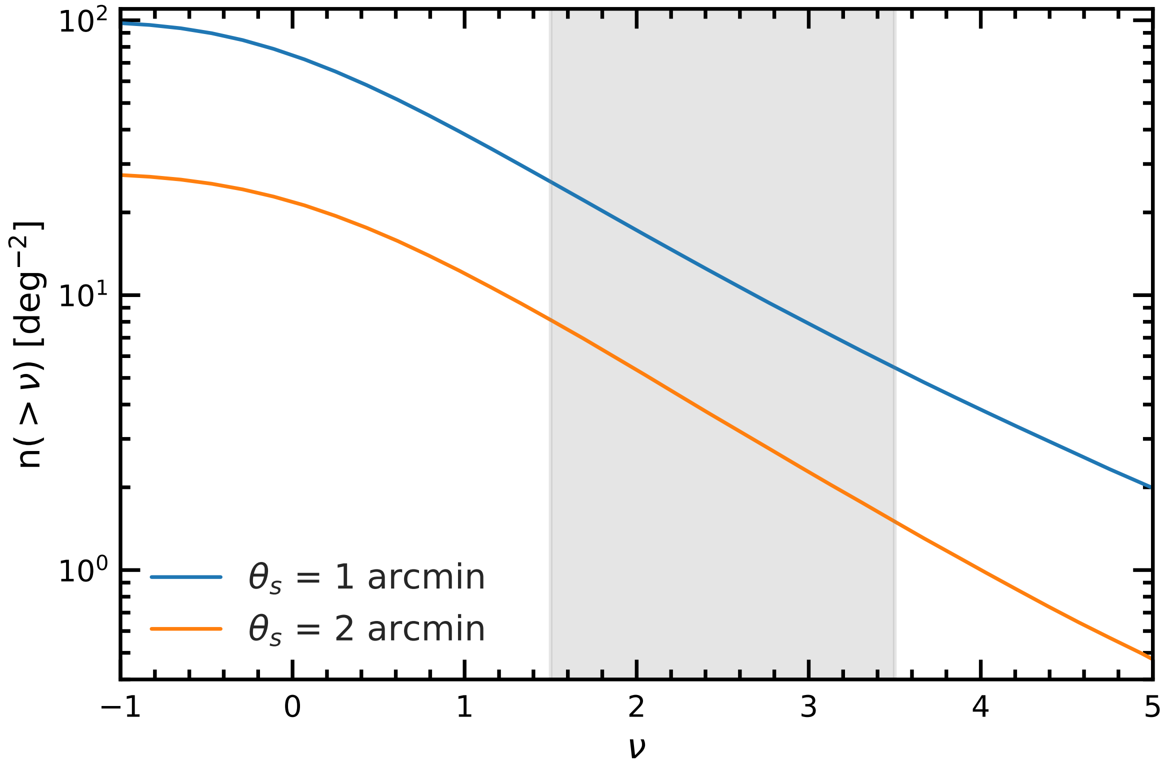

Figure 6.2: WL peak number density as a function of peak signal-to-noise, ν, for two smoothing scales, $\theta_s = 1$ arcmin (blue) and $\theta_s = 2$ arcmin (orange) from the T17 maps. The shaded grey region highlights the ν range that we study in this Chapter, discussed in section 6.3.3.

peaks whose SNRs are higher than ν. The peak abundance is illustrated in Fig. 6.2, where the results are averaged over the 184 T17 maps. The blue (upper) and orange (lower) curves correspond to a Gaussian smoothing kernel $\theta_s = 1$ and 2 arcmin, respectively. According to Eq. (6.2.1), the smoothing scale θ_s enters the definition of ν in two ways, by affecting the pixel values of κ and the overall rms κ fluctuation, σ. For the T17 maps we find $\sigma = 0.013$ and 0.010 respectively for $\theta_s = 1$ and 2 arcmin, and in the next section we will see that σ has a clear cosmology dependence as well.

The qualitative behaviour shown in Fig. 6.2 is as expected. There are very few peaks with high ν values since these correspond to massive dark matter structures, which are rare. As ν decreases, the peak abundance, $n(>\nu)$, increases quickly until $\nu \sim 0$ since lower ν values correspond to lower mass and thus more abundant dark matter structures. However, for $\nu \lesssim 0$[1] we see that $n(>\nu)$ flattens, showing that there are few peaks with $\nu < 0$. It highlights that there are few structures in underdense regions that are massive enough to lead to a local maximum, especially when smoothing over 1 and 2 arcmin. Increasing the

---

[1] Note that WL peaks can have $\nu < 0$, or equivalently $\kappa < 0$. These are local maxima in underdense regions of the convergence map.

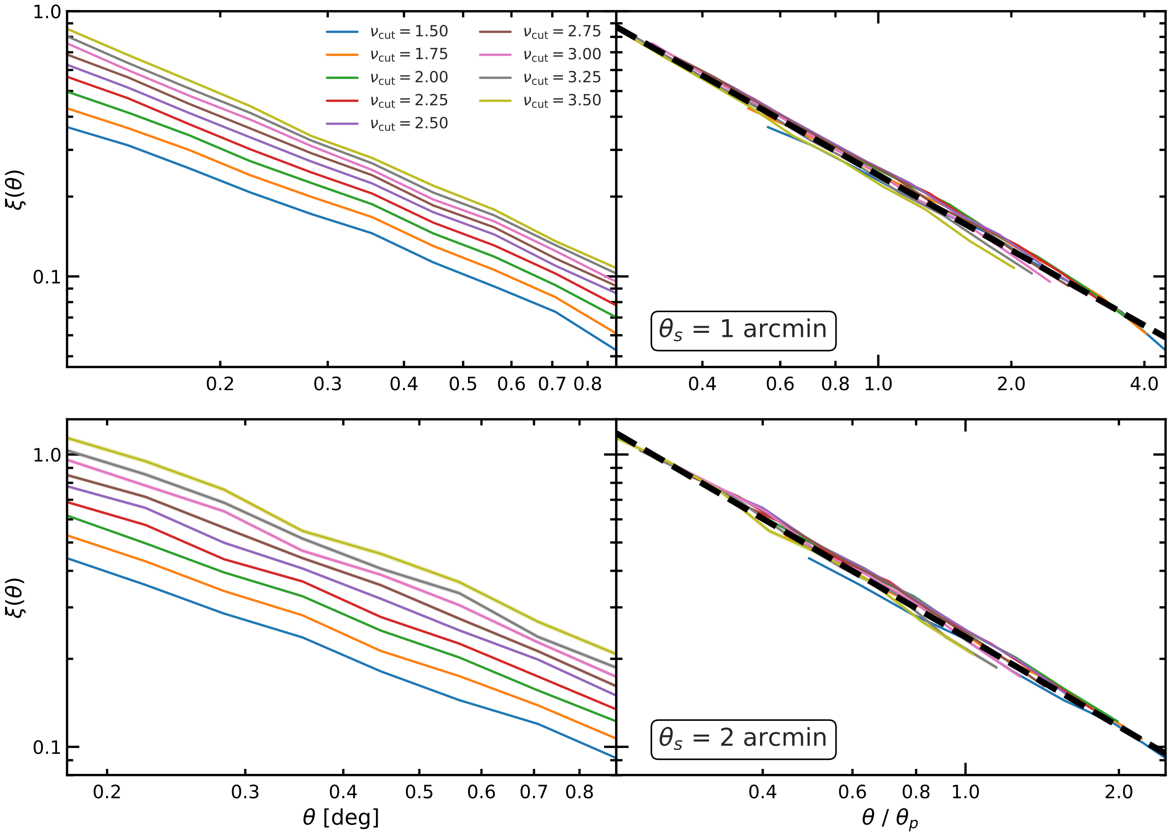

Figure 6.3: The 2PCFs of WL peaks for different peak catalogues obtained by varying the threshold, $\nu_{\rm cut}$, in the range $[1.5, 3.5]$ in increments of $\Delta\nu_{\rm cut} = 0.25$. The results are for the T17 maps and for two different smoothing scales, $\theta_s = 1$ (top-row) and 2 arcmin (bottom-row). The left column shows the 2PCFs as a function of angular separation, θ. The right hand column shows the rescaled 2PCFs,which are the 2PCFs expressed in terms of θ/θ_p, with θ_p the mean peak separation in the catalogue. The 2PCFs displays a striking self-similar behaviour, with all rescaled 2PCFs curves lying on top of each other. The black dashed line in the right-hand column shows the best fitting power law to the rescaled 2PCFswith gradients -0.94 (top) and -1.02 (bottom).

smoothing scale θ_s leads to a lower peak abundance at fixed ν, since smoothing over a larger region tends to eliminate some peaks.

We have checked that the WL peak abundance shown in Fig. 6.2 can be well fitted by the function $n(>\nu) = -a\,[\tanh(b\nu) - 1]$ for the entire ν range. However, for reasons that will become clear in Section 6.3.3, in this Chapter we are interested in the range $\nu \in [1.5, 3.5]$ (shown as the grey shaded region in Fig. 6.2), where $n(> \nu)$ can be modelled as a power law (see Section 6.4.2). Note that Fig. 6.2 also shows the uncertainties in the $n(> \nu)$ measurement, which are the standard errors of the mean of the 184 T17 maps; however, these error bars are not visible as they are roughly of the same size as the line width.

6.3.2 Peak two point correlation function and $\nu_{\rm cut}$ dependence

For WL peaks it has been suggested that the 2PCF can be well modelled by a power law (Shan et al., 2014). In this section, we will confirm this power-law description using the T17 convergence maps, and show that it works well for peak catalogues with a wide range of $\nu_{\rm cut}$ thresholds.

The 2PCF dependence on $\nu_{\rm cut}$ is of particular interest, because by decreasing $\nu_{\rm cut}$ we are including lower peaks into the analysis, which is equivalent to incorporating smaller dark matter structures into the clustering statistics. In the current standard cosmological paradigm, large-scale structures (LSS) evolve hierarchically, with larger objects forming from higher initial density peaks. This means that by varying $\nu_{\rm cut}$ we probe the different regimes of nonlinear LSS formation and thus potentially provides more powerful cosmological tests. As an example, in certain modified gravity models, smaller structures experience a stronger boost in their nonlinear growth (e.g., Clifton et al., 2012, and references therein), and we expect this to leave potentially detectable signatures in the peak 2PCFs at different $\nu_{\rm cut}$ values. In addition, as we have seen above, lowering the $\nu_{\rm cut}$ threshold increases the number of peaks included in the catalogue, and this can help increase the statistical constraining power. We will see shortly that there is a self-similarity in the peak 2PCF, which means that having peak catalogues for multiple $\nu_{\rm cut}$ values does not require separate modelling for each catalogue; this can potentially strongly improve the constraining power by WL peaks.

The left panels of Fig. 6.3 show the mean 2PCFs of the T17 maps for a range of $\nu_{\rm cut}$ values and for two smoothing scales, $\theta_s = 1$ and 2 arcmin. The error bars, which are the standard errors of the 184 maps, are shown as shaded regions around the curves, but they are very small and barely visible.

A quick inspection of Fig. 6.3 by eye confirms that the 2PCFs are well described by power laws. We can see that as $\nu_{\rm cut}$ increases the amplitude of the 2PCF, $\xi(\theta)$, also increases. This is intuitive to understand: the high WL peaks correspond to more massive structures which tend to cluster more strongly. Moreover, the 2PCF amplitude is higher for peak catalogues obtained using a larger smoothing length, θ_s. This is because a higher θ_s value suppresses peaks originating from low mass dark matter structures that cluster less. The gradient of the 2PCFs from maps with a fixed θ_s increases slightly with $\nu_{\rm cut}$, but this effect is weak for both smoothing scales shown, and the dominant effect of varying $\nu_{\rm cut}$ is in the amplitude of the 2PCF.

Note that smoothing can lead to a merging of peaks separated by distances comparable to the smoothing scale θ_s, and therefore eliminates some peaks which are close to each other. This leads to a drop off of the 2PCF from the power law on scales $\lesssim \theta_s$, which is why we show a different θ range in the two left panels of Fig. 6.3. Additionally, for a given WL map size, the 2PCFs cannot be reliably measured at large separations as there are too few peak pairs, which is why in Fig. 6.3 we adopted a conservative θ_{max} which is 1/10 the map size. Therefore, the smoothing scale and the map size set a limited range in θ within which we can measure the 2PCF. More explicitly, while for the T17 maps we use $\theta_s \in [1, 3]$ arcmin in this study, for the smaller Z16 maps we only use $\theta_s = 1$ arcmin to avoid having a too narrow θ range. A larger θ_s is necessary for maps where galaxy shape noises (GSNs) are included, to suppress the biasing effects caused by the latter (shown in Chapter 2); we will come back to this point in Section 6.6 below.

6.3.3 2PCF rescaling and self-similarity

We now move on to one of the most important results of this Chapter: the self similarity of the peak 2PCFs. This has been first studied (very briefly) in Chapter 2 in the context of explaining the self-similar behaviour of the abundances for voids identified from WL peaks with varying ν_{cut}. As we show later, the 2PCF self similarity is a very useful property that merits the more detailed investigation presented here.

The quest for a self-similar behaviour in the peak 2PCFs is motivated by the following observations: the 2PCF amplitude is lower for peak catalogues with lower ν_{cut}; meanwhile, these catalogues have more peaks and hence a smaller mean peak separation, θ_p. By expressing the 2PCF in terms of θ/θ_p the various curves could potentially be brought closer together. The question is whether after this rescaling the 2PCF curves for different ν_{cut} thresholds can be made to overlap, in which case their modelling can be significantly simplified.

The right panels in Fig. 6.3 show the rescaled 2PCF, that is the 2PCF expressed as a function of θ/θ_p instead of θ. To obtain this result, we calculated the mean peak separation as $\theta_p = (N/A)^{-1/2}$, where N is the number of peaks in a catalogue and A is the area of the map. The θ_p value for a peak catalogue can be directly inferred from the peak abundance, $n(>\nu)$, as $\theta_p = n(\nu > \nu_{\text{cut}})^{-1/2}$. We find that the rescaled 2PCFs lie on top of each other and thus it indicates that the peak 2PCF is self similar. This shows that the one-point statistic of WL peaks, $n(>\nu)$, can be tied to the amplitude of the 2PCF to achieve the mentioned self similarity. The self-similar behaviour is mainly limited to the range $\nu_{\text{cut}} \in [1.5, 3.5]$, with the rescaled 2PCFs starting to peel off from the average relation for $\nu_{\text{cut}} < 1.5$ and

$\nu_{\text{cut}} > 3.5$. At this stage it is unclear whether the breakdown of self-similarity at $\nu_{\text{cut}} > 3.5$ is physical or due to the small number of high SNR peaks in our maps which, (as discussed in Appendix .8, could bias the estimation of the two-point correlation function); this will be investigated in more detail in the future. Bearing this issue in mind, in this Chapter we limit our investigation to the modelling of WL peak statistics for $1.5 < \nu_{\text{cut}} < 3.5$ only. Note that this happens to be the same range within which the peak abundance can be well described by a power law (see Section 6.3.1).

The self-similar behaviour holds for both smoothing scales shown in Fig. 6.3, however, the rescaled 2PCFs for the larger smoothing length ($\theta_s = 2$ arcmin; bottom right panel of Fig. 6.3) are shifted to lower θ/θ_p values than the results for $\theta_s = 1$ arcmin. It suggests that 2PCFs are self-similar when keeping the smoothing scale constant, and that the self-similarity behaviour does not hold when comparing 2PCFs obtained for peak catalogues with different smoothing scales.

The panels in the right column of Fig. 6.3 also show that the rescaled 2PCFs are well fitted by a power law, as shown by the black dashed curves with gradients -0.94 ($\theta_s = 1$ arcmin) and -1.02 ($\theta_s = 2$ arcmin) .

6.4 Cosmology dependence and universal fitting functions

In this section we study the dependence of peak abundance and peak 2PCF on the Ω_m and σ_8 cosmological parameters by analysing these statistics for the set of 96 different cosmologies used for the Z16 maps. The (Ω_m,σ_8) parameter space of the Z16 maps is indicated by the points in Fig. 6.4. The parameter space is densely sampled around $\Omega_m = 0.26$ and $\sigma_8 = 0.8$, which corresponds to the fiducial cosmology, and only sparsely sampled for models with very different parameter values. In particular, when describing the cosmology dependence of various peak statistics, we will limit our fitting procedure to the (Ω_m, σ_8) pairs shown as orange points in the figure. This removes extreme and unrealistic cosmological parameters from our analysis. For comparison, the parameters used for the T17 maps are indicated by the black triangle in Fig. 6.4.

The two cosmological parameters, Ω_m and σ_8, are degenerate because they can impact the size of the matter fluctuations in similar ways, and the direction of degeneracy depends on the physical quantity which is being studied. In order to better assess the potential and limitations of using WL peak statistics to constrain these cosmological parameters, it is

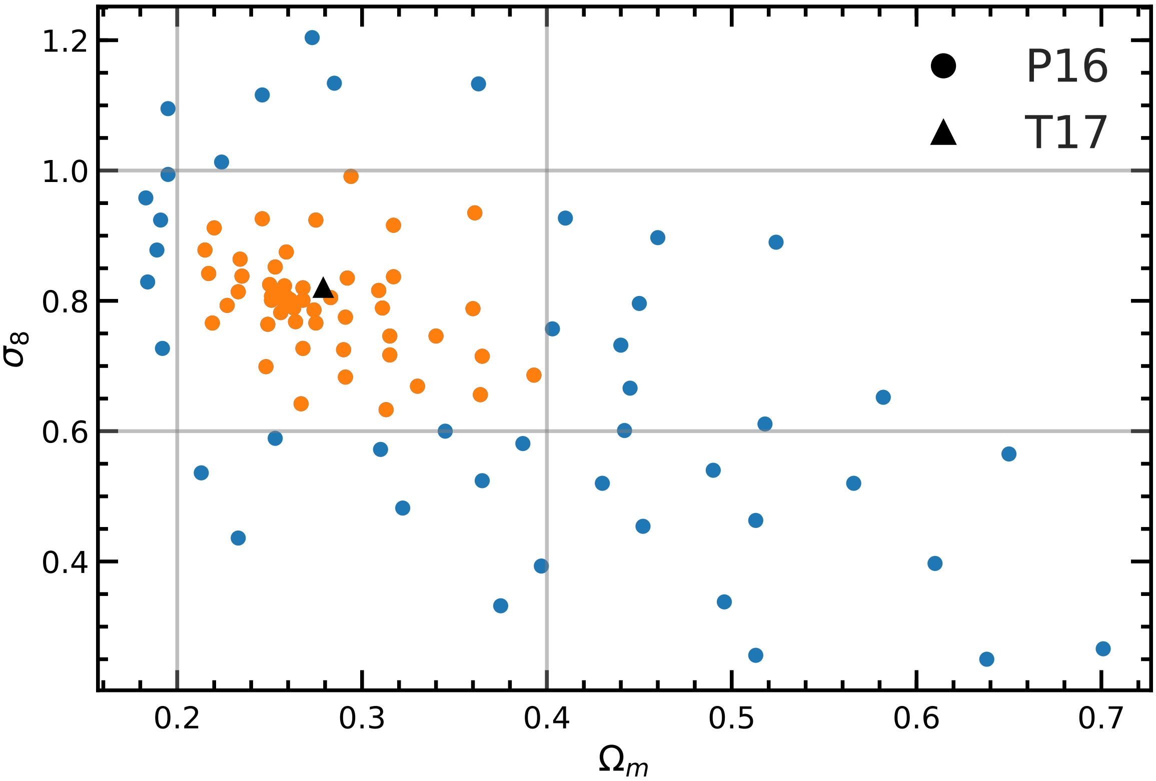

Figure 6.4: The (Ω_m,σ_8) parameter space that is probed with our suite of 96 simulations from Z16. The faded grey lines indicate the cuts that are made to remove extreme cosmological parameters and give the orange points which we use to construct our Ω_m,σ_8 dependant model for 2PCF reconstruction in section 6.4. The black triangle shows the Ω_m and σ_8 values of the T17 simulations.

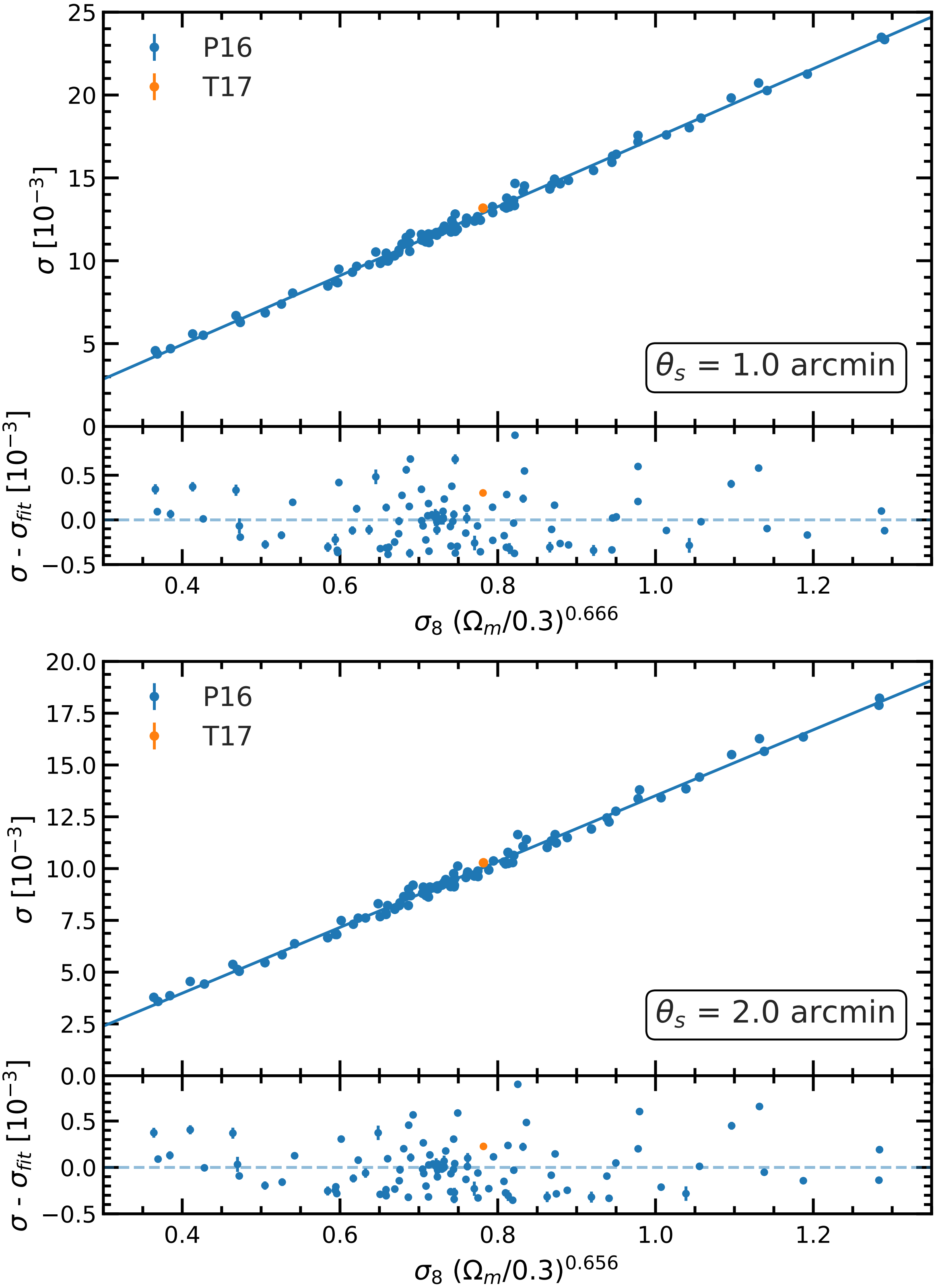

Figure 6.5: The rms fluctuations, σ, of the WL convergence map as a function of $\sigma_8(\Omega_m/0.3)^\alpha$. The power α indicates the degeneracy direction between σ_8 and Ω_m that gives the same rms fluctuations in the convergence field. The blue points correspond to the 96 cosmologies from Z16 (see Fig. 6.4) and the orange point corresponds to the T17 one. The top and bottom panels show the mean σ values for two smoothing scales, $\theta_s = 1$ and 2 arcmin, respectively. The bottom sub-panels show the residuals between the mean σ values and the best fitting line (blue). The vertical bars show the standard errors, which may be underestimated as discussed in Appendix .9.

important to know the degeneracy direction for the physical quantities of interest. Following the usual approach, we define the parameter combination, $\Sigma_8(\alpha) \equiv \sigma_8\,(\Omega_m/0.3)^{\alpha}$, where α characterises the degeneracy for a given statistic (α is allowed to vary for different statistics since they usually do not have exactly identical degeneracy directions). Note that for studying the cosmology dependence we use only the Z16, and not the T17, convergence maps, and the latter is used as a consistency check of the fitted models.

The fittings carried out in this section are mainly to exemplify the cosmology dependence of the self-similar feature present in the 2PCF in Fig. 6.3, which applies only to theoretical (simulated) lensing maps with no noises and with a specific smoothing length. Before this approach can be used for observational constraints, further development will be required, notably the inclusion of galaxy shape noise. We discuss briefly the impact the latter has on the self similarity of the 2PCF in Section 6.6. In order to study the rescaled 2PCF for a range of cosmologies using more realistic noise-added maps, larger simulations for this range of models are required, which we leave to future work.

6.4.1 Convergence rms fluctuation

We describe peaks in terms of the convergence SNR value at their position. To calculate this, we use the root-mean-square (rms) fluctuations, σ, of the convergence field (see e.g. Eq. 6.2.1). In principle, σ is used merely as a normalisation factor and it is not entirely unreasonable to use the same value to define ν across all cosmologies. However, the standard deviation (or rms fluctuation) of the corresponding WL convergence map, σ is a quantity with a clear physical meaning, and hence it is natural to use its correct value for a given cosmology. Therefore, we need a general description of σ as a function of input cosmological parameters, $\sigma = \sigma(\Omega_m, \sigma_8)$. Having this function is also of interest on its own, since it is useful to know how the rms fluctuation of the WL convergence field depends on the cosmological model.

The dependence of the convergence rms fluctuation, σ, on σ_8 and Ω_m is illustrated in Fig. 6.5, where we show the results for two smoothing lengths, $\theta_s = 1$ (left panel) and 2 arcmin (right panel). In both cases we varied α such that σ is well described by a linear function of $\Sigma_8(\alpha)$, that is:

$$\sigma = m\Sigma_8(\alpha) + c \equiv m\sigma_8\left(\frac{\Omega_m}{0.3}\right)^{\alpha} + c\,. \tag{6.4.1}$$

We achieved this by performing a χ^2 minimisation procedure with three free parameters: m, c and α. The best fitting parameter values are: $m = 2.08 \times 10^{-2}$, $c = -3.39 \times 10^{-3}$ and $\alpha = 6.66 \times 10^{-1}$ for $\theta_s = 1$ arcmin and $m = 1.59 \times 10^{-2}$, $c = -2.37 \times 10^{-3}$ and $\alpha = 6.56 \times 10^{-1}$

for $\theta_s = 2$ arcmin. For these fits, we used the standard errors in the determination of σ. These errors are shown in Fig. 6.5 as vertical error bars, however in most cases the error bars are smaller than the size of the data points plotted and are not visible. The bottom panels in Fig. 6.5 show the residuals, i.e., the deviations of the σ values for each cosmology from the best-fitting lines. The fit residuals are small when compared to the absolute values of σ and show no systematic trend with Σ_8, indicating that Eq. (6.4.1) provides an excellent description for both smoothing lengths. In particular, we notice that the best-fit value of α is similar for $\theta_s = 1$ and 2 arcmin, and thus weakly dependent on the smoothing scale,. It is also reassuring to note that T17 is in very good agreement with the best-fitting lines, which are obtained from the Z16 convergence maps only, even though the two sets of maps are constructed from very different simulations.

Even though it is not the main line pursued in this Chapter, we note that the measured standard deviation of the (reconstructed) WL maps is a useful quantity (see, e.g., Van Waerbeke et al., 2013) and therefore a simple fitting formula for σ in terms of Ω_m and σ_8 will be useful both theoretically and observationally. However, because GSN introduces a major systematic uncertainty in real WL maps, it is necessary to study the Eq. (6.4.1) fitting formula using maps in which realistic GSN is included; this is beyond the scope of this study, because the Z16 maps used in the analysis above have relatively small sizes. In this Chapter, instead, the primary use of Eq. (6.4.1) will be to define ν for a convergence map with given Ω_m and σ_8 values.

As shown in Figure 6.5, within the large range of cosmological parameters covered in this study, σ varies strongly, by up to a factor of 5-7. By defining ν relative to the σ of the corresponding model, we are able to define the SNR in different models relative to their own clustering amplitude. The alternative way to is use a constant σ definition, such as the value for a fiducial model or the rms of the typical noise map. However, in our case this would mean comparing the clustering of map pixels with smaller κ values in one model to the clustering of pixels with large κ values in another model, when using the same $\nu_{\rm cut}$, and so a cosmology dependant $\nu_{\rm cut}$ range would have to be applied which is a far more complicated approach. We have explicitly checked by defining the SNR ν in Eq. (6.2.1) using the σ of the fiducial model where $\sigma_8 = 0.8$ and $\Omega_m = 0.3$, and found that the self-similar behaviour still holds though slightly worse than shown here. Later in Section 6.6, when dealing with noisy maps, we shall use the σ measured from the smoothed noisy maps to define the SNR.

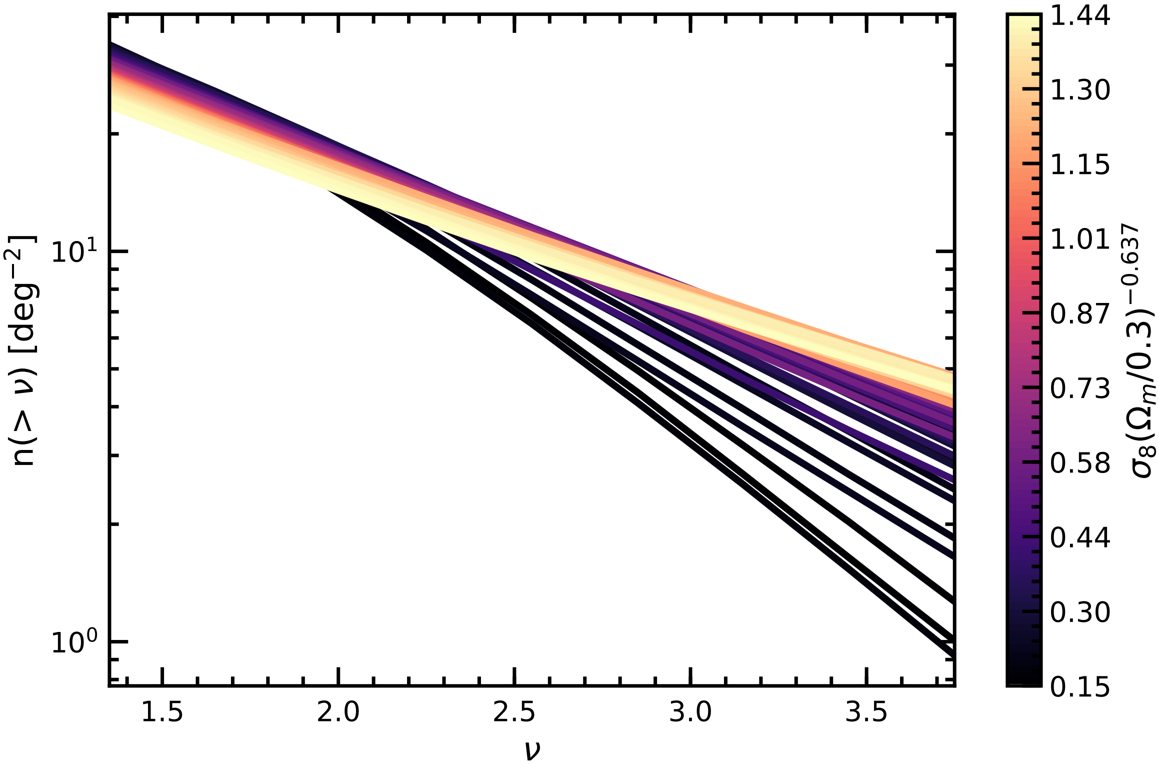

Figure 6.6: The peak abundance, $n(>\nu)$, for the 96 cosmologies from Z16 plotted against ν. The lines are coloured according to a combination of the cosmological parameters Ω_m and σ_8 (see colour bar).

6.4.2 WL peak abundance

The peak abundances for the 96 models in the Z16 simulations are shown in Fig. 6.6. The colour-bar shows the cosmological parameters for a given curve with the form $\Sigma_8 = \sigma_8(\Omega_m/0.3)^{-0.637}$. The spread of the amplitudes of the peak abundances across the 96 cosmologies is up to a factor of two. Most of the curves appear straight, indicating that the peak abundance is well described by a power law. The only exceptions are the black curves with very small values of Σ_8: these curves will be removed in the analysis as they correspond to the extreme cosmological parameter values indicated by the blue points in Fig. 6.4. As Σ_8 increases, the slope of the peak abundance decreases, while its amplitude increases at larger ν ($\nu \gtrsim 2.5$) and decreases for small ν ($\nu \lesssim 2.5$). This 'rotation' of the curves about $\nu \approx 2.5$ as Σ_8 changes implies a correlation between the slope and amplitude of the peak abundances as the cosmological parameters vary, and we shall see shortly that this fact can be utilised to reduce the number of fitting parameters in our peak abundance model.

In the range $1.5 < \nu_{\rm cut} < 3.5$, the peak abundance as a function of ν is well described by the power-law,

$$\log n(>\nu) = B_n\nu + A_n, \tag{6.4.2}$$

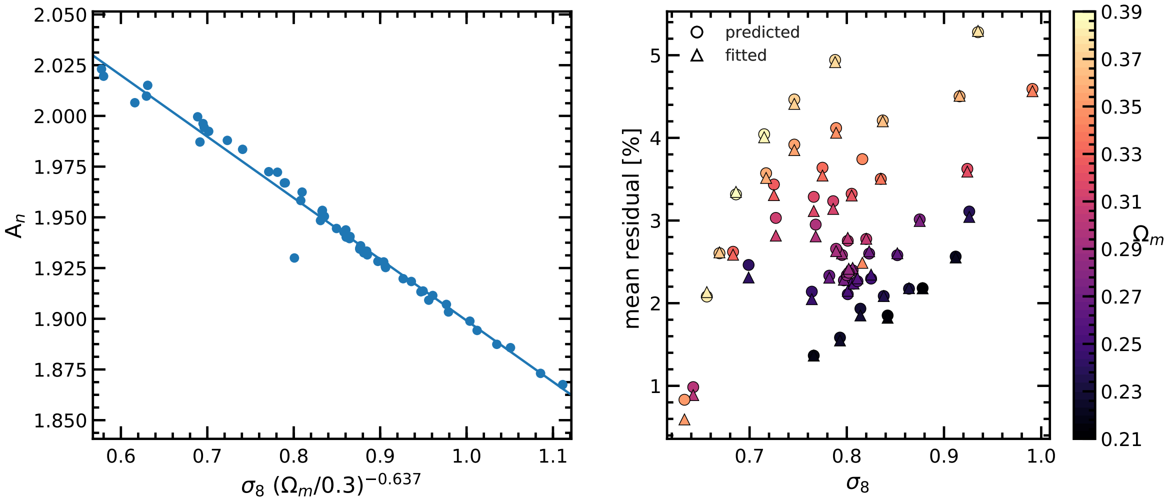

Figure 6.7: *Left panel:* the dependence of A_n, which is the one parameter fit to the peak abundance (see Eq. 6.4.3), on a combination of σ_8 and Ω_m parameters. The exact combination is $\sigma_8(\Omega_m/0.3)^{-0.637}$, where the power represents the degeneracy direction between σ_8 and Ω_m that gives the same A_n value. The blue line shows the best fitting linear function (see Eq. 6.4.5). *Right panel:* the triangle symbols show the percentage residuals of the one parameter power law fit to the peak abundance. The circle symbols show the extent to which our model can predict the peak abundance. The model works in two steps: i) use the blue solid line shown in the left panel to predict A_n for a pair of σ_8 and Ω_m values, and ii) given A_n, infer the peak abundance using Eq. (6.4.3). The various symbols are coloured according to the Ω_m cosmological parameter (see colour bar on the right).

in which the fitting parameters A_n and B_n depend on the input cosmology.

In order to model $A_n = A_n(\Omega_m, \sigma_8)$ and $B_n = B_n(\Omega_m, \sigma_8)$, we fit Eq. (6.4.2) to the peak abundance for each of the cosmological models indicated by the orange points in Fig. 6.4. The fitting results confirm that A_n and B_n – which respectively characterise the amplitude and slope of the peak abundance – are strongly correlated, so that B_n can be replaced with a function of A_n, $B_n(A_n)$, and the peak abundance can now be described using a one-parameter power law of the form

$$\log n(>\nu) = \nu B_n(A_n) + A_n, \tag{6.4.3}$$

with

$$B_n(A_n) = -0.33 A_n + 0.28. \tag{6.4.4}$$

This indicates that a universal model for WL peak abundance that works for a wide range of cosmological models can be obtained if one can fit the cosmology dependence of the single parameter A_n. The result is shown in the left panel of Fig. 6.7, where the A_n values measured from the 96 Z16 cosmologies are plotted against $\Sigma_8(\alpha)$ with $\alpha = -0.637$. The value of α corresponds to the one for which A_n is well fitted by a linear function of $\Sigma_8(\alpha)$. The latter is shown as the solid line in the left panel of Fig. 6.7, and is given by

$$A_n = -0.30\,\sigma_8(\Omega_m/0.3)^{-0.637} + 2.20\,. \tag{6.4.5}$$

For fitting the above equation the errors in A_n are given by the uncertainties of fitting Eq. (6.4.4) to the peak abundance. These errors are small and are not visible in Fig. 6.7 since they are smaller than the symbol size. We note that there is an outlier in this panel. We have checked the corresponding convergence maps and have not found an explanation for this outlier.

Eqs. (6.4.3)-(6.4.5) can be used to predict the peak abundance for any input Ω_m and σ_8 values. For this, we first use Eq. (6.4.5) to calculate A_n for given (Ω_m, σ_8), and then infer $n(>\nu)$ using Eq. (6.4.4). The accuracy of this prediction is shown by circle symbols in the right panel of Fig. 6.7. We quantify the success of the method in terms of the mean percentage residual, which is defined as the absolute value of the fractional difference between the measured peak abundance and the predicted one, averaged over all bins in $\nu \in [1.5, 3.5]$. We find a mean percentage residual of $1-5$ percent, indicating that the model performs well. To understand what is the major factor affecting the model accuracy, we also calculate the mean percentage residual between the measured $n(>\nu)$ and the direct one-parameter power-law fit to it, which is shown as triangles in the right panel of Fig. 6.7. There is only a very slight difference between the triangles and the circles, with the former being generally lower. This indicates that our prediction of the peak abundance is very similar in accuracy to the original fit, which is further supported by the fact that the blue line in the left panel fits the various A_n data points rather well. In summary, our model is able to predict the peak abundance to within ∼3 percent accuracy for most of the chosen cosmological models.

If we use the original form of the power law, Eq. (6.4.2), to model the peak abundance, with the two parameters, A_n and B_n, both left to vary freely in the fitting, we get fits and predictions that match the raw data at the sub percent level. However, in attempt to minimise the number of parameters in our model we chose the one parameter power law, Eq. (6.4.3), at the cost of roughly a 2% loss in accuracy.

6.4.3 Peak two-point correlation functions

We now move on to check whether peak 2PCFs display the self-similar behaviour described in Section 6.3.3 for a wide range of cosmological models. The result is shown in Fig. 6.8, where we plot the rescaled 2PCFs for all the pairs of (Ω_m, σ_8) values of the Z16 maps (96

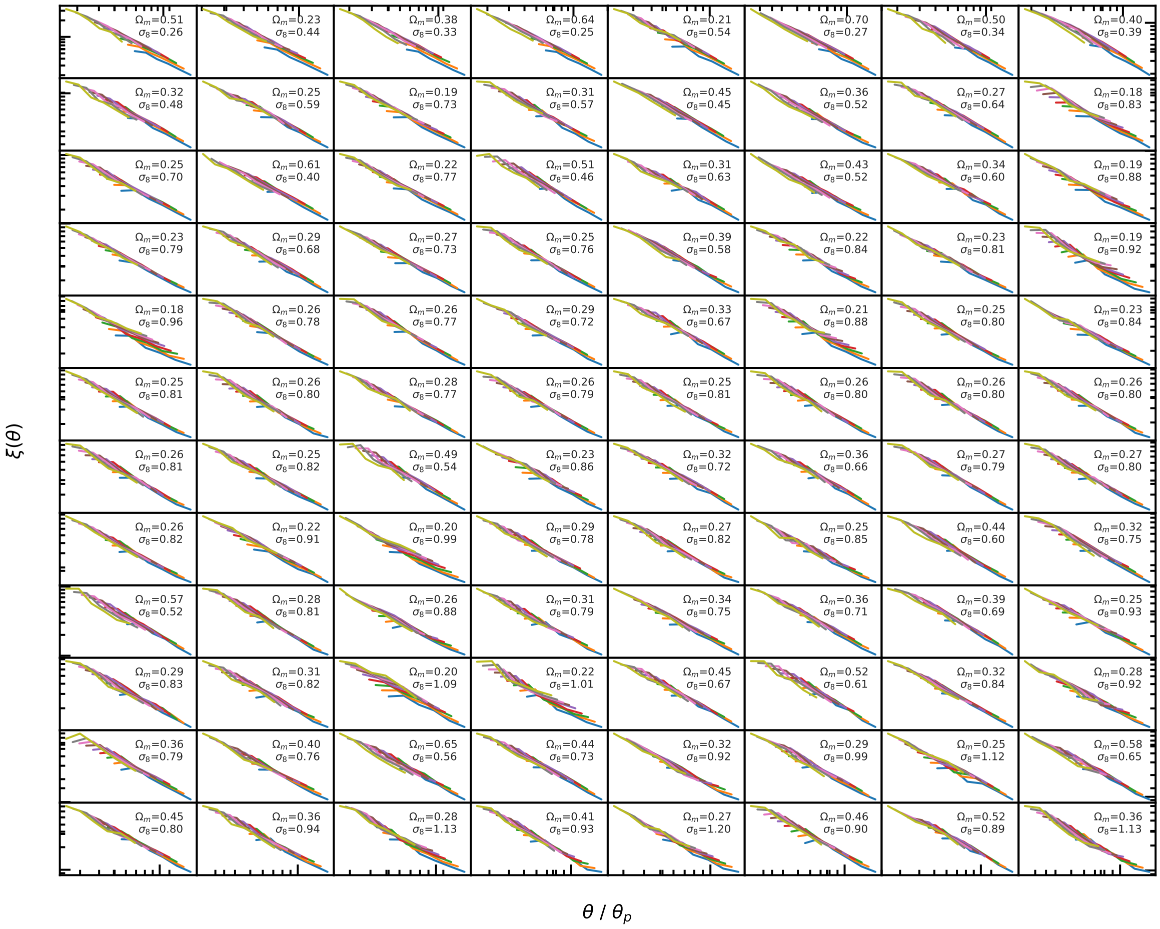

Figure 6.8: The rescaled 2PCFs as a function of θ/θ_p for various cosmological models. Each panel corresponds to a pair of (Ω_m, σ_8) parameters (see labels in each panel). The lines in each panel correspond to peak catalogues with different $\nu_{\rm cut}$ thresholds, with $\nu_{\rm cut}$ varying from 1.5 to 3.5 in $\Delta\nu_{\rm cut} = 0.25$ increments. We find that all cosmologies have self-similar 2PCFs for peak catalogues with $\nu_{\rm cut} \in [1.5, 3.5]$. The x- and y-axis amplitudes of each sub-panel have been normalised to their respective centers to highlight the presence of the rescaled self-similarity across all of the Ω_m, σ_8 models. For this reason, axis labels are not included to avoid overcrowding.

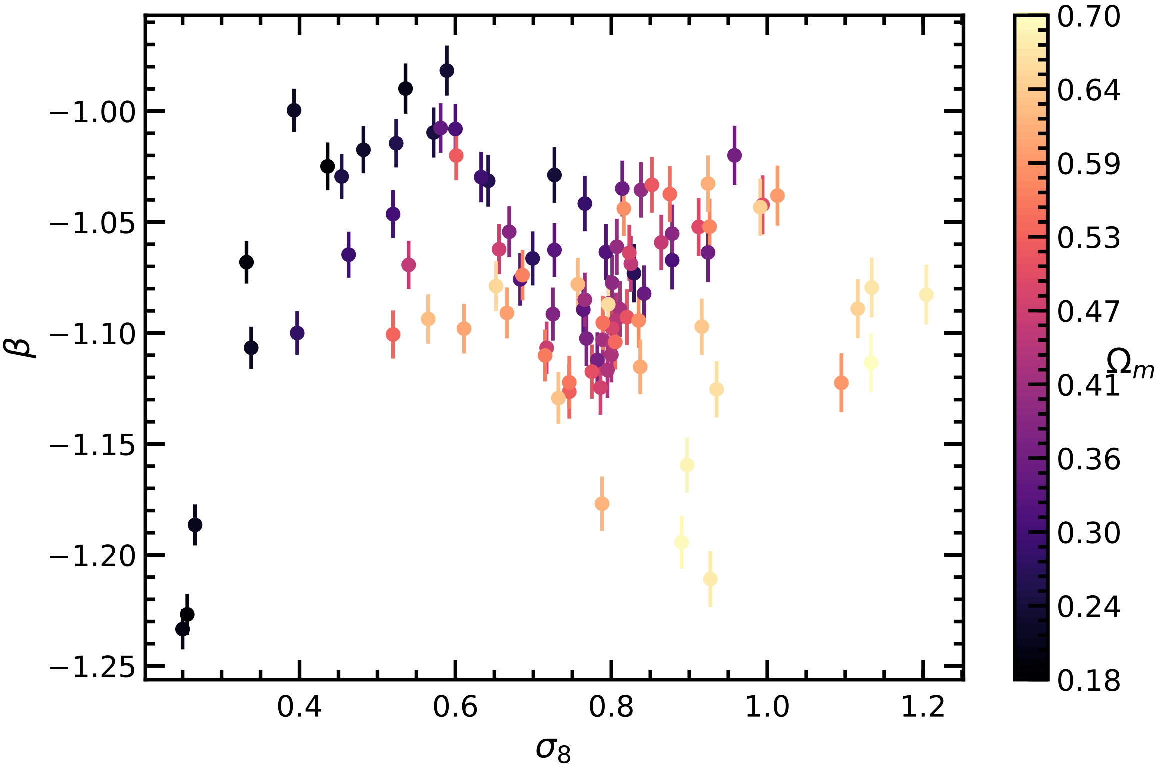

Figure 6.9: The gradient, β, of the power laws fitted to each of the rescaled self-similar 2PCFs in Fig. 6.8 plotted against the σ_8 of the respective model with the associated Ω_m value given by the colour-bar. The vertical bars show the uncertainties in determining β.

models in total). The re-scaled 2PCFs are normalised to the center of the panels to exemplify the self-similar behaviour. Fig. 6.8 illustrates that the self-similarity of the 2PCFs is indeed robust against the change of cosmological parameters σ_8 and Ω_m. The parameter space in Figs. 6.4 and 6.8 is much larger than what is allowed by current constraints. Thus a model describing this self similarity will not only have the potential to provide additional cosmological constraints, but can also be applied to scenarios where predictions for a large parameter space is required, such as generating training sets for machine learning algorithms.

Fig. 6.8 also shows that the rescaled 2PCFs are well described by power laws which have very similar slopes across all cosmological models. To be more quantitative, we have fitted the following power-law function,

$$\xi = \xi_0 \left(\frac{\theta}{\theta_p} \right)^{\beta}, \tag{6.4.6}$$

to the curves in each of the panels, with each data point weighted by its standard error (see Appendix .9 for details about the error calculation). The best-fitting slope, β, as a function of cosmological parameters is shown in Fig. 6.9, where the horizontal axis shows σ_8 while the colour of the points indicates the Ω_m value. The scatter of the points in Fig. 6.9 does not follow any clear trends, and combinations of σ_8 and Ω_m in the form of $\sigma_8(\Omega_m/0.3)^{\alpha}$,

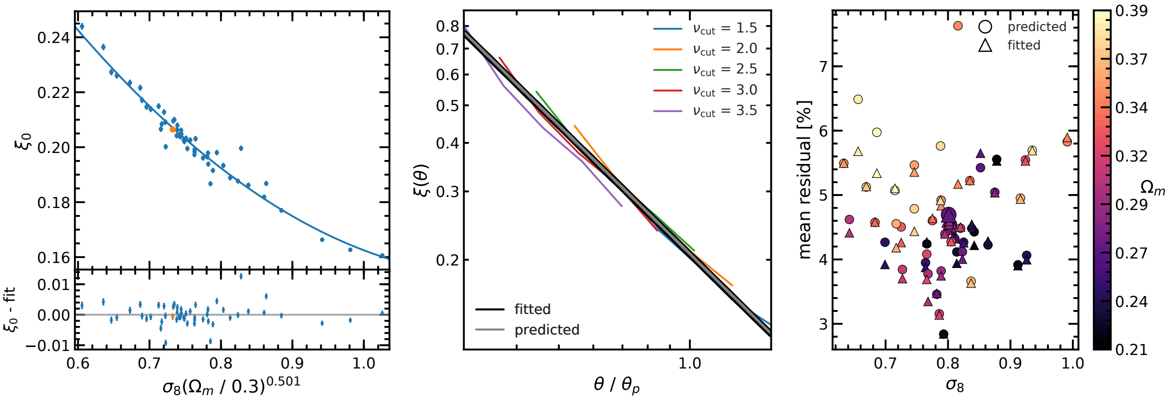

Figure 6.10: *Left panel:* the amplitude parameter of the power-law best fitting the rescaled 2PCFs as a function of σ_8 and Ω_m. Each blue point shows the amplitude for a pair of (σ_8, Ω_m) values and the solid line shows the best fitting quadratic function. *Middle panel:* an example of the rescaled 2PCF for different $\nu_{\rm cut}$ values and and its best fitting power law (black line). The solid grey line shows our reconstructed power law, which was calculated using the best fitting line from the left panel. *Right panel:* the percentage residuals between the fitted power law and the data (triangles), and between the reconstructed power law and the data (circles). The x-axis (σ_8) and the colour-bar (Ω_m) indicate the cosmology of the model for which the residuals are being measured.

where α is allowed to vary, does not to lead to improvements in the correlation between β and the input cosmology. In Fig. 6.9 we find that the mean value across the entire sample is $\beta \approx -1.1$. As such, for simplicity, we take $\beta = -1.1$ as the power-law slope of the rescaled 2PCF (we have checked that the results are not particularly sensitive to the value of β).

On the other hand, we find that the amplitude of the rescaled peak 2PCFs, $\xi_0 = \xi_0(\Omega_m, \sigma_8)$ in Eq. (6.4.6), shows a systematic dependence on the cosmological parameters. Therefore, in order to have a complete description we also need to model $\xi_0(\Omega_m, \sigma_8)$. The fitting result for ξ_0 for the selected cosmological models (orange points in Fig. 6.4) is displayed in the left panel in Fig. 6.10, where it is plotted against $\sigma_8(\Omega_m/0.3)^{0.501}$ with the index $\alpha = 0.501$ characterising the degeneracy direction between Ω_m and σ_8 for the rescaled 2PCF amplitude ξ_0. The value 0.501 is tuned such that the data points on the left panel of Fig. 6.10 are fitted using a smooth quadratic curve with the lowest χ^2. This is shown as the blue solid line in the left panel of Fig. 6.10, which takes the form

$$\xi_0 = \xi_{0,a} x^2 + \xi_{0,b} x + \xi_{0,c}\,, \tag{6.4.7}$$

where

$$\xi_{0,a} = 0.253\,, \qquad \xi_{0,b} = -0.605\,, \qquad \xi_{0,c} = 0.514\,, \tag{6.4.8}$$

and $x = \sigma_8(\Omega_m/0.3)^{0.501}$. The lower sub-panel of the left panel shows the residual between the measured amplitude ξ_0 and its fitted values. The residuals show no systematic trends with varying $\sigma_8(\Omega_m/0.3)^{0.501}$, indicating that the fitting function works equally well for all cosmologies.

In the middle panel of Fig. 6.10 we have randomly selected one of the cosmologies from the Z16 maps, and compared the rescaled 2PCFs at several $\nu_{\rm cut}$ values between 1.5 and 3.5 (coloured lines), the power-law fit to these rescaled 2PCFs (black solid line, which we call the 'fitted' curve), and the predicted rescaled 2PCF for this particular cosmology (the grey straight line, which we call the 'predicted' curve). The latter was obtained by calculating ξ_0 using Eq. (6.4.7), and then inferring the 2PCF from Eq. (6.4.6). This matches the original fitted power law very closely, indicating that the model described by Eqs. (6.4.6) and (6.4.7) works very well.

We next quantify the accuracy of our prediction for the rescaled 2PCF. For a given cosmological model, such as the one shown in the middle panel of Fig. 6.10, we calculate the residuals, i.e., the fractional differences of the 'fitted' and 'reconstructed' curves with respect to the rescaled measured 2PCFs. This is done for each of the five $\nu_{\rm cut}$ values shown in Fig. 6.10, and we define the mean residual as the average over all θ/θ_p bins and all $\nu_{\rm cut}$ values. The mean residuals for the fitted and predicted curves are respectively shown by a large triangle and a large circle in the right panel of Fig. 6.10. We have repeated this procedure for all the cosmological models and have plotted their residuals in the right panel, with the associated σ_8 values shown in the x-axis and Ω_m values shown by the colour bar to the right. We find that the model prediction is almost as accurate as the direct fitting, and is able to match the rescaled 2PCFs at about 5% accuracy level. The large symbols in the right panel correspond to the model shown in the middle panel, to give a visual illustration about how well the 2PCF model in Eqs. (6.4.6, 6.4.7) works for an 'average' cosmology for which the mean residual is 4.8%.

6.5 A pipeline for 2PCF Reconstruction

We can combine the models developed in the previous section for the convergence rms fluctuation, peak abundance and rescaled peak 2PCF, to develop an integrated pipeline that allows us to predict the (un-rescaled) peak 2PCFs, $\xi(\theta)$, as a function of $\nu_{\rm cut}$. The procedure is schematically illustrated in Fig. 6.11 and outlined as follows:

1. For chosen Ω_m and σ_8 values, one can use the models to predict the peak abundance

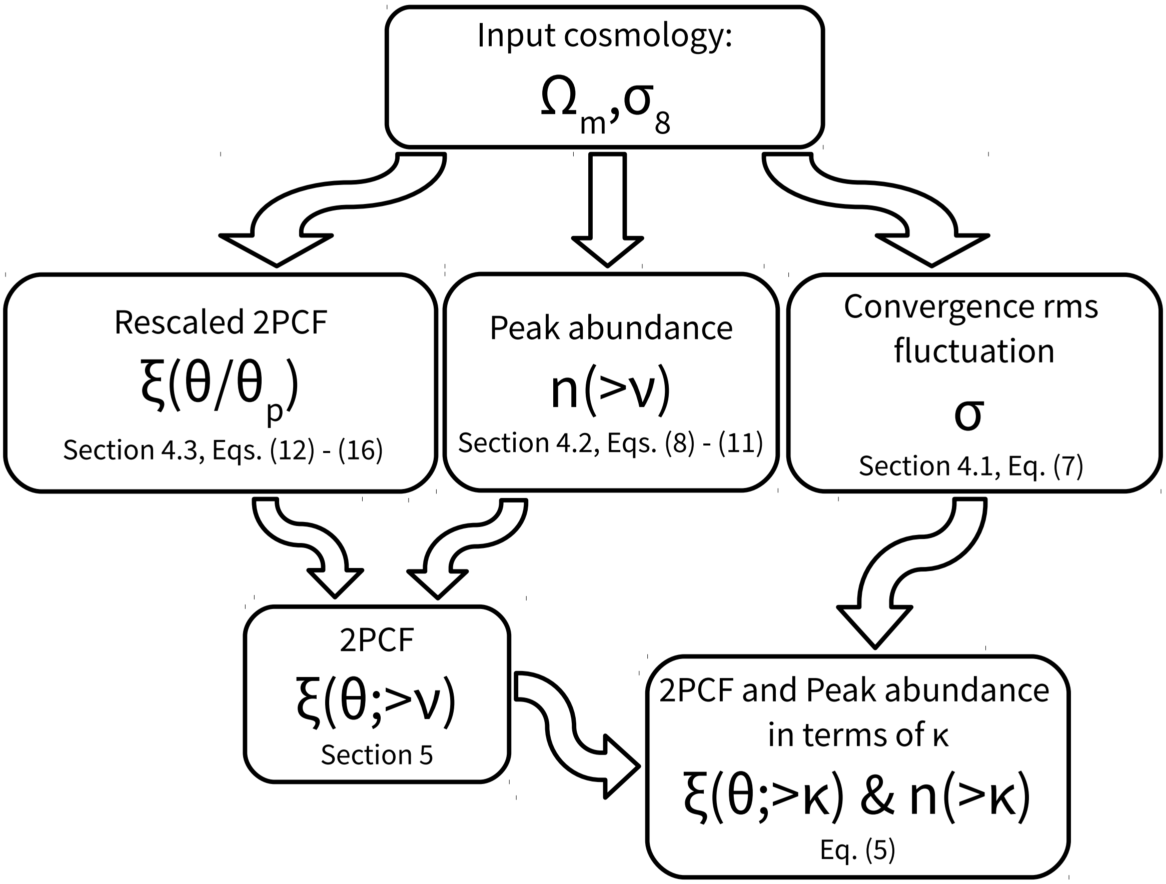

Figure 6.11: This flowchart describes the pipeline our model uses to reconstruct the peak 2PCF by exploiting its self similarity. First we take input cosmological parameters, Ω_m and σ_8, which our model uses to predict the rescaled 2PCF, the peak abundance and the rms fluctuations of the convergence map. These statistics can then be combined to give the original 2PCF for peaks of different heights, expressed in terms of either ν or κ.

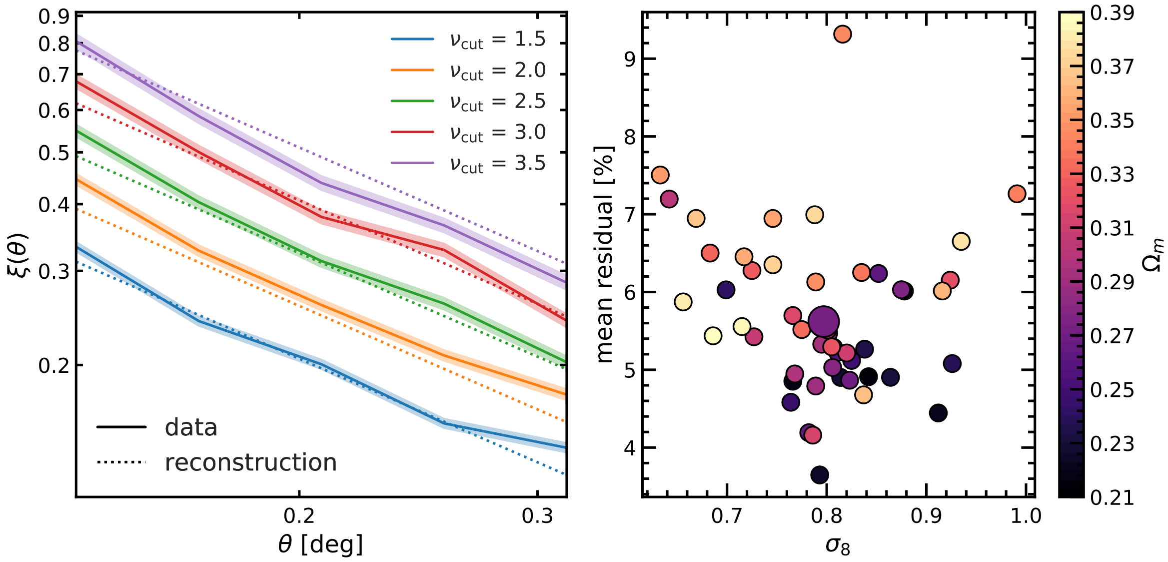

Figure 6.12: *Left panel:* Reconstructed 2PCFs from our model (dashed) compared to measured 2PCFs from N-body simulations (solid), for peak catalogues with $\nu_{\rm cut} \in [1.5, 3.5]$. *Right panel:* Mean percentage residuals between the reconstructed and measured 2PCFs. The larger symbol indicates the example model that is shown in the left panel. The x-axis and colour-bar indicate the σ_8 and Ω_m values of the models respectively.

(Section 6.4.2) and the rescaled 2PCF (Section 6.4.3).

2. These two statistics are combined, using $\theta_p = 1/\sqrt{n(>\nu_{\rm cut})}$, to give the 2PCF, $\xi(\theta)$, for peak catalogues with $\nu_{\rm cut} \in [1.5, 3.5]$.
3. If needed, the above-predicted peak abundance and 2PCFs can then be expressed in terms of κ by using the $\sigma(\Sigma_8)$ fit in Section 6.4.1.

This pipeline offers a simple apparatus to make predictions of the one- and two-point statistics for intermediate ($\nu \in$ [1.5,3.5]) WL peaks, which can be used (on its own or together with other cosmological probes) to constrain the parameters (σ_8, Ω_m) using observational data. It will be interesting to see if these new statistics are complementary to other probes, such as the shear-shear correlation, when constraining (Ω_m,σ_8), but this will be left for future follow up works, with the peak 2PCF specifically studied in the next Chapter. In the next section we will discuss further aspects which need to be checked before applying this method.

As a proof of concept, we show an example of this 2PCF reconstruction pipeline in the left panel of Fig. 6.12. The solid curves show the 2PCFs measured from the simulation data for an arbitrarily selected cosmology, with shaded regions showing the (under) estimated standard error (see Appendix .9 for more detail). The dashed lines show the predictions by our 2PCF reconstruction pipeline. We find a reasonably good agreement between the simulated and reconstructed 2PCFs, with the latter mostly lying within or just outside the (under)estimated errors bars. The second panel in Fig. 6.12 shows the mean percentage difference between the reconstructed and measured 2PCFs, averaged over the 5 plotted 2PCFs and all θ bins with $\nu_{\rm cut} \in [1.5, 3.5]$ separated by a $\Delta\nu_{\rm cut} = 0.5$ increment. The model that has been selected to exemplify the reconstruction is indicated by the large symbol in the left panel of Fig. 6.12, which is an "average" one in terms of the performance the reconstruction (there are many models for which the reconstruction works better). We can see that for all of the selected cosmologies, our model is able to predict the 2PCF to within a roughly 6% uncertainty on average. Relative to the estimated errors bars, the quality of our reconstruction is reasonably good.

We find that generally the amplitude of the 2PCFs is overestimated for the larger $\nu_{\rm cut}$ catalogues. This could be a fundamental aspect of the 2PCF evolution, however due to small map sizes and low peak number densities (at approximately 7 deg^{-2}) it is likely that 2PCFs with $\nu > 3.5$ are biased. The true amplitude of the 2PCFs with larger $\nu_{\rm cut}$ could be measured more accurately with larger weak lensing maps, which we leave to further study.

6.6 The impact of galaxy shape noise

Up to here, we have discussed the WL peak abundance and 2PCF in a theoretical context with the aim of having a model that allows us to accurately describe and predict these statistics in an idealised situation. Whilst this theoretical model can have useful applications in, e.g., mock WL peak catalogue generation, to be more useful for cosmological constraints, we need to investigate the self similarity of the 2PCF in more realistic situations. One of the things we have not included in our analysis so far is galaxy shape noise (GSN).

GSN is a source of uncertainty in WL observations, where the measured ellipticity of galaxies is dominated by their random orientation, and only weakly correlated due to gravitational lensing on scales much larger than the galaxy-galaxy separation. Observations of cosmic shear, and therefore cosmic convergence, is contaminated by this noise. One usually uses large smoothing lengths to suppress this noise in order to recover statistics more reliably. However, large smoothing lengths could either dampen the amplitude of the measured statistics, which is evident from the decrease of the WL peak abundance with increasing smoothing scales in Fig. 6.2, or increase the noise in the measurements, which can be seen to a small extent in the 2PCFs for different smoothing lengths in Fig. 6.3. Therefore, a trade-off has to be struck between using a large enough smoothing length in order to suppress the galaxy shape noise,

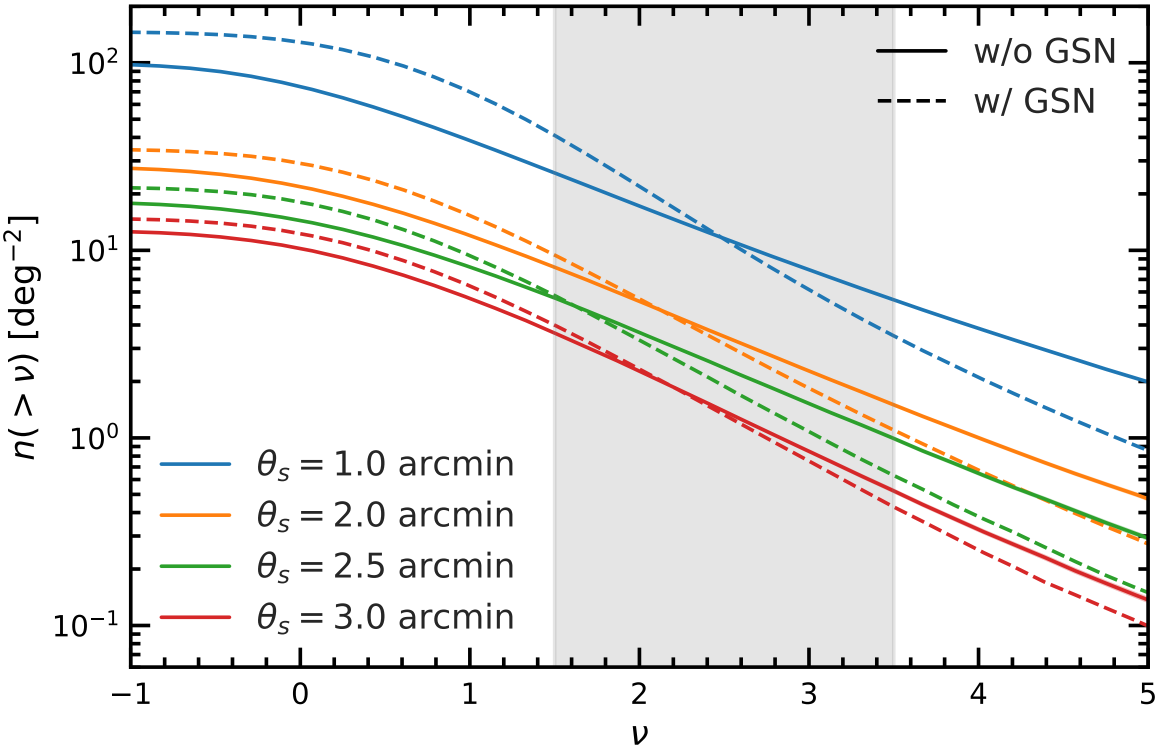

Figure 6.13: Weak lensing peak abundances for four smoothing scales, $\theta_s = 1.0$, 2.0, 2.5 and 3.0 arcmin (see labels), for peaks extracted from convergence maps without GSN (solid) and for peaks extracted from convergence maps with added GSN (dashed). Here the added GSN matches LSST specifications ($\sigma_{\rm int} = 0.4$, $n_{\rm gal} = 40$ arcmin^{-2}).

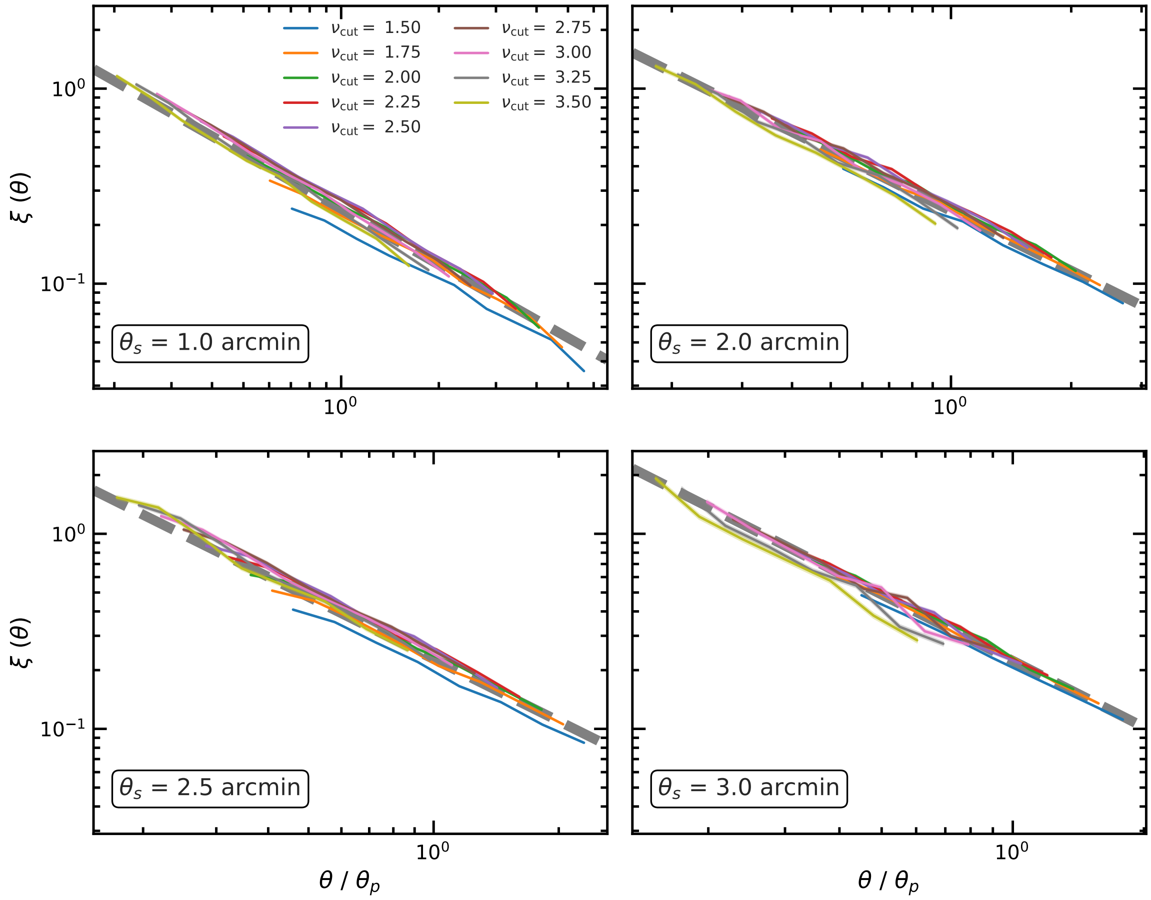

Figure 6.14: Rescaled 2PCFs for four smoothing scales, θ_s = 1.0, 2.0, 2.5 and 3.0 arcmin (see label in each panel), for peak catalogues extracted from convergence maps with added GSN that matches LSST specifications ($\sigma_{\rm int} = 0.4$, $n_{\rm gal} = 40$ arcmin^{-2}). The various solid coloured lines correspond to peak catalogues with different $\nu_{\rm cut}$ thresholds (see legend in the upper left panel), with $\nu_{\rm cut} \in [1.5, 3.5]$ incremented in steps $\Delta\nu_{\rm cut} = 0.25$. The grey thick dashed lines show the fits to the rescaled 2PCFs for the same smoothing scales but without GSN.

and not over smoothing so that interesting statistics are not suppressed more than they need to be. With convergence maps from N-body simulations, we can test the difference in the peak abundance and 2PCF for cases with and without GSN for a range of smoothing lengths.

For this section, we include GSN in the T17 convergence maps that match LSST specifications by adding to each pixel within a map random values drawn from a Gaussian distribution with a standard deviation $\sigma_{\rm pix}$ given by Eq. (1.2.15). To match LSST specification we use $\sigma_{\rm int} = 0.4$ and $n_{\rm gal} = 40$ arcmin^{-2} (LSST Science Collaboration et al., 2009)

After GSN is added to the pixels, we smooth the maps, identify peaks in the noise-added smoothed WL maps using Eq. (6.2.1) with σ also directly measured from the noisy maps, recalculate the peak abundance and peak 2PCFs, and compare these statistics to the case with no GSN, with the same smoothing.

The impact of GSN on the WL peak abundance is shown in Fig. 6.13, where the solid and dashed lines respectively correspond to peaks identified in WL maps with and without GSN. Here we study four smoothing scales, $\theta_s = 1$, 2, 2.5 and 3 arcmin. In each instance, ν is defined relative to the WL map in which the peaks are identified, so for the GSN added case, σ in Eq. (6.2.1) includes contributions to the rms fluctuations from both GSN and the underlying convergence signal, while for the no GSN case ν is defined by taking σ as the rms convergence fluctuation.

For all smoothing lengths, by adding GSN, the peak abundance increases at low ν and decreases at high ν, with a crossover between $\nu = 1.5$ and 2.5 depending on the smoothing scale. GSN has the largest impact on the peak abundance for the smallest smoothing length, while for larger θ_s the agreement between the peak abundances in the GSN and no GSN cases is better, although substantial difference remains even in the case of $\theta_s = 3$ arcmin. This means that the fitting formulae, Eqs. (6.4.3, 6.4.4), which describe the cosmology dependence of peak abundance, need to be recalibrated by using peaks extracted from GSN-added maps. Due to the small size of the Z16 WL maps, this will be left as future work when larger simulations of different cosmologies are available.

Note that in Fig. 6.13 the peaks are defined using Eq. (6.2.1), where σ is the total rms convergence that includes contributions from the physical rms convergence and from the rms of noise. This explains the crossover mentioned above: because σ is increased, for the high peaks their ν values actually decrease, and the number of such high peaks does not increase quickly enough to maintain $n(<\nu)$ at large ν, which causes the latter to drop compared with the no GSN case. We have explicitly checked (not shown here) that, if one defines ν in

Eq. (6.2.1) by using the same σ for the GSN and no GSN cases, then the peak abundance is consistently higher in the former case, due to artificial peaks created by noise.

In order to closely inspect the impact of using different smoothing lengths on the self similarity of the rescaled 2PCFs, we have tried four different θ_s values, respectively $\theta_s = 1$, 2, 2.5 and 3 arcmin. The results are shown in Fig. 6.14, where the peaks are all identified from, and the σ used to define the SNR ν are all measured by using, the smoothed noisy maps. Interestingly, we find that the rescaled 2PCFs are still on top of each other for all four smoothing lengths. With $\theta_s = 1$ arcmin, the agreement between the rescaled 2PCFs is weaker, where only the curves with $2 \leq \nu_{\rm cut} \leq 3.5$ appear to be self similar. For 2 arcmin smoothing the 2PCFs appear to be self similar in the entire $1.5 \leq \nu_{\rm cut} \leq 3.5$ range, and shows that the self-similarity of 2PCFs is robust against GSN. With 2.5 arcmin smoothing the overall self similarity appears to be tighter, however the $\nu_{\rm cut} = 1.5$ appears to be outside the self similar range. Finally, for 3 arcmin smoothing we see that the self similarity of the 2PCFs holds up to $\nu_{\rm cut} = 3$, after which the rescaled 2PCFs drop off in amplitude. It is possible that this drop in amplitude is caused by the small map size (10×10 deg^2) and low number density of tracers (≈ 0.5 deg^{-2}), rather than a breakdown of the self similarity. As θ_s increase it also appears that the overall gradient of the rescaled 2PCFs decreases.

Having verified that the 2PCFs remain self similar in the presence of GSN, next we want to see how including the latter affects the power law of the rescaled self-similar peak 2PCFs. In each subpanel of Fig. 6.14, we have overplotted, as the grey dashed lines, the best-fit power-law functions for the rescaled 2PCFs of the peaks extracted from the T17 maps smoothed using the same θ_s values but without adding GSN (the grey dashed lines in the top two panels of Fig. 6.14 are the same as the black dashed lines in Fig. 6.3). The two cases are in good agreement for all four smoothing scales, which shows that the impact of GSN on the rescaled 2PCF is minor. This is a nice property, since it indicates that GSN will not significantly contaminate the underlying cosmology dependence of the rescaled 2PCF if the same observation applies to other cosmologies. However, due to the limited map size from Z16 we leave this investigation to future study.

In short, we conclude that the prevalence of the self similarity in the 2PCFs for peaks extracted from GSN-added WL maps shows that this feature is robust to this observational systematic, and therefore has the potential to be used in cosmological constraints.

6.7 Discussion and Conclusions

In this Chapter, we have investigated the one- and two-point statistics for intermediate peaks, with SNR values $\nu \in [1.5, 3.5]$, from weak lensing convergence maps. These WL peaks contain useful information about the LSS formation, and the analyses of them are expected to place complementary constraints on the cosmological model. However, unlike high peaks, the intermediate WL peaks are not individually associated to the most massive dark matter structures, making the modelling of their statistical properties more challenging. To overcome this difficulty, we rely on WL convergence maps constructed from a large number of N-body simulations with varying cosmological parameters and technical specifications, to attempt to find patterns of the peak statistics and their cosmology dependence. Our main findings are summarised as follows:

- The rms fluctuation of WL convergence, σ, has a linear dependence on a particular combination of Ω_m and σ_8 via $\sigma_8\,(\Omega_m/0.3)^\alpha$, with the parameter α weakly dependent on the smoothing length of the convergence map, cf. Fig. 6.5. This linear dependence is given in Eq. (6.4.1), and highlights a universal behaviour within ΛCDM which may be exploited to make cosmological constraints.

- A universal one-parameter power law function is found, which can describe the WL peak count for $\nu \in [1.5, 3.5]$ with an accuracy of within $\approx$ 1-5%, for a large range of Ω_m and σ_8 values, cf. Fig. 6.2 and Eq. (6.4.3). The accuracy of the power-law description of the peak abundance can reach the sub-percent level if two free parameters are used in the power-law function.

- A self-similar behaviour of the WL peak 2PCF has been found by rescaling the angular separation, θ, between a pair of peaks by the mean inter-peak separation, θ_p. While the amplitude of the original 2PCF increases with $\nu_{\rm cut}$, the rescaled 2PCFs for $\nu_{\rm cut} \in [1.5, 3.5]$ lie on top of each other cf. Fig. 6.3.

- This self-similar behaviour holds for a very wide range of (Ω_m, σ_8) values, and we find a simple quadratic dependence of the amplitude of the rescaled 2PCFs on $\sigma_8\,(\Omega_m/0.3)^\alpha$, while the slope of the rescaled 2PCFs have negligible dependence on Ω_m and σ_8, cf. Figs. 6.8, 6.9 and 6.10. A fitted model to predict the peak 2PCF for any chosen Ω_m and σ_8 is given in Eq. (6.4.6).

- A pipeline is developed which combines the above three fitted models, for the convergence rms fluctuation, WL peak abundance and rescaled peak 2PCF respectively, to predict the raw peak 2PCF $\xi(\theta; \nu_{\rm cut})$ for $\nu_{\rm cut} \in [1.5, 3.5]$ and any given Ω_m and σ_8 with good accuracy, cf. Fig. 6.12.

- We found that the self similarity of the peak 2PCF holds in the presence of galaxy shape noise and larger smoothing lengths, cf. Fig. 6.14.

The most important application of the results presented in this Chapter is in constraining the Ω_m and σ_8 cosmological parameters. As demonstrated above, the pipeline integrating the models for WL peak abundance and self-similar rescaled 2PCFs is able to reconstruct the raw, unrescaled, peak 2PCFs for various $\nu_{\rm cut}$ values with a typical accuracy of better than 6%. Furthermore, we have seen that the WL peak abundance and 2PCFs depend on very different combinations of Ω_m and σ_8, one with $\sigma_8\,(\Omega_m/0.3)^{-0.638}$ and the other $\sigma_8\,(\Omega_m/0.3)^{0.501}$. This indicates that a simultaneous use of these statistics already holds the potential of breaking the degeneracy between Ω_m and σ_8 before including other cosmological probes. Marian et al. (2013) found that the 2PCFs of high WL peaks only provide weakly complementary constraints on (Ω_m,σ_8) when combined with the peak abundance. In this Chapter we investigate the 2PCFs of WL peaks with intermediate heights and above, as well as combining the 2PCFs from multiple peak catalogues in the form of a rescaled 2PCF described by a single power law. The powerlaw describing the rescaled 2PCF may be more sensitive to cosmology than the 2PCF of high peaks.

We note that the degeneracy direction of the peak abundance of intermediate height peaks, which are studied in this Chapter, are very different to that of low and high peaks, which has also been observed in Liu et al. (2015) and explained in Yang et al. (2011). Therefore, using the counts of intermediate height peaks may be complementary to using the full peak abundance and could aid in breaking the Ω_m and σ_8 degeneracy.

Another potential application of our results is the generation of mock WL peak catalogues. For a given input cosmological model, the pipeline can be used to predict the WL peak counts and 2PCFs as described above. Random realisations of peaks can then be generated with the peaks arranged such that they have the desired number density and spatial clustering. One technique to do this is point process (see, e.g., Öztireli & Gross, 2012, for some recent progress and applications). This is a Monte Carlo approach where a candidate point (e.g., a WL peak) is placed in a field, which is accepted if its inclusion into the field pushes the measured 2PCF closer to the input one, and rejected otherwise. Point process is a well-developed and widely-used technique to generate point catalogues. In the WL peak case, the situation is slightly more complicated, because the generated catalogue should have peaks of different SNR (or ν values), which simultaneously have the desired 2PCFs at different $\nu_{\rm cut}$ values. We expect that the good agreement between the rescaled peak 2PCFs will prove useful in dealing with this issue, though a detailed investigation into this interesting question will be left for a future work. The fast generation of mock WL peak catalogues can be used for evaluating covariance matrices and studying other cosmological quantities, such as voids identified from WL peaks.

The proof-of-concept study in this Chapter has also left various possible further extensions of the analyses presented here. One of the most important considerations for future WL surveys and their cosmological applications is the effect of galaxy shape noise. Using the all-sky maps from T17, we have shown that (i) the inclusion of GSN necessitates a larger smoothing length than used in the bulk of this Chapter, θ_s = 2-3 arcmin, to suppress its impact on the extracted cosmological statistics, and (ii) with a suitable smoothing, the self-similarity of the peak 2PCFs still holds for the cosmology used in the T17 simulations. While we expect these conclusions to apply for other cosmological models, Fig. 6.14 shows that the use of GSN and larger θ_s does indeed affect the slope of the rescaled peak 2PCF. Therefore, in the presence of GSN our fitted models need to be re-analysed before it can be directly useful for cosmological tests.

Unfortunately, the 96 Z16 maps with varying cosmological parameters have a relatively small size, at 3.5×3.5 deg^2. Including GSN in these maps and increasing the smoothing length will reduce both the number of peaks in the maps and the dynamical range over which the 2PCFs can be reliably studied. This consideration makes a compelling case that larger convergence maps, constructed from N-body simulations with larger boxes and varying cosmologies, are a natural next step, to re-calibrate our peak models so that they can be readily applied for upcoming WL surveys. Again, we leave these to a future, more comprehensive, study.

The planned larger simulations will have other applications as well. For example, they will allow us to study low/intermediate WL peaks and the high peaks, as well as other statistics such as the WL shear power spectrum, simultaneously. It will also be possible to look at source galaxies with a certain redshift distribution compared to the currently idealised case with a single source redshift, $z_s = 1$. Larger WL maps will also allow us to more accurately estimate the errors on the 2PCFs, with large-scale modes properly included. Further more, in future studies we will try methods of extracting WL peaks that are more similar to approaches taken in observations, such as starting with the shear field and adding GSN to this before we then transform to the convergence field.

Finally, it will also be interesting to analyse the rescaled WL peak 2PCFs in cosmological models beyond ΛCDM. We can envisage two possible scenarios here: the first is that the rescaled 2PCFs may not be self similar, which would offer a potentially strong constraint on these models. Alternatively, the detailed properties of the self-similarity in the 2PCFs may change, in the form of a different amplitude or slope, which can also be used to test models with observational data. Therefore, it will be important to consider models which are expected to alter the large-scale clustering of matter. These include the various dark energy models which may couple to dark matter or have different equation-of-state w parameters. The neutrino mass is another interesting possibility, as massive neutrinos tend to dampen structure formation, which leaves signatures in the WL peak abundance and 2PCF. Modified gravity models can also be potentially tested since they generally introduce fifth forces on cosmological scales, which modify the clustering of matter or even the geodesics of photons. The studies of these topics will require new simulations and dedicated effort, and will be deferred for the future.

Chapter 7

Cosmological forecasts with the clustering of weak lensing peaks

7.1 Introduction

In order to more deeply probe the nature of the Universe, it is important to measure cosmological parameters as precisely as possible. This can be achieved by maximising the information that can be extracted from a given survey. The standard approach for weak lensing surveys is to measure ΛCDM parameters with two-point statistics, such as the shear-shear correlation function (Schneider et al., 2002; Semboloni et al., 2006; Hoekstra et al., 2006; Fu et al., 2008; Heymans et al., 2012; Kilbinger et al., 2013; Hildebrandt et al., 2017; Troxel et al., 2018; Hikage et al., 2019; Aihara et al., 2019; Asgari et al., 2020; DES Collaboration et al., 2021). However, the shear two-point correlation function (2PCF) does not capture non-Gaussian information, and, due to the non-linear evolution of the Universe, weak lensing data are highly non-Gaussian. To fully exploit the data, many non-Gaussian statistics have been developed, which encapsulate information beyond two-point statistics. A well-established example is the abundance of WL peaks (local maxima in the convergence field), which has been shown to be complementary to the shear two-point function and helps break the Ω_m-σ_8 parameter degeneracy (Jain & Van Waerbeke, 2000; Pen et al., 2003; Dietrich & Hartlap, 2010). Peaks are also shown to outperform the standard methods for constraining the sum of neutrino mass (Li et al., 2019) and w_0 (Martinet et al., 2020), and can be used to provide constraints on modified gravity theories (Liu et al., 2016b). When used in conjunction with the shear two point correlation function, WL peaks have been used to provide the tightest constraints on S_8 from DES-Y1 WL data (Harnois-Déraps et al., 2020). WL peaks also offer utility for other non-Gaussian statistics, such as WL voids (see previous Chapters), where the peaks can be used as tracers to identify the voids. By including WL peaks as a complementary statistic, the measurement errors on cosmological parameters can be reduced, which will help inform the statistical significance of any parameter tensions between multiple observations.

When used to constrain cosmological parameters, peak analyses typically focus on the WL peak abundance, which is the number density of WL peaks as a function of their lensing amplitude. Studies have shown that the WL peaks with the highest amplitudes tend to correspond to large haloes along the line of sight (Hamana et al., 2004; Liu & Haiman, 2016; Wei et al., 2018). For this reason, WL peaks identified in surveys such as HSC can be used to search for galaxy clusters (e.g., Hamana et al., 2020). Furthermore, shear 2PCF measurements are typically combined with measurements of galaxy clustering (and galaxy-galaxy lensing) to further tighten the cosmological constraints (e.g., DES Collaboration et al., 2021). So, if WL peaks correspond to massive haloes, and hence massive galaxies, and the clustering of these galaxies is known to contain complementary information, then studying and exploiting the clustering of WL peaks is a natural next step in maximising the utility of WL peaks.

Previously, Marian et al. (2013) have shown that the 2PCF of WL peaks with high lensing amplitudes does not contain much complementary information to the peak abundance alone. In Chapter 6, we presented some simple scaling relations for the WL peak 2PCF, and found that the clustering of low-amplitude WL peaks also appears to be sensitive to the cosmological parameters Ω_m and σ_8. In this Chapter, with a more detailed analysis, we show that the clustering of low-amplitude peaks contains significant complementary information to the clustering of high peaks, and that when the clustering of multiple peak height ranges are combined, the WL peak 2PCF offers similar constraining power to the peak abundance alone, where the two probes have different degeneracy directions. Therefore, we also show that, when their abundance and 2PCF are combined, the total cosmological information that is extracted from the WL peaks is significantly improved.

We use the *cosmo*-SLICS simulation suite (Harnois-Déraps et al., 2019) to measure the peak abundance and 2PCF, for a range of cosmological parameters. This data is then used to train a Gaussian process regression emulator, which, combined with Markov chain Monte Carlo, allows us to generate likelihood contours and provide forecast parameter constraints for an LSST-like survey.

The layout of the Chapter is as follows. In Section 7.3 we describe how we generate our mock observational data, and our emulation and likelihood analysis pipeline. In Section 7.4 we present the WL peak statistics used in the analysis, first from the mock data, and then from the emulator, in order to understand how these statistics depend on the cosmological parameters Ω_m, S_8, h and w_0. In Section 7.5 we present the parameter constraint forecasts for the WL peak 2PCF and peak abundance. Finally, our conclusions are presented in Section 7.6. We also have two appendices where we present the covariance matrix used in our analysis, and study the accuracy of our emulator.

7.2 Theory

This section briefly outlines the theory relevant for the 2PCF measurements.

As mentioned previously, WL peaks are closely related to the dark matter haloes along the line of sight. In cosmology, both the abundance and large-scale clustering of haloes encode useful information about the underlying cosmological model and parameter values. Therefore, as well as studying the abundance of WL peaks, we will also study their clustering. The extent to which objects are clustered can be measured through the two-point correlation function (2PCF) which is defined as the excess probability, relative to a random distribution, of finding a pair of objects at a given separation θ. Formally, this is written as

$$dP_{ij}(\theta) = \overline{n}^2(1 + \xi(\theta))dV_i dV_j \, , \tag{7.2.1}$$

where $\overline{n}$ is the expected tracer number density, dV_i and dV_j are two sky area elements that are separated by a displacement $\boldsymbol{\theta}$ with amplitude θ, and $\xi(\theta)$ is the 2PCF. We have $\xi(\boldsymbol{\theta}) = \xi(\theta)$ thanks to statistical isotropy. In practice, the 2PCF can be measured through the Landy-Szalay estimator which requires the generation of matching catalogues containing randomly distributed points and is given by

$$\xi_{\rm LS}(\theta) = 1 + \left(\frac{N_R}{N_D}\right)^2 \frac{DD(\theta)}{RR(\theta)} - \left(\frac{N_R}{N_D}\right) \frac{DR(\theta)}{RR(\theta)}. \tag{7.2.2}$$

In the above N_D and N_R are the numbers of data and random points, and DD, DR and RR are the numbers of data-data, data-random and random-random pairs in bins $\theta \pm \delta\theta$, respectively. See Chapter 6 and Appendix .8 for more details about the measurement of the peak 2PCF, which are important for small lensing maps.

7.3 Methodology

In this section we describe the methodology followed in this Chapter, including the simulations, mock lensing data, emulation and likelihood analysis.

7.3.1 Mock Data

In this Chapter we use the SLICS and *cosmo*-SLICS (Harnois-Déraps & van Waerbeke, 2015; Harnois-Déraps et al., 2018, 2019) mock WL convergence maps, which we briefly outline in this subsection.

cosmo-SLICS is a suite of high-resolution N-body simulations that were run for 26 sets of $[\Omega_m, S_8, h, w_0]$ cosmological parameters. Here $S_8 \equiv \sigma_8(\Omega_m/0.3)^{0.5}$, $h = H_0/100\text{kms}^{-1}\ \text{Mpc}^{-1}$ is the reduced Hubble constant, and w_0 the dark energy equation-of-state parameter, which is assumed to be a constant that is allowed to deviate from -1 (cosmological constant).

The four dimensional parameter space is sampled using a Latin hypercube, which maximises the interpolation accuracy for a low node count. The exact cosmological parameter space that is probed by *cosmo*-SLICS is shown in Fig. 7.1. The simulation volume is a cube with length $L = 505\ h^{-1}$Mpc, with $N = 1536^3$ dark matter particles. To reduce the impact of cosmic variance, two simulations are run for each cosmology, starting from different (paired) initial conditions. For each node, i.e., set of cosmological parameters, 50 pseudo-independent light-cones are constructed by resampling projected mass sheets, which are then ray-traced under the Born approximation to construct lensing maps and catalogues (see Harnois-Déraps et al., 2019, for full details about the light-cone and catalogue construction).

We use the *cosmo*-SLICS source catalogue down-sampled to match LSST specifications with a source redshift distribution of $z_s = [0.6, 1.4]$, which gives a conservative source galaxy number density of 20 arcmin^{-2}. From this we generate 50 WL convergence maps for each of the nodes, with a sky coverage of 10×10 deg^2 each and 3600^2 pixels (Giblin et al., 2018). These maps are then smoothed with a Gaussian filter with smoothing scale $\theta_s = 1$ arcmin. Chapter 6 contains a study of the impact of different smoothing scales on the WL peak 2PCF.

For estimates of the covariance matrices, we use the SLICS suite to produce 615 WL convergence maps at the fiducial cosmology, which match the properties of the *cosmo*-SLICS maps. The larger number of SLICS realisations relative to *cosmo*-SLICS allows us to calculate robust covariance matrices and to use large data vectors in the likelihood analysis below when combining probes.

7.3.2 Emulation and likelihood analysis

In this subsection, we outline the procedure used to test the sensitivity of WL peak statistics to the cosmological parameters Ω_m, S_8, h and w_0.

First, we measure the WL peak statistics from the 50 convergence maps for each of the nodes shown in Fig. 7.1. Then, in order to predict the WL peak statistics at arbitrary points in this parameter space, we use the Gaussian process (GP) regression emulator from SCIKIT-LEARN (Pedregosa et al., 2011) to interpolate the peak statistics between nodes. GP regression is a non-parametric Bayesian machine learning algorithm used to make probabilistic predictions that are consistent with the training data (see, e.g., Habib et al., 2007; Schneider et al., 2008, for some of its early applications in cosmology). The accuracy of the GP emulator trained on *cosmo*-SLICS has been tested extensively and shown to reach a few percent level in predictions of weak lensing shear two-point correlation functions (Harnois-Déraps et al., 2019), density split statistics (Burger et al., 2020), persistent homology statistics (Heydenreich et al., 2020), aperture mass statistics (Martinet et al., 2020) and WL void statistics (see previous Chapters). In this Chapter the average peak statistics and their standard errors at each node are used as the training data. We present results of the accuracy of the emulator for the peak statistics in Appendix .11.

Finally, once the emulator has been trained and tested, we use Monte Carlo Markov Chain (MCMC) to estimate the posteriors of the parameters for the entire parameter space and produce likelihood contours. We use the EMCEE Python package (Foreman-Mackey et al., 2013) to conduct the MCMC analysis in this Chapter sampling the 4D parameter space as follows. We employ a Bayesian formalism, in which the likelihood, $P(\boldsymbol{p}|\boldsymbol{d})$, of the set of cosmological parameters $\boldsymbol{p} = [\Omega_m, S_8, h, w_0]$ given a data set $\boldsymbol{d}$, is given, according to Bayes' theorem, by

$$P(\boldsymbol{p}|\boldsymbol{d}) = \frac{P(\boldsymbol{p})P(\boldsymbol{d}|\boldsymbol{p})}{P(\boldsymbol{d})}\,, \tag{7.3.1}$$

where $P(\boldsymbol{p})$ is the prior, $P(\boldsymbol{d}|\boldsymbol{p})$ is the likelihood of the data conditional on the parameters, and $P(\boldsymbol{d})$ is the normalisation. In this Chapter we use flat priors with the following upper and lower limits respectively for Ω_m: [0.10, 0.55], S_8: [0.61, 0.89], h: [0.60, 0.81], w_0: [-1.99, -0.52], which matches the parameter space sampled by *cosmo*-SLICS. The log likelihood can be expressed as

$$\log(P(\boldsymbol{d}|\boldsymbol{p})) = -\frac{1}{2}\left[\boldsymbol{d} - \mu(\boldsymbol{p})\right] C^{-1} \left[\boldsymbol{d} - \mu(\boldsymbol{p})\right]\,, \tag{7.3.2}$$

where $\mu(\boldsymbol{p})$ is the prediction generated by the emulator for a set of parameters $\boldsymbol{p}$, and C^{-1} is the inverse of the covariance matrix. We use the emulator's prediction of a statistic at the fiducial cosmology as the data $\boldsymbol{d}$. This choice is for simplicity and presentation purposes, which ensures that the confidence intervals are always centred on the true values of the cosmological parameters allowing for easier comparisons between multiple probes.

The likelihood returns a 4D probability distribution that indicates how well different regions of the parameter space match the input data $\boldsymbol{d}$. Note that Eq. (7.3.2) assumes that the covariance matrix does not depend on the cosmological parameters.

We use the 615 SLICS WL map realisations (which match the fiducial cosmology) to calculate the covariance matrices, and then divide it by a factor of 180 to rescale the covariance matrix from a 100 deg^2 area to the LSST survey area, which we take as $18,000$ deg^2. The joint covariance matrix for the peak probes studied in this Chapter is presented appendix .12. We also multiply the inverse covariance matrix by a factor α, which accounts for the bias introduced when inverting a noisy covariance matrix (Anderson, 2003; Hartlap et al., 2007), given by:

$$\alpha = \frac{N - N_{\text{bin}} - 2}{N - 1}\,, \tag{7.3.3}$$

where $N = 615$ is the number of WL maps used to calculate the covariance matrix and N_{bin} is the number of bins used to measure the statistic.

7.4 Weak lensing peak statistics

In this section, we present the weak lensing peak statistics studied in this Chapter, which include the peak abundance and the peak 2PCF. For each statistic, we first show their measurements from the *cosmo*-SLICS nodes which are used as the training data for the emulator. We then present emulations of the statistic by varying one cosmological parameter at a time, to exemplify its sensitivity to different cosmological parameters, which will aid the interpretation of the forecast cosmological constraints in Section 7.5.

7.4.1 Weak lensing peak abundance

Fig. 7.2 shows the differential WL peak abundance (number density) measured in each of the 26 nodes in Fig. 7.1. The abundance of the fiducial cosmology is shown by the blue curve, with the rest of the cosmologies plotted in grey.

First, the figure shows that there are an appreciable number of peaks with amplitudes below $\nu = 0$, which correspond to local maxima in regions that are underdense. In this analysis we do not use peaks with $\nu < 0$ for our forecast constraints for the following two reasons. First, Martinet et al. (2018) have shown that negative peaks correlate very strongly with positive peaks, and so there is little gain in parameter constraints when negative peaks are included. Second, in Section 7.5 we introduce the cosmological forecasts for WL voids from Chapter 4, which correspond to 2D underdense regions in WL maps. So we leave the study of underdense regions of the WL maps to WL void analysis, rather than WL peak analysis.

The maximum of the peak abundance is just above $\nu = 1$ for all cosmologies. Due to the low signal-to-noise ratio, this indicates that a large fraction of the total number of peaks correspond to spurious local maxima induced by galaxy shape noise, rather than a physical signal induced by matter overdensities along the line of sight, while more peaks at the high-ν end are produced by a true physical signal.

As the peak abundance approaches higher ν values, the spread in the peak abundances between different cosmologies increases significantly, where the abundance of peaks at $\nu = 6$

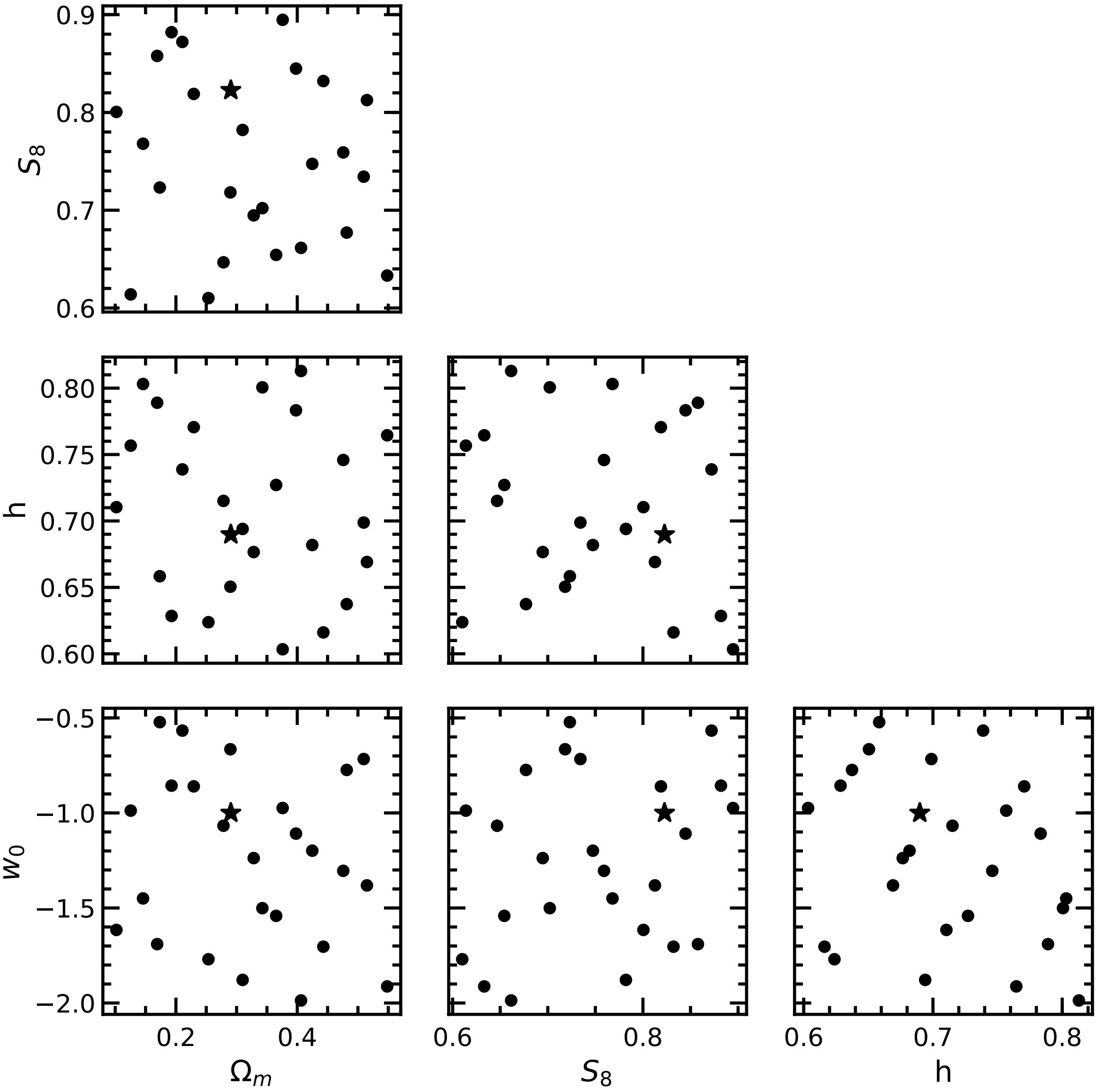

Figure 7.1: The 4-dimensional parameter space ($[\Omega_m, S_8, h, w_0]$) sampled by the *cosmo*-SLICS simulation suite. The fiducial cosmology is indicated by a star with parameter values [0.29, 0.82, 0.69, −1.00].

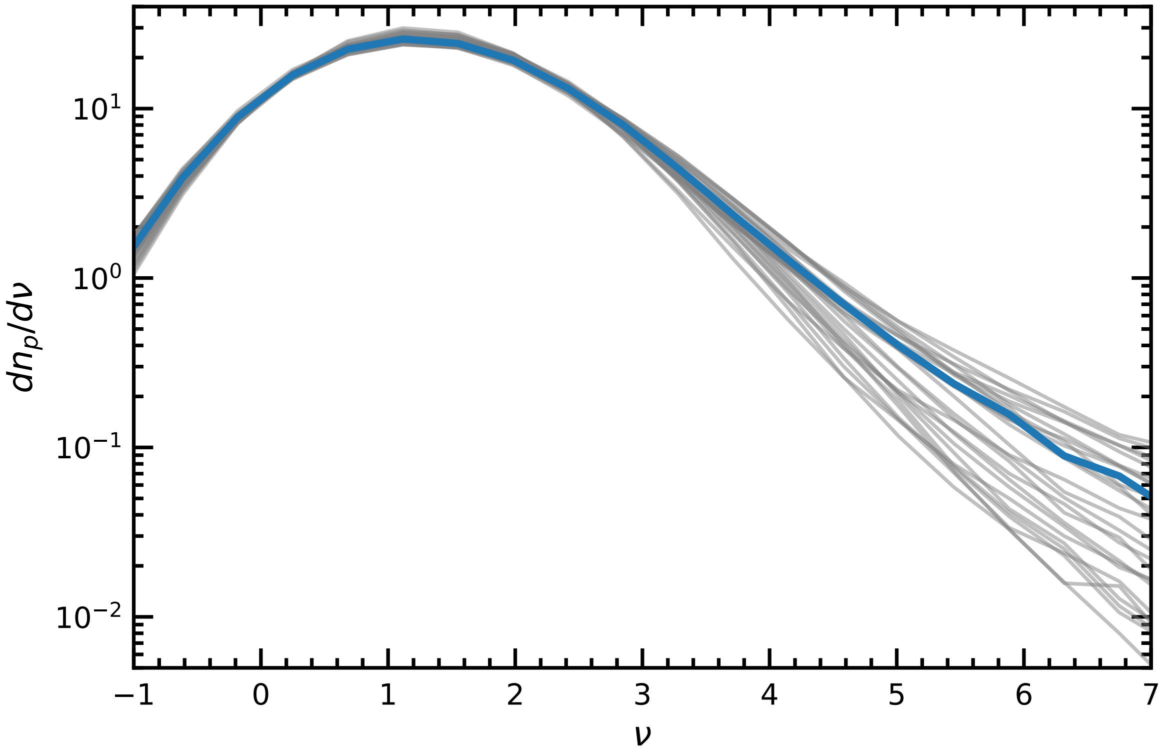

Figure 7.2: (Colour Online) The differential WL peak number density (abundance) as a function of peak height ν. The grey curves correspond to the 26 *cosmo*-SLICS nodes in Fig. 7.1, with the fiducial cosmology plotted as a blue thick curve.

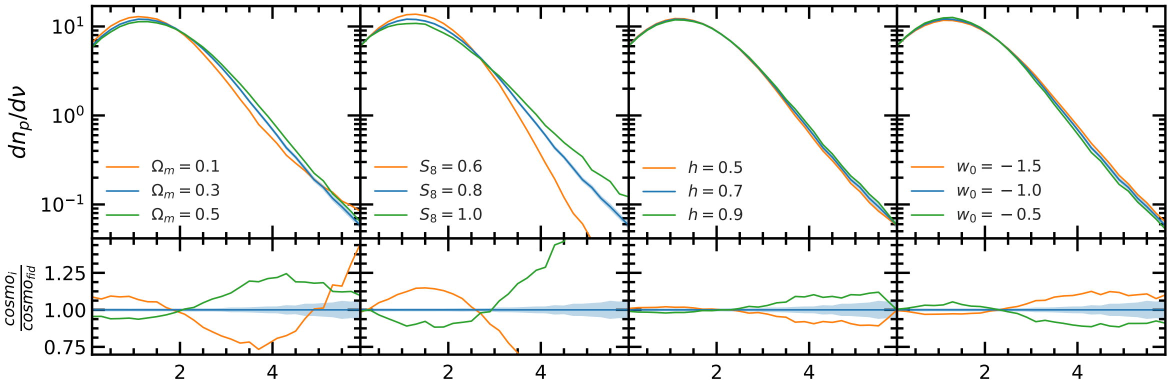

Figure 7.3: (Colour Online) *Top row*: the emulated peak abundance. The curves correspond to the cosmological parameters [Ω_m, S_8, h, w_0] with values [0.3, 0.8, 0.7, −1.0], unless otherwise stated in the sub-panel legends. Each sub-panel corresponds to varying one cosmological parameter at a time, denoted in the legend. *Bottom row*: The curves from the top row, divided by the fiducial cosmology (blue curve in the top row). The 1σ standard errors measured from the 50 *cosmo*-SLICS realisations are included on the fiducial (blue) curves, and they are barely visible in the upper sub-panels.

can differ by an order of magnitude between the most extreme cosmologies. This is due to two factors. First, because the peaks at this amplitude are not dominated by noise, differences in the physical signal are more visible. Second, because the high mass end of the halo mass function varies more significantly as a function of cosmological parameters, so does the peak abundance, since the largest peaks are created by the largest haloes (Liu & Haiman, 2016; Wei et al., 2018).

Whilst the high ν end of the abundance exhibits the greatest variation amongst the different cosmological parameters, this region also has the highest sample variance, since high peaks are orders of magnitude less abundant than low peaks. Therefore, as ν increases, the increased spread between cosmologies is in direct competition with the increased statistical uncertainty. For this reason it is important to consider the abundance of peaks over a wide ν range in our forecasts.

Next, in order to aid the physical interpretation of how the WL peak abundances (Fig. 7.2) depend on the four parameters, Ω_m, S_8, h and w_0, individually, we use the *cosmo*-SLICS data to train a GP emulator as discussed in 7.3.2 and present emulated peak abundances in the *cosmo*-SLICS parameter space by varying one parameter at a time. The results are plotted in Fig. 7.3.

The emulated peak abundances plotted in Fig. 7.3 are for the cosmological parameters $[\Omega_m, S_8, h, w_0] = [0.3,\ 0.8,\ 0.7,\ -1.0]$, unless otherwise stated in a sub-panel legend. Each sub-panel contains curves for the varied parameter above and below the fiducial value. The bottom row of sub panels shows the ratio of the curves relative to the fiducial cosmology. 1σ standard errors measured from the 50 *cosmo*-SLICS realisations are included on the fiducial cosmology, shown by the shaded blue region. Finally, the ν range plotted here is slightly narrower than that presented in Fig. 7.2, since we are now showing the ν range that will be used to forecast the peak abundance constraints, which is $\nu \in [0, 6]$.

The left panel shows how the peak abundance depends on Ω_m. Increasing Ω_m reduces the abundance of peaks with amplitudes $\nu < 2$ but increases the abundance of peaks with amplitudes $\nu > 2$, relative to the fiducial case. This is because a higher Ω_m increases the matter content of the universe, which allows dark matter haloes to grow more massive, increasing their lensing signal and the resulting peak amplitudes. The opposite behaviour can be seen when Ω_m is reduced relative to the fiducial case, with more peaks below $\nu = 2$ and fewer above. There is an upturn in the peak abundance for $\Omega_m = 0.1$ at $\nu \approx 5$, which is due to the fact that S_8 is held constant, rather than σ_8. Since $S_8 = \sigma_8(\Omega_m/0.3)^{0.5}$, σ_8 increases when

Ω_m is reduced, in order for S_8 to remain constant.

The middle left panel shows the peak abundance for different S_8 values. The results presented in this sub-panel vary more strongly compared to all other sub-panels, verifying that the peak abundance is the most sensitive to S_8 of all the parameters studied here. Similar to the behaviour seen for Ω_m, increasing S_8 reduces the number of small peaks below $\nu \approx 2.7$, but increases the number of large peaks above this point. The opposite behaviour is seen for decreasing S_8. Increasing S_8 leads to greater clustering of matter, which will place more haloes closer together. The increased mass along an overdense line of sight translates into a greater lensing signal, which produces more peaks of higher amplitudes. This also reduces the number of small peaks since fewer haloes are in isolation which would produce small peaks.

The middle right panel shows how the peak abundance changes with h. Peaks with amplitudes $\nu < 3$ are mostly unaffected, however there is a small amount of sensitivity to h at the high ν end, where increasing h slightly increases the number of high peaks and vice versa. This result is not entirely surprising: from Eq. (1.2.10) we can see that the dependencies of h, or equivalently H_0, cancel out, because the comoving distance can be written as

$$\chi(z) = \frac{c}{H_0} \int \frac{1}{E(z')} dz' \,, \tag{7.4.1}$$

where $E_{\Lambda\mathrm{CDM}}(z)$ is defined as

$$E_{\Lambda\mathrm{CDM}}(z) \equiv \frac{H_{\Lambda\mathrm{CDM}}(z)}{H_0} = \Omega_m (1+z)^3 + 1 - \Omega_m \,, \tag{7.4.2}$$

for a flat ΛCDM cosmology (as is the case of our fiducial cosmology), and is independent of h. This means that the H_0 factors in the pre-factor, and the χ and $d\chi$ terms of Eq. (1.2.10) cancel out, so that the only dependence on H_0 in κ would come through the matter density contrast δ. In the linear-perturbation regime, the evolution of δ can be expressed in the linear growth factor D_+, which for a flat ΛCDM cosmology is given by the following solution:

$$D_+(z) = E_{\Lambda\mathrm{CDM}}(z) \left[\int_0^\infty \frac{(1+z')}{E^3_{\Lambda\mathrm{CDM}}(z')} dz' \right]^{-1} \int_z^\infty \frac{(1+z')}{E^3_{\Lambda\mathrm{CDM}}(z')} dz', \tag{7.4.3}$$

where the term in the bracket offers the normalisation to ensure that $D_+(z=0) = 1$ as per the usual convention—this suggests that for flat ΛCDM models with the same Ω_m, σ_8 and D_+, κ is independent of h. However, we remark that the above argument only applies to a strictly matter-dominated Universe. In practice, increasing h with Ω_m fixed would mean that the physical matter density today, $\Omega_m h^2$, increases, which brings the matter-radiation equality to higher redshift. Since the growth of matter perturbations is slower during radiation domination but faster during matter domination, this means that *small-scale* matter perturbations experience a stronger growth in the case of a larger h, and therefore it requires a *lower* value of A_s (the amplitude of the primordial power spectrum) to reach the desired σ_8. Consequently, the matter clustering on *large scales*—e.g., at k smaller than $\simeq 0.01h\mathrm{Mpc}^{-1}$, which corresponds to the horizon scale at matter-radiation equality—will indeed be *weaker*. Actually, a more detailed calculation shows that, when comparing the cases of $h = 0.9$ and 0.7 (with Ω_m and σ_8 fixed), the late-time matter power spectrum $P(k)$ is higher (lower) in the latter than in the former for $k \gtrsim 0.1h\mathrm{Mpc}^{-1}$ ($k \lesssim 0.1h\mathrm{Mpc}^{-1}$). This will have nontrivial implications for the peak 2PCFs as we shall see shortly. Nevertheless, for the peak abundance, the most relevant scales are $k \simeq 0.1$–$1h\mathrm{Mpc}^{-1}$, where the cases of $h = 0.7$ and 0.9 have similar matter clustering amplitudes, which is slightly higher for larger h: as this k range corresponds to the sizes of halo-forming regions, this is consistent with the high-ν behaviour of the middle right panel.

The right panel shows the peak abundances with varying w_0. Similar to h, the peak abundance does not appear to be very sensitive to changes in w_0, but increasing w_0 does indeed create slightly more low-ν peaks and fewer high-ν peaks compared to the fiducial case, and vice versa. A different dark energy equation of state can change the expansion rate, therefore affecting the comoving distances, the lensing kernel in Eq. (1.2.10), and the growth rate of matter perturbation δ. The physics underlying the qualitative behaviours shown in these panels is actually complicated and quite interesting. Usually, a more negative w_0, e.g., $w_0 < -1.0$, implies an increase of the dark energy density with time and therefore (for the same matter density) a faster transition from the phase of decelerated expansion to an accelerated one dominated by dark energy, compared to standard ΛCDM. But given that we fix h and therefore H_0, at $z > 0$ the expansion rate is actually slower than the fiducial ΛCDM model, because the density of dark energy in this case decreases with redshift, and so at $z > 0$ the total density of matter and dark energy is smaller than in ΛCDM. More explicitly, we have $E_{w_0}(z) \leq E_{\Lambda\mathrm{CDM}}(z)$ for $w_0 < -1$, where

$$E_{w_0}(z) = \frac{H_{w_0}(z)}{H_0} = \Omega_m(1+z)^3 + [1-\Omega_m]\,(1+z)^{3(1+w_0)}, \tag{7.4.4}$$

which reduces to Eq. (7.4.2) when $w_0 = -1$. Because the dark energy in our simulations is assumed to be non-clustering, the only effect of varying w_0 is to modify the background expansion history, which leads to a scale-*independent* change in the linear matter clustering, $P(k)$. It may seem that, since $w_0 = -1.5$ leads to a slower expansion, it will increase matter clustering. While this is true, we have to note that in this comparison we have fixed S_8 (and equivalently σ_8) today in all three cases, and so this means that, in order to have the same σ_8 at the present day, the primordial power spectrum must be lower in the $w_0 = -1.5$ case (we have explicitly checked this using CAMB). At an initial sight, this seems to suggest that this model predicts less structure formation than ΛCDM (until $z = 0$), which is against the results of Fig. 7.3. However, recall that another effect of having a slower expansion is that the Universe becomes older at $z = 0$, and distances to the same redshift become larger; the latter, in particular, means that in between the observer and the source(s) there would be more volume, and more structures such as large dark matter haloes. Since these haloes are what produce the high-ν peaks, the net effect is that the case of $w_0 = -1.5$ actually gives a larger peak abundance at $\nu \gtrsim 2$. The behaviour of the $w_0 = -0.5$ model can be similarly explained.

Figs. 7.2 and 7.3 show that the peak abundance is mostly sensitive to changes in Ω_m and S_8, and less so to h and w_0, with sensitivity to cosmology coming from both the high and low amplitude peaks.

7.4.2 Weak lensing peak two-point correlation function

In order to measure the WL peak 2PCF, we first remove peaks with amplitudes below a given ν threshold, and then repeat this step with different ν thresholds in order to create multiple peak catalogues. This procedure is motivated by the following factors.

First, as discussed in Section 7.4.1, a significant fraction of the WL peak population is noise-dominated (low ν), suggesting that their spatial distribution (to which the 2PCF is sensitive) may not contain useful cosmological information. We have tested this assertion, and found that the WL peak 2PCF measured using peaks of all heights has a very low amplitude and exhibits only small variations between the 26 *cosmo*-SLICS nodes. This indicates that when no distinction is made based on peak heights, the average clustering of WL peaks is close to that of a randomly distributed sample. Therefore, in order to extract useful information on the clustering of WL peaks, we must first remove the low-amplitude noise-dominated peaks. This can be achieved with a threshold as low as $\nu = 1$.

Second, varying the ν threshold and using multiple WL peak catalogues produces multiple WL peak 2PCF measurements. The change in the 2PCF as the ν threshold changes is also sensitive to the underlying cosmology, so we expect that the different 2PCF measurements will contain complementary information to each other, so that combining these measurements will yield tighter cosmological parameter constraints.

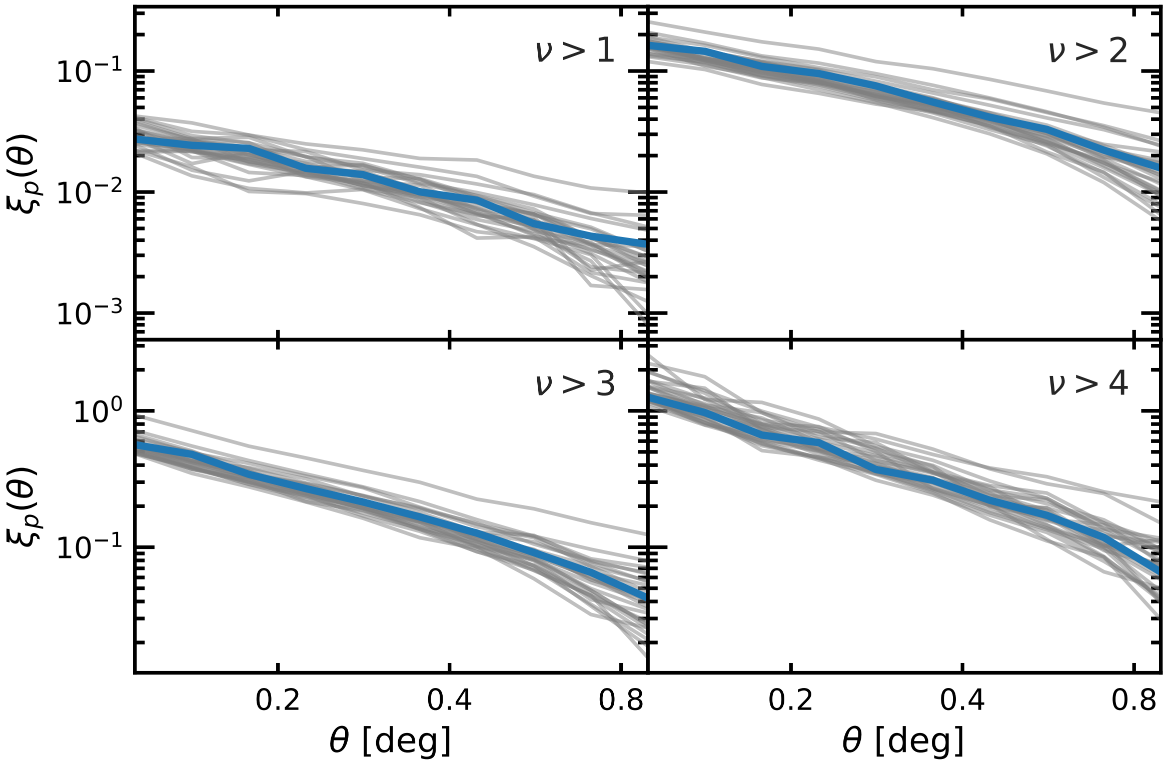

Figure 7.4: (Colour Online) The WL peak 2PCF, where each subpanel corresponds to the 2PCF of a different peak catalogue. The various peak catalogues (and hence their 2PCF) only contain peaks with amplitudes $\nu > 1$ (top left), $\nu > 2$ (top right), $\nu > 3$ (bottom left) and $\nu > 4$ (bottom right). The curves in each subpanel correspond to the 26 *cosmo*-SLICS nodes in Fig. 7.1, with the fiducial cosmology plotted in colour.

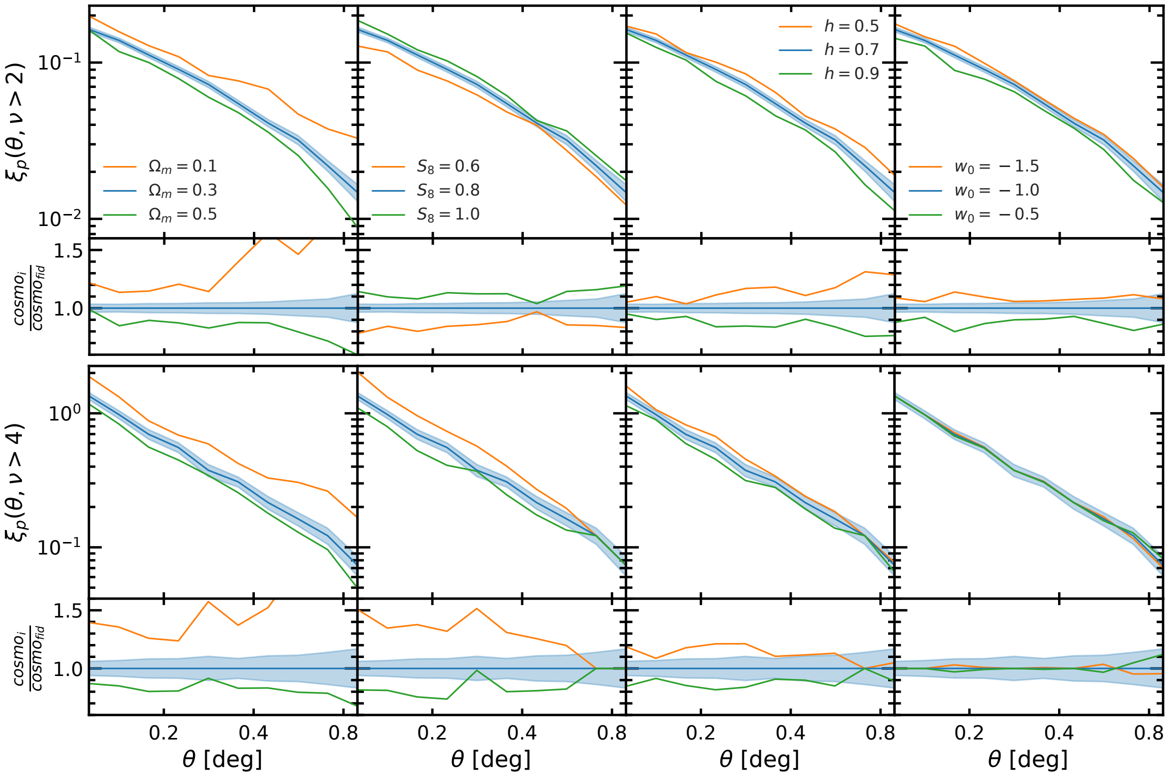

Figure 7.5: (Colour Online) The emulated peak 2PCF for two different peak catalogues, $\nu > 2$ (top section) and $\nu > 4$ (bottom section). The curves correspond to the cosmological parameters $[\Omega_m,\ S_8,\ h,\ w_0]$ with values $[0.3,\ 0.8,\ 0.7,\ -1.0]$, unless otherwise stated in the sub-panel legends. Each sub-panel corresponds to varying one cosmological parameter at a time, as specified in the legend. The bottom rows in each section show the ratio of the curves relative to the fiducial cosmology. The 1σ standard errors measured from the 50 *cosmo*-SLICS realisations are shown for the fiducial cosmology by the shaded blue region.

Fig. 7.4 shows the 2PCFs for four WL peak catalogues with $\nu > 1$ (top left), $\nu > 2$ (top right), $\nu > 3$ (bottom left) and $\nu > 4$ (bottom right). The 2PCFs for the 26 *cosmo*-SLICS nodes are plotted, with the fiducial cosmology plotted in blue, and all other cosmologies plotted in grey.

The 2PCF measurements for the $\nu > 1$ catalogue have the lowest amplitude. As the ν threshold increases, so does the amplitude of the 2PCF for all cosmologies, indicating that the high ν peaks are more clustered than the low ν peaks. Both the gradient and the amplitude of the 2PCF change as the ν threshold increases, however the changes in amplitude appear to be the most dominant feature. This can be explained by the relationship between WL peaks and dark matter haloes – more massive haloes are known to be more strongly biased and clustered, because they form from higher density peaks of the primordial density field.

Similar to Section 7.4.1, we use the *cosmo*-SLICS data from Fig. 7.4 to train a GP emulator as discussed in 7.3.2, and present emulated peak 2PCFs in the *cosmo*-SLICS parameter space by varying one parameter at a time. The results are plotted in Fig. 7.5. The bottom row in each section shows the ratio relative to the fiducial cosmology. The 1σ standard errors measured from the 50 *cosmo*-SLICS realisations are included for the fiducial cosmology and are shown by the shaded blue region. The top and bottom sections of Fig. 7.5 shows results for the 2PCF of peaks with $\nu > 2$ and $\nu > 4$ respectively. We choose to show results for $\nu > 2$ rather than $\nu > 1$ since, as we will see in Fig. 7.6, $\nu > 2$ gives stronger parameter constraints than the $\nu > 1$ case.

The top left panel shows the emulated 2PCF for $\nu > 2$ varying only Ω_m. Increasing Ω_m has less of an impact on the 2PCF for small θ compared to large θ, effectively steepening the curve relative to the fiducial case by a small amount. When decreasing Ω_m, the above behaviour is mirrored, except the overall magnitude of the change is larger compared to the case where Ω_m is increased. This shows that Ω_m dictates the gradient of the 2PCF, and appears to be more sensitive to low Ω_m values. It may seem counter-intuitive that a model with smaller Ω_m would predict a stronger cluster for WL peaks, but we note again that here S_8 has been fixed when Ω_m is being varied, so that a smaller Ω_m corresponds to a larger σ_8, and the latter means there is more matter clustering.

The bottom left panel shows the peak 2PCFs for $\nu > 4$ for the same Ω_m values. Similar to the $\nu > 2$ case, increasing Ω_m decreases the 2PCF amplitude and vice versa, and the behaviour relative to the fiducial case is asymmetric, where changing Ω_m by a fixed amount in either direction has a larger impact on the amplitude when Ω_m is decreased, suggesting that the

$\nu > 4$ catalogue is also more sensitive to small Ω_m. However, compared to the $\nu > 2$ case, there appears to be slightly less change to the overall slope of the 2PCF as Ω_m is varied.

The top middle-left panel is the same as the previous panels except S_8 is varied in this case. The figure shows that changes to S_8 affect the amplitude of the 2PCF, where lowering S_8 lowers the 2PCF amplitude since it corresponds to a smaller σ_8 and therefore less clustering of matter. Increasing S_8 by the same amount increases the amplitude relative to the fiducial case, but the magnitude of the change is slightly smaller compared to the decreased S_8 case. The bottom middle-left panel shows the $\nu > 4$ 2PCF for the same three S_8 values. The overall trend is the opposite as in the $\nu > 2$ case. Initially it seems counter-intuitive that higher S_8 values will lead to a lower clustering amplitude, however, as shown by Fig. 7.3 the abundance of peaks is also larger for this catalogue. Therefore, when S_8 increases, the number of peaks with $\nu > 4$ increases, meaning that smaller maxima in the primordial density field—which are less biased and hence less clustered tracers of the matter density field—end up contributing to this peak catalogue, and so the clustering of the peaks decreases and vice versa.

The top middle-right panel shows how the 2PCF for the $\nu > 2$ catalogue depends on h. The 2PCF appears to be sensitive to changes in h, where increasing h decreases its amplitude, and vice versa. This observation is actually consistent with the discussion above about the physical impact of varying h—with Ω_m and σ_8 fixed—on matter clustering: increasing h from 0.7 to 0.9 weakens the late-time matter clustering at $k \lesssim 0.1h\mathrm{Mpc}^{-1}$, and these are the scales most relevant for the peak clustering (which is expected to trace the dark matter clustering) as well. Unlike the behaviour seen for Ω_m and S_8, changing h by a fixed amount in either direction appears to change the 2PCF amplitude by an equal amount. The bottom middle-right panel shows the $\nu > 4$ 2PCF for the same three h values. As for the case of $\nu > 2$, the 2PCF amplitude increases when h decreases and vice versa. Indeed, the impacts of varying h are similar for both the $\nu > 2$ and the $\nu > 4$ catalogues, except the $\nu > 2$ case appears to be more sensitive to h at large θ.

The top right panel shows the $\nu > 2$ 2PCFs for different values of w_0. Increasing w_0 decreases the amplitude and vice versa, with no apparent changes to the gradient. This behaviour also appears to be symmetric relative to the fiducial cosmology, similar to that seen for h, and unlike Ω_m and S_8. The bottom right panel is the same but shows the $\nu > 4$ 2PCF, which appears to have little sensitivity to changes in w_0. In both catalogues, we think that the physical reason underlying the w_0 dependence is the same as in the case of peak abundance.

Although naively it seems that the case of $w_0 = -1.5$—which has faster growth of structures at late times and hence requires a lower initial power spectrum amplitude to achieve the same σ_8 or S_8 at $z = 0$—should predict less matter clustering during the entire lensing kernel and so lead to a lower amplitude of the peak 2PCF, we note that this model also covers a larger volume for the same redshift range and therefore receives contribution from a greater number of massive haloes. Also, the peak 2PCF is a projection effect, and the projection depth is larger for the case of $w_0 = -1.5$, which leads to a larger line-of-sight integration. These different effects compete with each other and can have cancellations, which may explain why for the $\nu > 4$ catalogue there is almost no dependence on w_0 (also note that the same $\nu > 4$ peak height threshold can lead to different peak populations for the different models, which could also have an impact on the peak correlation).

Comparing the bottom row ($\nu > 4$) to the top row ($\nu > 2$), we see that the amplitudes of the 2PCFs are all higher. Given that fewer tracers are used for the $\nu > 4$ measurements, the errors on these curves should be larger. This will be in direct competition with any increased sensitivity to the cosmological parameters relative to the $\nu > 2$ case. Nonetheless, separate catalogues still contain complementary information to each other regardless of which factors wins out, as we will show later.

7.5 Parameter constraints forecast

In this section we present parameter constraint forecasts for the statistics studied in Section 7.4.

Figure 7.6 shows the parameter constraint forecasts for an LSST-like survey for the WL peak 2PCF. We present constraints for the four WL peak 2PCFs measured from WL peak catalogues with four heights $\nu > 1, 2, 3$ and 4, and the combination of all four catalogues. The true cosmological parameter values used to generate the data are indicated by the black point. The diagonal panels show the 1D marginalised probability distributions, while the remaining panels show the marginalised 2D probability contours enclosing the 68% and 95% confidence intervals. All confidence intervals, along with the true parameter values, are explicitly stated in the table in the top right of the figure.

In general, as the ν threshold increases, the contour sizes start off large ($\nu > 1$), begin to shrink ($\nu > 2$ and $\nu > 3$), and become large again ($\nu > 4$). The shape and orientation of the contours also change significantly as the ν threshold increases. For example, in the Ω_m–S_8

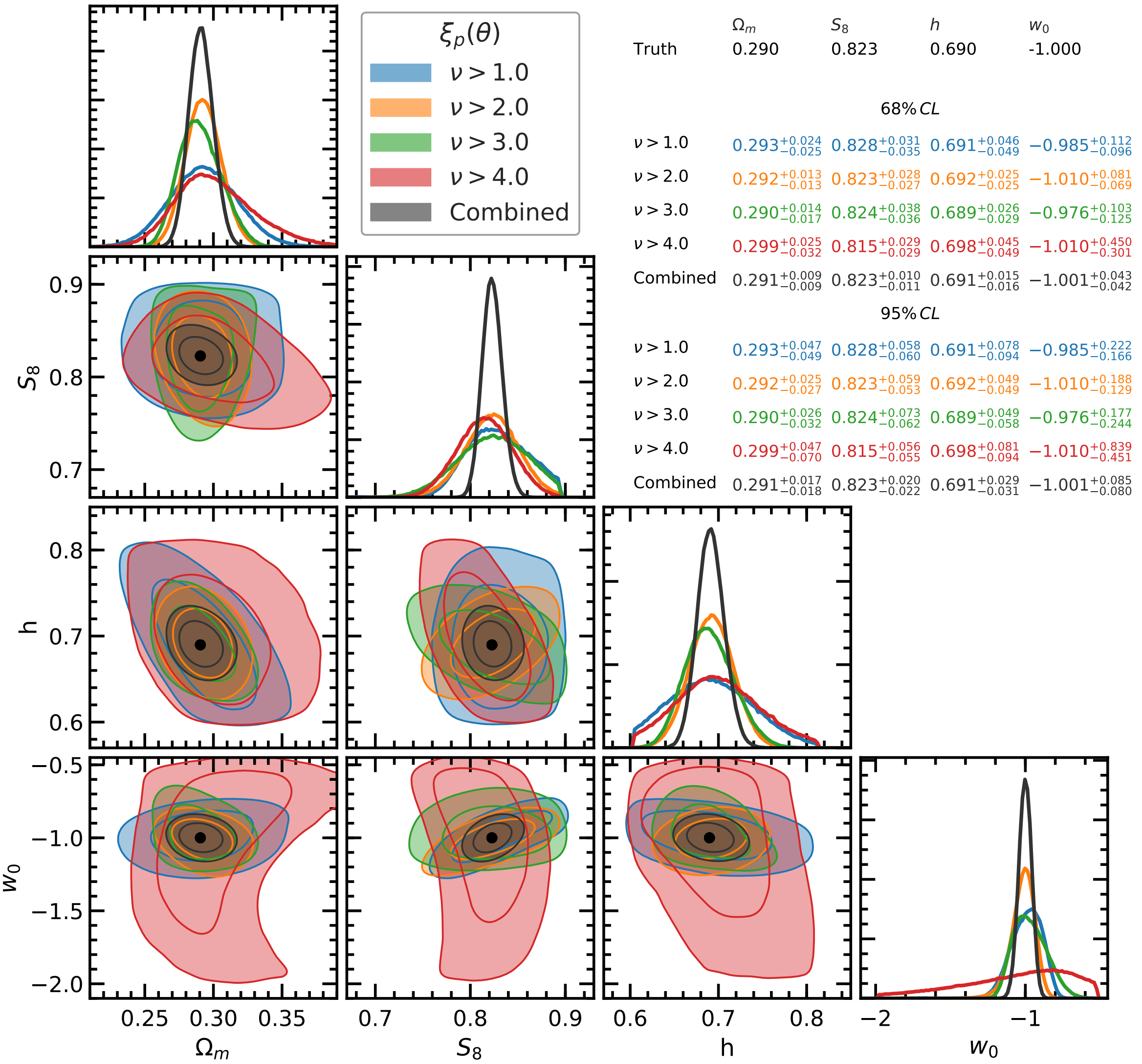

	Ω_m	S_8	h	w_0
Truth	0.290	0.823	0.690	-1.000
		68% *CL*		
$\nu > 1.0$	$0.293^{+0.024}_{-0.025}$	$0.828^{+0.031}_{-0.035}$	$0.691^{+0.046}_{-0.049}$	$-0.985^{+0.112}_{-0.096}$
$\nu > 2.0$	$0.292^{+0.013}_{-0.013}$	$0.823^{+0.028}_{-0.027}$	$0.692^{+0.025}_{-0.025}$	$-1.010^{+0.081}_{-0.069}$
$\nu > 3.0$	$0.290^{+0.014}_{-0.017}$	$0.824^{+0.038}_{-0.036}$	$0.689^{+0.026}_{-0.029}$	$-0.976^{+0.103}_{-0.125}$
$\nu > 4.0$	$0.299^{+0.025}_{-0.032}$	$0.815^{+0.029}_{-0.029}$	$0.698^{+0.045}_{-0.049}$	$-1.010^{+0.450}_{-0.301}$
Combined	$0.291^{+0.009}_{-0.009}$	$0.823^{+0.010}_{-0.011}$	$0.691^{+0.015}_{-0.016}$	$-1.001^{+0.043}_{-0.042}$
		95% *CL*		
$\nu > 1.0$	$0.293^{+0.047}_{-0.049}$	$0.828^{+0.058}_{-0.060}$	$0.691^{+0.078}_{-0.094}$	$-0.985^{+0.222}_{-0.166}$
$\nu > 2.0$	$0.292^{+0.025}_{-0.027}$	$0.823^{+0.059}_{-0.053}$	$0.692^{+0.049}_{-0.049}$	$-1.010^{+0.188}_{-0.129}$
$\nu > 3.0$	$0.290^{+0.026}_{-0.032}$	$0.824^{+0.073}_{-0.062}$	$0.689^{+0.049}_{-0.058}$	$-0.976^{+0.177}_{-0.244}$
$\nu > 4.0$	$0.299^{+0.047}_{-0.070}$	$0.815^{+0.056}_{-0.055}$	$0.698^{+0.081}_{-0.094}$	$-1.010^{+0.839}_{-0.451}$
Combined	$0.291^{+0.017}_{-0.018}$	$0.823^{+0.020}_{-0.022}$	$0.691^{+0.029}_{-0.031}$	$-1.001^{+0.085}_{-0.080}$

Figure 7.6: (Colour Online) Constraint forecasts on cosmological parameters measured from the WL peak 2PCF. Contours are shown for 2PCFs measured from WL peak catalogues with $\nu > 1$ (blue), $\nu > 2$ (orange), $\nu > 3$ (green) and $\nu > 4$ (red) and the combination of all four catalogues (black). The true cosmological parameter values used to generate the data are indicated by the black point. The diagonal panels show the 1D marginalised probability distribution, and the remaining panels show the marginalised 2D probability contours enclosing the 68% and 95% confidence intervals. The table in the top right shows true parameter values (top) and the inferred parameter values for the different peak catalogues with 68% (upper section) and 95% (lower section) confidence limits.

plane, the $\nu > 3$ contour is smaller than the $\nu > 4$ contour; however, the two are orthogonal to each other. This behaviour shows that the constraining power of the WL peak 2PCF can be significantly improved when the 2PCFs of multiple peak catalogues are combined. Even in the case of very large contours which fully enclose the contours from lower ν thresholds, the presence of complementary information between the different 2PCFs is not ruled out. This is because it depends not only on the size, shape and orientation of the contours, but also on the correlation between the contours. This is discussed in detail in Appendix .12. The benefit to combining multiple peak catalogues is shown by the grey contours, which are significantly smaller than any individual contour in all cases.

We find that the $\nu > 2$ and $\nu > 3$ peak 2PCFs give the tightest constraints on Ω_m, the $\nu > 2$ and 4 2PCFs both give the similar constraint on S_8, $\nu > 2$ and 3 are tightest on h and $\nu > 2$ gives the best constraint on w_0. It is interesting to note that the constraints on w_0 are roughly nine times smaller for the combination of all catalogues compared to $\nu > 4$ alone, indicating that a significant amount of cosmological information is contained in the clustering of low amplitude peaks.

Fig. 7.7 shows parameter constraint forecasts for the combination of the peak 2PCFs from eight peak catalogues with $\nu > 1.0, 1.5, ..., 4.5$ in orange. The constraints from the peak abundance for peaks with heights $0 < \nu < 6$ are shown in blue, and the combination of the abundance and 2PCFs are shown in green. We note that when multiple probes are combined, it is important to account for any duplicate information between the probes through the covariance matrix of the data vector, including the cross correlation between the multiple probes. The covariance matrix of all probes studied in this Chapter is presented in Appendix .12 and discussed in detail therein. The orange contour shows how the parameter constraints are improved when the 2PCFs of many more WL peak catalogues are combined: constraints from the combined 2PCFs are much smaller than the best constraints from any individual catalogue (cf. Fig. 7.6). Increasing the number of catalogues used in the combined case from four to eight, improves the constraints on Ω_m and S_8 by roughly 30% and 20% respectively, there is only a small improvement for h, and the w_0 constraints improve by nearly a factor of two.

As shown by the table in Fig. 7.7, the peak abundance and peak 2PCF provide similar constraints on Ω_m, however the constraints on S_8 are twice as strong for the peak abundance compared to the peak 2PCF: in the Ω_m–S_8 plane, the peak abundance contour is significantly tighter than the peak 2PCF contour in the S_8 direction. When the two probes are combined,

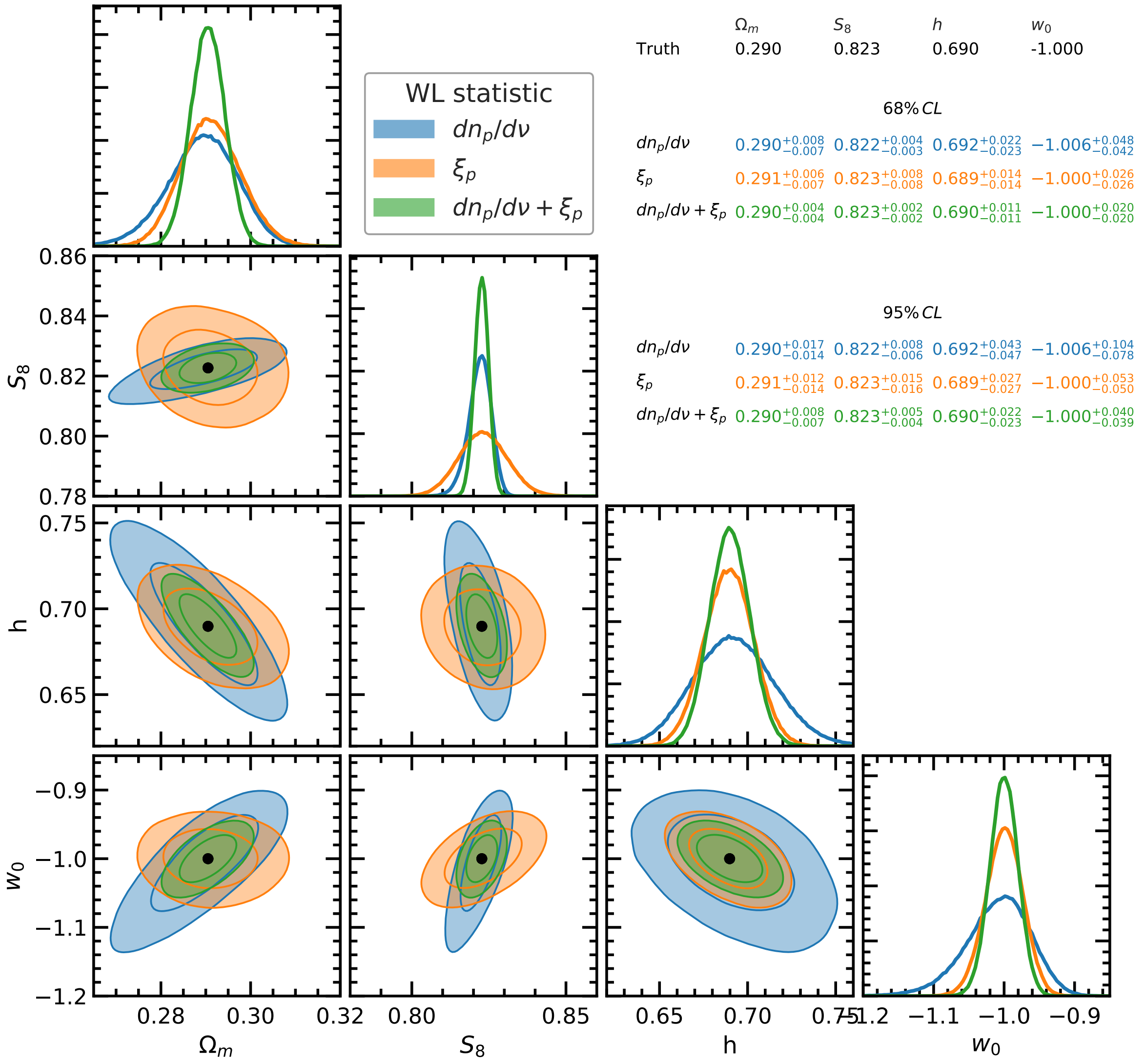

	Ω_m	S_8	h	w_0
Truth	0.290	0.823	0.690	-1.000
		68% CL		
$dn_p/d\nu$	$0.290^{+0.008}_{-0.007}$	$0.822^{+0.004}_{-0.003}$	$0.692^{+0.022}_{-0.023}$	$-1.006^{+0.048}_{-0.042}$
ξ_p	$0.291^{+0.006}_{-0.007}$	$0.823^{+0.008}_{-0.008}$	$0.689^{+0.014}_{-0.014}$	$-1.000^{+0.026}_{-0.026}$
$dn_p/d\nu + \xi_p$	$0.290^{+0.004}_{-0.004}$	$0.823^{+0.002}_{-0.002}$	$0.690^{+0.011}_{-0.011}$	$-1.000^{+0.020}_{-0.020}$
		95% CL		
$dn_p/d\nu$	$0.290^{+0.017}_{-0.014}$	$0.822^{+0.008}_{-0.006}$	$0.692^{+0.043}_{-0.047}$	$-1.006^{+0.104}_{-0.078}$
ξ_p	$0.291^{+0.012}_{-0.014}$	$0.823^{+0.015}_{-0.016}$	$0.689^{+0.027}_{-0.027}$	$-1.000^{+0.053}_{-0.050}$
$dn_p/d\nu + \xi_p$	$0.290^{+0.008}_{-0.007}$	$0.823^{+0.005}_{-0.004}$	$0.690^{+0.022}_{-0.023}$	$-1.000^{+0.040}_{-0.039}$

Figure 7.7: (Colour Online) The same a Fig. 7.6 but for the combination of eight peak 2PCFs from peak catalogues with $\nu > 1.0, 1.5, ..., 4.5$ (orange), the peak abundance (blue), and the combination of the two (green).

there is an overall improvement on the Ω_m and S_8 constraints by a factor of two, relative to the peak abundance alone. This leads to a good overall improvement in the Ω_m–S_8 plane when the peak abundance and 2PCF are combined, as shown by the green contour.

The peak 2PCF is able to constrain both h and w_0 with greater accuracy than the peak abundance. There also appears to be some orthogonality between the abundance and 2PCF constraints in the h–S_8 and w_0–Ω_m planes. In the w_0–h plane, the parameter constraints are dominated by the peak 2PCF contours, while the peak abundance contours are significantly larger than the former. This indicates that the peak 2PCF offers a great deal of complementary information to the peak abundance, and combining the two probes can significantly improve constraints in the four dimensional parameter space studied here. The behaviour of the constraints from peak abundance and 2PCF, especially those on h and w_0, are consistent with the observations we made above for Figs. 7.3 and 7.5.

In Fig. 7.8 we also introduce the parameter constraint forecasts for WL voids from Chapter 4, which are measured with the same methodology and specifications used in this Chapter, to compare the constraining power of these two different probes. This is important since the voids studied in Chapter 4, which are a promising void definition, are identified as underdense regions in the distribution of WL peaks. This means that the properties of WL voids are likely correlated with the number and clustering of peaks, and we need a joint analysis to reveal the amount of complementary information contained in the two probes. The forecasts from the WL voids (blue), making use of both their abundances and tangential shear profiles, are compared with the WL peak forecasts (orange), which combine the peak abundance and peak 2PCF. We note that both the void and peak contours presented here, are for the combination of the $\nu > 1, 2, 3$ and 4 peak catalogues (excluding the peak abundance which does not combine multiple catalogues). This is to provide a fair comparison between the voids and the peaks. In principle, the void contours could be measured for the eight catalogues used for the orange peak 2PCF contours in Fig. 7.7, however this would cause our data vector to become too large, even for our high number of SLICS realisations.

Overall, both the peaks and voids are able to measure the four cosmological parameters with similar accuracy. The voids provide notably tighter measurements of h and w_0. The void contours are smaller than the peak contours, and follow similar degeneracy directions for all combinations of parameters. The void and peak contours are most similar in the S_8–w_0 plane, and most distinct in the w_0–h plane. When the peaks and voids are combined (green contours), there is a small improvement on the Ω_m, S_8 and h measurements, and, there is

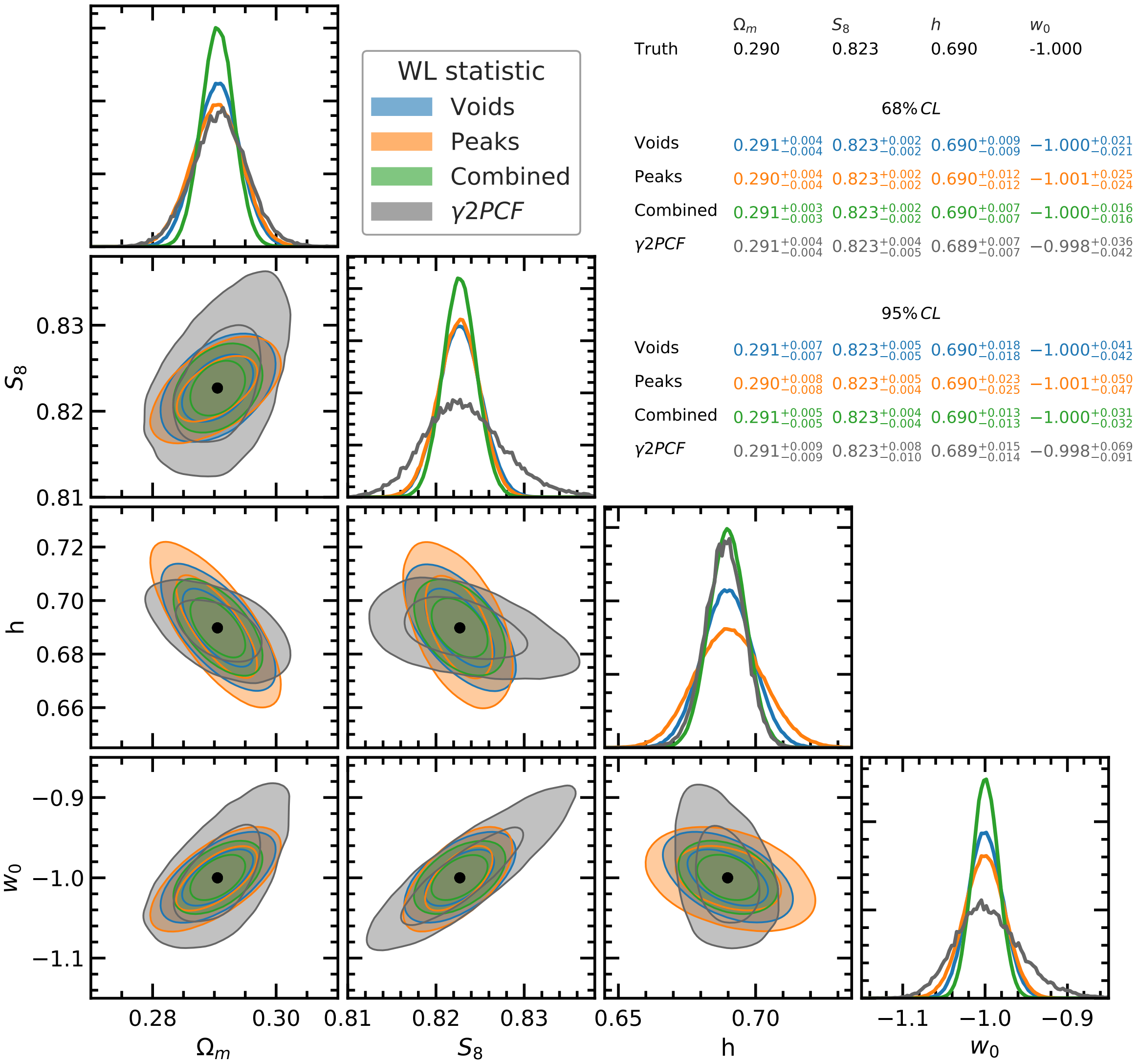

	Ω_m	S_8	h	w_0
Truth	0.290	0.823	0.690	-1.000
		68% *CL*		
Voids	$0.291^{+0.004}_{-0.004}$	$0.823^{+0.002}_{-0.002}$	$0.690^{+0.009}_{-0.009}$	$-1.000^{+0.021}_{-0.021}$
Peaks	$0.290^{+0.004}_{-0.004}$	$0.823^{+0.002}_{-0.002}$	$0.690^{+0.012}_{-0.012}$	$-1.001^{+0.025}_{-0.024}$
Combined	$0.291^{+0.003}_{-0.003}$	$0.823^{+0.002}_{-0.002}$	$0.690^{+0.007}_{-0.007}$	$-1.000^{+0.016}_{-0.016}$
γ2PCF	$0.291^{+0.004}_{-0.004}$	$0.823^{+0.004}_{-0.005}$	$0.689^{+0.007}_{-0.007}$	$-0.998^{+0.036}_{-0.042}$
		95% *CL*		
Voids	$0.291^{+0.007}_{-0.007}$	$0.823^{+0.005}_{-0.005}$	$0.690^{+0.018}_{-0.018}$	$-1.000^{+0.041}_{-0.042}$
Peaks	$0.290^{+0.008}_{-0.008}$	$0.823^{+0.005}_{-0.004}$	$0.690^{+0.023}_{-0.025}$	$-1.001^{+0.050}_{-0.047}$
Combined	$0.291^{+0.005}_{-0.005}$	$0.823^{+0.004}_{-0.004}$	$0.690^{+0.013}_{-0.013}$	$-1.000^{+0.031}_{-0.032}$
γ2PCF	$0.291^{+0.009}_{-0.009}$	$0.823^{+0.008}_{-0.010}$	$0.689^{+0.015}_{-0.014}$	$-0.998^{+0.069}_{-0.091}$

Figure 7.8: (Colour Online) The same as Fig. 7.6, but for void statistics presented in Chapter 4 (blue), peak statistics (orange) and the combination of peak and void statistics (green). Both the peak and void statistics use the combination of the $\nu > 1, 2, 3$ and 4 catalogues. Shear 2PCF forecasts are shown in grey.

also a reasonable improvement on w_0, indicating that the WL peak and void statistics are complementary to each other.

As a comparison, we also include the forecast contours using the standard cosmic shear 2PCFs (ξ_+ and ξ_- combined) in grey. For fair comparisons, the cosmological model dependence and covariance matrix for these were both obtained using the same simulation data as used for the peak and void analyses throughout this Chapter. For Ω_m and h, WL peaks or WL voids (or both of them) give similar constraints as the shear 2PCFs; however, for S_8 and w_0, the former probes actually can place tighter constraints (for this survey specification), indicating again the benefit of exploring beyond-two-point WL statistics to help maximise the information that can be extracted. In some parameter planes, such as S_8–h and h–w_0, there is a clear orthogonality between the degeneracy directions of the peak/void statistics and the shear 2PCFs.

7.6 Discussion and conclusions

We have tested the sensitivity of the WL peak statistics to the cosmological parameters Ω_m, S_8, h and w_0 and compared the peak 2PCF to the peak abundance. In order to achieve this, we have trained a Gaussian Process emulator with 26 cosmologies sampled in the 4D parameter space using a Latin hypercube, which can be used to predict the peak statistics for arbitrary cosmologies (within the range spanned by the training cosmologies). We have run Markov Chain Monte Carlo samplings from our mock weak lensing data to forecast the accuracies at which these four parameters can be constrained by a future, LSST-like, lensing survey, using the above WL peak statistics.

Using the emulators, we have studied the behaviour of the WL peak 2PCF in detail, and made connections to the well-established peak abundance. A main feature of our peak 2PCF analysis is that we generate a WL peak catalogue from the entire peak population by introducing a peak height (ν) threshold, below which all peaks are removed, and then vary this threshold to generate multiple catalogues. We then study the behaviour of the WL peak 2PCF of these catalogues as this ν threshold changes.

In Marian et al. (2013), it has been shown that the WL peak 2PCF of high-amplitude peaks provides little complementary information to the peak abundance. In this Chapter, we have presented some additional steps that are able to further push the utility of the WL peak 2PCF. These additional steps significantly improve the overall constraining power of WL peaks when the abundance and 2PCFs are combined. First, we study the 2PCF of low-amplitude (ν) peaks, and find that it contains significant cosmological information compared to the 2PCF of high-amplitude peaks. For example, in Fig. 7.6 the constraints on w_0 are roughly four times stronger for the $\nu > 2$ catalogue compared to the $\nu > 4$ catalogue. Second, we find that the 2PCFs of multiple catalogues are complementary to each other, and when combined, the peak 2PCF can constrain Ω_m with tighter accuracy than the peak abundance, and that it is able to constrain both h and w_0 with significantly greater accuracy than the peak abundance alone. We also find that the peak abundance provides constraints that are twice as tight on S_8 than the combined peak 2PCF, indicating that in order to fully exploit the cosmological information contained in WL peaks, both their abundance and their clustering should be measured and combined. This is illustrated by the green contours in Fig. 7.7, which show the total constraints from WL peaks in which the abundance is combined with the combined 2PCF from different ν catalogues. Here, the abundance plus the clustering forecasts are roughly twice as strong as those for either of the individual cases (orange for 2PCF and blue for abundance). When we compare the constraints from the peak abundance plus the peak 2PCF to those from the shear 2PCF, we find that the peaks are able to constrain Ω_m, S_8 and w_0 with greater accuracy than the shear 2PCF, the most significant improvement is for w_0. Finally, the information required to measure the peak 2PCF is already present when the peak abundance is measured. Therefore, the addition of the peak 2PCF to any preexisting peak abundance analysis pipeline will require minimal modifications, making the peak 2PCF a very promising probe.

We also include a comparison of the forecasts from WL peaks to the WL voids studied in Chapter 4, and find that the combination of the two can only weakly improve the constraints on Ω_m, S_8 and h, but can provide significantly stronger improvements on the w_0 measurements. The WL voids are sensitive to the N-point correlation function of peaks (White, 1979), and the improved constraints resulting from combining WL peaks and voids shows that three and higher-order correlation functions in the peak distribution contain complementary cosmological information. WL voids are one simple way to access the information contained in the higher order correlation functions of peaks.

We highlight that the work carried out here applies to the 4D parameter space in Fig. 7.1, and may change if additional parameters in the ΛCDM model, such as the spectral index, are included. Our results may also be sensitive to changes in curvature, massive neutrinos or other sources of additional physics. For example in Chapter 5 we found that the peak abundance is sensitive to the nDGP modified gravity model, and Liu et al. (2016b) have used the WL peak abundance to constrain $f(R)$ gravity.

In addition, the simulations used to construct the emulators for the different WL statistics analysed here are limited in their number of nodes sampled with the Latin hypercube. As the results of this Chapter suggest, future WL observations can place competitive constraints on the various cosmological parameters, with significantly smaller contours than the current status. As the contours keep shrinking around the best-fit model, improved emulators which can more accurately capture the small effects induced by small variations of parameters will be needed. In the future, it will be necessary to simulate cosmological models sampled using a nested Latin hypercube, or nested Latin hypercubes, to refine the emulators used in this Chapter.

Finally, in order to use the WL peak 2PCF in observations, it will be important to understand the impact of baryonic physics. It is already established that the presence of baryons can alter the WL peak abundance (Osato et al., 2015; Weiss et al., 2019; Coulton et al., 2019b; Fong et al., 2019) and so it will also be necessary to test how the WL peak 2PCF is affected.

Chapter 8

Conclusions

8.1 Overview

Throughout this thesis I have shown that there is a wealth of cosmological information contained within WL convergence maps. These maps correspond very closely to the underlying distribution of dark matter, which otherwise has very few avenues to be observed directly. WL is therefore a key probe for modern cosmology, that still remains to be fully exploited, as the current generation of WL surveys continue to release their data. Typically, the cosmological information in WL maps is accessed through the shear 2PCF, or with WL peaks. However, due to the highly non-Gaussian nature of the convergence maps, no single statistic is able to completely capture all of the present information.

In this thesis, I have proposed a new WL statistic, WL voids, as a way to access more of the non-Gaussian information contained within WL maps, and performed multiple tests which allowed their utility to be evaluated. I found that WL voids are indeed a very useful statistic, that offers advantages over voids identified in the galaxy distribution and contain complementary information to other WL statistics, which is outlined in this Chapter.

Additionally, I also studied the properties of WL peaks beyond their abundance, which was motivated by the following two factors. First, since the most promising method of identifying WL voids relies on the spatial distribution of WL peaks, it is important to explore the clustering properties of WL peaks. Second, the statistics describing WL peaks are valuable in their own right, and so I have tested the utility of WL peaks beyond their abundance, and shown that the clustering of WL peaks can both be modelled with simple scaling relations, and that it contains useful cosmological information.

8.2 The properties of weak lensing voids (Chapters 2 & 3)

In Chapter 2 I have defined a new class of voids - WL voids - which correspond to extended underdense regions of a WL convergence map. The WL voids were identified using the spatial distribution of WL peaks, coupled with a tunnel algorithm, which constructed a Delaunay triangulation with the WL peaks as vertices. The WL voids regions then, by definition, enclose no WL peaks. I then presented two summary statistics for the WL voids, their abundance, and their tangential shear profiles. I compared the lensing profiles of WL voids to that of galaxy voids, and found that the lensing profile amplitude is significantly larger for WL voids than for galaxy voids. This increased amplitude will in turn correspond to an increased SNR, which makes WL voids a promising new class of voids, competitive with galaxy voids.

In Chapter 3 I have tested how the properties of WL voids depend on the void finder that is used in their identification. To this end I have adapted the most commonly used galaxy void finders for the purposes of WL voids, and measured the properties of 7 different WL void definitions. The new WL void definitions range from the previously defined tunnels, to local minima, to watershed WL voids. I then tested the quality of each WL void definition based on two criteria, the extent to which the void properties change in the presence of GSN, and the SNR of their tangential shear profiles. I found that the two criteria are somewhat anti-correlated, where the WL void definitions most impacted by GSN also receive the largest boost in tangential shear SNR. My conclusion was then that the tunnel algorithm offers the best trade off between the competing effects.

8.3 The cosmological information of weak lensing voids (Chapters 4 & 5)

In Chapter 4 I tested the cosmological information that can be extracted through WL voids. To achieve this I employed cosmoSLICS, a suite of dark matter only simulations that occupy 26 distinct regions in a 4 dimensional wCDM parameter space, organised in a latin hypercube. The WL void statistics were measured at each cosmoSLICS node, and used to train a Gaussian process emulator. This emulator was then coupled with MCMC to produce likelihood contours for a LSST-like survey. I then compared the posteriors for the WL void statistics to the posteriors for the shear 2PCF (which is also calculated using the same methodology as WL voids). The results showed that the WL void cosmological parameter constraints are both tighter and complementary to those from the shear 2PCF.

In addition, in Chapter 5 I also tested the prospect for WL voids to be used to constrain modified gravity theories. To this end I measured the WL void statistics from three dark matter only simulations, one for ΛCDM and two for modified gravity. I then compared the WL voids statistics in the three cases, and measure the SNR with which the WL voids statistics can be used to distinguish between ΛCDM and the two modified gravity models. I found that both the abundance and lensing profiles of the WL voids offer high SNR values in this case, and that compared to galaxy voids the lensing profile SNR is twice as high for WL voids.

8.4 The clustering of weak lensing peaks (Chapters 6 & 7)

As well as studying the properties of WL voids, I have also studied the clustering of WL peaks. Since WL voids can be identified from the spatial peak distribution, it is important to understand how the WL peaks cluster. In Chapter 6 I presented some simple scaling relations for the WL peak two-point correlation function. These scaling relations are numerically calibrated on a set of 96 dark matter only simulations, that cover distinct nodes in the Ω_m-σ_8 parameter space, organised in a latin hypercube. I showed that this scaling relation is present in both independent sets of simulations and for all regions in the Ω_m-σ_8 parameter space. The numerical fits can be used analytically to predict the peak two point correlation function with good accuracy, and provide a basis for the future development of the WL void abundance scaling relations, which may be connected to the clustering of WL peaks.

Finally, in Chapter 7 I adopted the same methodology as in Chapter 4 to test the cosmological information that can be extracted from the WL peak 2PCF. As before, I generated posteriors in the 4D wCDM parameter space (again for an LSST-like survey), for the peak 2PCF, as a function of peak height, and found that the clustering of low amplitude peaks is complementary to that of the high amplitude peaks. For this reason, when the 2PCF of multiple peak catalogues is combined, the cosmological parameter constraints become very competitive with the WL peak abundance. When the peak 2PCF and the peak abundance are combined, the parameter constraints are further improved, indicating that the clustering is complementary to the abundance. It is most interesting to note that the constraints on h and w_0 are significantly tighter for the peak clustering than for the peak abundance. I also compared the combined constraints from the peak abundance and the peak clustering to those from the combination of the WL void abundance and lensing profiles. I found that the constraints from the WL voids are tighter than those from the WL peaks, however when the two are combined, the constraints continue to tighten, indicating that the peaks and voids are also complementary to each other. Finally, I compared these results to the posteriors from the shear 2PCF, which are the same as those presented in Chapter 4, and found that through the addition of the peak clustering the peak constraints become tighter than those from the shear 2PCF. In addition to this, the peaks also offer complementary degeneracy directions to the shear 2PCF.

8.5 Future work

Overall I have shown that it is possible to achieve significant gains through the higher order WL statistics presented in this thesis. It will therefore be important to apply these methodologies to real observational WL data, so that the improved cosmological parameter measurements can be realised. In order to achieve this goal, further work and considerations must be made, to take into account the differences between the simulated data used in this thesis and the features of real observational data. In the remainder of this section I discuss what further development is required to apply WL voids to observational data.

8.5.1 Preparing to use WL voids with observational data

The mock observational data used in the analysis within this thesis is somewhat idealised. In order to apply the methods development here to real observational data, it will be important to account for certain limitations in the observed data. These include the presence of masks on the observational data, intrinsic alignments between source galaxies, and baryonic physics.

All of the convergence maps used in this thesis correspond to unobstructed patches of the sky. In real observations however, certain regions of the WL maps will need to be masked due to various obstructions limiting the collection of the required data, such as bright stars in the field of view, or obstruction from the Milky Way. It will therefore be important to adjust the methodologies with which the statistics proposed here are identified in order to account for a mask. Typically the WL peak abundance is not significantly impacted by a mask, since this statistic only requires the binning of WL peaks as a function of their height. Initially it may seem that the peak 2PCF will be more severely limited by a mask, since it depends on the spatial distribution of the peaks, which may be affected by the mask. However, this problem can be avoided with the Landy-Szalay estimator, which estimates the 2PCF by comparing the tracer distribution to a random distribution. As long as the randoms match the geometry of the survey, which includes a mask, the estimator will give an unbiased estimate of the true peak 2PCF. However, for the identification of WL voids with the tunnel algorithm, different steps must be taken to deal with the presence of a mask. Since the WL voids are identified through a triangulation of the WL peaks, some voids will intersect the mask. This will then cause problems for measuring the lensing profiles in these voids. Additionally, the mask may be concealing WL peaks, which if present, would alter the resulting WL void distribution. It will therefore be important to test if removing voids near the mask boundary is sufficient to perform unbiased measurements. Therefore, masks should be included in the mock observations to allow their impact on the WL void statistics to be forward modelled.

Finally, all analysis carried out here has used dark matter only simulations. This neglects the presence of baryonic physics, which can have an impact on the large scale distribution of matter (McCarthy et al., 2017). Many tests have established that the WL peak abundance is altered in presence of baryons (Osato et al., 2015; Weiss et al., 2019; Coulton et al., 2019b; Fong et al., 2019) and intrinsic galaxy alignments (Harnois-Déraps et al., 2021), so considerations must be made for their impact on WL voids and the WL peak 2PCF. Coulton et al. (2019b) have show that WL minima are less impacted by baryonic physics than WL peaks, since the underdense regions contain less matter by definition and so there are fewer baryonic processes in these regions, which is a promising result suggesting that WL voids may also be minimally impacted by baryonic physics. However, there is a corollary to this argument, that since some WL void definitions are identified from the distribution of WL peaks, they should be similarly impacted. Nonetheless, WL void definitions beyond the tunnel algorithm may circumvent this issue.

8.5.2 Final remarks

In addition to making wCDM forecasts as in Chapters 4 and 7 it will also be interesting to apply the same methodology to modified gravity, where a parameter dictating the deviation from GR can be varied instead of w_0. This will be especially interesting since Chapter 5 has shown the potential for WL voids to test modified gravity theories. The modified gravity parameter will have degeneracies with other cosmological parameters, so it will be important to constrain multiple parameters at the same time in order to account for this.

It will be useful to apply other void finders to the above constraints, which may offer complementary information or respond to masking, baryonic physics, and intrinsic alignments differently.

Finally, I have shown that WL voids are a very promising void definition that offer many advantages over galaxy voids, and that they are able to access a great deal of extra information within WL convergence maps. I have also shown how the utility of WL peaks for cosmological parameter constraints can be pushed past their abundance. Both the WL voids and the improved WL peaks are forecast to be able to constrain wCDM parameters with higher accuracy than the standard shear 2PCF for an LSST-like survey. This makes the new statistics presented in this thesis invaluable for the future of cosmological inference.

.1 Correlation matrices for different void finders

In this Appendix we present the tangential shear correlation matrices for the void finders we have studied. For simplicity we present all correlation matrices for a smoothing scale of $\theta_{\rm s} = 2.5$ arcmin and for peak catalogues with $\nu > 2$ where applicable. Fig. 1 shows the tangential shear correlation matrices for WL voids identified in WL maps without GSN, and Fig. 2 is the same but for WL maps with GSN included. The correlation matrix R_{ij} is related to the covariance matrix, cov_{ij} (which is used to calculate SNR values in Eq. (3.5.1)), through the equation,

$$R_{ij} = \frac{\mathrm{Cov}_{ij}}{\sigma_i \sigma_j}\,, \tag{.1.1}$$

where i and j are radial bin indices, R is the correlation matrix, cov is the covariance matrix and σ_i is the standard deviation in bin i, where the variance, σ^2, is given by the diagonal elements of the covariance matrix. The covariance matrix is calculated as

$$\mathrm{Cov}_{ij} = \frac{1}{N-1}\sum_{k=1}^{N}[\gamma_{\rm t}(i) - \bar{\gamma}_{\rm t}(i)][\gamma_{\rm t}(j) - \bar{\gamma}_{\rm t}(j)]\,, \tag{.1.2}$$

where $N = 192$ is the number of WL maps, $\gamma_{\rm t}$ the tangential shear, and an over-bar denotes the mean from N maps.

Fig. 1 shows the $\gamma_{\rm t}$ correlation matrices for maps without GSN. The seven panels correspond to the seven WL void finders studied in this work, where dark colours indicate an anti-correlation between bins and bright colours indicate a correlation between bins (as indicated by the colour bar). In all cases, the region around the diagonal is close to unity, illustrating that neighbouring bins are highly correlated. Of all the void finding algorithms, the ones with the most correlated bins appear to be the two trough finders. This is due to the large degree of overlap between neighbouring troughs as seen in Fig. 3.2, and it is this correlation between far apart bins that produces a lower SNR for the trough algorithms relative to the other void finders in the right panel of Fig. 3.10. Similarly, Fig. 3.2 also shows that the SVF κ voids tend to clump together and overlap with each other, which explains why there is also a significant correlation between different radial bins. The same happens, though to a lesser extent, to WL minima, because there is a large number of them and so the large radius bins (of which the radii become a substantial fraction of the inter-minimum separation) start to overlap between neighbouring minima.

Fig. 2 is the same as Fig. 1, except that here we study void populations identified in WL maps that include GSN. The correlation matrices are significantly more diagonal when GSN

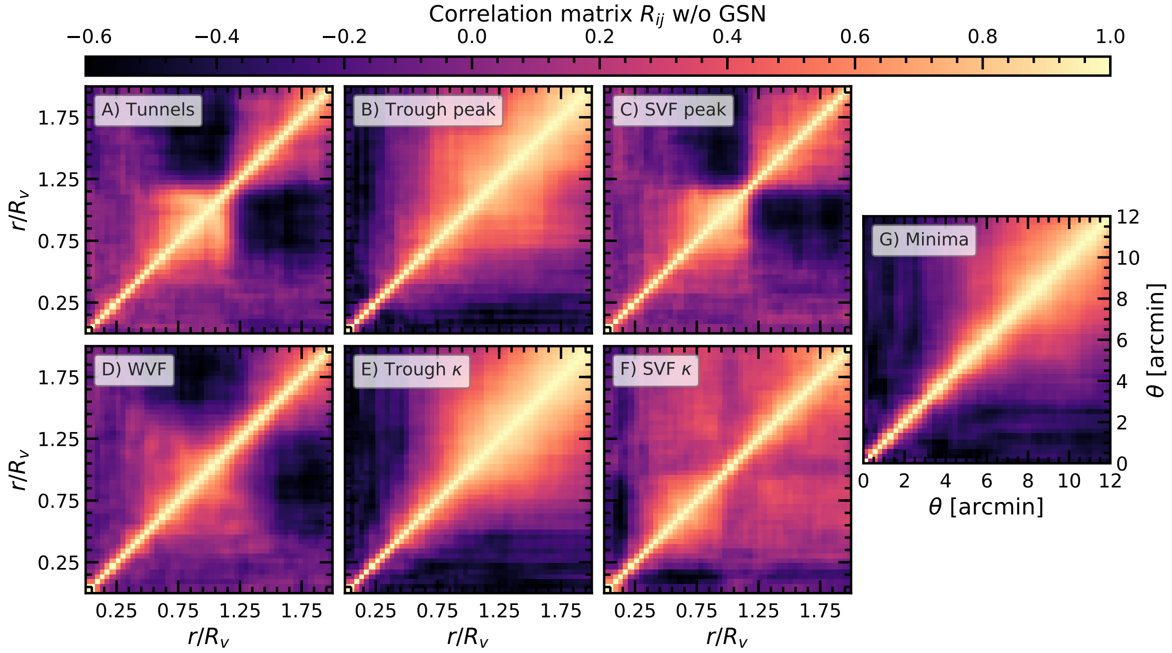

Figure 1: The tangential shear correlation matrices for all void finders discussed in this work, calculated from maps with no GSN and smoothed with $\theta_\mathrm{s} = 2.5$ arcmin. For WL void finders applied to the WL peak distribution, results are presented for peak catalogues with $\nu > 2$.

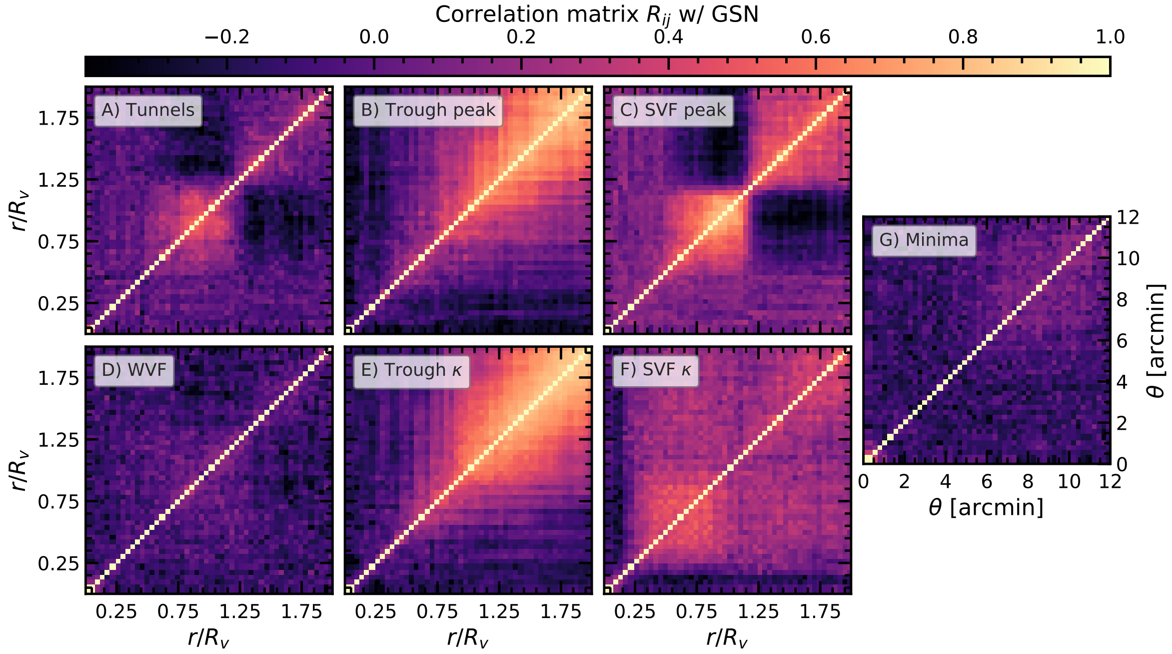

Figure 2: The same as Fig. 1 but for convergence maps that include GSN.

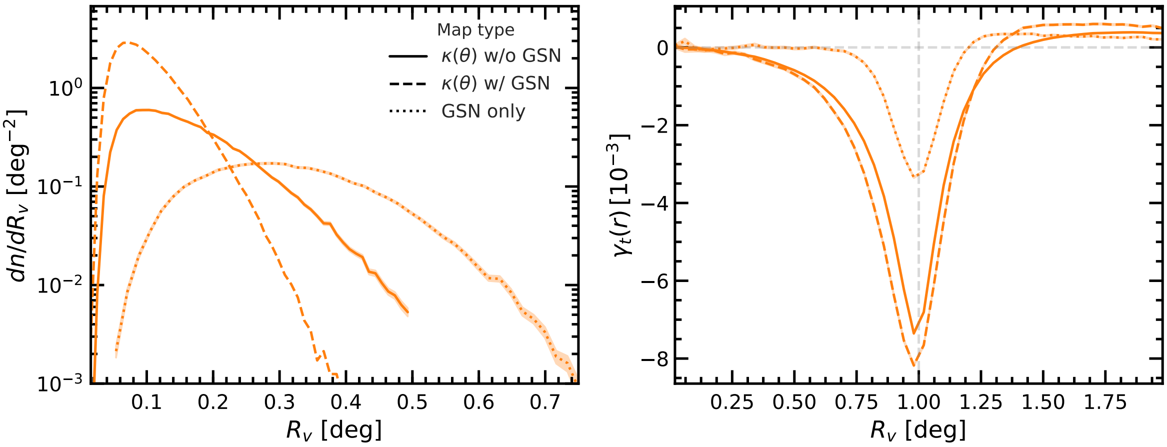

Figure 3: Tunnels identified in three different convergence maps: physical convergence without GSN (solid), physical convergence with GSN added (dashed), and GSN-only (dotted). The tunnels are identified in peak catalogues with heights $\nu > 2$, and using a smoothing scale $\theta_\mathrm{s} = 2.5$ arcmin. The shaded regions around the lines indicate the one sigma standard error bars.

is included, which shows that GSN reduces the correlation between all bins; this is partly responsible for the increase in SNR when GSN is included as shown in the right panel of Fig. 3.10. Since GSN does not reduce the amplitude of the tangential shear profiles, but does reduce the covariance between different bins, the γ_t and Cov^{-1} terms in Eq. (3.5.1) increase, yielding a larger SNR. Despite the reduction in correlation between bins from GSN, the troughs algorithms, and to a lesser extent SVF κ, still have a considerable correlation between bins with $r \gtrsim R_\mathrm{v}$, which again is due to many troughs overlapping in maps with GSN. Interestingly, adding GSN seems to reduce the correlation between different bins more efficiently for tunnels than for SVF peak voids. Finally we have checked and verified that the covariance matrices presented here agree with covariance matrices calculated from a bootstrapped version of our data set.

.2 WL voids in GSN only maps

Typically, 3D voids in the LSS are identified in galaxy distributions, where galaxies are used as tracers for a given void finder. The void lensing signal is then extracted from lensing measurements that are separate from the galaxy position measurements. This means that the observational noise and systematics associated with the galaxy positions are (mostly) independent of the noise and systematics in the lensing measurements.

In the case of WL voids, the same measurement (the WL convergence map) is used to identify voids and to measure their lensing profiles. This means that the void identification process and void lensing profiles will be closely connected, and impacted by noise in similar ways. The connection between WL void identification and the corresponding lensing profiles can be further strengthened by the fact that each void finder yields distinct lensing profile shapes that are determined by the definition employed to identify the voids, as shown and discussed in Section 3.4. Taking tunnels as an example: because by definition each tunnel contains no WL peaks and has at least three peaks on its boundary, we should expect the convergence profile to have a peak at the tunnel radius, being negative inside and approaching the background value far away (i.e., the same qualitative behaviour as seen in the physical signal in Fig. 3.9), even if the peaks are identified from a pure noise map. In other words, the WL void lensing profiles could simply be a consequence of the way 2D voids are identified from *any* WL convergence or peak distribution, rather than a physical effect.

Given that observed WL convergence maps are significantly contaminated by GSN, this means that voids identified in WL maps could potentially be due to noise, or they could be indistinguishable from spurious voids that result from noise. It is therefore important to understand how to distinguish between voids that are produced by physical signals in the WL maps and spurious voids that are the result of noise. This is the primary reason why in this paper we have tried to smooth the WL maps using filters as large as 5 arcmin, in order to suppress the impact of GSN on the measured peak and void statistics, so that the results from the no-GSN and GSN-added maps agree with each other. For completeness, in this appendix we give a slightly more detailed comparison, where we show how WL void statistics behave when these void finders are applied directly to a noise map, which is a mock WL map which contains no physical signal whatsoever.

In order to generate a GSN-only WL map, we follow the same GSN prescription used throughout this work. We first define a grid of pixels which matches the same angular size and resolution of the WL maps used in the rest of this work, and set the value of each pixel to zero. For each pixel we then add randomly drawn values from the Gaussian distribution described in Section 3.2.2, and via Eq. (1.2.15).

Fig. 3 shows tunnels identified in three WL maps: without GSN (solid), with GSN (dashed) and GSN-only (dotted). The results shown correspond to a smoothing scale, $\theta_{\rm s} = 2.5$ arcmin, and are obtained using WL peaks with heights, $\nu > 2$. The left panel shows the abundances of the tunnels in the three map types. The GSN-only maps produce fewer tunnels, which are typically larger than the tunnels in the physical maps. In particular, the GSN-only maps produces fewer small voids and more large voids, when compared to the other two map types.

This results from WL peaks clustering in the maps that contain a physical signal, and thus many of peaks are close together and produce smaller tunnels. Whereas the GSN-only maps have fewer peaks that by definition do not cluster, which results in larger voids.

The right panel shows the tangential shear profiles for tunnels identified in the three map types. As shown by the dotted line, the tangential shear profiles for the GSN-only maps remain flat at $\gamma_{\mathrm{t}} = 0$ for most of the void interior, where departure from zero only occurs near the void boundary at $r \sim 0.75R_{\mathrm{v}}$. This is due to the fact that the void interiors in the GSN-only maps are on average not underdense, which in turn is because of the random nature of the pure GSN map and the lack of gravity to physically evacuate matter from the void. Furthermore, the amplitude of γ_{t} at $r \simeq R_{\mathrm{v}}$ is significantly lower than for the maps that contain the physical signal. This is due to noise-only tunnels having less overdense boundaries than their physical counterparts. This can be understood as follows. For the noise-only maps, the three peaks which determine the tunnel boundary are overdense, but, since different points in noise-only maps are uncorrelated, the remaining pixels along the boundary can take any values and thus they would have a mean convergence of 0. In contrast, the correlations present in the physical maps mean that the pixels found at the boundary of physical tunnels are on average overdense since they are close to the overdense peaks used to define the tunnel.

We also find that the γ_{t} profile for WL tunnels identified in a pure noise map is much more sensitive to the smoothing scale θ_{s} used to smooth the convergence map. Although not shown here for the sake of clarity, we have checked the cases $\theta_{\mathrm{s}} = 1$ and 5 arcmin respectively. In the former case, the peak of the tangential shear profile from the pure noise map is as deep as that from the physical WL map, whereas in the latter case, the peak of the tangential shear profile from the pure noise map is further suppressed and becomes very weak. The same is found for WL peak catalogues with other ν thresholds.

It is evident from these tests that the statistics used to describe WL voids in this work give distinct results for the GSN-only maps, relative to the physical WL maps. This shows that WL voids are sensitive to the physical information present in WL maps, even when GSN is included.

.3 Void emulator accuracy

In order to test the accuracy of the GP emulator used to interpolate statistics between the cosmological parameter nodes in Fig. 4.1, we perform a cross validation test, which is outlined

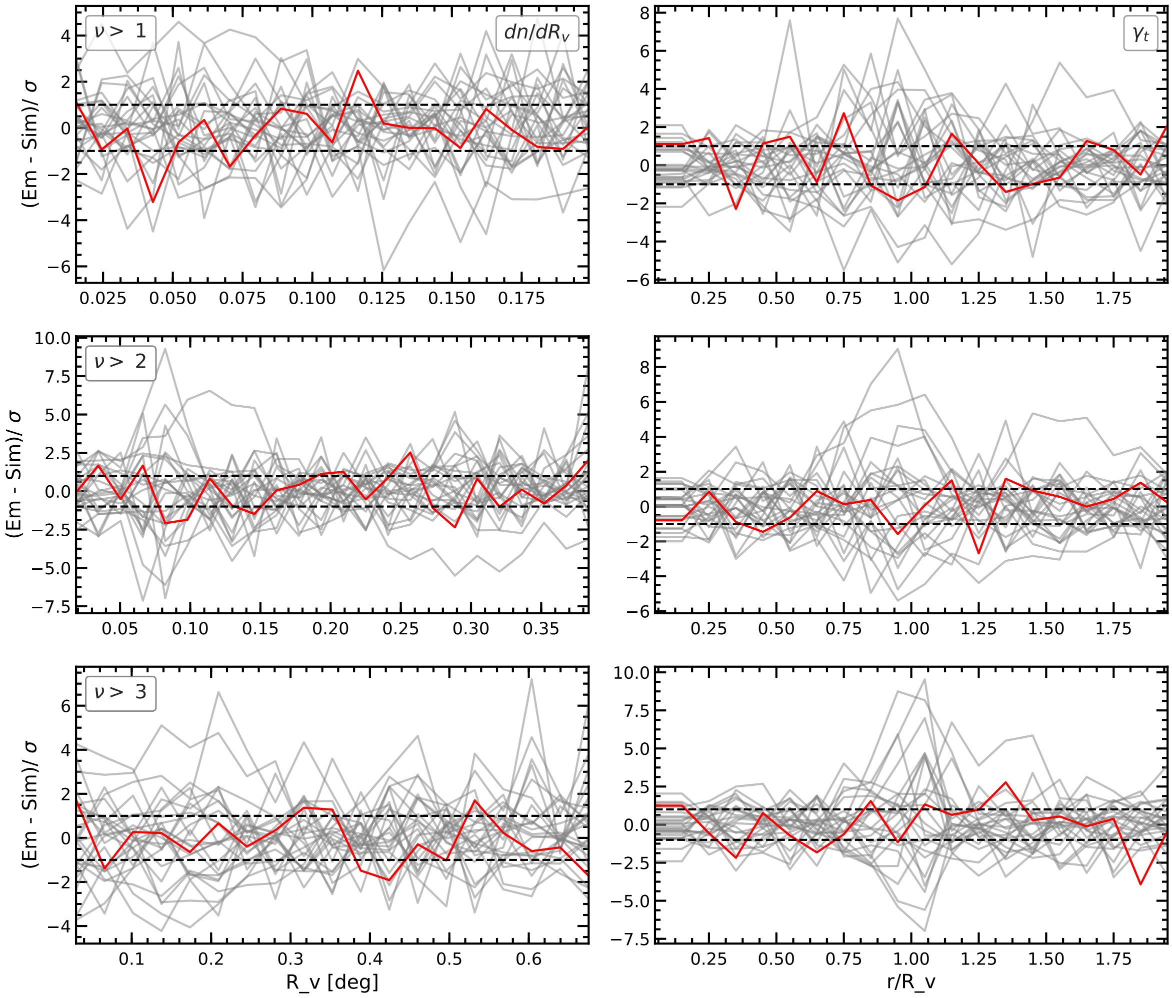

Figure 4: (Colour Online) The cross validation of the emulator accuracy. One node is removed from the training set and the emulation and simulation of the removed nodes are compared relative to its standard error. This is repeated for each of the 26 nodes, which gives an upper limit on the emulator accuracy. The left and right columns show results for the WL void abundance and tangential shear profiles respectively.

as follows. First, we remove one node from the training set of simulated data, and train the emulator with the remaining 25 cosmologies. An emulator prediction for the missing node is then calculated. The result is compared to the simulated version, by taking the difference between the two and dividing it by the standard error of the simulated data for that node. The above steps are then repeated 25 more times, by removing a different node from the training set at each iteration, which results in measurements of the emulator accuracy at each node. We note that the above procedure provides an upper limit for the emulator accuracy, since the emulator accuracy increases as more training data is used, and the cross validation measurements uses training data with one less node than the training data used in the main analysis.

Fig. 4 shows the cross validation test performed for the WL void abundance (left column) and the tangential shear profiles (right column). Results are shown for the catalogues with $\nu > 1, 2$ and 3 in the top, middle and bottom rows respectively. The cross validation test at each node is plotted in grey, with the fiducial cosmology plotted in red. We highlight the fiducial cosmology because we use it as our mock observed data when generating likelihood contours. This makes it the most important region of the parameter space to emulate accurately.

The figure shows that the emulator accuracy does not vary greatly as a function of the ν threshold. We find that the emulator is able to accurately predict both the WL void abundance and the tangential shear profiles at roughly the 1σ level, as denoted by the black dashed lines.

Regions towards the center of the 4D parameter space will be emulated more accurately than those at the boundary, since there is less training data for the GP emulator to train from at the edges of the parameter space. This is what creates the large spread amongst the grey curves in each panel, where curves towards the center of the 4D parameter space are more accurate, as shown by the fiducial cosmology. We are currently developing a suite of simulations to sample areas of the *cosmo*-SLICS parameter space more densely, which will help to further improve the accuracy of the emulator by providing more training cosmologies that more densely sample the parameters space through Latin hypercubes or other node design schemes.

.4 The impact of the map smoothing scale

The analyses carried out in this work used smoothed WL convergence maps, which is required to suppress GSN. However this introduces an additional free parameter in the analysis – the

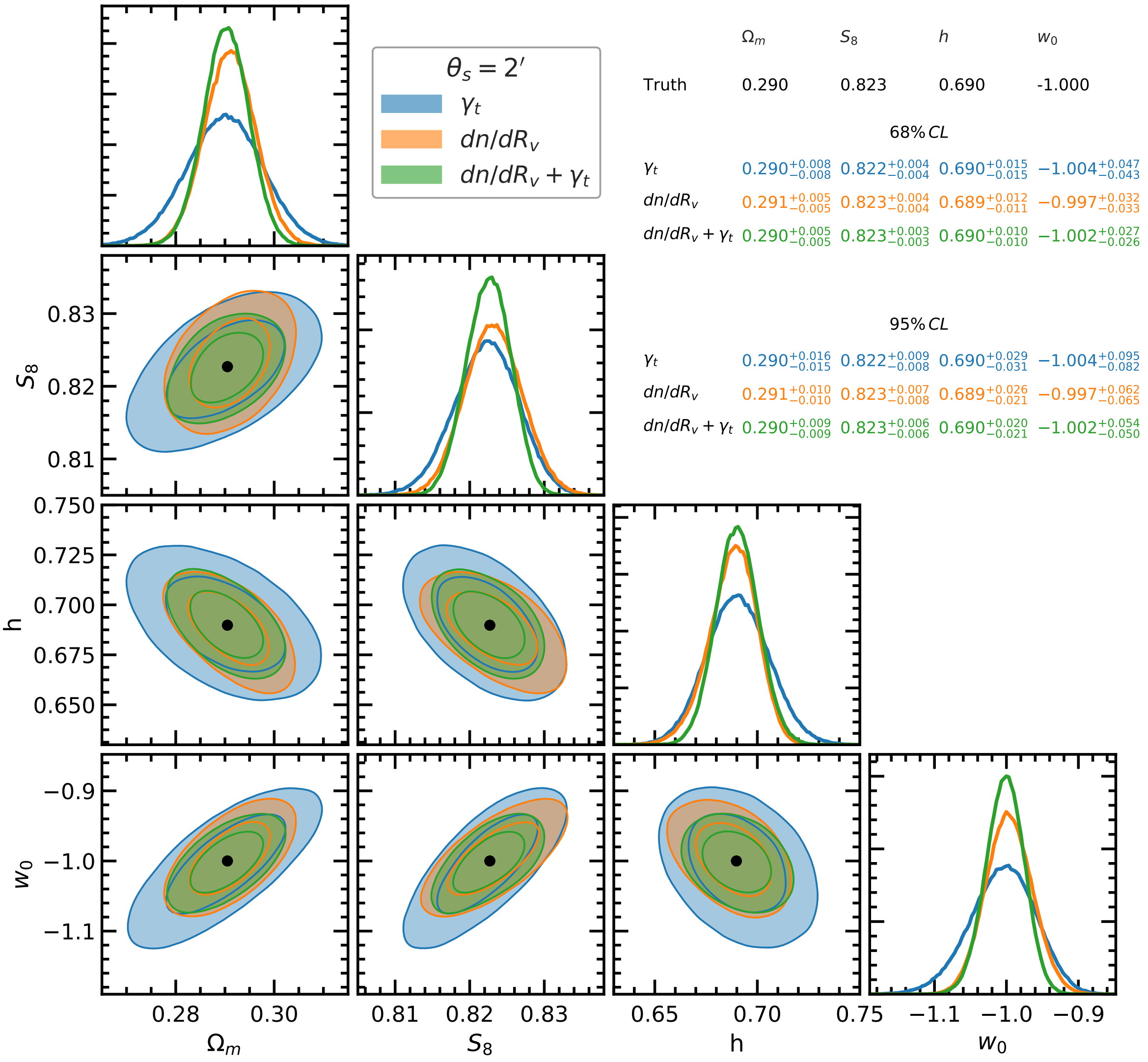

	Ω_m	S_8	h	w_0
Truth	0.290	0.823	0.690	-1.000
		68% CL		
γ_t	$0.290^{+0.008}_{-0.008}$	$0.822^{+0.004}_{-0.004}$	$0.690^{+0.015}_{-0.015}$	$-1.004^{+0.047}_{-0.043}$
dn/dR_v	$0.291^{+0.005}_{-0.005}$	$0.823^{+0.004}_{-0.004}$	$0.689^{+0.012}_{-0.011}$	$-0.997^{+0.032}_{-0.033}$
$dn/dR_v + \gamma_t$	$0.290^{+0.005}_{-0.005}$	$0.823^{+0.003}_{-0.003}$	$0.690^{+0.010}_{-0.010}$	$-1.002^{+0.027}_{-0.026}$
		95% CL		
γ_t	$0.290^{+0.016}_{-0.015}$	$0.822^{+0.009}_{-0.008}$	$0.690^{+0.029}_{-0.031}$	$-1.004^{+0.095}_{-0.082}$
dn/dR_v	$0.291^{+0.010}_{-0.010}$	$0.823^{+0.007}_{-0.008}$	$0.689^{+0.026}_{-0.021}$	$-0.997^{+0.062}_{-0.065}$
$dn/dR_v + \gamma_t$	$0.290^{+0.009}_{-0.009}$	$0.823^{+0.006}_{-0.006}$	$0.690^{+0.020}_{-0.021}$	$-1.002^{+0.054}_{-0.050}$

Figure 5: (Colour Online) Likelihood contours for the statistics presented in Table 4.1, with WL void statistics identified in WL convergence maps smoothed over a 2 arcmin scale.

smoothing scale applied to the maps, where we use a Gaussian smoothing of 1 arcmin in the main body of this work. In Davies et al. (2021) we studied how varying the smoothing scale impacts the resulting WL void statistics, and Liu et al. (2015) have shown that parameter constraints from WL peaks can be improved when multiple smoothing scales are combined. It is therefore useful to also show results for a different smoothing scale.

The likelihood contours for the statistics presented in Table 4.1 are shown in Fig. 5, but for a smoothing scale of 2 arcmin. These contours behave in a similar way to the case of 1 arcmin smoothing, with tighter constraints coming from the WL void abundance compared to the tangential shear profiles. Overall these constraints are only slightly poorer than for the smaller smoothing scale.

It is possible to create constraints from combining multiple smoothing scales. However, for brevity, we leave this analysis to a future work.

.5 Correlation matrix for combined void probes

In Eq. (4.2.2) the (inverted) covariance matrix of the data vector is used to calculate the log likelihood. The diagonal elements of the matrix are the variance of each bin in the data vector and the off diagonal elements are the covariance between all possible pairs of bins. When combining multiple probes into a single data vector, it is important to include the cross covariance to ensure that any correlated or duplicate information between the probes is appropriately modelled.

As such, in Fig. 6 we present the correlation matrix for the data vector containing each of the WL probes studied in this work, which correspond to the red likelihood contour in Fig. 4.7. The correlation matrix allows for easier visual interpretation and is related to the covariance matrix as follows

$$R_{ij} = \frac{cov(i,j)}{\sigma_i \sigma_j} \tag{.5.1}$$

Where R is the correlation matrix, cov is the covariance matrix and σ is the standard deviation.

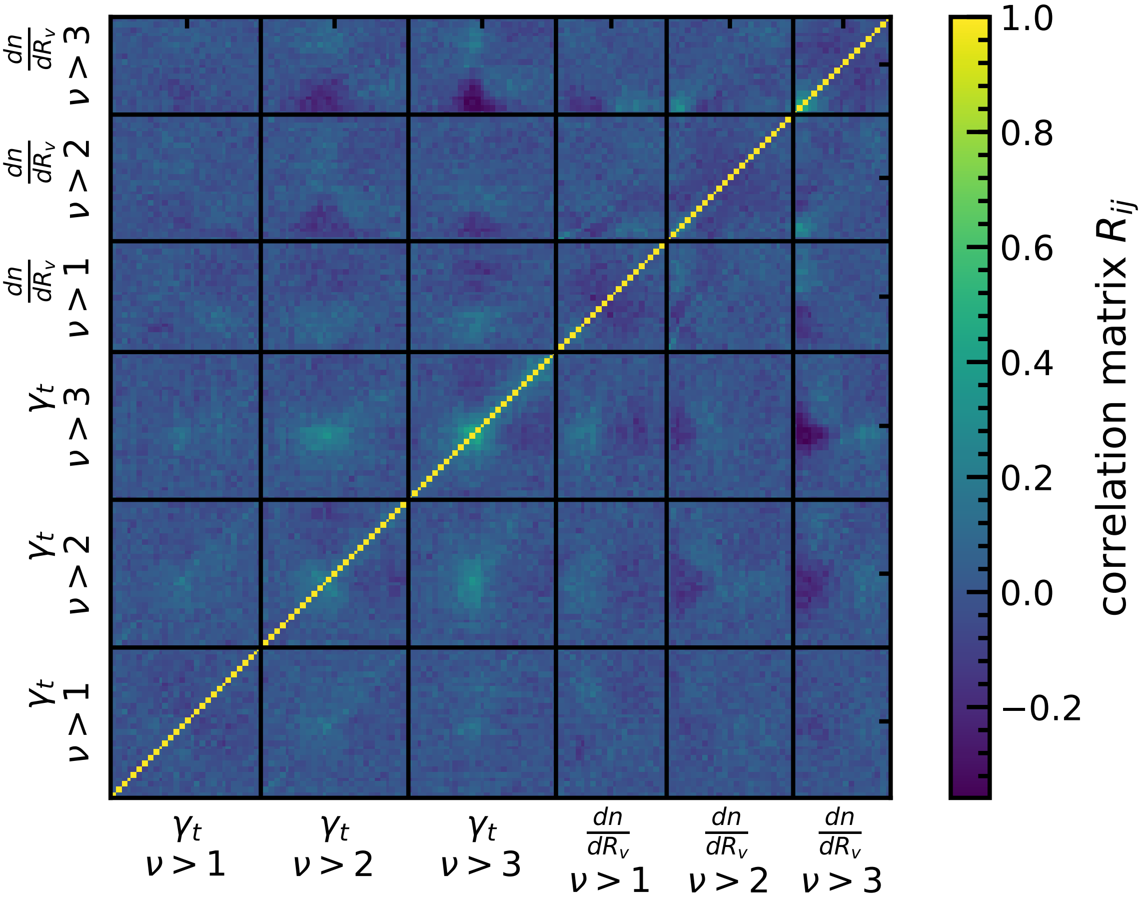

Figure 6: (Colour Online) Correlation matrix for the combination of all WL void statistics presented in this work.

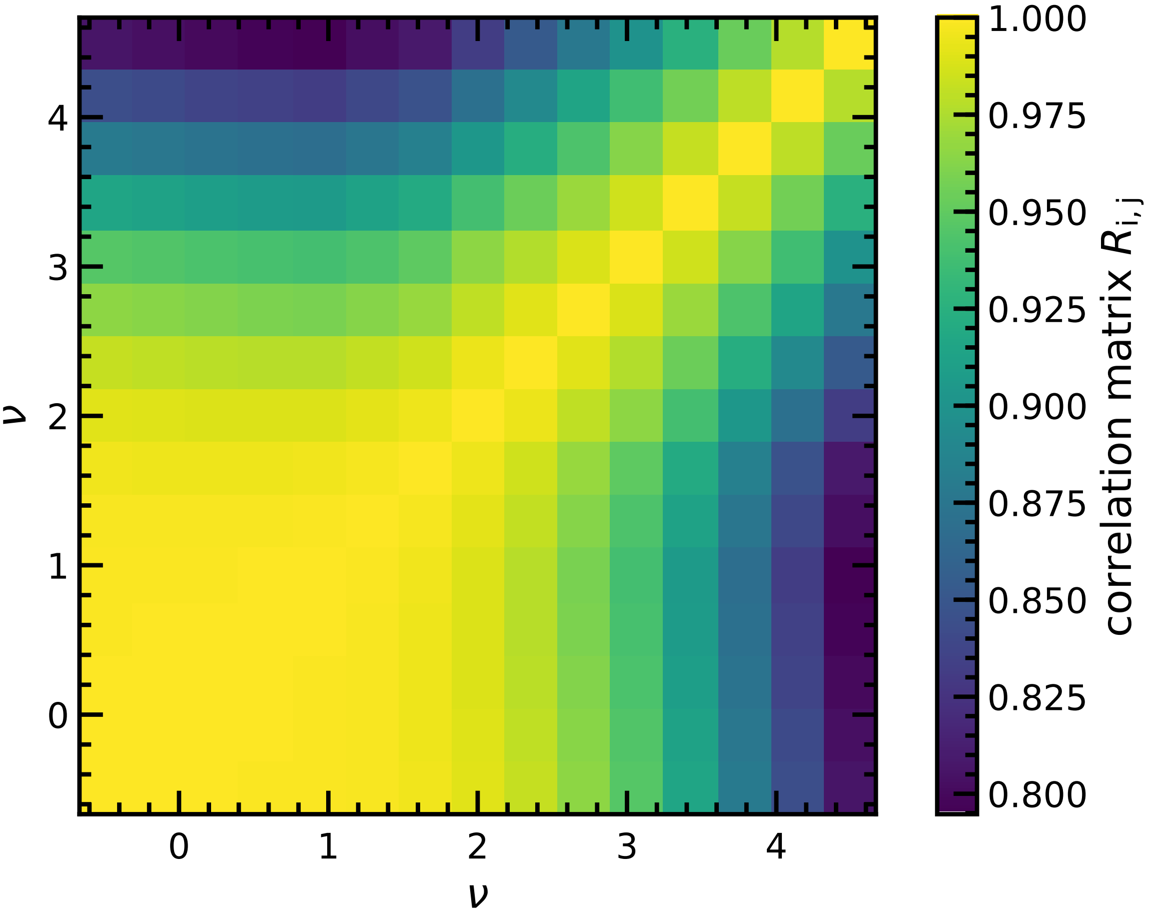

Figure 7: Correlation matrix for the peak abundance extracted from 184 100 deg^2 WL maps, where the colour-bar indicates the amplitude of $R_{i,j}$.

.6 Correlation matrices (Chapter 5)

Here we present the covariance matrices for the statistics studied in the paper. All of the covariance matrices are calculated from the statistics extracted from the 184 100 deg^2 WL maps from the T17 simulations described in section 4.2.1, using Eq. (3.5.1). To aid interpretation we have rescaled all covariance matrices to their corresponding correlation matrix using

$$R_{i,j} = \frac{\mathrm{cov(i,j)}}{\sigma_i \sigma_j}. \tag{.6.1}$$

Figs. 7, 8, and 9 show the correlation matrices for the peak abundances, void abundances, and tangential shear profiles for peaks and voids identified in the T17 WL maps.

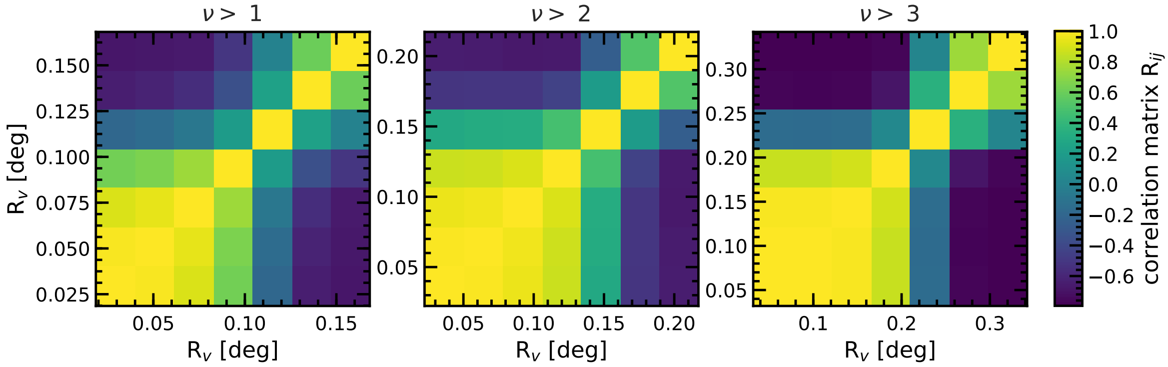

Figure 8: Correlation matrices for the void abundances extracted from 184 100 deg^2 WL maps, for three peak height cuts, $\nu > 1$ (left), $\nu > 2$ (middle) and $\nu > 3$ (right). The colour-bar indicates the amplitude of $R_{i,j}$.

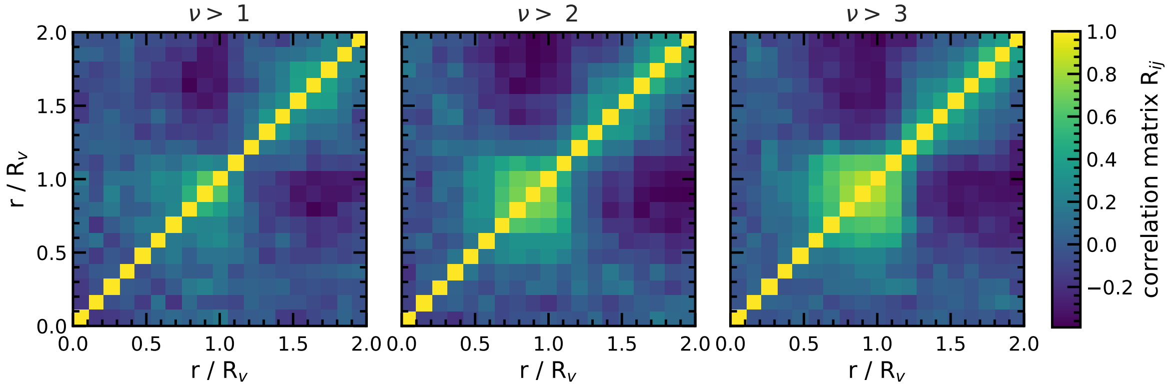

Figure 9: Correlation matrices for the tangential shear profiles extracted from 184 100 deg^2 WL maps, for three void catalogues with peak height cuts $\nu > 1$ (left), $\nu > 2$ (middle) and $\nu > 3$ (right). The colour-bar indicates the amplitude of $R_{i,j}$.

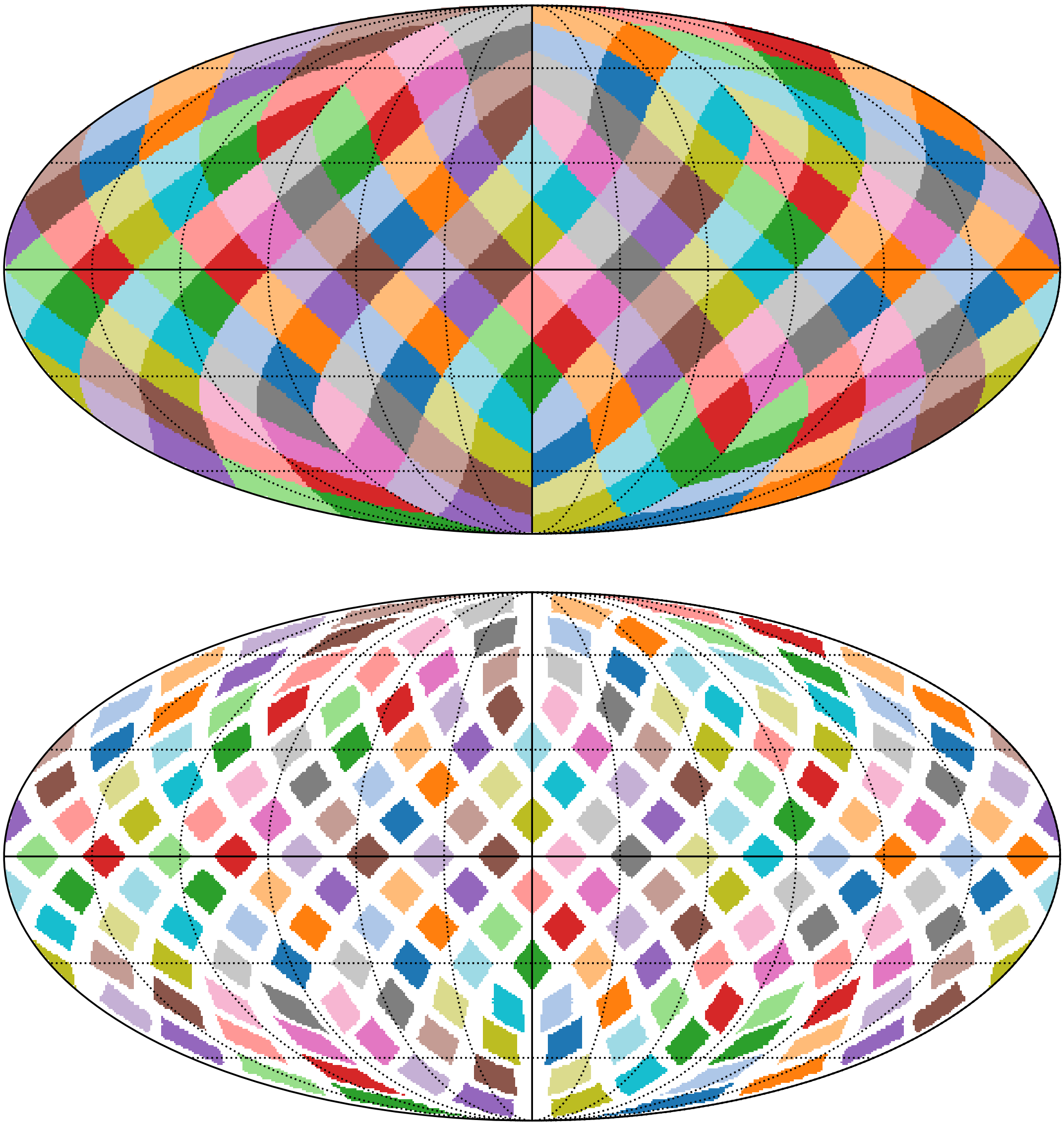

Figure 10: An illustration of our procedure of partitioning an all-sky map into smaller non-overlapping maps. We first tile the sky using a HEALPix grid with $N_{\text{side}} = 4$. This step is shown in the top panel, with each coloured patch corresponding to a HEALPix pixel. Then, we further extract a 10×10 deg^2 map from the centre of each HEALPix pixel. The resulting square maps are shown as coloured patches in the bottom panel. The white space between the patches shows that our small maps are non-overlapping. Each small square patch is then projected on to a plane tangential to their centre, giving us a 10×10 deg^2 flat map.

.7 Partitioning an all-sky map into smaller non-overlapping maps

The T17 maps are all-sky maps with a HEALPix data structure, in which pixels are stored on the surface of a sphere. To simplify our analysis, we used the flat-sky approximation and thus we needed to partition the all-sky map into smaller, and preferably, non-overlapping maps.

To achieve this, we capitalise on the HEALPix data structure and first define a set of coarser HEALPix pixels with a resolution of $N_{\mathrm{side}} = 4$, which corresponds to a pixel area of roughly 215 deg^2. We then assign each of the (higher resolution) data pixels to the coarser pixel that they are enclosed by. This is shown by the illustration on the left in Fig. 10 (using Mollweide projection), where each coloured patch shows a course pixel. Next, for each sub region defined by the coarse pixels, we define a (flat) plane tangential to the centre of the coarse pixels and project the data pixels onto that plane. We then extract a square of 10×10 deg^2 (centred on the centre of the plane) from each plane giving us 184 10×10 deg^2 flat maps. The HEALPix pixels that are projected onto the flat maps are converted into regular square pixels, where we interpolate between HEALPix pixels for square pixels that overlap with multiple HEALPix pixels. The benefit of this approach is that there is no overlap between any two maps as illustrated in the right panel of 10.

We note that a HEALPix resolution of $N_{\mathrm{side}} = 4$ actually gives 192 pixels, however due to the irregular shapes of HEALPix pixels (which arises from the requirement that all pixels have the same area), we find that 8 pixels have to be discarded since they cannot enclose squares of size 10×10 deg^2.

.8 Biased 2PCF estimation for small maps

Estimation of 2PCFs is straightforward in idealised situations. The 2PCF, $\xi(r)$, characterises the excess probability of finding a pair of tracers in two volume elements, $\mathrm{d}V_i$ and $\mathrm{d}V_j$, that are separated by a distance r:

$$\mathrm{d}P_{ij}(r) = \bar{n}^2 \left[1 + \xi(r)\right] \mathrm{d}V_i \mathrm{d}V_j, \tag{.8.1}$$

where $\bar{n}$ represents the expected tracer number density. In N-body simulations with periodic boundary conditions, as an example, $\bar{n}$ is the known mean number density and so the excess probability $\mathrm{d}P_{ij}$ can be evaluated by counting the number of pairs that are separated by a distance $r - \Delta r$ to $r + \Delta r$ and comparing that against $\bar{n}^2$. In realistic situations, $\bar{n}$ is not always known – this can for example be due to the geometry, mask, fibre collision and redshift failure in a galaxy redshift survey, or the small map size with boundaries in our WL peak catalogues. The uncertainty in the expected number of tracers in a given volume can cause biased 2PCF estimations. It is known that, for examples, the Peebles & Hauser (1974) estimator

$$\xi_{\mathrm{PH}}(\theta) = \left(\frac{N_R}{N_D}\right)^2 \frac{DD(\theta)}{RR(\theta)} - 1, \tag{.8.2}$$

and the Davis & Peebles (1983) estimator

$$\xi_{\mathrm{DP}}(\theta) = 2\frac{N_R}{N_D}\frac{DD(\theta)}{DR(\theta)} - 1, \tag{.8.3}$$

have errors that depend to the first order on the uncertainty of the expected tracer number density. On the other hand, the Hamilton (1993) and the Landy & Szalay (1993) estimators have errors which are second order in this uncertainty and are more commonly used. In the above N_D and N_R are the numbers of data and random points, and DD, DR and RR are the numbers of data-data, data-random and random-random pairs in bins $\theta \pm \delta\theta$ respectively.

The Landy-Szalay estimator is given by,

$$\xi_{\mathrm{LS}}(\theta) = 1 + \left(\frac{N_R}{N_D}\right)^2 \frac{DD(\theta)}{RR(\theta)} - \left(\frac{N_R}{N_D}\right)\frac{DR(\theta)}{RR(\theta)}. \tag{.8.4}$$

When analysing n maps, there are n different N_D, DD and DR values, that is one per map (N_R and RR can be taken as constants since the same random catalogue can be used for each map). We checked that our results are stable to a change in the number of randoms used.

Given the expression of Eq. (.8.4), there are two possible ways to calculate the mean 2PCF, $\langle\xi\rangle$, where $\langle\cdot\rangle$ denotes the mean value over the n maps, given respectively by

$$\langle\xi_{\mathrm{LS}}(\theta)\rangle_1 = \left\langle 1 + \left(\frac{N_R}{N_D}\right)^2 \frac{DD}{RR} - \left(\frac{N_R}{N_D}\right)\frac{DR}{RR}\right\rangle, \tag{.8.5}$$

and

$$\langle\xi_{\mathrm{LS}}(\theta)\rangle_2 = 1 + \left(\frac{\langle N_R\rangle}{\langle N_D\rangle}\right)^2 \frac{\langle DD\rangle}{\langle RR\rangle} - \left(\frac{\langle N_R\rangle}{\langle N_D\rangle}\right)\frac{\langle DR\rangle}{\langle RR\rangle}, \tag{.8.6}$$

where we have dropped the θ dependence of DD, DR and RR to lighten the notations. For Eq. (.8.5), we calculate n 2PCFs from the n maps and take the mean value. For Eq. (.8.6), we first calculate the mean over all maps of N_D, DD and DR, and then use these mean values to calculate the mean 2PCF. In general, these two approaches do not give identical results,

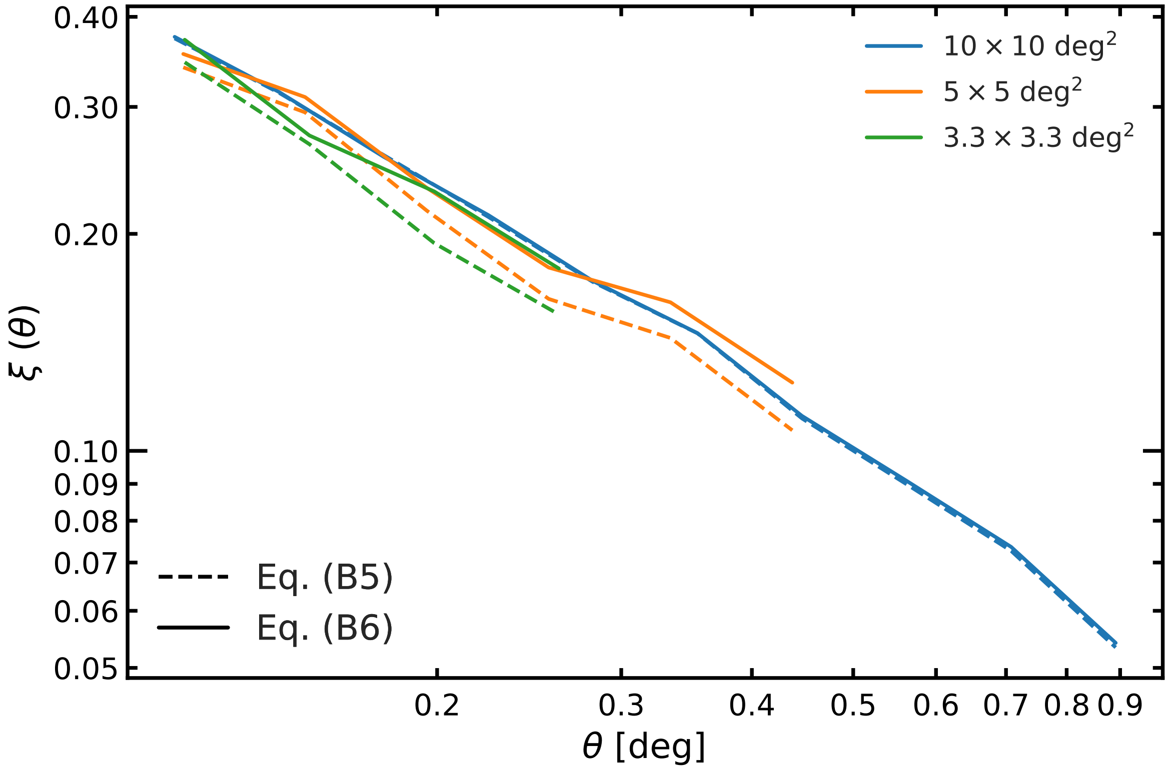

Figure 11: Mean 2PCFs calculated using Eqs. (.8.5) (dashed) and (.8.6) (solid), for maps of size 10 × 10 deg^2 (blue), 5 × 5 deg^2 (orange) and 3.3 × 3.3 deg^2 (green).

that is

$$\langle \xi_{\rm LS}(\theta) \rangle_1 \neq \langle \xi_{\rm LS}(\theta) \rangle_2. \tag{.8.7}$$

Naively, it seems natural to calculate the mean 2PCF using Eq. (.8.5) – after all, if we only had a single map, we would use this formula (excluding the outer $\langle\cdot\rangle$) to estimate the 2PCF. However, we found that this approach actually leads to biased estimates when the number of tracers varies considerably between the different maps. This is particularly the case when the number of peaks in a catalogue is low, and the effect is particularly strong for peaks with high ν values, for which the number density is low, and for small maps, such as the 3.5×3.5 deg^2 ones.

To see this point, we compare these two approaches as follows. First, we split each of the 184 T17 maps, whose size is 10×10 deg^2, into four 5×5 deg^2 maps and nine 3.3×3.3 deg^2 maps, which give us in total 184, 736 and 1656 maps of the three sizes respectively. Then, using respectively Eqs. (.8.5) and (.8.6), we calculate the mean 2PCF for the three different maps sizes, and the results are shown in Fig. 11.

Fig. 11 clearly shows that, as the T17 maps are split into progressively smaller sections, the mean 2PCF calculated using Eq. (.8.5) drops in amplitude, whereas using Eq. (.8.6) leads to a constant amplitude. The difference between the two approaches is small for the 10×10 deg^2 maps and only becomes significant for the smaller maps. This implies that the bias from Eq. (.8.5) depends on the map size, or more exactly the number of tracers used for the 2PCF estimation. We have performed similar tests for 3D galaxy 2PCFs and found a similar bias effect when using small box sizes. Finally, the mean 2PCFs from Eq. (.8.6) for the different maps sizes do not line up exactly, which is due to some pairs being lost at the sub-map boundaries as large maps are split up into smaller maps. We checked for this and found that the inclusion of cross sub-map pairs restores the original 2PCFs.

Physically, the reason why Eq. (.8.5) leads to biased 2PCF estimations is that the number of WL peaks per map is small and this translates into a large uncertainty in the mean tracer number density when estimated individually for each map. Even though this uncertainty enters the 2PCF estimation only at second order for the Landy-Szalay estimator, it can still strongly affect the latter. In contrast, Eq. (.8.6) essentially treats the n maps as a single (combined) one, for which the uncertainty in the expected mean peak number is small.

The biased 2PCF estimation using the Landy-Szalay estimator caused by the small tracer number is important for this study, since the WL maps from the Z16 simulations have a map size of 3.5×3.5 deg^2, which is in the regime where the biasing effect is strong. As a result, in this paper we calculate the mean 2PCF using Eq. (.8.6).

.9 2PCF Error estimates

For each of the Z16 cosmologies we used the $N = 512$ 3.5×3.5 deg^2 maps to evaluate the mean 2PCF $\langle \xi \rangle$. We estimate the standard error for $\langle \xi \rangle$ using the jackknife method, by calculating $N - 1$ mean values from sequentially removing individual maps from the sample, and taking the standard deviation of the $N - 1$ means from the 512 maps. However, we found the error to be significantly smaller than expected, of roughly $< 1\%$ of $\langle \xi \rangle$ itself. On the other hand, when repeating the same practice on 512 3.5×3.5 deg^2 maps extracted from the T17 all-sky map, we found the standard errors were larger and more reasonable, of roughly 2-3% of the mean 2PCF.

This discrepancy in the magnitudes of the standard errors in the two different suites of maps is likely caused by the way in which the multiple convergence maps were generated. In the Z16 case, the 512 maps were generated from multiple lines of sight by shifting, reorienting and tiling a single simulation box of size $240h^{-1}$Mpc, which means that the scatter in the different

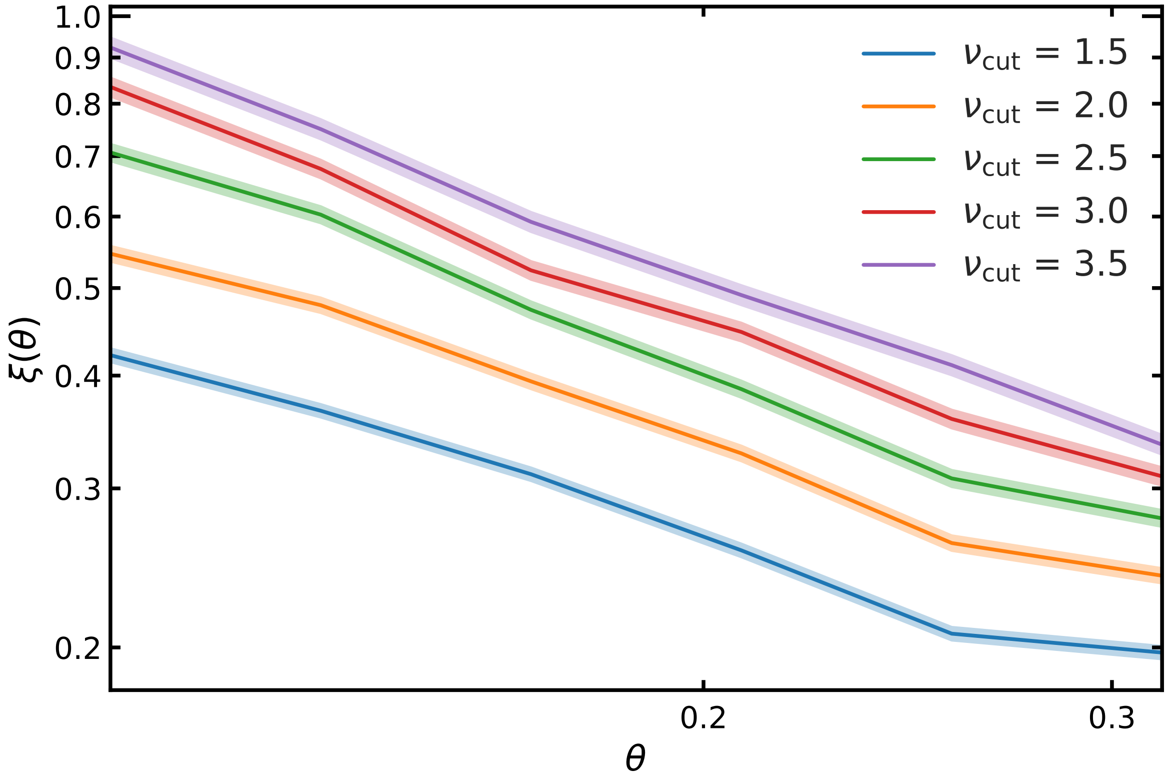

Figure 12: The mean 2PCFs of 512 3.5×3.5 deg^2 maps extracted from the T17 all sky map for peak catalogues with $\nu_{\rm cut} \in [1.5,3.5]$. The shaded regions show the jackknifed error bars.

maps is likely to only contain an error component representing the line-of-sight variation. In contrast, the T17 maps were all-sky maps generated using much larger boxes with minimal repetition of structures along the lines of sight, which means that these maps better sample the variation due to large-scale modes. The additional source of variance in the T17 maps can explain the increase in their measured standard error.

In order to have a more realistic estimate of the standard error associated to the Z16 maps, we extract 512 3.5×3.5 deg^2 maps from the T17 all-sky map and use jackknife to find the error of the mean 2PCFs, $\langle \xi \rangle$. For illustration purposes, the resulting $\langle \xi \rangle$ and their errors for a few values of $\nu_{\rm cut}$ are shown in Fig. 12 as respectively lines and shaded regions.

We then take this relative error as our estimate of the standard error for the mean 2PCFs from the Z16 maps, as a way to (approximately) include the contributions to the error from large-scale modes.

The above estimate of the error associated to the Z16 maps is likely to be an underestimate since the estimated error corresponds to the case when each of the 512 Z16 maps would have been obtained from a different N-body simulation. However, this is not the case since all the Z16 maps were obtained from the same simulation. Thus, the errors used in this paper

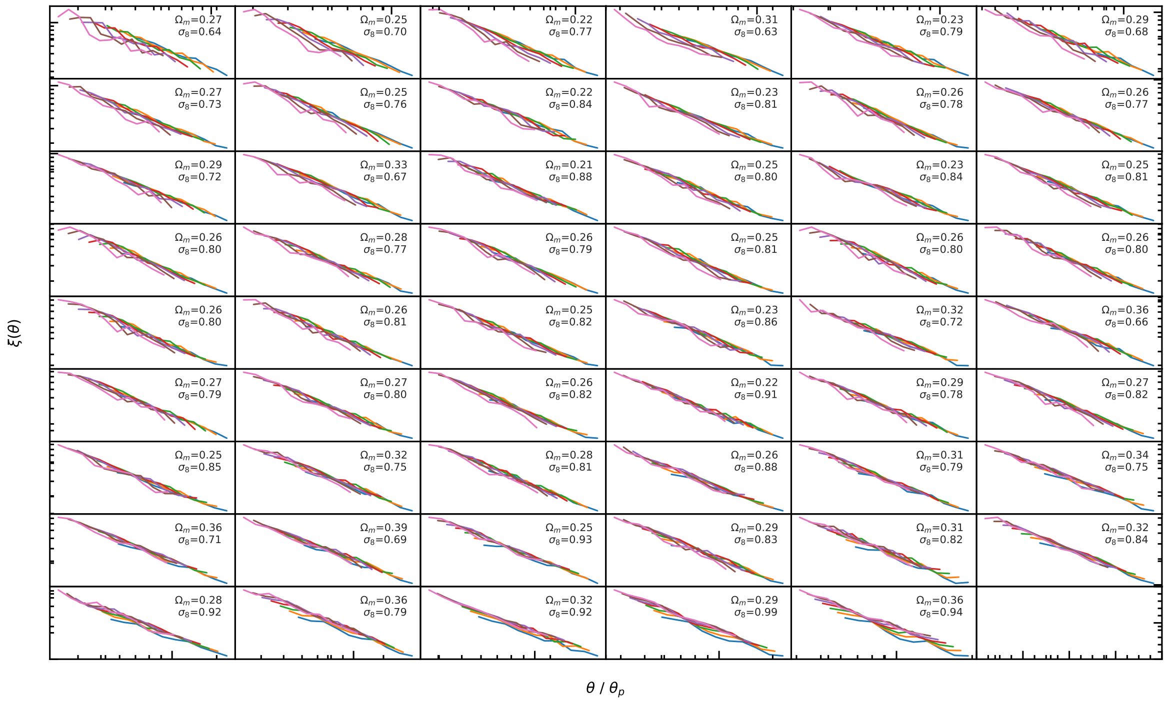

Figure 13: The same as Fig. 6.8, except only the cosmological models shown as orange points in Fig. 6.4 are plotted and the definition for ν is changed from Eq. (6.2.1) to $\nu = (\kappa - \mu)/\sigma_{\rm GSN}$ where $\sigma_{\rm GSN} = 0.013$ for all models.

serve only as a way to gain rough indications of the quality of our models for the WL peak statistics, which we present as a proof of concept. In a future work, we plan to run a suite of large simulations similar to those used by T17, for different cosmological models, to further study the self-similar properties of the rescaled peak 2PCFs.

.10 The independence of self-similarity on the ν definition

In Eq. (6.2.1) we choose to define the SNR, ν, in terms of a cosmology-dependent rms convergence, σ, which is analytically parameterised through a simple dependence on (Ω_m, σ_8), as exemplified in Fig. 6.5. Besides having a readily-predictable σ, this approach has the added benefit of allowing us to more naturally define the amplitude of WL peaks for a given cosmology relative to its own convergence rms, bearing in mind that the wide coverage of cosmological parameters means that the σ values can vary by a factor of a few across the Z16 maps; cf. Fig. 6.5.

One can argue that given an observational WL map, the value of σ receives contributions from both the physical convergence rms and the GSN, and that the actual value of σ as measured from such noisy maps is a natural choice that can be used to define ν. Such is the logic followed in Section 6.6 where we analysed the rescaled peak 2PCFs in the GSN-added maps.

Alternatively, one may argue that in real observations we do not necessarily know the true cosmology, but we do understand the survey specifications well enough to know the expected noise level. This leads to another natural way to define ν, namely by using $\sigma \equiv \sigma_{\rm GSN}$. Given this flexibility in ν definition, we would like to check that the self-similar behaviour of the 2PCFs for the resulting peak catalogues is not affected by it. This is done in Fig. 13, which is similar to Fig. 6.8 but for a subset of cosmological models (the ones represented by the orange symbols in Fig. 6.4), and where ν is defined as $\nu = (\kappa - \mu)/\sigma_{\rm GSN}$ with $\sigma_{\rm GSN} = 0.013$, which corresponds to the rms of a GSN only map smoothed with $\theta_s = 1$ arcmin, is used for all models.

We find that the cosmology-dependent description of WL peak amplitude results in a (marginal) improvement of the self similarity of the 2PCFs for all cosmologies (shown in Fig. 6.8) compared to using a σ definition that is constant across all cosmologies, which is shown in Fig. 13. It can be seen that the self similarity of the 2PCFs worsens notably for some of the panels, which correspond to models with more extreme (Ω_m, σ_8) values. This is not surprising because, as mentioned above, the models studied here vary wildly in their σ values, and by using a constant $\sigma_{\rm GSN}$ to define ν one is essentially selecting very different peak populations in them – in the more extreme models the peaks that end up being selected do not possess the self-similarity (remember that this property is only present for a limited range of peak heights). Hence, by using the cosmology dependent form of ν in Eq. (6.2.1), the 2PCF is self similar for a larger range of cosmologies. However, if one focuses on the more realistic (Ω_m, σ_8) parameters, then using a constant $\sigma_{\rm GSN}$ to define ν should not affect the potential of the rescaled peak 2PCF as a cosmological probe.

.11 Peak emulator accuracy

In this section we present the accuracy of the emulator used for our cosmological forecasts.

In order to test the accuracy of the emulator, we employ a cross validation test, which is outlined as follows. First, one node from the training data (simulated data) is removed, and the emulator is then trained with the remaining 25 nodes, for a given statistic. The emulator prediction for the removed node is then calculated, and this result is compared to the simulated version, by taking the difference between the two and dividing it by the standard error measured in the simulated data for that node. The above steps are repeated 25 more times, removing a different node from the training data at each iteration. This results

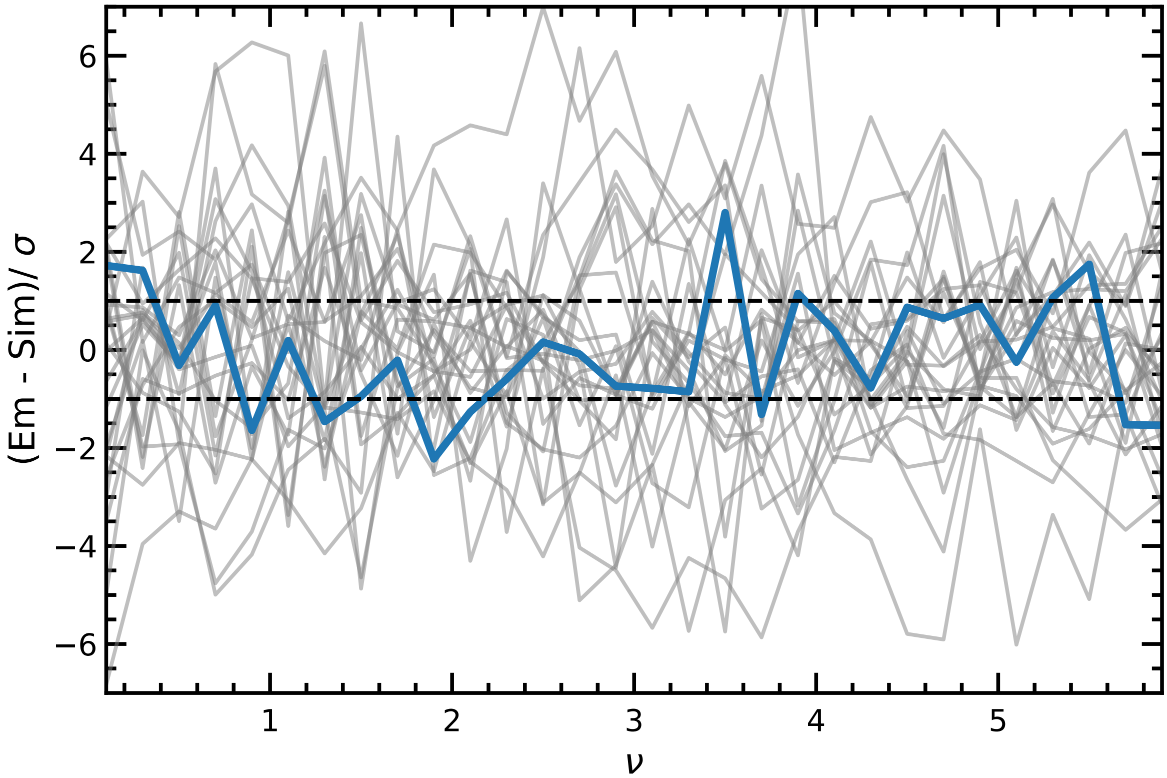

Figure 14: (Colour Online) The cross validation of the WL peak abundance emulator accuracy. One node is removed from the training set, and the difference between the emulation (Em) and simulation (Sim) predictions of the removed node are compared relative to the simulation standard error (σ). This process is repeated for each of the 26 nodes, giving an upper limit on the emulator accuracy. The iteration where the node for the fiducial cosmology is removed is shown by the blue line. Dashed lines are added at the 1σ level to help guide the reader.

in measurements of the emulator accuracy at each node, which is an upper limit, since the accuracy increases as more training data is used, and the cross validation measurements use training data with one less node than the training data used in the main analysis.

Fig. 14 shows the cross validation test for WL peak abundance. The cross validation for the fiducial cosmology is shown in blue, and the remaining nodes are shown in grey. The fiducial cosmology is the node of most interest, as all posterior contours presented in this work reside close to this region. The dashed lines delineate the region where the accuracy of the emulator is within the standard error of the simulated data. The blue curve shows that, for the fiducial cosmology, the emulator is accurate to within 1σ, as roughly 68% of the bins are within the 1σ region. The grey curves show that the accuracy is lower for the other nodes, and we find that the accuracy decreases as we approach the edges of the *cosmo*-SLICS parameter space. This is to be expected, as the emulator has less data to train from for these regions. Fig. 15 is similar to Fig. 14, but shows the percentage accuracy of the emulator for the cross validation

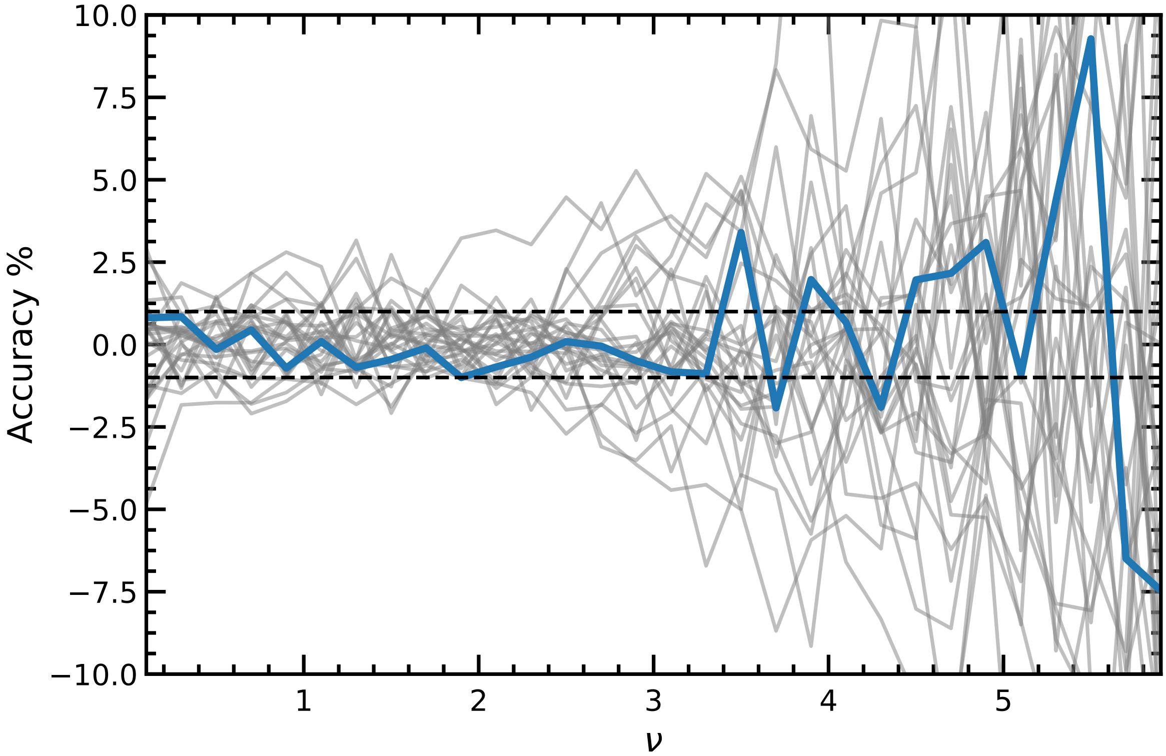

Figure 15: (Colour Online) The same as Fig. 14, but showing the percentage accuracy relative to the simulated predictions. The dashed lines enclose the 1% region.

test. We can observe that the accuracy is within roughly 1% for $\nu \lesssim 3$, increasing to up to 4% at $\nu \gtrsim 5$ due to the more noisy measurement for the high-ν peaks.

Fig. 16 is the same as Fig. 14, but shows the cross validation test for the WL peak 2PCF, for peak catalogues with heights $\nu > 1$ (top left), $\nu > 2$ (top right), $\nu > 3$ (bottom left) and $\nu > 4$ (bottom right). The figure shows that, similar to the WL peak abundance, the emulator is accurate to within 1σ at the fiducial cosmology for the peak 2PCF for all four catalogues. Fig. 17 is the same as Fig. 16, but shows the percentage accuracy of the peak 2PCF emulator applied in the cross-validation test. For the $\nu > 1$ catalogue, the accuracy is mostly within 10%, with a few bin at 20%. The accuracy is within 10% for the $\nu > 2$ and 3 peak catalogues, and for $\nu > 4$ the accuracy is within 10% except for the final bin.

.12 Peak covariance and peak-void cross covariance

As shown by Eq. (7.3.2) we require the (inverted) covariance matrix of the data vector in order to produce our forecasts. Within the matrix, the diagonal elements correspond to the variance of each of the data vector bins and the off-diagonal elements give the covariance between all possible pairs of bins. When multiple probes are combined into a single data

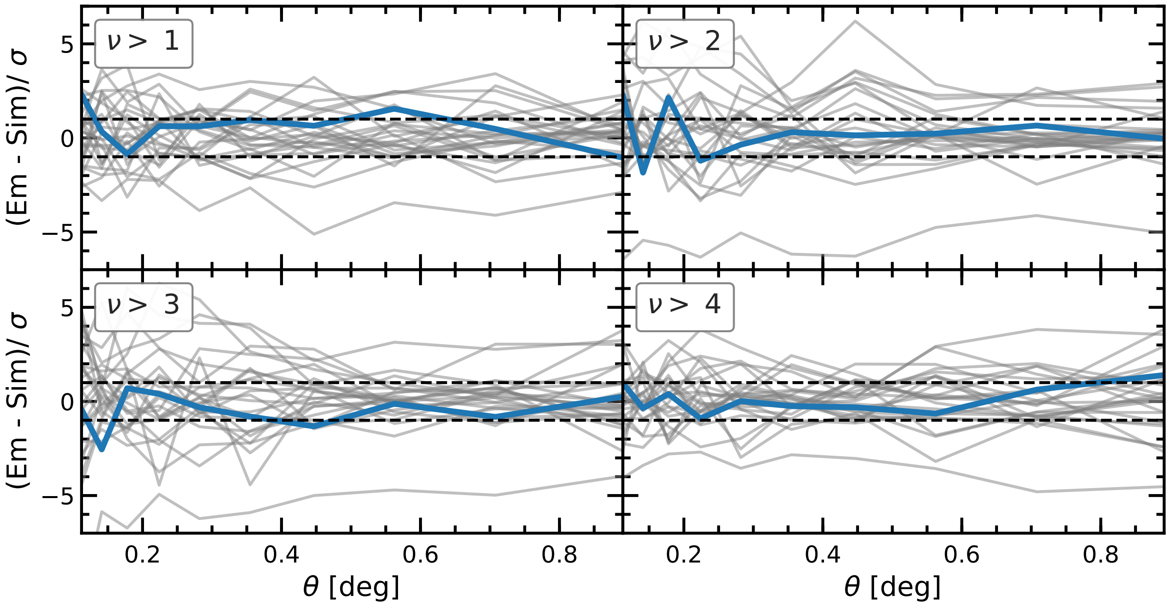

Figure 16: The same as Fig. 14 but for the WL peak 2PCFs. The four panels correspond to the WL peak 2PCFs of WL peaks with heights $\nu > 1$ (top left), $\nu > 2$ (top right), $\nu > 3$ (bottom left) and $\nu > 4$ (bottom right).

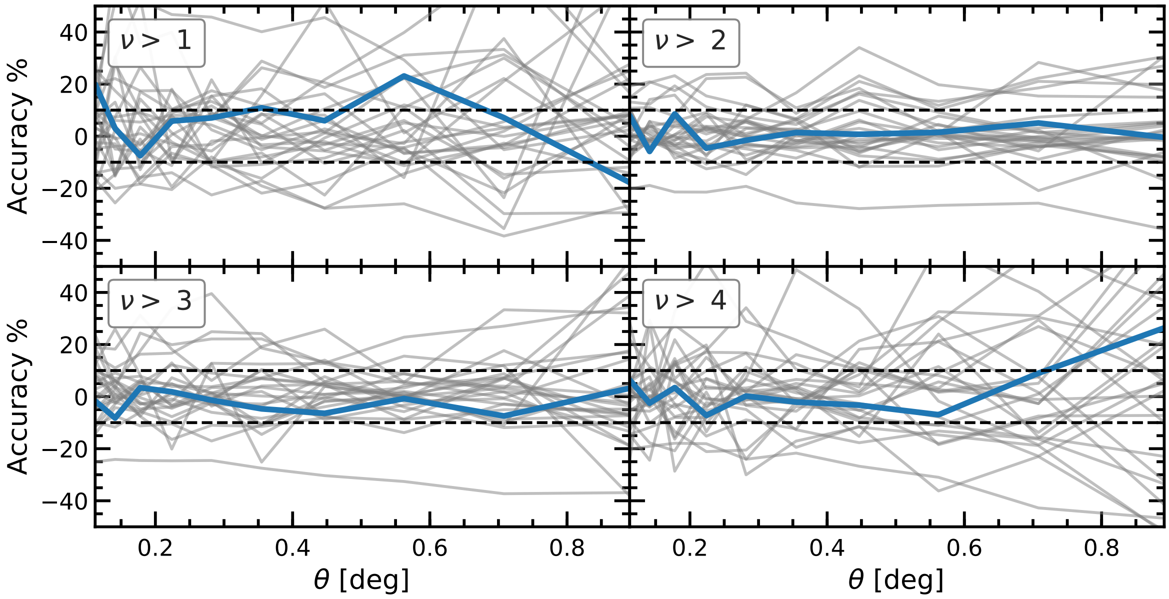

Figure 17: The same as Fig. 16 but for the percentage accuracy relative to the simulated predictions. The dashed lines enclose the 10% region.

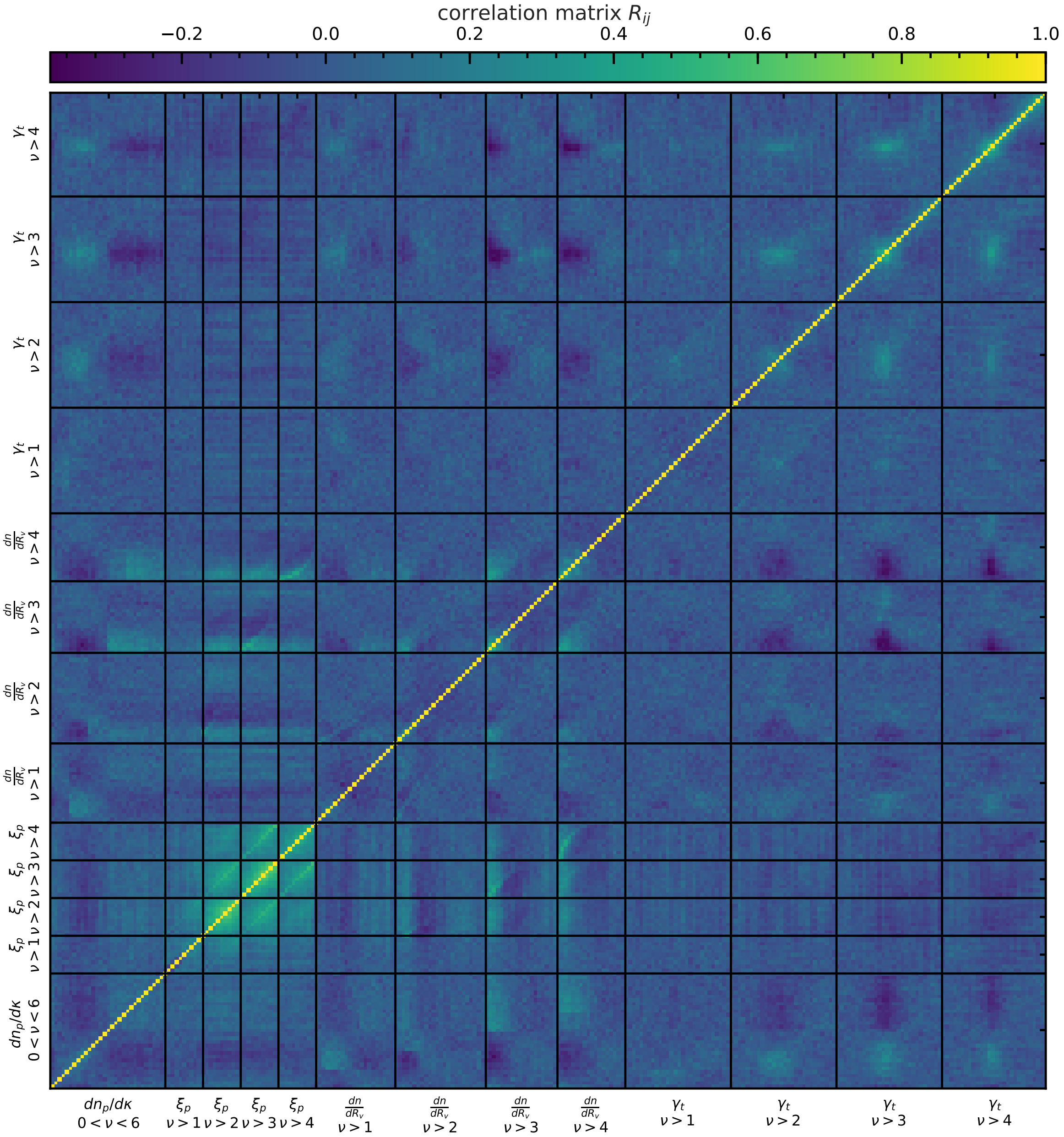

Figure 18: (Colour Online) The correlation matrix for all probes studied in this work, which are as follows (from left to right): peak abundance ($dn/d\kappa$), peak 2PCF (ξ_p), void abundance (dn/dR_v) and void tangential shear profiles (γ_t).

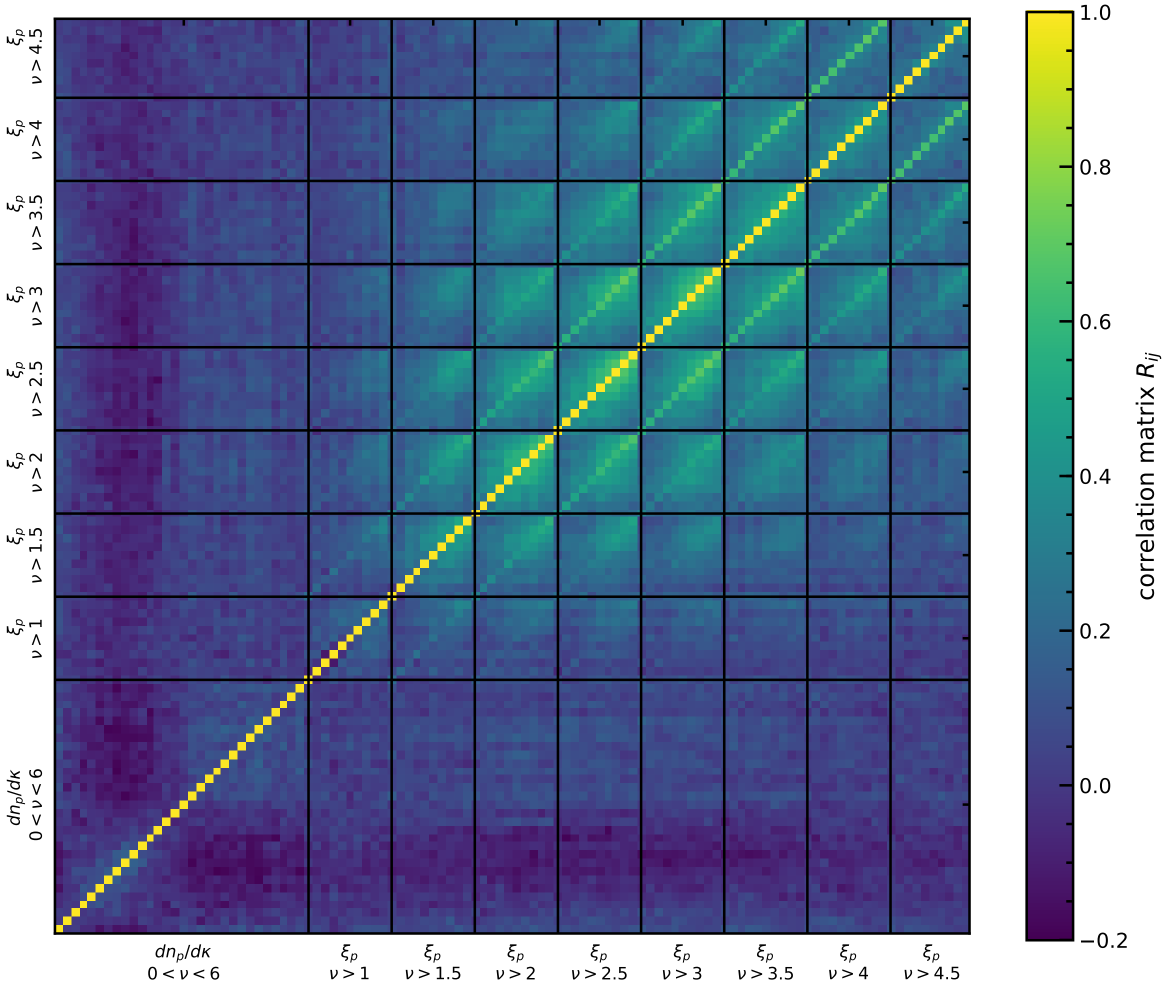

Figure 19: (Colour Online) The correlation matrix for the combination of the peak abundance $(dn/d\kappa)$ and the peak 2PCF (ξ_p, for eight catalogues with $\nu > 1.0, 1.5, ..., 4.5$).

vector, any correlated or duplicate information between the probes is accounted for by the cross covariance within the matrix.

In Fig. 18 we present the total correlation matrix for the all of the probes studied in this work. This corresponds to the matrix that is used to produce the green likelihood contour in Fig. 7.8. We present the correlation matrix instead of the covariance matrix, as it allows for easier visual interpretation, which is expressed in terms of the covariance matrix as follows

$$R_{ij} = \frac{\mathrm{cov}(i,j)}{\sigma_i \sigma_j} \, , \tag{.12.1}$$

where R is the correlation matrix, cov is the covariance matrix and σ is the standard deviation for a given bin.

Starting from the bottom left of the figure, the diagonal tiles enclosed by the black lines show the correlation for the following statistics (which are labelled with the range of peak heights used in their identification): peak abundance ($0 < \nu < 6$), peak 2PCF (four catalogues with thresholds $\nu > 1, 2, 3, 4$), and WL void abundance and WL void tangential shear profiles where the voids are identified using the same four peak catalogues. The remaining off-diagonal terms show the cross-covariances between all possible combinations of the probes.

For the peak abundance, the figure shows that the low amplitude peaks are somewhat correlated with other low amplitude peaks, and a similar behaviour is present for the high amplitude peaks, as shown by the green regions in the bottom left and top right of the peak abundance correlation tile. There also appears to be a small amount of anti-correlation between low and high amplitude peaks, as shown by the dark regions in the top left and bottom right of the tile.

For the diagonal peak 2PCF tiles, each bin in the 2PCF appears to be correlated with all of the other bins. For the off-diagonal tiles between the different peak 2PCFs, there is also a high amount of correlation, which is again expected, as the main difference between the 2PCFs is simply a change in amplitude, and all catalogues have some fraction of their tracer population in common.

For the tiles representing the correlation between the peak 2PCFs and the WL void abundances, we see some correlation between the peak 2PCFs and the small radii WL voids (especially for high ν thresholds). This is also to be expected since the WL voids are identified from a Delaunay triangulation of the peaks, which will be sensitive to the peak clustering. It is interesting to see that this correlation drops off as the void size increases, which may indicate that higher-order clustering such as the three-point correlation function of WL peaks dictates the abundance of large voids.

In Fig. 19 we show the correlation matrix for the peak abundance combined with the eight peak 2PCFs with $\nu > 1.0, 1.5, ..., 4.5$. The figure shows that, for the peak 2PCF, adjacent catalogues (similar ν thresholds) are highly correlated. This is to be expected as the tracer populations are very similar for adjacent catalogues. The correlation reduces significantly as the difference between the ν thresholds increases, which is again expected as this is where the tracer populations will differ the most. The low correlation between the peak 2PCFs with very different ν thresholds is a strong contribution to the improved constraining power from the combination of multiple peak 2PCFs, alongside any complementary parameter degeneracy directions.

Bibliography

Aihara, H., AlSayyad, Y., Ando, M., et al. *Second data release of the Hyper Suprime-Cam Subaru Strategic Program.* PASJ, **71**(6) (2019), 114. `1905.12221`.

Albrecht, A., Bernstein, G., Cahn, R., et al. *Report of the Dark Energy Task Force.* ArXiv e-prints (2006), astro-ph/0609591. `astro-ph/0609591`.

Amendola, L., Appleby, S., Bacon, D., et al. *Cosmology and Fundamental Physics with the Euclid Satellite.* Liv. Rev. Rel., **16**(1) (2013), 6. ISSN 1433-8351. URL `https://doi.org/10.12942/lrr-2013-6`.

Anderson, T.W. *An introduction to multivariate statistical analysis.* Wiley-Interscience (2003).

Aragon-Calvo, M.A., Szalay, A.S. *The hierarchical structure and dynamics of voids.* MNRAS, **428** (2013), 3409. `1203.0248`.

Asgari, M., Lin, C.A., Joachimi, B., et al. *KiDS-1000 Cosmology: Cosmic shear constraints and comparison between two point statistics.* arXiv e-prints (2020), arXiv:2007.15633. `2007.15633`.

Aubert, M., Cousinou, M.C., Escoffier, S., et al. *The Completed SDSS-IV Extended Baryon Oscillation Spectroscopic Survey: Growth rate of structure measurement from cosmic voids.* arXiv e-prints (2020), arXiv:2007.09013. `2007.09013`.

Bacon, D.J., Refregier, A.R., Ellis, R.S. *Detection of weak gravitational lensing by large-scale structure.* Mon. Not. Roy. Astron. Soc., **318**(2) (2000), 625. ISSN 0035-8711. `http://oup.prod.sis.lan/mnras/article-pdf/318/2/625/18641910/318-2-625.pdf`, URL `https://dx.doi.org/10.1046/j.1365-8711.2000.03851.x`.

Baker, T., Clampitt, J., Jain, B., et al. *Void Lensing as a Test of Gravity.* Phys. Rev. D, **98**(2) (2018), 023511. `1803.07533`.

Baker, T., et al. *The Novel Probes Project – Tests of Gravity on Astrophysical Scales.* ArXiv e-prints (2019), arXiv:1908.03430. `1908.03430`.

Barreira, A., Bose, S., Li, B., et al. *Weak lensing by galaxy troughs with modified gravity.* J. Cosmo. Astropart. Phys., **2017**(2) (2017), 031. `1605.08436`.

Barreira, A., Bose, S., Li, B., et al. *Weak lensing by galaxy troughs with modified gravity.* J. Cosmo. Astropart. Phys., **02** (2017), 031. `1605.08436`.

Barreira, A., Cautun, M., Li, B., et al. *Weak lensing by voids in modified lensing potentials.* J. Cosmo. Astropart. Phys., **2015**(08) (2015), 028. URL `https://doi.org/10.1088%2F1475-7516%2F2015%2F08%2F028`.

Barreira, A., Llinares, C., Bose, S., et al. *RAY-RAMSES: a code for ray tracing on the fly in N-body simulations.* J. Cosmo. Astropart. Phys., **2016**(5) (2016), 001. `1601.02012`.

Bartelmann, M., Schneider, P. *Weak gravitational lensing.* Phys. Rept., **340** (2001), 291. `astro-ph/9912508`.

Bertotti, B., Iess, L., Tortora, P. *A test of general relativity using radio links with the Cassini spacecraft.* Nature, **425** (2003), 374.

Biswas, R., Alizadeh, E., Wandelt, B.D. *Voids as a precision probe of dark energy.* Phys. Rev. D, **82**(2) (2010), 023002. `1002.0014`.

Bond, J.R., Kofman, L., Pogosyan, D. *How filaments of galaxies are woven into the cosmic web.* Nature, **380** (1996), 603. `astro-ph/9512141`.

Bos, E.G.P., van de Weygaert, R., Dolag, K., et al. *The darkness that shaped the void: dark energy and cosmic voids.* Mon. Not. Roy. Astron. Soc., **426**(1) (2012), 440. ISSN 0035-8711. `http://oup.prod.sis.lan/mnras/article-pdf/426/1/440/3273501/426-1-440.pdf`, URL `https://doi.org/10.1111/j.1365-2966.2012.21478.x`.

Brax, P. *Screening mechanisms in modified gravity.* CQG, **30**(21) (2013), 214005. URL `https://doi.org/10.1088%2F0264-9381%2F30%2F21%2F214005`.

Burger, P., Schneider, P., Demchenko, V., et al. *An adapted filter function for density split statistics in weak lensing.* A&A, **642** (2020), A161. `2006.10778`.

Cai, Y.C., Neyrinck, M., Mao, Q., et al. *The lensing and temperature imprints of voids on the cosmic microwave background.* MNRAS, **466** (2017), 3364. `1609.00301`.

Cai, Y.C., Padilla, N., Li, B. *Testing gravity using cosmic voids.* Mon. Not. Roy. Astron. Soc., **451**(1) (2015), 1036. ISSN 0035-8711. `http://oup.prod.sis.lan/mnras/article-pdf/451/1/1036/4166730/stv777.pdf`, URL `https://doi.org/10.1093/mnras/stv777`.

Cai, Y.C., Taylor, A., Peacock, J.A., et al. *Redshift-space distortions around voids.* MNRAS, **462** (2016), 2465. `1603.05184`.

Caldwell, R.R., Kamionkowski, M. *The Physics of Cosmic Acceleration.* ARNPS, **59**(1) (2009), 397. `0903.0866`.

Cardone, V.F., Camera, S., Mainini, R., et al. *Weak lensing peak count as a probe of f(R) theories.* Mon. Not. Roy. Astron. Soc., **430** (2013), 2896. `1204.3148`.

Cautun, M., Cai, Y.C., Frenk, C.S. *The view from the boundary: a new void stacking method.* Mon. Not. Roy. Astron. Soc., **457**(3) (2016), 2540. `1509.00010`.

Cautun, M., Paillas, E., Cai, Y.C., et al. *The Santiago-Harvard-Edinburgh-Durham void comparison - I. SHEDding light on chameleon gravity tests.* Mon. Not. Roy. Astron. Soc., **476** (2018), 3195. `1710.01730`.

Cautun, M.C., van de Weygaert, R. *The DTFE public software: The Delaunay Tessellation Field Estimator code.* ArXiv e-prints (2011), arXiv:1105.0370. `1105.0370`.

Chang, C., Pujol, A., Mawdsley, B., et al. *Dark Energy Survey Year 1 results: curved-sky weak lensing mass map.* Mon. Not. Roy. Astron. Soc., **475**(3) (2018), 3165. ISSN 0035-8711. `https://academic.oup.com/mnras/article-pdf/475/3/3165/23827388/stx3363.pdf`, URL `https://doi.org/10.1093/mnras/stx3363`.

Clampitt, J., Cai, Y.C., Li, B. *Voids in modified gravity: excursion set predictions.* Mon. Not. Roy. Astron. Soc., **431**(1) (2013), 749. ISSN 0035-8711. `http://oup.prod.sis.lan/mnras/article-pdf/431/1/749/18243874/stt219.pdf`, URL `https://doi.org/10.1093/mnras/stt219`.

Clampitt, J., Jain, B. *Lensing measurements of the mass distribution in SDSS voids.* Mon. Not. Roy. Astron. Soc., **454**(4) (2015), 3357. ISSN 0035-8711. `https://academic.oup.com/mnras/article-pdf/454/4/3357/18509360/stv2215.pdf`, URL `https://doi.org/10.1093/mnras/stv2215`.

Clampitt, J., Jain, B., Sánchez, C. *Clustering and bias measurements of SDSS voids.* MNRAS, **456** (2016), 4425. `1507.08031`.

Clerkin, L., Kirk, D., Manera, M., et al. *Testing the lognormality of the galaxy and weak lensing convergence distributions from Dark Energy Survey maps.* Mon. Not. Roy. Astron. Soc., **466**(2) (2017), 1444. `1605.02036`.

Clifton, T., Ferreira, P.G., Padilla, A., et al. *Modified gravity and cosmology.* Phys. Rep., **513** (2012), 1. `1106.2476`.

Colberg, J.M., Pearce, F., Foster, C., et al. *The Aspen-Amsterdam void finder comparison project.* Mon. Not. Roy. Astron. Soc., **387**(2) (2008), 933. `0803.0918`.

Cooray, A., Hu, W. *Weak Gravitational Lensing Bispectrum.* Astrophys. J., **548**(1) (2001), 7. URL `https://doi.org/10.1086%2F318660`.

Coulton, W.R., Liu, J., Madhavacheril, M.S., et al. *Constraining neutrino mass with the tomographic weak lensing bispectrum.* J. Cosmo. Astropart. Phys., **2019**(5) (2019a), 043. `1810.02374`.

Coulton, W.R., Liu, J., McCarthy, I.G., et al. *Weak Lensing Minima and Peaks: Cosmological Constraints and the Impact of Baryons.* ArXiv e-prints (2019b), arXiv:1910.04171. `1910.04171`.

Davies, C.T., Cautun, M., Li, B. *Weak lensing by voids in weak lensing maps.* Mon. Not. Roy. Astron. Soc., **480** (2018), L101. `1803.08717`.

Davies, C.T., Cautun, M., Li, B. *Cosmological test of gravity using weak lensing voids.* Mon. Not. Roy. Astron. Soc., **490**(4) (2019a), 4907. `1907.06657`.

Davies, C.T., Cautun, M., Li, B. *The self-similarity of weak lensing peaks.* Mon. Not. Roy. Astron. Soc., **488**(4) (2019b), 5833. `1905.01710`.

Davies, C.T., Paillas, E., Cautun, M., et al. *Optimal void finders in weak lensing maps.* MNRAS, **500**(2) (2021), 2417. `2004.11387`.

Davis, M., Peebles, P.J.E. *A survey of galaxy redshifts. V - The two-point position and velocity correlations.* ApJ, **267** (1983), 465.

DES Collaboration, Abbott, T.M.C., Aguena, M., et al. *Dark Energy Survey Year 3 Results: Cosmological Constraints from Galaxy Clustering and Weak Lensing.* arXiv e-prints (2021), arXiv:2105.13549. `2105.13549`.

Dietrich, J.P., Hartlap, J. *Cosmology with the shear-peak statistics.* Mon. Not. Roy. Astron. Soc., **402**(2) (2010), 1049. ISSN 0035-8711. `http://oup.prod.sis.lan/mnras/article-pdf/402/2/1049/3855286/mnras0402-1049.pdf`, URL `https://dx.doi.org/10.1111/j.1365-2966.2009.15948.x`.

Dvali, G., Gabadadze, G., Porrati, M. *Metastable gravitons and infinite volume extra dimensions.* PLB, **484**(1-2) (2000), 112. `hep-th/0002190`.

Erben, T., Hildebrandt, H., Miller, L., et al. *CFHTLenS: the Canada–France–Hawaii Telescope Lensing Survey – imaging data and catalogue products.* Mon. Not. Roy. Astron. Soc., **433**(3) (2013), 2545. ISSN 0035-8711. `http://oup.prod.sis.lan/mnras/article-pdf/433/3/2545/13761746/stt928.pdf`, URL `https://doi.org/10.1093/mnras/stt928`.

Falck, B., Koyama, K., Zhao, G.B., et al. *Using voids to unscreen modified gravity.* Mon. Not. Roy. Astron. Soc., **475**(3) (2018), 3262. `1704.08942`.

Fan, Z., Shan, H., Liu, J. *Noisy Weak-lensing Convergence Peak Statistics Near Clusters of Galaxies and Beyond.* ApJ, **719** (2010), 1408. `1006.5121`.

Fang, Y., Hamaus, N., Jain, B., et al. *Dark Energy Survey year 1 results: the relationship between mass and light around cosmic voids.* Mon. Not. Roy. Astron. Soc., **490**(3) (2019), 3573. ISSN 0035-8711. `https://academic.oup.com/mnras/article-pdf/490/3/3573/30338054/stz2805.pdf`, URL `https://doi.org/10.1093/mnras/stz2805`.

Fong, M., Choi, M., Catlett, V., et al. *The impact of baryonic physics and massive neutrinos on weak lensing peak statistics.* arXiv e-prints (2019), arXiv:1907.03161. `1907.03161`.

Foreman-Mackey, D., Hogg, D.W., Lang, D., et al. *emcee: The MCMC Hammer.* PASP, **125**(925) (2013), 306. `1202.3665`.

Fry, J.N. *Statistics of Voids in Hierarchical Universes.* Astrophys. J., **306** (1986), 358.

Fu, L., Semboloni, E., Hoekstra, H., et al. *Very weak lensing in the CFHTLS wide: cosmology from cosmic shear in the linear regime.* A&A, **479** (2008), 9. `0712.0884`.

Gammaitoni, L., Hänggi, P., Jung, P., et al. *Stochastic resonance.* RMP, **70** (1998), 223. URL `https://link.aps.org/doi/10.1103/RevModPhys.70.223`.

Giblin, B., Heymans, C., Harnois-Déraps, J., et al. *KiDS-450: enhancing cosmic shear with clipping transformations.* Mon. Not. Roy. Astron. Soc., **480**(4) (2018), 5529. `1805.12084`.

Giocoli, C., Moscardini, L., Baldi, M., et al. *Weak-lensing peaks in simulated light cones: investigating the coupling between dark matter and dark energy.* Mon. Not. Roy. Astron. Soc., **478** (2018), 5436. `1801.01886`.

Granett, B.R., Neyrinck, M.C., Szapudi, I. *An Imprint of Superstructures on the Microwave Background due to the Integrated Sachs-Wolfe Effect.* ApJ, **683** (2008), L99. `0805.3695`.

Gruen, D., Friedrich, O., Amara, A., et al. *Weak lensing by galaxy troughs in DES Science Verification data.* Mon. Not. Roy. Astron. Soc., **455**(3) (2015), 3367. ISSN 0035-8711. `https://academic.oup.com/mnras/article-pdf/455/3/3367/9384570/stv2506.pdf`, URL `https://doi.org/10.1093/mnras/stv2506`.

Gruen, D., Friedrich, O., Krause, E., et al. *Density split statistics: Cosmological constraints from counts and lensing in cells in DES Y1 and SDSS data.* Phys. Rev. D, **98**(2) (2018), 023507. `1710.05045`.

Gruen, D., et al. (DES). *Weak lensing by galaxy troughs in DES Science Verification data.* Mon. Not. Roy. Astron. Soc., **455**(3) (2016), 3367. `1507.05090`.

Gupta, A., Matilla, J.M.Z., Hsu, D., et al. *Non-Gaussian information from weak lensing data via deep learning.* Phys. Rev. D, **97**(10) (2018), 103515. `1802.01212`.

Habib, S., Heitmann, K., Higdon, D., et al. *Cosmic calibration: Constraints from the matter power spectrum and the cosmic microwave background.* Phys. Rev. D, **76** (2007), 083503. URL `https://link.aps.org/doi/10.1103/PhysRevD.76.083503`.

Hamana, T., Oguri, M., Shirasaki, M., et al. *Scatter and bias in weak lensing selected clusters.* Mon. Not. Roy. Astron. Soc., **425**(3) (2012), 2287. ISSN 0035-8711. `http://oup.prod.sis.lan/mnras/article-pdf/425/3/2287/18188254/425-3-2287.pdf`, URL `https://dx.doi.org/10.1111/j.1365-2966.2012.21582.x`.

Hamana, T., Sakurai, J., Koike, M., et al. *Cosmological constraints from Subaru weak lensing cluster counts.* PASJ, **67** (2015), 34. `1503.01851`.

Hamana, T., Shirasaki, M., Lin, Y.T. *Weak-lensing clusters from HSC survey first-year data: Mitigating the dilution effect of foreground and cluster-member galaxies.* PASJ, **72**(5) (2020), 78. `2004.00170`.

Hamana, T., Yoshida, N., Takada, M. *Searching for massive clusters in weak lensing surveys.* Mon. Not. Roy. Astron. Soc., **350**(3) (2004), 893. ISSN 0035-8711. `http://oup.`

prod.sis.lan/mnras/article-pdf/350/3/893/2931855/350-3-893.pdf, URL https://dx.doi.org/10.1111/j.1365-2966.2004.07691.x.

Hamaus, N., Pisani, A., Choi, J.A., et al. *Precision cosmology with voids in the final BOSS data.* J. Cosmo. Astropart. Phys., **2020**(12) (2020), 023. 2007.07895.

Hamaus, N., Pisani, A., Sutter, P.M., et al. *Constraints on Cosmology and Gravity from the Dynamics of Voids.* Phys. Rev. Lett., **117**(9) (2016), 091302. 1602.01784.

Hamaus, N., Sutter, P.M., Lavaux, G., et al. *Probing cosmology and gravity with redshift-space distortions around voids.* J. Cosom. Astropart. Phys., **2015**(11) (2015), 036. 1507.04363.

Hamaus, N., Sutter, P.M., Wandelt, B.D. *Universal Density Profile for Cosmic Voids.* Phys. Rev. Lett., **112**(25) (2014), 251302. 1403.5499.

Hamilton, A.J.S. *Toward Better Ways to Measure the Galaxy Correlation Function.* ApJ, **417** (1993), 19.

Harnois-Déraps, J., Amon, A., Choi, A., et al. *Cosmological simulations for combined-probe analyses: covariance and neighbour-exclusion bias.* Mon. Not. Roy. Astron. Soc., **481**(1) (2018), 1337. 1805.04511.

Harnois-Déraps, J., Giblin, B., Joachimi, B. *Cosmic shear covariance matrix in wCDM: Cosmology matters.* A&A, **631** (2019), A160. 1905.06454.

Harnois-Déraps, J., Martinet, N., Castro, T., et al. *Cosmic Shear Cosmology Beyond 2-Point Statistics: A Combined Peak Count and Correlation Function Analysis of DES-Y1.* arXiv e-prints (2020), arXiv:2012.02777. 2012.02777.

Harnois-Déraps, J., Martinet, N., Reischke, R. *Cosmic shear beyond 2-point statistics: Accounting for galaxy intrinsic alignment with projected tidal fields.* arXiv e-prints (2021), arXiv:2107.08041. 2107.08041.

Harnois-Déraps, J., van Waerbeke, L. *Simulations of weak gravitational lensing - II. Including finite support effects in cosmic shear covariance matrices.* Mon. Not. Roy. Astron. Soc., **450**(3) (2015), 2857. 1406.0543.

Hartlap, J., Simon, P., Schneider, P. *Why your model parameter confidences might be too optimistic. Unbiased estimation of the inverse covariance matrix.* A&A, **464**(1) (2007), 399. astro-ph/0608064.

Hennawi, J.F., Spergel, D.N. *Shear-selected Cluster Cosmology: Tomography and Optimal Filtering.* The Astrophysical Journal, **624**(1) (2005), 59. URL `https://doi.org/10.1086%2F428749`.

Heydenreich, S., Brück, B., Harnois-Déraps, J. *Persistent homology in cosmic shear: constraining parameters with topological data analysis.* arXiv e-prints (2020), arXiv:2007.13724. `2007.13724`.

Heymans, C., Rowe, B., Bonnett, C., et al. *CFHTLenS: the Canada–France–Hawaii Telescope Lensing Survey.* Mon. Not. Roy. Astron. Soc., **427**(1) (2012), 146. ISSN 0035-8711. `http://oup.prod.sis.lan/mnras/article-pdf/427/1/146/18231420/427-1-146.pdf`, URL `https://dx.doi.org/10.1111/j.1365-2966.2012.21952.x`.

Higuchi, Y., Shirasaki, M. *The imprint of f(R) gravity on weak gravitational lensing - I. Connection between observables and large-scale structure.* Mon. Not. Roy. Astron. Soc., **459** (2016), 2762. `1603.01325`.

Hikage, C., Oguri, M., Hamana, T., et al. *Cosmology from cosmic shear power spectra with Subaru Hyper Suprime-Cam first-year data.* Pub. Astron. Soc. Japan, **71**(2) (2019). ISSN 0004-6264. 43, `https://academic.oup.com/pasj/article-pdf/71/2/43/28463847/psz010.pdf`, URL `https://doi.org/10.1093/pasj/psz010`.

Hildebrandt, H., Viola, M., Heymans, C., et al. *KiDS-450: cosmological parameter constraints from tomographic weak gravitational lensing.* Mon. Not. Roy. Astron. Soc., **465** (2017), 1454. `1606.05338`.

Hoekstra, H., Mellier, Y., van Waerbeke, L., et al. *First Cosmic Shear Results from the Canada-France-Hawaii Telescope Wide Synoptic Legacy Survey.* Astrophys. J., **647**(1) (2006), 116. URL `https://doi.org/10.1086%2F503249`.

Huterer, D. *Weak lensing, dark matter and dark energy.* GRG, **42** (2010), 2177. `1001.1758`.

Jain, B., Van Waerbeke, L. *Statistics of Dark Matter Halos from Gravitational Lensing.* Astrophys. J., **530** (2000), L1. `astro-ph/9910459`.

Jennings, E., Li, Y., Hu, W. *The abundance of voids and the excursion set formalism.* Mon. Not. Roy. Astron. Soc., **434**(3) (2013), 2167. `1304.6087`.

Kaiser, N., Wilson, G., Luppino, G.A. *Large-Scale Cosmic Shear Measurements.* ArXiv e-prints (2000), astro-ph/0003338. `astro-ph/0003338`.

Kilbinger, M. *Cosmology with cosmic shear observations: a review.* Rept. Prog. Phys., **78**(8) (2015), 086901. `1411.0115`.

Kilbinger, M., Fu, L., Heymans, C., et al. *CFHTLenS: combined probe cosmological model comparison using 2D weak gravitational lensing.* Mon. Not. Roy. Astron. Soc., **430** (2013), 2200. `1212.3338`.

Kratochvil, J.M., Haiman, Z., May, M. *Probing cosmology with weak lensing peak counts.* Phys. Rev. D, **81** (2010), 043519. URL `https://link.aps.org/doi/10.1103/PhysRevD.81.043519`.

Kratochvil, J.M., Lim, E.A., Wang, S., et al. *Probing cosmology with weak lensing Minkowski functionals.* Phys. Rev. D, **85**(10) (2012), 103513. `1109.6334`.

Krause, E., Chang, T.C., Doré, O., et al. *The Weight of Emptiness: The Gravitational Lensing Signal of Stacked Voids.* ApJ, **762** (2013), L20. `1210.2446`.

Landy, S.D., Szalay, A.S. *Bias and variance of angular correlation functions.* Astrophys. J., **412** (1993), 64.

Lavaux, G., Wandelt, B.D. *Precision Cosmography with Stacked Voids.* Astrophys. J., **754**(2) (2012), 109. `1110.0345`.

Lee, J., Park, D. *Constraining the Dark Energy Equation of State with Cosmic Voids.* Astrophys. J., **696**(1) (2009), L10. `0704.0881`.

Li, B. *Voids in coupled scalar field cosmology.* Mon. Not. Roy. Astron. Soc., **411**(4) (2011), 2615. ISSN 0035-8711. `http://oup.prod.sis.lan/mnras/article-pdf/411/4/2615/3053373/mnras0411-2615.pdf`, URL `https://doi.org/10.1111/j.1365-2966.2010.17867.x`.

Li, B., King, L.J., Zhao, G.B., et al. *An analytic ray-tracing algorithm for weak lensing* . Mon. Not. Roy. Astron. Soc., **415**(1) (2011), 881. `1012.1625`.

Li, B., Zhao, G.B., Koyama, K. *Exploring Vainshtein mechanism on adaptively refined meshes.* J. Cosmo. Astropart. Phys., **2013**(5) (2013), 023. `1303.0008`.

Li, B., Zhao, G.B., Teyssier, R., et al. *ECOSMOG: an Efficient COde for Simulating MOdified Gravity.* J. Cosmo. Astropart. Phys., **2012**(1) (2012), 051. `1110.1379`.

Li, Z., Liu, J., Matilla, J.M.Z., et al. *Constraining neutrino mass with tomographic weak lensing peak counts.* Phys. Rev. D, **99**(6) (2019), 063527. `1810.01781`.

Lin, C.A., Kilbinger, M. *A new model to predict weak-lensing peak counts. I. Comparison with N-body simulations.* A&A, **576** (2015), A24. `1410.6955`.

Ling, C., Wang, Q., Li, R., et al. *Distinguishing general relativity and $f(R)$ gravity with the gravitational lensing Minkowski functionals.* Phys. Rev. D, **92** (2015), 064024. URL `https://link.aps.org/doi/10.1103/PhysRevD.92.064024`.

Liu, J., Haiman, Z. *Origin of weak lensing convergence peaks.* Phys. Rev. D, **94** (2016), 043533. `1606.01318`.

Liu, J., Hill, J.C., Sherwin, B.D., et al. *CMB lensing beyond the power spectrum: Cosmological constraints from the one-point probability distribution function and peak counts.* Phys. Rev. D, **94** (2016a), 103501. `1608.03169`.

Liu, J., Petri, A., Haiman, Z., et al. *Cosmology constraints from the weak lensing peak counts and the power spectrum in CFHTLenS data.* Phys. Rev. D, **91** (2015), 063507. `1412.0757`.

Liu, X., Li, B., Zhao, G.B., et al. *Constraining $f\ (R\ )$ Gravity Theory Using Weak Lensing Peak Statistics from the Canada-France-Hawii-Telescope Lensing Survey.* Phys. Rev. Lett., **117** (2016b), 051101. `1607.00184`.

Liu, X., Pan, C., Li, R., et al. *Cosmological constraints from weak lensing peak statistics with Canada-France-Hawaii Telescope Stripe 82 Survey.* Mon. Not. Roy. Astron. Soc., **450** (2015), 2888. `1412.3683`.

LSST Dark Energy Science Collaboration. *Large Synoptic Survey Telescope: Dark Energy Science Collaboration.* ArXiv e-prints (2012), arXiv:1211.0310. `1211.0310`.

LSST Science Collaboration, Abell, P.A., Allison, J., et al. *LSST Science Book, Version 2.0.* ArXiv e-prints (2009), arXiv:0912.0201. `0912.0201`.

Mao, Q., Berlind, A.A., Scherrer, R.J., et al. *A Cosmic Void Catalog of SDSS DR12 BOSS Galaxies.* Astrophys. J., **835**(2) (2017), 161. `1602.02771`.

Marian, L., Schneider, P., Smith, R.E., et al. *Optimized detection of shear peaks in weak lensing maps.* Mon. Not. Roy. Astron. Soc., **423**(2) (2012), 1711. ISSN 0035-8711. `http://oup.prod.sis.lan/mnras/article-pdf/423/2/1711/2913978/mnras0423-1711.pdf`, URL `https://dx.doi.org/10.1111/j.1365-2966.2012.20992.x`.

Marian, L., Smith, R.E., Hilbert, S., et al. *The cosmological information of shear peaks: beyond the abundance.* Mon. Not. Roy. Astron. Soc., **432**(2) (2013), 1338. `1301.5001`.

Marques, G.A., Liu, J., Zorrilla Matilla, J.M., et al. *Constraining neutrino mass with weak lensing Minkowski Functionals.* J. Cosmo. Astropart. Phys., **2019**(6) (2019), 019. `1812.08206`.

Martinet, N., Harnois-Déraps, J., Jullo, E., et al. *Probing dark energy with tomographic weak-lensing aperture mass statistics.* arXiv e-prints (2020), arXiv:2010.07376. `2010.07376`.

Martinet, N., Schneider, P., Hildebrandt, H., et al. *KiDS-450: cosmological constraints from weak-lensing peak statistics - II: Inference from shear peaks using N-body simulations.* MNRAS, **474**(1) (2018), 712. `1709.07678`.

Massara, E., Villaescusa-Navarro, F., Viel, M., et al. *Voids in massive neutrino cosmologies.* J. Cosmo. Astropart. Phys., **2015**(11) (2015), 018. URL `https://doi.org/10.1088%2F1475-7516%2F2015%2F11%2F018`.

Matilla, J.M.Z., Haiman, Z., Hsu, D., et al. *Do dark matter halos explain lensing peaks?* Phys. Rev. D, **94**(8) (2016), 083506. `1609.03973`.

Maturi, M., Meneghetti, M., Bartelmann, M., et al. *An optimal filter for the detection of galaxy clusters through weak lensing.* A&A, **442** (2005), 851. `astro-ph/0412604`.

McCarthy, I.G., Schaye, J., Bird, S., et al. *The BAHAMAS project: calibrated hydrodynamical simulations for large-scale structure cosmology.* MNRAS, **465**(3) (2017), 2936. `1603.02702`.

Melchior, P., Sutter, P.M., Sheldon, E.S., et al. *First measurement of gravitational lensing by cosmic voids in SDSS.* Mon. Not. Roy. Astron. Soc., **440**(4) (2014), 2922. ISSN 0035-8711. `https://academic.oup.com/mnras/article-pdf/440/4/2922/3856351/stu456.pdf`, URL `https://doi.org/10.1093/mnras/stu456`.

Munshi, D., Namikawa, T., Kitching, T.D., et al. *The Weak Lensing Bispectrum Induced By Gravity.* Mon. Not. Roy. Astron. Soc. (2020). `1910.04627`.

Nadathur, S. *Testing cosmology with a catalogue of voids in the BOSS galaxy surveys.* Mon. Not. Roy. Astron. Soc., **461**(1) (2016), 358. `1602.04752`.

Nadathur, S., Carter, P.M., Percival, W.J., et al. *Beyond BAO: Improving cosmological constraints from BOSS data with measurement of the void-galaxy cross-correlation.* Phys. Rev. D, **100**(2) (2019), 023504. `1904.01030`.

Neyrinck, M.C., Aragón-Calvo, M.A., Jeong, D., et al. *A halo bias function measured deeply into voids without stochasticity.* MNRAS, **441** (2014), 646. `1309.6641`.

Osato, K., Shirasaki, M., Yoshida, N. *Impact of Baryonic Processes on Weak-lensing Cosmology: Power Spectrum, Nonlocal Statistics, and Parameter Bias.* Astrophys. J., **806**(2) (2015), 186. `1501.02055`.

Öztireli, A.C., Gross, M. *Analysis and Synthesis of Point Distributions Based on Pair Correlation.* ACM Trans. Graph., **31**(6) (2012), 170:1. ISSN 0730-0301. URL `http://doi.acm.org/10.1145/2366145.2366189`.

Padilla, N.D., Ceccarelli, L., Lambas, D.G. *Spatial and dynamical properties of voids in a cold dark matter universe.* Mon. Not. Roy. Astron. Soc., **363**(3) (2005), 977. ISSN 0035-8711. `https://academic.oup.com/mnras/article-pdf/363/3/977/3955836/363-3-977.pdf`, URL `https://doi.org/10.1111/j.1365-2966.2005.09500.x`.

Paillas, E., Cautun, M., Li, B., et al. *The Santiago-Harvard-Edinburgh-Durham void comparison II: unveiling the Vainshtein screening using weak lensing.* Mon. Not. Roy. Astron. Soc., **484**(1) (2019), 1149. `1810.02864`.

Paillas, E., Lagos, C.D.P., Padilla, N., et al. *Baryon effects on void statistics in the EAGLE simulation.* Mon. Not. Roy. Astron. Soc., **470**(4) (2017), 4434. `1609.00101`.

Pan, D.C., Vogeley, M.S., Hoyle, F., et al. *Cosmic voids in Sloan Digital Sky Survey Data Release 7.* Mon. Not. Roy. Astron. Soc., **421**(2) (2012), 926. ISSN 0035-8711. `https://academic.oup.com/mnras/article-pdf/421/2/926/3908051/mnras0421-0926.pdf`, URL `https://doi.org/10.1111/j.1365-2966.2011.20197.x`.

Paz, D., Lares, M., Ceccarelli, L., et al. *Clues on void evolution-II. Measuring density and velocity profiles on SDSS galaxy redshift space distortions.* Mon. Not. Roy. Astron. Soc., **436**(4) (2013), 3480. `1306.5799`.

Pedregosa, F., Varoquaux, G., Gramfort, A., et al. *Scikit-learn: Machine Learning in Python.* Journal of Machine Learning Research, **12**(85) (2011), 2825. URL `http://jmlr.org/papers/v12/pedregosa11a.html`.

Peebles, P.J.E., Hauser, M.G. *Statistical Analysis of Catalogs of Extragalactic Objects. III. The Shane-Wirtanen and Zwicky Catalogs.* ApJS, **28** (1974), 19.

Peel, A., Pettorino, V., Giocoli, C., et al. *Breaking degeneracies in modified gravity with higher (than 2nd) order weak-lensing statistics.* A&A, **619** (2018), A38. `1805.05146`.

Pen, U.L., Zhang, T., van Waerbeke, L., et al. *Detection of Dark Matter Skewness in the VIRMOS-DESCART Survey: Implications for {upOmega0.* Astrophys. J., **592**(2) (2003), 664. URL `https://doi.org/10.1086%2F375734`.

Perlmutter, S., Aldering, G., Goldhaber, G., et al. *Measurements of* Ω *and* Λ *from 42 High-Redshift Supernovae.* Astrophys. J., **517**(2) (1999), 565. `astro-ph/9812133`.

Petri, A. *Mocking the weak lensing universe: The LensTools Python computing package.* AC, **17** (2016), 73. `1606.01903`.

Petri, A., Haiman, Z., Hui, L., et al. *Cosmology with Minkowski functionals and moments of the weak lensing convergence field.* Phys. Rev. D, **88**(12) (2013), 123002. `1309.4460`.

Pisani, A., Sutter, P.M., Hamaus, N., et al. *Counting voids to probe dark energy.* Phys. Rev. D, **92** (2015), 083531. URL `https://link.aps.org/doi/10.1103/PhysRevD.92.083531`.

Planck Collaboration, Aghanim, N., Akrami, Y., et al. *Planck 2018 results. VI. Cosmological parameters.* arXiv e-prints (2018), arXiv:1807.06209. `1807.06209`.

Platen, E., Van De Weygaert, R., Jones, B.J.T. *A cosmic watershed: the WVF void detection technique.* Mon. Not. Roy. Astron. Soc., **380**(2) (2007), 551. `https://academic.oup.com/mnras/article-pdf/380/2/551/18422647/mnras0380-0551.pdf`, URL `https://doi.org/10.1111/j.1365-2966.2007.12125.x`.

Pollina, G., Hamaus, N., Paech, K., et al. *On the relative bias of void tracers in the Dark Energy Survey.* Mon. Not. Roy. Astron. Soc., **487**(2) (2019), 2836. ISSN 0035-8711. `https://academic.oup.com/mnras/article-pdf/487/2/2836/28806970/stz1470.pdf`, URL `https://doi.org/10.1093/mnras/stz1470`.

Refregier, A., Amara, A., Kitching, T.D., et al. *Euclid Imaging Consortium Science Book.* arXiv e-prints (2010), arXiv:1001.0061. `1001.0061`.

Riess, A.G., Casertano, S., Yuan, W., et al. *Large Magellanic Cloud Cepheid Standards Provide a 1% Foundation for the Determination of the Hubble Constant and Stronger Evidence for Physics beyond* Λ*CDM.* Astrophys. J., **876**(1) (2019), 85. `1903.07603`.

Riess, A.G., Filippenko, A.V., Challis, P., et al. *Observational Evidence from Supernovae for an Accelerating Universe and a Cosmological Constant.* AJ, **116**(3) (1998), 1009. `astro-ph/9805201`.

Rizzato, M., Benabed, K., Bernardeau, F., et al. *Tomographic weak lensing bispectrum: a thorough analysis towards the next generation of galaxy surveys.* Mon. Not. Roy. Astron. Soc., **490**(4) (2019), 4688. ISSN 0035-8711. `https://academic.oup.com/mnras/article-pdf/490/4/4688/30489644/stz2862.pdf`, URL `https://doi.org/10.1093/mnras/stz2862`.

Sánchez, C., Clampitt, J., Kovacs, A., et al. *Cosmic voids and void lensing in the Dark Energy Survey Science Verification data.* Mon. Not. Roy. Astron. Soc., **465**(1) (2017), 746. `1605.03982`.

Schaap, W.E., van de Weygaert, R. *Continuous fields and discrete samples: reconstruction through Delaunay tessellations.* A&A, **363** (2000), L29. `astro-ph/0011007`.

Schmidt, F. *Weak lensing probes of modified gravity.* Phys. Rev. D, **78** (2008), 043002. `0805.4812`.

Schneider, M.D., Knox, L., Habib, S., et al. *Simulations and cosmological inference: A statistical model for power spectra means and covariances.* Phys. Rev. D, **78** (2008), 063529. URL `https://link.aps.org/doi/10.1103/PhysRevD.78.063529`.

Schneider, P. *Detection of (dark) matter concentrations via weak gravitational lensing.* Mon. Not. Roy. Astron. Soc., **283** (1996), 837. `astro-ph/9601039`.

Schneider, P., van Waerbeke, L., Kilbinger, M., et al. *Analysis of two-point statistics of cosmic shear. I. Estimators and covariances.* A&A, **396** (2002), 1. `astro-ph/0206182`.

Sellentin, E., Heavens, A.F. *Parameter inference with estimated covariance matrices.* Mon. Not. Roy. Astron. Soc., **456**(1) (2016), L132. `1511.05969`.

Semboloni, E., Mellier, Y., van Waerbeke, L., et al. *Cosmic shear analysis with CFHTLS deep data.* A&A, **452** (2006), 51. `astro-ph/0511090`.

Shan, H., Courbin, F., Meylan, G., et al. *Weak lensing mass map and peak statistics in Canada–France–Hawaii Telescope Stripe 82 survey.* Mon. Not. Roy. Astron. Soc., **442**(3) (2014), 2534. ISSN 0035-8711. `http://oup.prod.sis.lan/mnras/article-pdf/442/3/2534/3518079/stu1040.pdf`, URL `https://dx.doi.org/10.1093/mnras/stu1040`.

Shan, H., Kneib, J.P., Tao, C., et al. *WEAK LENSING MEASUREMENT OF GALAXY CLUSTERS IN THE CFHTLS-WIDE SURVEY.* Astrophys. J., **748**(1) (2012), 56. URL `https://doi.org/10.1088%2F0004-637x%2F748%2F1%2F56`.

Shan, H., Liu, X., Hildebrandt, H., et al. *KiDS-450: cosmological constraints from weak lensing peak statistics - I. Inference from analytical prediction of high signal-to-noise ratio convergence peaks.* Mon. Not. Roy. Astron. Soc., **474** (2018), 1116. `1709.07651`.

Sheth, R.K., van de Weygaert, R. *A hierarchy of voids: much ado about nothing.* MNRAS, **350** (2004), 517. `astro-ph/0311260`.

Shirasaki, M. *Statistical connection of peak counts to power spectrum and moments in weak-lensing field.* Mon. Not. Roy. Astron. Soc., **465** (2017), 1974. `1610.00840`.

Shirasaki, M., Hamana, T., Yoshida, N. *Probing cosmology with weak lensing selected clusters - I. Halo approach and all-sky simulations.* Mon. Not. Roy. Astron. Soc., **453** (2015), 3043. `1504.05672`.

Shirasaki, M., Nishimichi, T., Li, B., et al. *The imprint of f(R) gravity on weak gravitational lensing – II. Information content in cosmic shear statistics.* Mon. Not. Roy. Astron. Soc., **466**(2) (2017), 2402. `1610.03600`.

Shirasaki, M., Yoshida, N., Ikeda, S. *Denoising Weak Lensing Mass Maps with Deep Learning.* arXiv e-prints (2018), arXiv:1812.05781. `1812.05781`.

Sutter, P.M., Lavaux, G., Wandelt, B.D., et al. *Voids in the SDSS DR9: observations, simulations, and the impact of the survey mask.* Mon. Not. Roy. Astron. Soc., **442**(4) (2014), 3127. `1310.7155`.

Takahashi, R., Hamana, T., Shirasaki, M., et al. *Full-sky Gravitational Lensing Simulation for Large-area Galaxy Surveys and Cosmic Microwave Background Experiments.* Astrophys. J., **850** (2017), 24. `1706.01472`.

Teyssier, R. *Cosmological hydrodynamics with adaptive mesh refinement. A new high resolution code called RAMSES.* A&A, **385** (2002), 337. `astro-ph/0111367`.

Troxel, M.A., MacCrann, N., Zuntz, J., et al. (Dark Energy Survey Collaboration). *Dark Energy Survey Year 1 results: Cosmological constraints from cosmic shear.* Phys. Rev. D, **98** (2018), 043528. URL `https://link.aps.org/doi/10.1103/PhysRevD.98.043528`.

Tsujikawa, S., Tatekawa, T. *The effect of modified gravity on weak lensing.* PLB, **665** (2008), 325. `0804.4343`.

Vainshtein, A. *To the problem of nonvanishing gravitation mass.* PLB, **39**(3) (1972), 393 . ISSN 0370-2693. URL `http://www.sciencedirect.com/science/article/pii/0370269372901475`.

van de Weygaert, R., Platen, E. *Cosmic Voids: Structure, Dynamics and Galaxies.* In *International Journal of Modern Physics Conference Series*, volume 1 of *International Journal of Modern Physics Conference Series* (2011), pages 41–66. `0912.2997`.

Van Waerbeke, L. *Noise properties of gravitational lens mass reconstruction.* Mon. Not. Roy. Astron. Soc., **313**(3) (2000), 524. `astro-ph/9909160`.

Van Waerbeke, L., Benjamin, J., Vafaei, S., et al. *CFHTLenS: mapping the large-scale structure with gravitational lensing.* Mon. Not. Roy. Astron. Soc., **433**(4) (2013), 3373. ISSN 0035-8711. `http://oup.prod.sis.lan/mnras/article-pdf/433/4/3373/4927505/stt971.pdf`, URL `https://dx.doi.org/10.1093/mnras/stt971`.

Van Waerbeke, L., Mellier, Y., Erben, T., et al. *Detection of correlated galaxy ellipticities from CFHT data: first evidence for gravitational lensing by large-scale structures.* A&A, **358** (2000), astro-ph/0002500. `astro-ph/0002500`.

Verde, L., Treu, T., Riess, A.G. *Tensions between the early and late Universe.* Nature Astronomy, **3** (2019), 891. `1907.10625`.

Wei, C., Li, G., Kang, X., et al. *The correspondence between convergence peaks from weak lensing and massive dark matter haloes.* Mon. Not. Roy. Astron. Soc., **478** (2018), 2987. `1805.04114`.

Weinberg, D.H., Mortonson, M.J., Eisenstein, D.J., et al. *Observational probes of cosmic acceleration.* Phys. Rept., **530** (2013), 87. `1201.2434`.

Weiss, A.J., Schneider, A., Sgier, R., et al. *Effects of baryons on weak lensing peak statistics.* J. Cosmo. Astropart. Phys., **2019**(10) (2019), 011. `1905.11636`.

White, M.J., Hu, W. *A New algorithm for computing statistics of weak lensing by large scale structure.* Astrophys. J., **537** (2000), 1. `astro-ph/9909165`.

White, S.D.M. *The hierarchy of correlation functions and its relation to other measures of galaxy clustering.* Mon. Not. Roy. Astron. Soc., **186** (1979), 145.

Will, C.M. *The Confrontation between General Relativity and Experiment.* Living Reviews in Relativity, **17**(1) (2014), 4. ISSN 1433-8351. URL `https://doi.org/10.12942/lrr-2014-4`.

Wittman, D.M., Tyson, J.A., Kirkman, D., et al. *Detection of weak gravitational lensing distortions of distant galaxies by cosmic dark matter at large scales.* Nature, **405** (2000), 143. `astro-ph/0003014`.

Yang, X., Kratochvil, J.M., Huffenberger, K., et al. *Baryon impact on weak lensing peaks and power spectrum: Low-bias statistics and self-calibration in future surveys.* Phys. Rev. D, **87**(2) (2013), 023511. `1210.0608`.

Yang, X., Kratochvil, J.M., Wang, S., et al. *Cosmological information in weak lensing peaks.* Phys. Rev. D, **84** (2011), 043529. `1109.6333`.